MULTISCALE COMPUTATIONAL METHODS FOR WAVE PROPAGATION IN 2D PHONONIC CRYSTALS AND ACOUSTIC METAMATERIALS

By

Ruize Hu

Dissertation

Submitted to the Faculty of the

Graduate School of Vanderbilt University

in partial fulfillment of the requirements

for the degree of

DOCTOR OF PHILOSOPHY

in

Civil Engineering

February 28, 2019

Nashville, Tennessee

Approved:

Caglar Oskay, Ph.D., Chair

Douglas E. Adams, Ph.D.

Prodyot K. Basu, Ph.D.

Ravindra Duddu, Ph.D.

Jason G. Valentine, Ph.D.

To my parents and wife

ACKNOWLEDGMENTS

Studying at Vanderbilt is a very enjoyable and inspiring experience. It is my privilege to learn from many remarkable people without whom this research would not have been possible.

First and foremost I would like to express my sincere gratitude to my advisor Professor Caglar Oskay, who has always been encouraging, supportive and holding high standard in guiding me along the research path over the past four years. Professor Oskay has taught me many valuable lessons which led me to be a better researcher. His vision, enthusiasm and dedication in multiscale mechanics greatly motivated me to pursue fundamental study in this area. His personality and opinion in many aspects have strongly influenced me, which will have a profound impact on my career. I gratefully acknowledge his guidance and mentorship.

I also would like to thank my committee members Dr. Douglas E. Adams, Dr. Prodyot K. Basu, Dr. Ravindra Duddu and Dr. Jason G. Valentine, for their crucial inputs to this research work. As the department chair, Dr. Adams is always easy-going and caring to the graduate students, which I benefit a lot. In the first year of my graduate study, I learned finite element method and structural dynamics with Dr. Basu. These courses are very well taught and equipped me with solid foundation for my research. He also shared his experience in conducting high quality research, which is a precious fortune to me. Dr. Duddu taught me many wonderful classes about mechanics and offered me numerous sound advice in my study. During the weekly joint group meeting, I enjoyed discussing and learning the critical opinion from him. In the last semester, I had an opportunity to audit Dr. Valentine's course on Nanophotonic materials, an exciting and closely related area to my research. His broad knowledge and in-depth understanding in photonic metamaterials significantly broadened my vision and inspired me in pursuing the frontier of architectured materials.

I thank my research group members who have been along with me for the pleasant journey of PhD study. The constructive advice and warm encouragement from them helped me overcome numerous hard times in the past four years. Especially, I would like to acknowledge Dr. Tong Hui, Dr. Hao Yan, Dr. Shuhai Zhang, Dr. Xiang Zhang and Mr. Xiaoyu Zhang for their help in technical details and valuable conversations on research ideas.

Last but not least, I would like to express the deepest appreciation to my parents, Yi Qu and Kuan Hu, for providing me a family of care and love. I am so proud of being their son. I sincerely thank my beautiful wife, Xuan Chen, for her tremendous encouragement and support. Her companion and understanding have always been the source of my strength throughout this entire process.

Finally, I acknowledge the financial support of the National Science Foundation, CMMI Mechanics of Materials and Structures Program, and the Computational and Data Enabled Science and Engineering (CDS&E) program (Grant No.: 1435115). I acknowledge the teaching assistantship offered by the Department of Civil and Environmental Engineering.

TABLE OF CONTENTS

LIST OF TABLES

LIST OF FIGURES

Chapter 1

INTRODUCTION

1.1 Background and Motivation

1.1.1 Band gap phenomenon and classical modeling approaches

Periodic composites with tailored microstructures and material properties such as phononic crystals [124, 106] and acoustic metamaterials [82, 36] exhibit extraordinary capability in controlling elastic waves by manipulating band gaps that forbid waves to propagate within targeted frequency ranges. Unique wave phenomenon can be achieved in these composites by tailoring the microstructures, enabling remarkable novel applications, such as elastic cloak [120], seismic wave mitigation [19, 25] and acoustic superlens [79, 71]. The majority of the effort in this area so far focused on elastic materials as composite constituents. It has been recently recognized that employing viscoelastic materials could significantly expand the possibilities for these materials by leveraging the interactions between material damping and heterogeneity induced dispersion, such as shifting the stop band to lower frequencies and enhancing wave attenuation [89, 90, 67].

Band gap phenomenon, i.e., complete attenuation of waves within certain frequency ranges, has been extensively investigated for composite materials with periodic microstructures. Two mechanisms contribute to its formation, Bragg scattering in phononic crystals and local resonance in acoustic metamaterials. Bragg scattering occurs when the wavelength is of the same order of the size of microstructure, where destructive interference of the scattered waves leads to strong attenuation. Local resonance, on the other hand, can be activated at much lower frequency, by embedding microstructures that are soft and dense. As a result, attenuation can be achieved for long wave with microstructures that are orders of smaller than it is required for

Bragg scattering. The existence of band gaps depends strongly on the properties of the constituent materials, the geometry of the microstructures and volume fraction, etc.

Numerical simulations typically used in design and analysis of dynamic behaviors of periodic composites can be classified as: unit cell band structure characterization and structure-scale wave propagation simulation. The former approach characterizes the band gaps of the unit cells of composites based on the Floquet-Bloch theorem, which assumes periodicity of the unit cells in an infinite domain. Significant advances have been made in efficiently calculating the dispersion band structures [66, 73]. While this approach provides salient information about the wave velocity, location and size of the band gaps in the frequency domain, macroscopic phenomenon, such as wave-boundary interaction and wave-wave interaction, is not captured. The structure-scale simulation of wave propagation, either finite element time domain or finite difference time domain, is typically employed as the "first-principle approach" in design and analysis of these architectured composites [72, 120, 97]. However, resolution of the microstructures along with the requirement of time step size leads to prohibitive computational cost. This motivates the development of multiscale methods over the past decade towards modeling periodic composites in a more efficient manner.

1.1.2 Existing multiscale approaches

Multiscale models for heterogeneous materials are broadly classified in two categories: (1) scale separation assumption dependent and (2) scale separation assumption independent. The scale separation assumption assumes that the deformation wavelength is much larger than the size of microstructures. Based on this assumption, various homogenization models have been developed in the literature, which upscale the microstructural information in the form of effective material properties at the macroscopic scale. This type of homogenization models are valid only up to

the scale separation assumption, and is not accurate for modeling short waves. The latter group of multiscale models do not make this assumption, therefore, can be applied to a broader range of wave frequencies. However, few works in this category have been proposed for wave propagation in composite materials with demonstrated computational efficiency.

Generalized continuum theories, pioneered by Mindlin [94], Suhubi and Eringen [121] and others were developed to describe the macroscopic phenomena accounting for the microstructural effects without the need to resolve them. Gradient elasticity modeling, a special class of the generalized theories, introduces higher order gradients in the governing equation in addition to the terms that pertain to the classical continuum theory. The resulting equations of motion capture the dispersive and attenuative behavior induced by the material heterogeneity. The fourth order gradient elasticity model (with fourth order spatial, fourth order temporal and mixed spatial-temporal derivative terms) has been investigated by Askes et al. [7], Metrikine [91], Pichugin et al. [109] and others. Dontsov et al. [33] demonstrated the capability of this model in predicting the dispersion relation of one-dimensional elastic layered composites up to the second pass band, provided that the length-scale parameters associated with the higher order gradients are appropriately calibrated. However, the identification of these parameters in multidimensional problems is an outstanding issue [6].

Based on the scale separation assumption, asymptotic homogenization, pioneered by Bensoussan et al. [13] and Sanchez-Palencia [114], is frequently employed to compute the effective material properties of complex heterogeneous materials [105, 135, 136]. In the context of dynamics, Boutin and Auriault [15] first investigated the role of higher order expansions in capturing wave dispersion. Fish et al. [42, 43] proposed a spatial nonlocal homogenization model that incorporates a fourth order spatial derivative term in addition to the terms that pertain to the classical local homogenization model. The spatial nonlocal model was shown to capture wave dis-

persion in the long-wavelength regime [4]. By deriving a homogenization model that employed a mixed spatial-temporal nonlocal term, Hui and Oskay [64] studied the dispersion and attenuation of transient waves in elastic composites. More recently, Wautier and Guzina [125] extended the spatial nonlocal homogenization model by incorporating the temporal and mixed spatial-temporal nonlocal terms using the argument of asymptotic equivalence [109]. With appropriately calibrated parameters associated with the nonlocal terms, this model was shown to capture the onset and size of the first stop band in the context of dispersion analysis for anti-plane shear waves.

Computational homogenization [96, 92, 37] is a well established technique in modeling complex material behaviors across multiple scales. It poses nested initial-boundary value problems at the macroscale and microscale, which are related by the Hill-Mandel energy consistency condition. At the macroscale, the constitutive behavior at a material point is obtained through numerical evaluation of a microscale problem defined over a unit cell. This approach has been demonstrated to successfully capture the band gaps due to local resonance within acoustic metamaterials [107, 116, 80, 81, 112, 113], which occur when the separation of scales is still strictly satisfied. In phononic crystals, band gaps occur when the macroscopic wavelength is on the same order of the unit cell size. Computational homogenization models have not demonstrated their capabilities in capturing band gaps in this regime.

When the wavelength is approaching the size of microstructures, the assumption of scale separation is no longer valid. The concept of effective material properties becomes ambiguous and the upscaling of the microscale information is not straightforward. Multiscale methods independent of this assumption may be promising in modeling wave propagation in this regime, such as the elastodynamic homogenization models based on Willis' theory [127, 93, 101, 100, 117, 88], multiscale finite element method [53, 20, 21] and the method of computational continua [41, 35, 38]. However,

transient wave propagation beyond the acoustic regime has not been demonstrated using these approaches.

While the approaches mentioned above account for wave dispersion due to material heterogeneity in elastic composites, the effects of material damping were typically not considered. In contrast, among many homogenization models developed to capture the wave attenuation due to material damping in viscoelastic composites [51, 128, 129], few investigated the dispersion due to material heterogeneity. Hui and Oskay [63, 65] investigated transient wave propagation in viscoelastic composites using the spatial nonlocal homogenization model which accurately captures wave dispersion induced by material heterogeneity in the long wavelength regime.

This dissertation is dedicated to the development of multiscale computational methods to efficiently model wave propagation in phononic crystals and acoustic metamaterials. In particular, it is focused on wave dispersion and the band gap phenomenon. Multiscale methods in both of the two categories (scale separation assumption dependent and independent) are proposed. Wave propagation in phononic crystals and acoustic metamaterials are investigated in two-dimensional domain. Viscoelastic materials are considered and the effect of viscoelasticity is investigated.

The specific research objectives and associated tasks are summarized below.

Objective 1 Develop a homogenization framework for wave dispersion and attenuation in periodic composites under the scale separation assumption.

Task 1.1: Formulate a 1D homogenization model that is nonlocal in both space and time based on asymptotic expansions for elastic and viscoelastic composites.

Task 1.2: Extend the spatial-temporal nonlocal homogenization model to 2D anti-plane shear wave for elastic and viscoelastic composites.

Task 1.3: Further develop the homogenization model for in-plane wave in elastic composites.

Objective 2 Develop a multiscale method for phononic crystals and acoustic meta-

materials independent of the scale separation assumption.

Task 2.1: Formulate a spectral multiscale method for 2D in-plane elastic wave in phononic crystals and acoustic metamaterials.

Task 2.2: Propose a model order reduction strategy for computational efficiency.

1.2 Dissertation Organization

The remainder of this dissertation is organized to present the efforts conducted in achieving the objectives listed above:

- Chapter 2 details the development of the spatial-temporal nonlocal homogenization model in 1D for elastic and viscoelastic composites. This chapter covers the work published in Ref. [54].

- Chapter 3 extends the developed nonlocal homogenization model to 2D anti-plane shear wave in elastic and viscoelastic composites. This chapter covers the work published in Ref. [55].

- Chapter 4 further develops the homogenization model for 2D in-plane wave in elastic composites. This chapter includes the work published in Ref. [56].

- Chapter 5 develops a spectral multiscale method for wave propagation in phononic crystals and acoustic metamaterials.

- Chapter 6 summarizes the research work and the overall contribution of this dissertation. Future work that builds upon this dissertation is also discussed.

Chapter 2

SPATIAL-TEMPORAL NONLOCAL HOMOGENIZATION MODEL FOR TRANSIENT WAVE PROPAGATION IN PERIODIC VISCOELASTIC COMPOSITES: ONE-DIMENSIONAL CASE

2.1 Introduction

In this chapter, we formulate a spatial-temporal nonlocal homogenization model that considers the asymptotic expansions of up to eighth order for wave propagation in periodic layered composites with elastic and viscoelastic phases. The resulting macroscopic momentum balance equation of the proposed model is of the same structure as gradient elasticity models (e.g. [91, 7, 33]), yet all the model parameters are computed directly from the microscale equilibrium equations and dependent on the microstructural material properties and geometry.

The two essential ingredients in developing the spatial-temporal nonlocal homogenization model are: (1) asymptotic expansions with high order corrections; (2) construction of the gradient-type spatial-temporal nonlocal governing equation. In the context of statics, the role of high order corrections in asymptotic expansion has been investigated by Gambin and Kröner [45] and Ameen et al. [1]. For wave propagation problems, it is demonstrated that the first few orders introduce wave dispersion, which is accurate in the long wavelength regime [15, 4, 42, 43, 63, 64, 65]. Higher order expansions for wave propagation problems have not been incorporated in the literature. The spatial-temporal nonlocal governing equation is constructed directly from the momentum balance equations of successive asymptotic orders, where the accuracy is controlled by the asymptotic residual term. Through minimizing the asymptotic residual, the optimal set of model parameters are determined. The nonlocal homogenization model is then employed to formulate an effective medium model

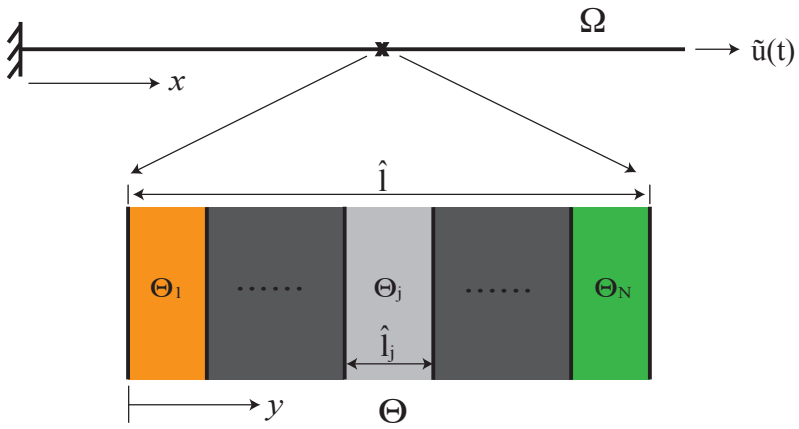

Figure 2.1: Two-scale problem description at multiscales.

that retains the nonlocal features in the form of a nonlocal effective modulus. It is second order in space, therefore does not require high order boundary conditions for transient simulations.

2.2 Multiscale Problem Setting

Consider a one-dimensional heterogeneous body with layered microstructure (e.g., 1D phononic crystal) as illustrated in Fig. 2.1. The domain of the body, $\Omega = [0, L]$ is formed by repetition of m locally periodic microstructures, Θ, with size $l = L/m$. The unit cell of the microstructure domain consists of N material phases, with the domain of phase j denoted by Θ_j. x and y indicate the position coordinates at macro- and micro- scales, respectively, where the two coordinates are related to each other by $y = x/\zeta$, and $0 < \zeta \ll 1$ is the small scaling parameter. In the context of dynamic analysis, the scaling parameter is defined as the ratio between the microstructure unit cell size and the length of deformation wave (i.e., $\zeta = l/\lambda$, where λ is the deformation wavelength).

Consider an arbitrary response field, $f^{\zeta}(x, t)$, which oscillates in space due to

fluctuations induced by material heterogeneity. A two scale spatial decomposition is applied to express the response field in terms of both macroscale and microscale coordinates, $f^\zeta(x,t) = f(x, y(x), t)$, where superscript ζ indicates the dependence of the response field on the microstructural heterogeneity. The spatial derivative of f^ζ is obtained by applying the chain rule, $f^\zeta_{,x}(x,t) = f_{,x}(x,y,t) + \frac{1}{\zeta} f_{,y}(x,y,t)$, where subscript comma followed by x and y denote the spatial derivative with respect to the macroscale and microscale coordinates, respectively. The response fields are assumed to be spatially periodic, $f(x,y,t) = f(x, y+\hat{l}, t)$, where $\hat{l}$ denotes the period of the microstructure in the microscale coordinate (i.e., $\hat{l} = l/\zeta$). The response field of the heterogeneous body subjected to dynamic load is governed by the momentum balance equation:

$$\sigma^\zeta_{,x}(x,t) = \rho^\zeta(x) u^\zeta_{,tt}(x,t) \tag{2.1}$$

in which, σ^ζ and u^ζ are the stress and displacement fields, respectively; and ρ^ζ denotes density.

The constitutive response is described by a generalized linear viscoelastic model:

$$\sigma^\zeta(x,t) = \int_0^t g^\zeta(x, t-\tau) \varepsilon^\zeta_{,\tau}(x,\tau) d\tau \tag{2.2}$$

where, g^ζ is the modulus function and $\varepsilon^\zeta(x,t) = u^\zeta_{,x}(x,t)$ is the strain. The dissipative process within viscoelastic constituents may lead to localized heating, which in turn changes the constitutive behavior [57]. This thermal effect is not considered in the current work. Elastic behavior can be recovered by setting $g^\zeta(x,t) = E^\zeta$, where E^ζ denotes the elastic modulus. We assume the material properties of each constituent are of the same order of magnitude.

The dynamic load is applied in the form of prescribed displacement at the boundaries:

$$u^\zeta(0,t) = 0; \quad u^\zeta(L,t) = \tilde{u}(t) \tag{2.3}$$

where, $\tilde{u}(t)$ is the prescribed boundary data. The initial conditions are:

$$u^{\zeta}(x,0) = u^0(x); \quad u^{\zeta}_{,t}(x,0) = v^0(x) \tag{2.4}$$

where, $u^0(x)$ and $v^0(x)$ are the prescribed data.

The particular forms of the generalized viscoelastic constitutive model and the momentum balance equation (Eq. 2.1) permit a simpler description of the governing boundary value problem in the Laplace domain. We introduce the key characteristics of the Laplace transform, recast the governing system of equations, and derive the nonlocal homogenization model in the Laplace domain. By this approach, the convolution integral form of the viscoelastic constitutive relation is transformed to multiplication of strain and modulus function, which is dependent on the Laplace variable.

The Laplace transform of an arbitrary, real valued, time varying function, f, is defined as:

$$\mathscr{F}(s) \equiv \mathscr{L}\left(f(t)\right) = \int_0^{\infty} e^{-st} f(t) dt \tag{2.5}$$

where, the Laplace variable, $s = \sigma + \mathrm{i}\omega$, and the transformed function in Laplace domain, $\mathscr{F}$, are complex valued (i.e., $s \in \mathbb{C}$ and $\mathscr{F} : \mathbb{C} \to \mathbb{C}$). The derivative rule for the Laplace transform is given as:

$$\mathscr{L}(f_{\underbrace{,tt\ldots t}_{n \text{ times}}}(t)) = s^n \mathscr{F}(s) - s^{n-1} f(0) - \ldots - f_{\underbrace{,tt\ldots t}_{n-1 \text{ times}}}(0) \tag{2.6}$$

For simplicity of the derivation in Laplace domain, statically undeformed initial condition is assumed, i.e., any field variables (displacement and its derivatives) are initially zeros, $u^0(x) = 0$ and $v^0(x) = 0$, thus:

$$\mathscr{L}(f_{\underbrace{,tt\ldots t}_{n \text{ times}}}(t)) = s^n \mathscr{F}(s) \tag{2.7}$$

The convolution integral rule is given as:

$$\mathscr{L}\left(\int_0^t f_1(t-\xi)f_2(\xi)d\xi\right) = \mathscr{L}(f_1)\mathscr{L}(f_2) \tag{2.8}$$

The momentum balance equation, Eq. 2.1, in the Laplace domain is:

$$\sigma^{\zeta}_{,x}(x,s) = \rho^{\zeta}(x)s^2u^{\zeta}(x,s) \tag{2.9}$$

Applying the convolution integral rule (Eq. 2.8) and derivative rule (Eq. 2.7) to the generalized linear viscoelastic model (Eq. 2.2), the viscoelastic constitutive relation in the Laplace domain is written as:

$$\sigma^{\zeta}(x,s) = E^{\zeta}(x,s)\varepsilon^{\zeta}(x,s) \tag{2.10}$$

where, the modulus function, $E^{\zeta}(x,s)$, in the Laplace domain is related to the modulus function in the time domain, g^{ζ}, as $E^{\zeta}(x,s) = s\mathscr{L}\left(g^{\zeta}(x,t)\right)$.

The boundary conditions in the Laplace domain are transformed from Eq. 2.3, and written as:

$$u^{\zeta}(0,s) = 0; \quad u^{\zeta}(L,s) = \hat{u}(s) \tag{2.11}$$

2.3 Two-Scale Asymptotic Analysis

Based on the two-scale description, the displacement is approximated by the following asymptotic expansion:

$$u^{\zeta}(x,s) \equiv u(x,y,s) = u_0(x,s) + \sum_{i=1}^{8}\zeta^i u_i(x,y,s) + O(\zeta^9) \tag{2.12}$$

where, u_0 denotes the macroscopic displacement field and is dependent on the macroscale coordinate only; and u_i are high order displacement fields which are functions of both

macroscale and microscale coordinates. The macroscopic nature of u_0 is not an assumption, but a well-known consequence of the asymptotic analysis [42]. The strain field at any order is obtained as:

$$O(\zeta^i): \quad \varepsilon_i(x,y,s) = u_{i,x} + u_{i+1,y}; \quad i = 0,1,... \tag{2.13}$$

Employing Eq. 2.13 along with the constitutive relation (Eq. 2.10), the stress field at each order is obtained as:

$$O(\zeta^i): \quad \sigma_i(x,y,s) = E(y,s)(u_{i,x} + u_{i+1,y}); \quad i = 0,1,... \tag{2.14}$$

Substituting the expanded displacement field (Eq. 2.12) and the constitutive equations at various orders (Eq. 2.14) into the momentum balance equation (Eq. 2.9), and collecting terms with equal orders yield the equilibrium equations at each order of ζ:

$$O(\zeta^{-1}): \quad \sigma_{0,y}(x,y,s) = 0 \tag{2.15a}$$

$$O(\zeta^i): \quad \sigma_{i,x}(x,y,s) + \sigma_{i+1,y}(x,y,s) = \rho(y)s^2 u_i(x,y,s), \quad i = 0,1,... \tag{2.15b}$$

The classical homogenization models consider the two lowest order equilibrium equations (Eq. 2.15a and Eq. 2.15b with $i = 0$), resulting in a local macroscopic description that does not capture wave dispersion or attenuation. This model is valid only when the deformation wavelength is large enough that the local dispersion due to material heterogeneities is negligible. Considering additional two equations at $O(\zeta^1)$ and $O(\zeta^2)$, it is possible to capture dispersive effects and wave propagation in shorter deformation wavelength scenarios [42, 4, 63].

The equilibrium equations (Eq. 2.15a, b) are evaluated sequentially by the decomposition of the corresponding displacement fields into macroscale components, which are independent of the microscale coordinate, and influence functions that incorpo-

rate the effect of microstructures. The following asymptotic procedure is well known and briefly explained herein since it sets the stage for the proposed nonlocal model. We start by considering the following decomposition:

$$u_1(x, y, s) = U_1(x, s) + H_1(y)U_{0,x}(x, s) \tag{2.16}$$

where, $H_1(y)$ denotes the first order microscopic influence function, and $U_1(x, s)$ is the first order macroscale displacement, and $U_0(x, s) = u_0(x, s)$. Combining Eqs. 2.14, 2.15a and 2.16 results in the linear equilibrium equation for the microscopic influence function at $O(\zeta^{-1})$:

$$\{E(y, s)(1 + H_{1,y})\}_{,y} = 0 \tag{2.17}$$

Considering the N-layered unit cell illustrated in Fig. 2.1, the equilibrium equation is evaluated uniquely by imposing the following constraints [63]:

$$\text{Periodicity}: \quad u_1(y = 0) = u_1(y = \hat{l}); \quad \sigma_0(y = 0) = \sigma_0(y = \hat{l}) \tag{2.18a}$$

$$\text{Continuity}: \quad [\![u_1(y = \sum_{j=1}^{n} \hat{l}_j)]\!] = 0; \quad [\![\sigma_0(y = \sum_{j=1}^{n} \hat{l}_j)]\!] = 0; \quad n = 1, 2, ..., N - 1 \tag{2.18b}$$

$$\text{Normalization}: \quad \langle u_1(x, y, t)\rangle = U_1(x, t) \rightarrow \langle H_1(y)\rangle = 0 \tag{2.18c}$$

where, $\hat{l}_j = l_j/\zeta$ denotes the length of j^{th} layer in microscale coordinate. l_j is the physical length of the j^{th} layer. $[\![\cdot]\!]$ denotes the jump operator and $y = \sum_{j=1}^{n} \hat{l}_j$ is the location of the constituent interfaces; and $\langle\cdot\rangle$ is defined as a spatial averaging operator over the unit cell:

$$\langle f\rangle = \frac{1}{\hat{l}} \int_0^{\hat{l}} f(x, y, s)dy \tag{2.19}$$

The $O(1)$ momentum balance equation is obtained by applying the averaging operator (i.e., Eq. 2.19) to the corresponding equilibrium equation (Eq. 2.15b with $i = 0$) and considering the local periodicity of $\sigma_1(x, y, s)$:

$$\rho_0 s^2 U_0 - E_0(s) U_{0,xx} = 0 \tag{2.20}$$

where, ρ_0 and $E_0(s)$ are the homogenized density and $O(1)$ homogenized modulus, respectively:

$$\rho_0 \equiv \langle \rho \rangle = \frac{1}{\hat{l}} \sum_{j=1}^{N} \hat{l}_j \rho_j \tag{2.21}$$

$$E_0(s) = \langle E(y, s)(1 + H_{1,y}) \rangle \tag{2.22}$$

The procedure to evaluate influence functions and derive momentum balance equations presented above can be generalized for arbitrary orders. The recursive influence function generation process is defined in Fig. 2.2. This process decomposes the microscale dependent displacement $u_i(x, y, s)$ into macroscale displacements and associated influence functions, and substitutes the decomposed displacements into equilibrium equation at $O(\zeta^{i-2})$. Considering the macroscale momentum balance equations and equilibrium equations for the influence functions derived from lower orders, an equilibrium equation for influence function at $O(\zeta^{i-2})$ is obtained. By evaluating this equation with periodicity, continuity and normalization conditions, the influence function H_i is calculated. The macroscale momentum balance equation at $O(\zeta^{i-1})$ is then determined by applying the averaging operator and considering the periodicity condition of σ_i. Examples of deriving the influence functions and momentum balance equations can be found in [40, 42, 63].

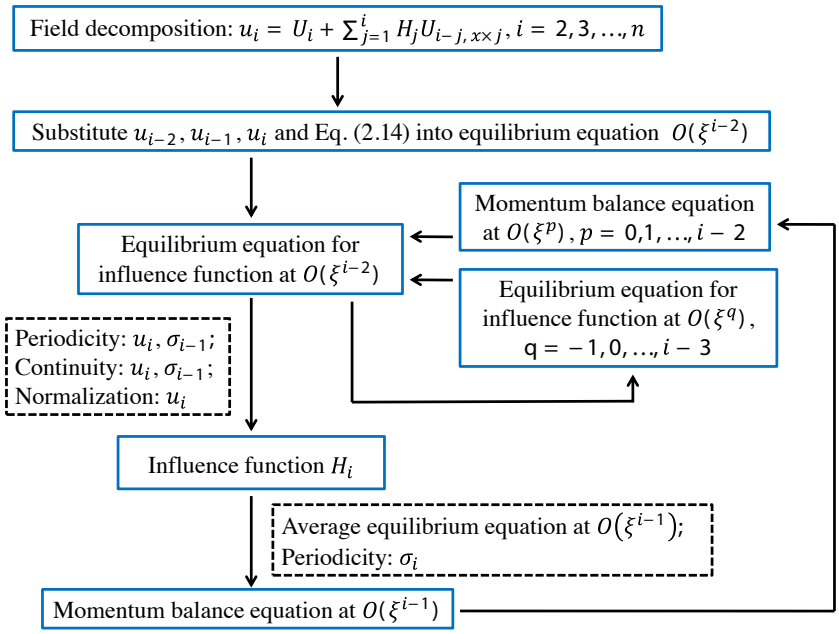

Figure 2.2: Recursive influence function generation procedure.

2.4 Spatial-Temporal Nonlocal Homogenization Model

2.4.1 Higher order gradient formulation

In this section, a novel nonlocal homogenization model is proposed for elastic and viscoelastic periodic layered media. A major contribution of this model is that we explore homogenization considering high order contributions, and the proposed model is derived such that the momentum balance equation shares the same structure as the gradient elasticity models [91, 7, 33]:

$$u_{,tt} - c_0^2 u_{,xx} + c_0^2 l_1^2 u_{,xxxx} - l_2^2 u_{,xxtt} + \frac{l_3^2}{c_0^2} u_{,tttt} = 0 \tag{2.23}$$

where $c_0^2 = E_0/\rho_0$. This equation has been shown to accurately capture the location and width of the first stop band, when the length scale parameters (l_1^2, l_2^2, l_3^2) are calibrated against the analytical solution [33]. In contrast to the gradient elasticity models, the parameters of the nonlocal homogenization model are derived directly

from the microstructural equilibrium.

As a result of the asymptotic analysis, the macroscale momentum balance equations are obtained up to $O(\zeta^7)$:

$$O(1): \quad \rho_0 s^2 U_0 - E_0(s) U_{0,xx} = 0 \tag{2.24a}$$

$$O(\zeta^1): \quad \rho_0 s^2 U_1 - E_0(s) U_{1,xx} = 0 \tag{2.24b}$$

$$O(\zeta^2): \quad \rho_0 s^2 U_2 - E_0(s) U_{2,xx} = \hat{E}_d(s) U_{0,xxxx} \tag{2.24c}$$

$$O(\zeta^3): \quad \rho_0 s^2 U_3 - E_0(s) U_{3,xx} = \hat{E}_d(s) U_{1,xxxx} \tag{2.24d}$$

$$O(\zeta^4): \quad \rho_0 s^2 U_4 - E_0(s) U_{4,xx} = \hat{E}_d(s) U_{2,xxxx} + \hat{E}_h(s) U_{0,xxxxxx} \tag{2.24e}$$

$$O(\zeta^5): \quad \rho_0 s^2 U_5 - E_0(s) U_{5,xx} = \hat{E}_d(s) U_{3,xxxx} + \hat{E}_h(s) U_{1,xxxxxx} \tag{2.24f}$$

$$O(\zeta^6): \quad \rho_0 s^2 U_6 - E_0(s) U_{6,xx} = \hat{E}_d(s) U_{4,xxxx} + \hat{E}_h(s) U_{2,xxxxxx} + \hat{E}_k(s) U_{0,xxxxxxxx} \tag{2.24g}$$

$$O(\zeta^7): \quad \rho_0 s^2 U_7 - E_0(s) U_{7,xx} = \hat{E}_d(s) U_{5,xxxx} + \hat{E}_h(s) U_{3,xxxxxx} + \hat{E}_k(s) U_{1,xxxxxxxx} \tag{2.24h}$$

where, U_i $(i = 0, 1, ..., 7)$ is the macroscale displacement at $O(\zeta^i)$; and, $\hat{E}_d(s), \hat{E}_h(s), \hat{E}_k(s)$ are the homogenized moduli at $O(\zeta^2), O(\zeta^4), O(\zeta^6)$, respectively:

$$\hat{E}_d(s) = \langle E(y,s)(H_2 + H_{3,y}) \rangle - \langle \theta(y) E_0(s) H_2 \rangle \tag{2.25a}$$

$$\hat{E}_h(s) = \langle E(y,s)(H_4 + H_{5,y}) \rangle - \langle \theta(y) \hat{E}_d(s) H_2 \rangle - \langle \theta(y) E_0(s) H_4 \rangle \tag{2.25b}$$

$$\hat{E}_k(s) = \langle E(y,s)(H_6 + H_{7,y}) \rangle - \langle \theta(y) \hat{E}_h(s) H_2 \rangle - \langle \theta(y) \hat{E}_d(s) H_4 \rangle - \langle \theta(y) E_0(s) H_6 \rangle \tag{2.25c}$$

For bilayer unit cell, the analytical expressions for E_0, $\hat{E}_d$ and $\hat{E}_h$ can be found in [40] and we provide $\hat{E}_k$ in Appendix A.

It is well known that solving Eqs. 2.24a-h sequentially at each order leads to secular solutions [40, 23]. The secularity can be eliminated by either introducing a slow

temporal scale to the asymptotic analysis [23] or combining macroscale momentum balance equations at different orders into a single nonlocal homogenized momentum balance equation by considering the average of the heterogeneous displacement, Eq. 2.12:

$$U^{(n)}(x,s) = \sum_{i=0}^{n} \zeta^i U_i(x,s) + O(\zeta^{n+1}) \tag{2.26}$$

where, $U^{(n)}$ denotes the approximation to the macroscale displacement of $O(\zeta^{n+1})$ accuracy. However, a direct weighted summation of Eqs. 2.24a-h will result in higher order spatial gradient terms (i.e., $\hat{E}_h(s)U_{,xxxxxx}$ and $\hat{E}_k(s)U_{,xxxxxxxx}$) in addition to the fourth-order spatial gradient term (i.e., $\hat{E}_d(s)U_{,xxxx}$). In what follows, we transform the higher order spatial gradient terms in Eqs. 2.24a-h to the fourth order gradient terms (i.e., spatial nonlocal, temporal nonlocal and mixed spatial -temporal nonlocal) based on the momentum balance of lower orders. Eqs. 2.24a-h are then combined to construct a homogenized momentum balance equation of the same form of Eq. 2.23. It is observed that Eqs. 2.24a, c, e, g and Eqs. 2.24b, d, f, h have identical equation form and coefficients. Therefore, all derivations on the former equations directly applies to the latter ones. Only the derivations on the even orders are presented in the remainder of this section.

Taking four spatial derivatives of Eq. 2.24a and substituting the resulting expression into Eq. 2.24e yields:

$$\rho_0 s^2 U_4 - E_0 U_{4,xx} = \hat{E}_d U_{2,xxxx} + \frac{\hat{E}_h}{E_0}\rho_0 s^2 U_{0,xxxx} \tag{2.27}$$

Inserting Eq. 2.24c into Eq. 2.27:

$$\rho_0 s^2 U_4 - E_0 U_{4,xx} = \hat{E}_d U_{2,xxxx} + \frac{\hat{E}_h \rho_0 s^2}{E_0 \hat{E}_d}(\rho_0 s^2 U_2 - E_0 U_{2,xx}) \tag{2.28}$$

Premultiplying Eq. 2.24a by $\hat{E}_h \rho_0 s^2 / \hat{E}_d E_0$, and adding the resulting expression to the

right hand side of Eq. 2.24c:

$$\rho_0 s^2 U_2 - E_0 U_{2,xx} = \hat{E}_d U_{0,xxxx} + \frac{\hat{E}_h \rho_0 s^2}{E_0 \hat{E}_d}(\rho_0 s^2 U_0 - E_0 U_{0,xx}) \tag{2.29}$$

Applying the same operations of Eqs. 2.24c and e to Eqs. 2.24d and f, respectively, premultiplying the resulting equations by ζ^3 and ζ^5, and Eqs. 2.29 and 2.28 by ζ^2 and ζ^4, respectively, adding the resulting equations with Eq. 2.24b multiplied by ζ and Eq. 2.24a, and considering Eq. 2.26 result in:

$$\rho_0 s^2 U^{(5)} - E_0 U^{(5)}_{,xx} - E_d U^{(5)}_{,xxxx} + \frac{E_h}{E_d}\rho_0 s^2 U^{(5)}_{,xx} - \frac{E_h}{E_0 E_d}\rho_0^2 s^4 U^{(5)} = O(\zeta^6) \tag{2.30}$$

where, $E_d = \zeta^2 \hat{E}_d$ and $E_h = \zeta^4 \hat{E}_h$ contain length scales l^2 and l^4, respectively, and are computed with the physical length of the unit cell. By truncating the $O(\zeta^6)$ perturbations in Eq. 2.30, we obtain the spatial-temporal nonlocal homogenization model of order $O(\zeta^6)$:

$$\text{STNHM6:} \qquad \rho_0 s^2 U - E_0 U_{,xx} - E_d U_{,xxxx} + \frac{E_h}{E_d}\rho_0 s^2 U_{,xx} - \frac{E_h}{E_0 E_d}\rho_0^2 s^4 U = 0 \tag{2.31}$$

The superscript (5) is dropped hereafter. The spatial nonlocal homogenization model [63] (SNHM) and classical local homogenization model (LHM) are recovered by neglecting the last two terms and last three terms on the left hand side of Eq. 2.31, respectively.

In order to achieve higher accuracy for shorter wave lengths, we add higher order corrections by employing Eqs. 2.24a-h. The procedure to obtain the higher order equation is similar to above and aimed at achieving the structure of Eq. 2.23 through analysis of higher order momentum balance equations. Consider the following de-

composition of Eq. 2.24g:

$$\begin{aligned}\rho_0 s^2 U_6 - E_0 U_{6,xx} = \hat{E}_d U_{4,xxxx} + \hat{E}_h U_{2,xxxxxx} + \nu \hat{E}_k U_{0,xxxxxxxx} \\ + (1-\nu)\,\hat{E}_k U_{0,xxxxxxxx}\end{aligned} \tag{2.32}$$

in which ν is the high order correction parameter. Taking two spatial derivatives of Eq. 2.24e, and substituting the resulting expression for $U_{0,xxxxxxxx}$ in the third term of the right hand side of Eq. 2.32:

$$\begin{aligned}\rho_0 s^2 U_6 - E_0 U_{6,xx} = \left(\hat{E}_d - \nu E_0 \frac{\hat{E}_k}{\hat{E}_h}\right) U_{4,xxxx} + \nu \frac{\hat{E}_k}{\hat{E}_h} \rho_0 s^2 U_{4,xx} \\ + \left(\frac{\hat{E}_h}{\hat{E}_d} - \nu \frac{\hat{E}_k}{\hat{E}_h}\right) \hat{E}_d U_{2,xxxxxx} + (1-\nu)\hat{E}_k U_{0,xxxxxxxx}\end{aligned} \tag{2.33}$$

Taking four spatial derivatives of Eq. 2.24c and substituting the resulting expression for $U_{2,xxxxxx}$ in Eq. 2.33:

$$\begin{aligned}&\rho_0 s^2 U_6 - E_0 U_{6,xx} = \\ &\left(\hat{E}_d - \nu E_0 \frac{\hat{E}_k}{\hat{E}_h}\right) U_{4,xxxx} + \nu \frac{\hat{E}_k}{\hat{E}_h} \rho_0 s^2 U_{4,xx} + \left(\frac{\hat{E}_h}{\hat{E}_d} - \nu \frac{\hat{E}_k}{\hat{E}_h}\right) \frac{\hat{E}_d}{E_0} \rho_0 s^2 U_{2,xxxx} \\ &+ \left[(1-\nu)\hat{E}_k - \left(\frac{\hat{E}_h}{\hat{E}_d} - \nu \frac{\hat{E}_k}{\hat{E}_h}\right) \frac{\hat{E}_d^2}{E_0}\right] U_{0,xxxxxxxx}\end{aligned} \tag{2.34}$$

Substituting Eq. 2.24e for $U_{2,xxxx}$ in Eq. 2.34, and taking six spatial derivatives of

Eq. 2.24a and inserting the resulting expression for $s^2U_{0,xxxxxx}$:

$$\begin{aligned}
&\rho_0 s^2 U_6 - E_0 U_{6,xx} = \\
&\left(\hat{E}_d - \nu E_0 \frac{\hat{E}_k}{\hat{E}_h}\right) U_{4,xxxx} + \left(2\nu \frac{\hat{E}_k}{\hat{E}_h} - \frac{\hat{E}_h}{\hat{E}_d}\right) \rho_0 s^2 U_{4,xx} + \left(\frac{\hat{E}_h}{E_0 \hat{E}_d} - \nu \frac{\hat{E}_k}{E_0 \hat{E}_h}\right) \rho_0^2 s^4 U_4 \\
&+ \left[(1-\nu)\hat{E}_k - \left(\frac{\hat{E}_h}{E_0 \hat{E}_d} - \nu \frac{\hat{E}_k}{E_0 \hat{E}_h}\right)(\hat{E}_d^2 + E_0 \hat{E}_h)\right] U_{0,xxxxxxxx}
\end{aligned} \tag{2.35}$$

Equation 2.24e is rewritten in the following form:

$$\begin{aligned}
\rho_0 s^2 U_4 - E_0 U_{4,xx} = &\left(\hat{E}_d - \nu E_0 \frac{\hat{E}_k}{\hat{E}_h}\right) U_{2,xxxx} + \nu \frac{\hat{E}_k}{\hat{E}_h} \rho_0 s^2 U_{2,xx} + \nu E_0 \frac{\hat{E}_k}{\hat{E}_h} U_{2,xxxx} \\
&- \nu \frac{\hat{E}_k}{\hat{E}_h} \rho_0 s^2 U_{2,xx} + \hat{E}_h U_{0,xxxxxx}
\end{aligned} \tag{2.36}$$

Premultiplying Eq. 2.24c by s^2, replacing the resulting $s^2U_{0,xxxx}$ by the expression resulting from taking four spatial derivatives of Eq. 2.24a, and substituting the resulting expression for $U_{0,xxxxxx}$ into Eq. 2.36:

$$\begin{aligned}
\rho_0 s^2 U_4 - E_0 U_{4,xx} = &\left(\hat{E}_d - \nu E_0 \frac{\hat{E}_k}{\hat{E}_h}\right) U_{2,xxxx} + \left(\nu \frac{\hat{E}_k}{\hat{E}_h} - \frac{\hat{E}_h}{\hat{E}_d}\right) \rho_0 s^2 U_{2,xx} \\
&+ \frac{\hat{E}_h}{E_0 \hat{E}_d} \rho_0^2 s^4 U_2 + \nu \frac{\hat{E}_k}{\hat{E}_h} \left(E_0 U_{2,xxxx} - \rho_0 s^2 U_{2,xx}\right)
\end{aligned} \tag{2.37}$$

In view of Eq. 2.24a and Eq. 2.24c, we have:

$$E_0 U_{2,xxxx} - \rho_0 s^2 U_{2,xx} = -\hat{E}_d U_{0,xxxxxx} = -\hat{E}_d \frac{\rho_0}{E_0} s^2 U_{0,xxxx} = \frac{\rho_0}{E_0} s^2 (E_0 U_{2,xx} - \rho_0 s^2 U_2) \tag{2.38}$$

Substituting Eq. 2.38 into Eq. 2.37:

$$\rho_0 s^2 U_4 - E_0 U_{4,xx} = \left(\hat{E}_d - \nu E_0 \frac{\hat{E}_k}{\hat{E}_h}\right) U_{2,xxxx} + \left(2\nu \frac{\hat{E}_k}{\hat{E}_h} - \frac{\hat{E}_h}{\hat{E}_d}\right) \rho_0 s^2 U_{2,xx} + \left(\frac{\hat{E}_h}{E_0 \hat{E}_d} - \nu \frac{\hat{E}_k}{E_0 \hat{E}_h}\right) \rho_0^2 s^4 U_2 \tag{2.39}$$

Considering Eq. 2.24a, we rewrite Eq. 2.24c as:

$$\rho_0 s^2 U_2 - E_0 U_{2,xx} = \left(\hat{E}_d - \nu E_0 \frac{\hat{E}_k}{\hat{E}_h}\right) U_{0,xxxx} + \left(2\nu \frac{\hat{E}_k}{\hat{E}_h} - \frac{\hat{E}_h}{\hat{E}_d}\right) \rho_0 s^2 U_{0,xx} + \left(\frac{\hat{E}_h}{E_0 \hat{E}_d} - \nu \frac{\hat{E}_k}{E_0 \hat{E}_h}\right) \rho_0^2 s^4 U_0 \tag{2.40}$$

Applying the same operations of Eqs. 2.24c, e and g to Eqs. 2.24d, f and h, respectively, premultiplying the resulting equations by ζ^3, ζ^5 and ζ^7, and Eqs. 2.40, 2.39, 2.35 by ζ^2, ζ^4 and ζ^6, respectively, adding the resulting equations with Eq. 2.24b multiplied by ζ and Eq. 2.24a, and considering Eq. 2.26:

$$\rho_0 s^2 U^{(7)} - E_0 U^{(7)}_{,xx} - \left(E_d - \nu E_0 \frac{E_k}{E_h}\right) U^{(7)}_{,xxxx} - \left(2\nu \frac{E_k}{E_h} - \frac{E_h}{E_d}\right) \rho_0 s^2 U^{(7)}_{,xx} - \left(\frac{E_h}{E_0 E_d} - \nu \frac{E_k}{E_0 E_h}\right) \rho_0^2 s^4 U^{(7)} = \zeta^6 Err U_{0,xxxxxxxx} + \zeta^7 Err U_{1,xxxxxxxx} + O(\zeta^8) \tag{2.41}$$

where Err is expressed as:

$$Err = (1-\nu)\hat{E}_k - \left(\frac{\hat{E}_h}{E_0 \hat{E}_d} - \nu \frac{\hat{E}_k}{E_0 \hat{E}_h}\right) (\hat{E}_d^2 + E_0 \hat{E}_h) \tag{2.42}$$

$E_k = \zeta^6 \hat{E}_k$ has length scale l^6 and is computed with physical length of the unit cell. We note that Eq. 2.41 has the same asymptotic accuracy as Eq. 2.31 for an arbitrarily chosen ν, due to the presence of $O(\zeta^6)$ term on the right-hand side. In particular, when $\nu = 0$, the left-hand side of Eq. 2.41 recovers Eq. 2.31. Therefore, Eq. 2.41

represents a one-parameter family of nonlocal homogenization models as a function of ν. $O(\zeta^8)$ accuracy could be achieved by setting ν such that the coefficient of $O(\zeta^6)$ and $O(\zeta^7)$ terms vanishes. The expression for the correction parameter is obtained as:

$$\nu = \frac{\hat{E}_h \left(\hat{E}_h^2 E_0 + \hat{E}_d^2 \hat{E}_h - E_0 \hat{E}_d \hat{E}_k \right)}{\hat{E}_d^3 \hat{E}_k} \tag{2.43}$$

By truncating the $O(\zeta^8)$ perturbations in Eq. 2.41, we obtain the spatial-temporal nonlocal homogenization model of order $O(\zeta^8)$:

$$\begin{aligned} \text{STNHM8:} \qquad & \rho_0 s^2 U - E_0 U_{,xx} - \left(E_d - \nu E_0 \frac{E_k}{E_h} \right) U_{,xxxx} \\ & - \left(2\nu \frac{E_k}{E_h} - \frac{E_h}{E_d} \right) \rho_0 s^2 U_{,xx} - \left(\frac{E_h}{E_0 E_d} - \nu \frac{E_k}{E_0 E_h} \right) \rho_0^2 s^4 U = 0 \end{aligned} \tag{2.44}$$

The superscript (7) is dropped hereafter.

The Laplace domain derivation presented above applies to both elastic and viscoelastic layered composites. For composites that only consist elastic phases, momentum balance equations, STNHM6 and STNHM8, can also be derived in time domain following a similar procedure and result in:

$$\text{STNHM6:} \qquad \rho_0 U_{,tt} - E_0 U_{,xx} - E_d U_{,xxxx} + \frac{E_h}{E_d} \rho_0 U_{,xxtt} - \frac{E_h}{E_0 E_d} \rho_0^2 U_{,tttt} = 0 \tag{2.45}$$

$$\begin{aligned} \text{STNHM8:} \qquad & \rho_0 U_{tt} - E_0 U_{,xx} - \left(E_d - \nu E_0 \frac{E_k}{E_h} \right) U_{,xxxx} \\ & - \left(2\nu \frac{E_k}{E_h} - \frac{E_h}{E_d} \right) \rho_0 U_{,xxtt} - \left(\frac{E_h}{E_0 E_d} - \nu \frac{E_k}{E_0 E_h} \right) \rho_0^2 U_{,tttt} = 0 \end{aligned} \tag{2.46}$$

The nonlocal homogenization model, STNHM8, possesses the same equation structure as the nonlocal equation (Eq. 2.23) of gradient elasticity models. One can easily observe the corresponding relation of $-\left(\frac{E_d}{E_0} - \nu \frac{E_k}{E_h} \right)$ and l_1^2, $\left(2\nu \frac{E_k}{E_h} - \frac{E_h}{E_d} \right)$ and l_2^2,

$-\left(\frac{E_h}{E_d}-\nu\frac{E_k}{E_h}\right)$ and l_3^2, respectively. While the latter parameters have to be calibrated in the gradient elasticity models, the former ones are fully determined through the homogenization process.

2.4.2 Nonlocal effective medium model

Substituting a harmonic wave $U = U_0(s)e^{\mathrm{i}kx}$ into Eq. 2.44, the dispersion relation in terms of Laplace variable is obtained:

$$(E_d-\nu E_0\frac{E_k}{E_h})k^4-\Big[(2\nu\frac{E_k}{E_h}-\frac{E_h}{E_d})\rho_0 s^2+E_0\Big]k^2+(\frac{E_h}{E_0E_d}-\nu\frac{E_k}{E_0E_h})\rho_0^2 s^4-\rho_0 s^2=0 \quad (2.47)$$

In general, the fourth order polynomial equation has four roots. Considering wave propagating in the positive direction:

$$\begin{aligned} k^{\{1\}} &= \sqrt{\frac{-B-\sqrt{B^2-4AC}}{2A}}; \quad k^{\{2\}} = \sqrt{\frac{-B+\sqrt{B^2-4AC}}{2A}} \\ A &= E_d - \nu E_0\frac{E_k}{E_h} \\ B &= -\left[(2\nu\frac{E_k}{E_h}-\frac{E_h}{E_d})\rho_0 s^2+E_0\right] \\ C &= (\frac{E_h}{E_0E_d}-\nu\frac{E_k}{E_0E_h})\rho_0^2 s^4-\rho_0 s^2 \end{aligned} \quad (2.48)$$

To seek the mathematical description of attenuation in stop bands, we rewrite the wavenumber k in the complex form, $k = k_{re} + ik_{im}$, where k_{re} and k_{im} are the real and imaginary part of wavenumber, respectively. Applying the complex wavenumber expression to the harmonic displacement solution, the displacement reads:

$$U(x,s) = U_0(s)e^{\mathrm{i}k_{re}x}e^{-k_{im}x} \quad (2.49)$$

in which, $U_0(s)e^{\mathrm{i}k_{re}x}$ contains the oscillatory feature of the displacement, while $e^{-k_{im}x}$ determines the solution to be attenuating or amplifying depending on whether k_{im} is

positive or negative. The physically meaningful wavenumber is taken as the one that has non-negative imaginary part:

$$\bar{k}^2(s) = \begin{cases} \left(k^{\{1\}}\right)^2, & \omega \leq \omega_c \quad (2.50a) \\ \left(k^{\{2\}}\right)^2, & \omega > \omega_c \quad (2.50b) \end{cases}$$

where the switch, ω_c, between the two branches is the imaginary part of the critical Laplace variable, $s_c = \sigma + \mathrm{i}\omega_c$. In order to ensure that the continuity of the physical wavenumber at the switch, $\left(k^{\{1\}}(s)\right)^2 = \left(k^{\{2\}}(s)\right)^2$ is satisfied:

$$-\sqrt{B^2(s) - 4A(s)C(s)} = \sqrt{B^2(s) - 4A(s)C(s)} \tag{2.51}$$

The complex-valued equation above is equivalent to the constrained system of equations:

$$\mathrm{Im}\left[B^2(s) - 4A(s)C(s)\right] = 0 \tag{2.52a}$$

$$\mathrm{Re}\left[B^2(s) - 4A(s)C(s)\right] \leq 0 \tag{2.52b}$$

Substituting the expressions for $A(s)$, $B(s)$ and $C(s)$ in Eq. 2.48 into Eq. 2.52a results in an equation from which ω_c is obtained. ω_c is evaluated analytically for elastic composites. For viscoelastic composites, ω_c is solved numerically, since the model parameters are dependent on the Laplace variable, resulting in a nonlinear equation. The inequality condition in Eq. 2.52b provides the criterion to choose the appropriate ω_c among the multiple solutions of Eq. 2.52a.

Selecting only the physical wavenumber for the solution of Eq. 2.47 is captured by the following dispersion equation:

$$k^2 - \bar{k}^2(s) = 0 \tag{2.53}$$

multiplying Eq. 2.53 with $-\rho_0 s^2/\bar{k}^2(s)$, the dispersion relation becomes:

$$\phi(s)E_0 k^2 + \rho_0 s^2 = 0 \tag{2.54}$$

where,

$$\phi(s) = \frac{-\rho_0 s^2}{\bar{k}^2(s)E_0} \tag{2.55}$$

Eq. 2.54 resembles the dispersion relation of the first two terms of Eq. 2.44 except the factor $\phi(s)$, as a result of the nonlocal terms in the higher order gradient formulation. Therefore, the nonlocal effective medium model may be expressed as:

$$\rho_0 s^2 U - E^e(s)U_{,xx} = 0 \tag{2.56}$$

in which, $E^e(s) = \phi(s)E_0(s)$.

2.5 Model Verification

In this section, two examples, elastic bilayer and viscoelastic four-layered microstructures are investigated to demonstrate the capability of the proposed nonlocal homogenization model in capturing the characteristics of dispersion and transient wave propagation in periodic layered media.

2.5.1 Elastic bilayer microstructure

Consider a bilayer unit cell as illustrated in Fig. 2.3(a). The phases within the unit cell, Θ, are characterized by the density, Young's modulus and length. The volume fraction of phase Θ_1 is taken as 0.5. Aluminum and steel are used for phases 1 and 2, respectively. The elastic modulus and density are 210 GPa and 7900 kg/m^3 for steel, and 68 GPa and 2700 kg/m^3 for aluminum, respectively.

The influence functions are obtained using the procedure shown in Fig. 2.2. Figure 2.4 shows the seven normalized influence functions that are used to compute the

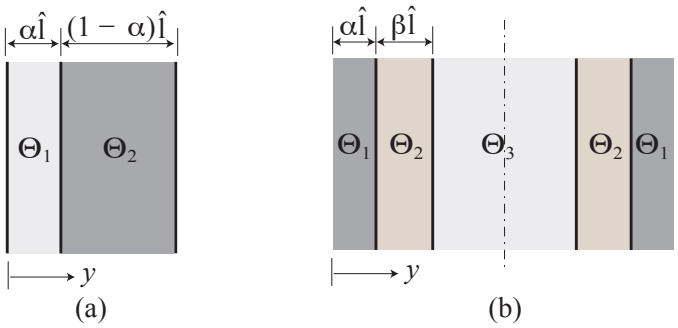

Figure 2.3: Unit cell of the microstructure: (a) elastic bilayer, (b) viscoelastic four-layered.

homogenized moduli. The first order influence function, $H_1(y)$ is piecewise linear. The high order influence functions are piecewise polynomials with progressively increasing polynomial order (e.g. $H_2(y)$ piecewise quadratic, etc.), satisfying the periodicity, continuity and normalization conditions. The influence functions are continuous in the entire unit cell domain, whereas their first derivatives are continuous only within each material phase. With the influence functions, the homogenized elastic moduli are obtained from Eqs. 2.25a-c.

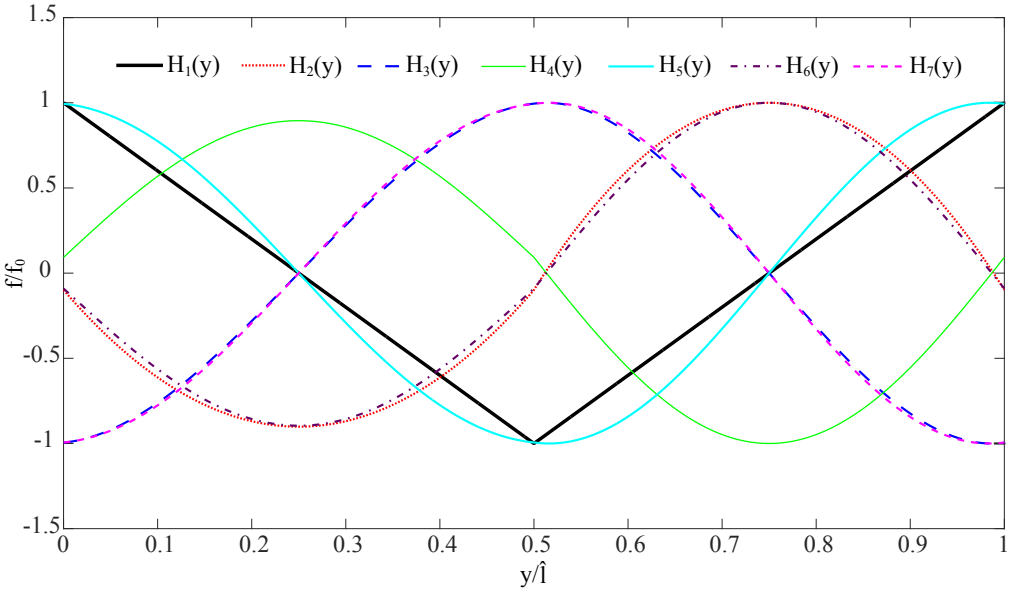

Figure 2.4: Normalized influence function associated with displacement field in each order,
$f = H_1(y), H_2(y), ..., H_7(y); f_0 = \max|f|$.

2.5.1.1 *Dispersion relation*

Figure 2.5 shows the dispersion relation of STNHM8 (Eq. 2.47) and the reference dispersion relation (real part of the wavenumber solution is plotted). The horizontal and vertical axes are the normalized wavenumber and normalized frequency, respectively, and c_0 is the homogenized wave speed (i.e., $c_0 = \sqrt{E_0/\rho_0}$). The reference dispersion relation is plotted following Bedford and Drumheller [12]. The two physical wavenumber solutions of STNHM8, k_1 and k_2, match with the analytical wavenumber solutions in the first pass band and second pass band, respectively. The non-physical solutions lead to negative group velocity, therefore not characteristic of wave propagation in the homogenized medium. STNHM8 captures the dispersion behavior accurately in the first pass band, and the initiation and end of the first stop band, where $kl/(2\pi) = l/\lambda = \zeta = 0.5$, the limit of the first Brillouin zone [18]. The model starts to deviate from the reference solution as the frequency further increases and $kl/(2\pi)$ approaches 1, where the second stop band initiates. As the scaling ratio reaches unity, the fundamental assumption of scale separation in homogenization is no longer valid [40, 14].

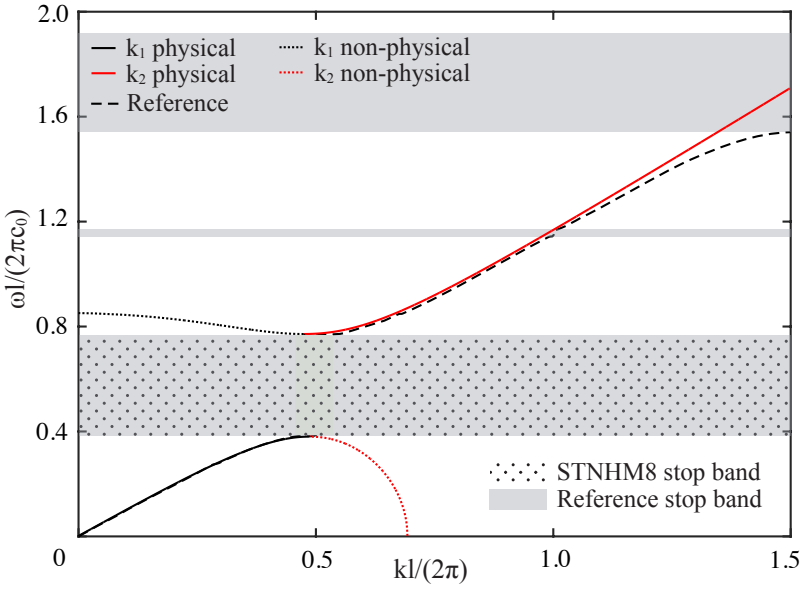

Figure 2.5: Dispersion relation of STNHM8 and the reference solution for bilayer microstructure.

2.5.1.2 *Effect of material property contrast on model accuracy*

A parametric study on the prediction error of STNHM8 in terms of capturing the initiation and end of the first stop band is conducted with a large number of constituent material property combinations for the unit cell. With the material phase 1 chosen as aluminum, the material property for phase 2 is sampled in two families of materials, i.e., metals and polymers, with the material property domains $\Omega_m = \{(E_2, \rho_2) \in \mathbb{R} \mid 100 \leq E_2 \leq 400 \text{ and } 4000 \leq \rho_2 \leq 10000\}$ and $\Omega_p = \{(E_2, \rho_2) \in \mathbb{R} \mid 1 \leq E_2 \leq 10 \text{ and } 1000 \leq \rho_2 \leq 2000\}$, respectively. In each of the material property domain, 100 samples are generated for E_2 and ρ_2, and the prediction error is computed as $|\omega_{STNHM8} - \omega_{ref}|/\omega_{ref}$ at the stop band initiation and end frequencies for each sample. Figure 2.6 shows the prediction error of STNHM8 for the two sets of constituent material combinations. Solid dots are the sampling points and the surface is created by quadratic fitting to the points to enhance visualization. The maximum error for stop band initiation prediction is approximately 2.5% for both Al-metal and Al-polymer microstructures. The error of stop band end prediction is relatively high compared to the initiation. In Figs. 2.6(b) and (d), it is noticeable that error grows as the Young's modulus ratio increases, especially for the cases which have low density ratio. The general trend of error indicates that STNHM8 accurately captures the initiation of stop band for a large range of constituent material combinations. It predicts the end of the stop band reasonably well for low stiffness contrast combinations, and starts to lose accuracy for high stiffness contrast cases.

2.5.1.3 *Models comparison*

The capability of STNHM in capturing the dispersion and band gap formation is due to the presence of high order terms. In order to further study the effects of the high order terms, we compare the dispersion curves of STNHM8 (Eq. 2.44), STNHM6 (Eq. 2.31), SNHM and LHM in Fig. 2.7. While all models capture the non-dispersive

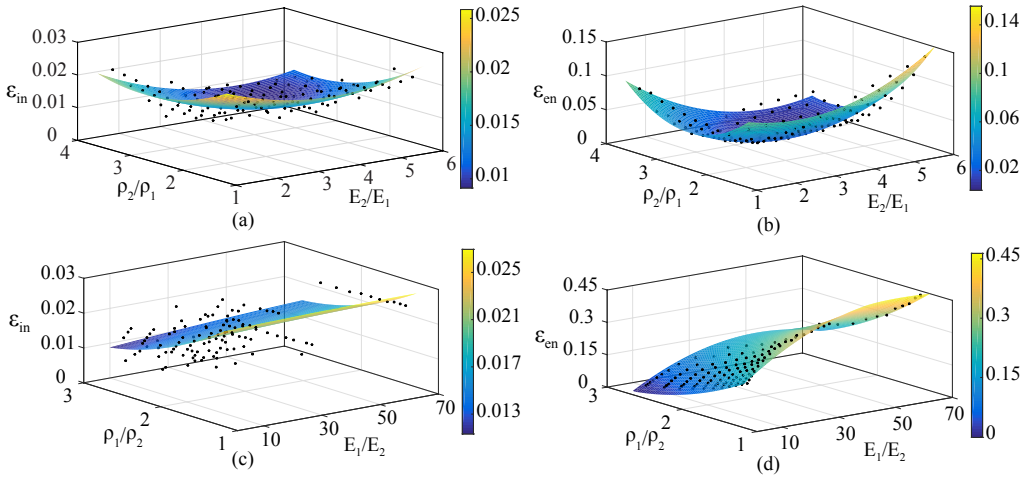

Figure 2.6: Error in the prediction of the stop band. (a) Al-metal stop band initiation, (b) Al-metal stop band end, (c) Al-polymer stop band initiation, (d) Al-polymer stop band end.

wave propagation characteristics at normalized frequency of less than 0.2, LHM and SNHM deviate from the reference dispersion relation and do not capture the band gap. STNHM6 captures the dispersion up to the onset of the first stop band, but not the bandwidth. By incorporating the high order correction, STNHM8 predicts the dispersion in the first and second pass band, as well as the onset and the width of the first stop band.

The dispersion relations of Eq. 2.46 and the gradient elasticity model in Eq. 2.23 are shown in Fig. 2.8 using material parameters provided in [33]. The two dispersion curves overlap with each other except the minor difference at the end of the stop band. In addition, $O\left(\frac{E_d}{E_0} - \nu\frac{E_k}{E_h}\right) = O(l_1^2) = O(10^{-4})$, $O\left(2\nu\frac{E_k}{E_h} - \frac{E_h}{E_d}\right) = O(l_2^2) = O(10^{-5})$ and $O\left(\frac{E_h}{E_d} - \nu\frac{E_k}{E_h}\right) = O(l_3^2) = O(10^{-4})$. The close match between the dispersion curves and the length-scale parameters indicates that the proposed model could serve as an alternative method for gradient elasticity models to determine the length-scale parameters directly from material properties and microstructures, without calibration against the analytical solution, which may not be available in multidimensional problems or in the presence of viscoelastic constituents.

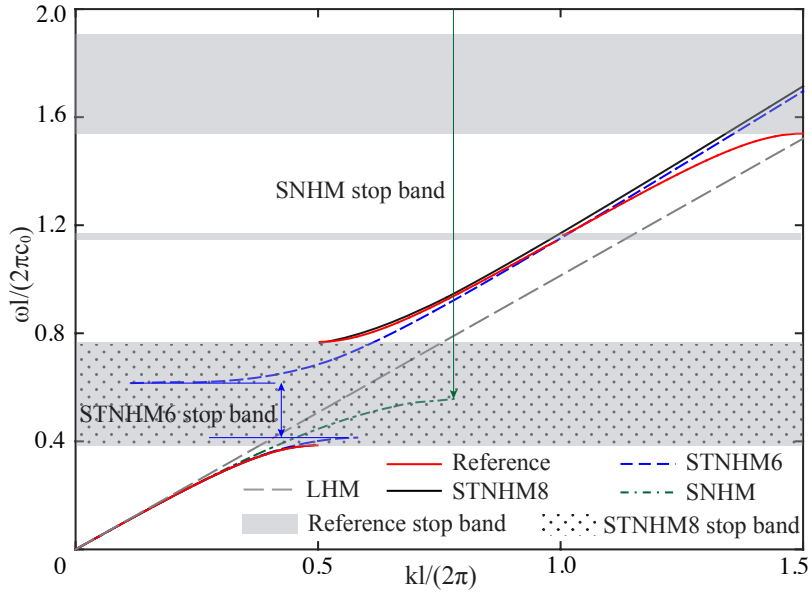

Figure 2.7: Dispersion curves of SNHM, STNHM6 and STNHM8 compared to the reference model.

2.5.1.4 *Transient wave propagation*

We consider the transient response of a composite structure with aluminum-steel bilayer microstructure (see Fig. 2.3(a)) subjected dynamic loads. The overall length of the structure is taken to be $L = 0.5$ m. The unit cell is taken to have $l = 0.01$ m. Two dynamic loads are considered, i.e., ramp load (Fig. 2.9(a)) and sinusoidal load (Fig. 2.9(b)). The study compares the responses computed by the nonlocal effective medium (NEM) model , LHM and the direct solution (DS) of the original problem, where each unit cell is resolved throughout the problem domain. Figure 2.10 shows the normalized displacement along the layered composite at $T = 0.05$ ms and $T = 0.1$ ms. The responses obtained from NEM and DS both show dispersion induced phase distortion, manifested by the oscillatory behavior behind the ramp wave front. Due to the presence of dispersion, both NEM and DS have peak amplitude of $1.1\mathrm{M}_0$. NEM shows good agreement with DS in terms of capturing the dispersive response under the prescribed ramp load.

Figure 2.11 shows the displacement histories of $x = 0.9L$ for 0.15 ms, with the

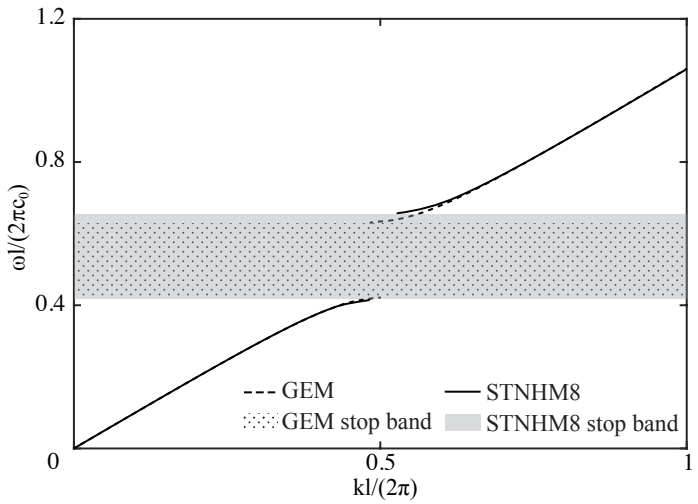

Figure 2.8: Dispersion curve of STNHM8 compared to the gradient elasticity model.

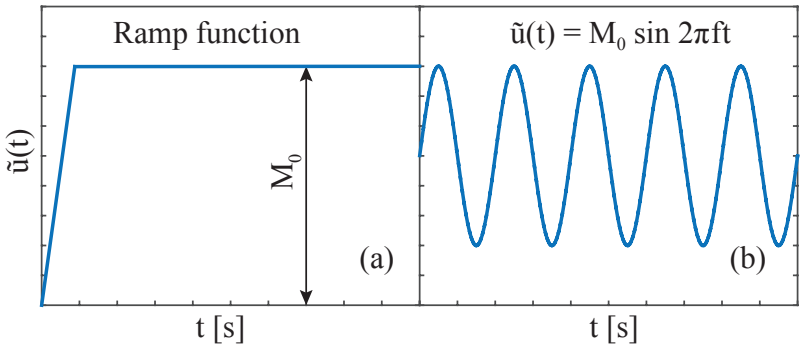

Figure 2.9: Applied loads: (a) ramp load, (b) sinusoidal load.

structure subjected to sinusoidal loads at frequencies 132.71 kHz and 221.18 kHz, corresponding to the normalized frequencies ($\omega l/(2\pi c_0)$) of 0.3 and 0.5, respectively. At $\omega l/(2\pi c_0) = 0.3$, the response is in the first pass band where dispersion occurs. NEM predicts the displacement time history accurately compared to DS. The dispersion is manifested by the distorted phase shape of the first two cycles and slight phase shift of the dispersive models (NEM and DS) compared to LHM. As the frequency is increased to 221.18 kHz, the response resides in the first stop band. At this frequency, the displacement response is significantly attenuated with peak normalized amplitude of 0.25, which asymptotes to complete attenuation in time.

Figure 2.12 shows the maximum transmitted wave amplitude at $x = 0.9L$ within

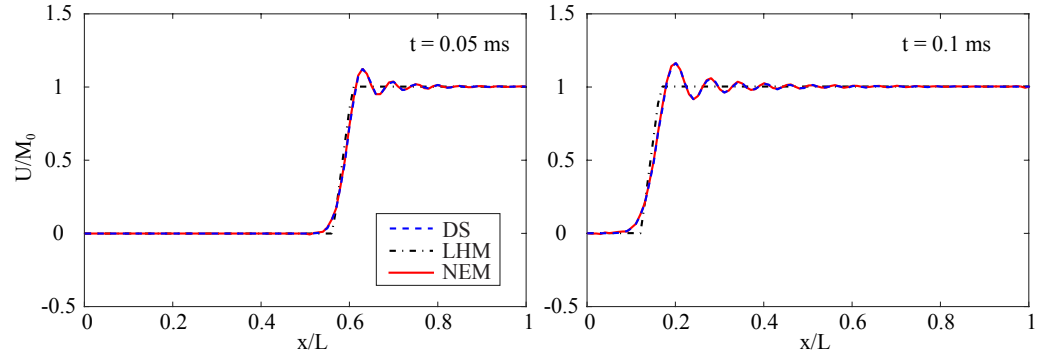

Figure 2.10: Responses at two time instances under step loading: (a) t=0.05 ms, (b) t=0.1 ms.

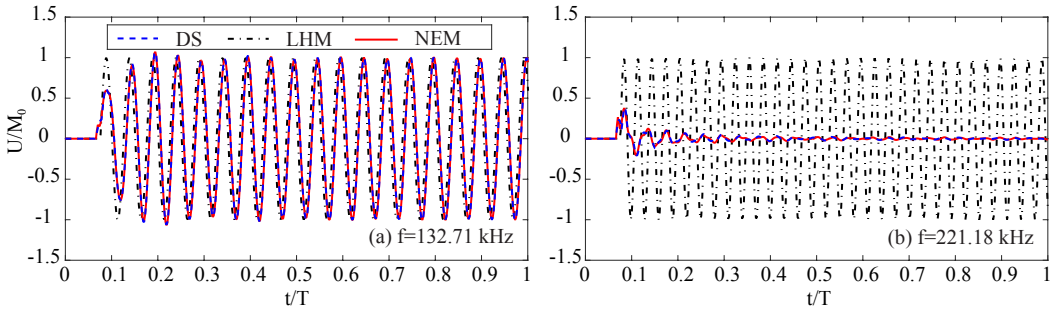

Figure 2.11: Displacement histories at x=0.9L under sinusoidal loading at frequencies: (a) 132.71 kHz, (b) 221.18 kHz.

$t/T \in [0.5, 1]$ for sinusoidal loads at a range of frequencies $f \in [10, 442.4]$ kHz. Solution of NEM is compared to DS. NEM leads to accurate wave amplitude for frequencies within the first pass band and stop band. It starts to over predict the amplitude in the second pass band due to the increasingly poor separation of scales at high frequencies.

2.5.2 Viscoelastic four-layered microstructure

In this section, the proposed model is assessed in the context of a four-layered microstructure (see Fig. 2.3(b)) with both elastic and viscoelastic phases. The unit cell is composed of elastic layers, epoxy (phase 1) and rubber (phase 3), with viscoelastic layers (phase 2) inserted in between. The volume fractions of phase 1 and phase 2 are 2α and 2β. In the following discussion, the volume fractions for phase 1 and phase 2

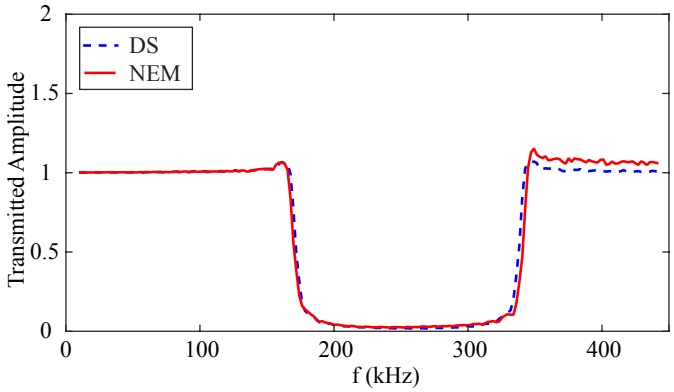

Figure 2.12: Transmitted wave amplitude at x=0.9L at frequency between 10 kHz and 442.4 kHz

are taken as $\alpha = 0.3$ and $\beta = 0.1$.

The constitutive relation of the viscoelastic phase is given by Eq. 2.2, where the modulus function is expressed with Prony series in time domain. After Laplace transformation, the modulus function is expressed as:

$$E_2(s) = E_{2(0)} \left(1 - \sum_{i=1}^{n} p_i \left(1 - \frac{s}{s + 1/q_i} \right) \right) \tag{2.57}$$

where, the material properties of the viscoelastic phase [2] is provided in Table 3.1.

Table 2.1: Material properties for elastic and viscoelastic phases.

Elastic phases			
E_1 [GPa]	ρ_1 [kg/m^3]	E_3 [GPa]	ρ_3 [kg/m^3]
1.0	1200	0.1	1100
Viscoelastic phase			
$E_{2(0)}$ [MPa]	ρ_2 [kg/m^3]		
770.6	1070		
p_1	p_2	p_3	p_4
0.074	0.147	0.313	0.379
q_1 [ms]	q_2 [ms]	q_3 [ms]	q_4 [ms]
463.4	0.06407	1.163×10^{-4}	7.321×10^{-7}

The sizes of the macro- and micro- structures are identical to the example for the

bilayer microstructure.

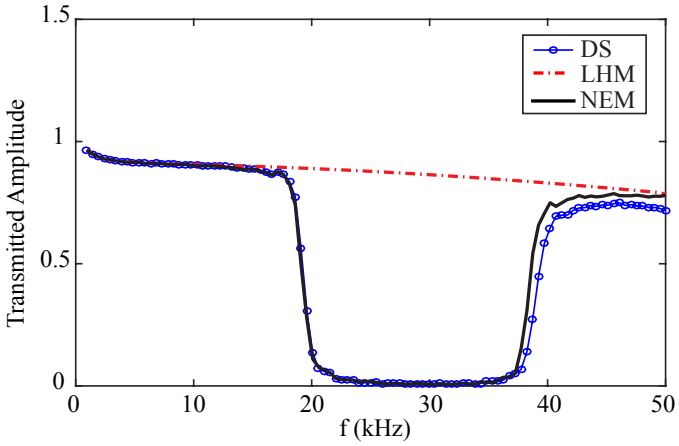

Figure 2.13: Transmitted wave amplitude at $x = 0.9L$ for the four-layered viscoelastic composite at frequency between 1 kHz and 50 kHz.

Figure 2.13 shows the transmitted wave amplitude at $x = 0.9L$ for the four-layered viscoelastic composite structure under sinusoidal load (see Fig. 2.9(b)). Loading frequency ranges from 1 to 50 kHz. Solution obtained by NEM is compared to DS and LHM. The wave amplitude reduction in the first pass band caused by viscoelastic dissipation, which increases monotonically as the loading frequency increases, is observed in all models. As is for elastic composite, LHM does not predict dispersion and band gap formation of viscoelastic composite. NEM captures wave attenuation due to both viscoelastic dissipation and stop band formation. The phase distortion and phase shift of the dispersive models (NEM and DS) in the first pass band are observed in Fig. 2.14(a). Within the stop band, near complete wave attenuation is present due to the combination of viscoelastic dissipation and destructive wave interactions, as is shown in Fig. 2.14(b).

The effect of viscoelasticity is investigated by comparing the transmitted wave amplitude for the viscoelastic composite to an elastic counterpart where the modulus function of the viscoelastic phase is replaced by its instantaneous modulus, $E_{2(0)}$. As is shown in Fig. 2.15, viscoelastic dissipation results in enhanced wave attenuation within the stop band, compared to the elastic case. Moreover, the first stop band of

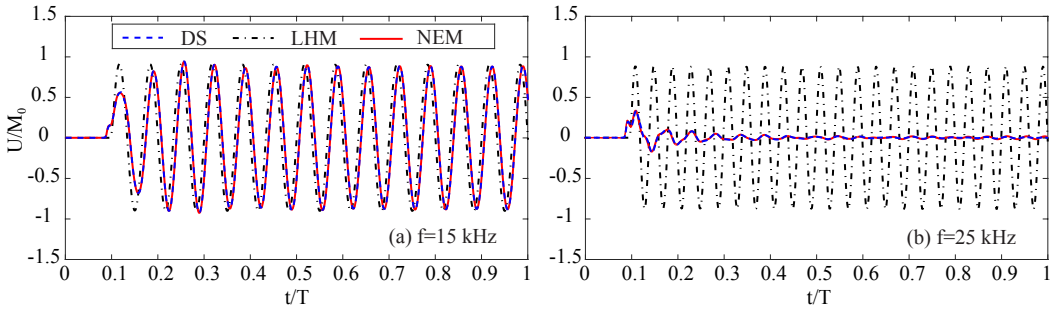

Figure 2.14: Displacement histories of viscoelastic composite at x=0.9L under sinusoidal loading at frequencies: (a) 15 kHz, (b) 25 kHz.

the viscoelastic composite is shifted towards lower frequency and its width becomes narrower. Similar observation was reported in [137] for one-dimensional bilayer viscoelastic phononic crystals using the plane wave expansion method. As a simple parametric study, we multiply a factor of 0.2 to q_i in Table 3.1, while keeping p_i unchanged, which corresponds to a viscoelastic material that has the same instantaneous modulus but takes 5 times shorter time for the stress to relax to quasi-static state in the relaxation test. It is observed that the viscoelastic composite with reduced parameters q_i results in more severe viscoelastic dissipation, featured by the more pronounced amplitude reduction in the pass bands. However, the location and size of the first stop band does not vary.

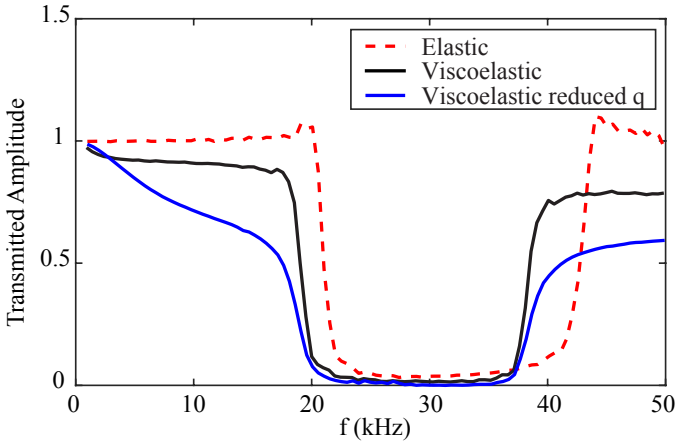

Figure 2.15: Transmitted wave amplitude of elastic and viscoelastic composite computed by NEM.

2.6 Summary

This chapter presented the spatial-temporal nonlocal homogenization model for transient wave propagation in periodic viscoelastic composite in one-dimensional setting. The proposed model is derived based on asymptotic expansions of up to the eighth order. By introducing high order corrections, a momentum balance equation that is nonlocal in both space and time is derived. The proposed model shares the same differential equation structure as the gradient elasticity models, whereas all parameters are computed directly from the microscale boundary value problems and dependent on the material properties and microstructure only.

The performance of the proposed model is assessed by investigating the wave propagation characteristics in elastic bilayer and viscoelastic four-layered composite structures, and verified against analytical solutions and direct numerical simulations. The spatial-temporal nonlocal homogenization model is accurate in predicting the dispersion relation of elastic wave propagation within the first pass band and the initiation and end of the first stop band for moderate material contrasts. The accuracy of predicting the end of the stop band decreases as the contrasts become high. In addition, the proposed model captures the transient wave dispersion and attenuation within the first pass band and stop band for elastic and viscoelastic composites. The effect of viscoelasticity is observed to introduce viscoelastic dissipation that monotonically intensifies as the frequency increases, shift the first stop band towards lower frequency, enhance wave attenuation within it and reduce its width.

The extension of the spatial-temporal nonlocal homogenization model to multidimensional problems is presented in the following chapters.

Chapter 3

SPATIAL-TEMPORAL NONLOCAL HOMOGENIZATION MODEL FOR TRANSIENT WAVE PROPAGATION IN PERIODIC VISCOELASTIC COMPOSITES: TWO-DIMENSIONAL ANTI-PLANE SHEAR WAVE

3.1 Introduction

In this chapter, we extend the spatial-temporal nonlocal homogenization model for transient anti-plane shear wave propagation in viscoelastic composites. The spatial-temporal nonlocal equation for anti-plane shear wave propagation in elastic composites has been analyzed by Wautier and Guzina [125] with calibrated length-scale parameters, a novelty of the proposed model in this regard is that it provides a consistent recipe for computing all model parameters including the high order ones, and extends the approach to viscoelastic composites. In addition, we propose a nonlocal effective medium model for transient wave propagation, which enables the characterization of wave dispersion and attenuation in the presence of structural effects, such as geometry and boundary conditions.

3.2 Multiscale Problem Setting

Let $\Omega \in \mathbb{R}^2$ denote the domain of a body constructed by periodic unit cells composed of two or more constituents. Ω is described using the Cartesian coordinate, $\mathbf{x}$. The momentum balance equation that governs wave propagation in this heterogeneous body is expressed as:

$$\boldsymbol{\nabla}_x . \boldsymbol{\sigma}^\zeta(\mathbf{x}, t) = \rho^\zeta(\mathbf{x}) \ddot{\mathbf{u}}^\zeta(\mathbf{x}, t) \tag{3.1}$$

where, $\boldsymbol{\sigma}^\zeta$ denotes the stress tensor; ρ^ζ the density; and $\mathbf{u}^\zeta$ the displacement vector. $\boldsymbol{\nabla}_x .$ is the divergence operator and superimposed dot denotes derivative with respect

to time. The superscript, ζ, indicates that the response fields oscillate spatially due to the microstructural heterogeneity.

Considering anti-plane shear deformation, the displacement field is expressed over the two-dimensional problem domain, whereas the displacement vector is normal to the plane:

$$\mathbf{u}^{\zeta}(\mathbf{x},t) = u^{\zeta}(\mathbf{x},t)\hat{\mathbf{e}}_3 \tag{3.2}$$

where, $\mathbf{x} = \{x_1, x_2\}$ denotes the position vector of the material point and $\hat{\mathbf{e}}_j$ is the unit vector in the x_j direction. $\hat{\mathbf{e}}_3$ is taken to be the normal to the plane of the problem domain. Under the assumption of small deformation, the engineering shear strain is expressed in vector form after degeneration by contraction with $\hat{\mathbf{e}}_3$:

$$\boldsymbol{\gamma}^{\zeta}(\mathbf{x},t) = \left[\boldsymbol{\nabla}_x \mathbf{u}^{\zeta} + (\boldsymbol{\nabla}_x \mathbf{u}^{\zeta})^T\right].\hat{\mathbf{e}}_3 = u^{\zeta}_{,x_j}(\mathbf{x},t)\hat{\mathbf{e}}_j \tag{3.3}$$

in which, the subscript dot denotes single contraction and subscript comma the spatial derivative. $\boldsymbol{\nabla}_x = \partial(\cdot)/\partial x_j \hat{\mathbf{e}}_j$ is the gradient operator.

The constitutive behavior at a material point is taken to be linear viscoelastic, expressed using the hereditary integral:

$$\boldsymbol{\tau}^{\zeta}(\mathbf{x},t) = \int_0^t G^{\zeta}(\mathbf{x}, t-t')\dot{\boldsymbol{\gamma}}^{\zeta}(\mathbf{x},t')dt' \tag{3.4}$$

where, $\boldsymbol{\tau}^{\zeta}(\mathbf{x},t)$ is the shear stress vector and $G^{\zeta}(\mathbf{x},t')$ is the time-varying relaxation modulus. Elastic behavior is recovered by taking G^{ζ} as constant in time. The densities and relaxation moduli of all constituents forming the composite are assumed of the same order of magnitude.

Under the anti-plane shear wave propagation condition, the momentum balance equation (Eq. 5.1) reduces to:

$$\boldsymbol{\nabla}_x.\boldsymbol{\tau}^{\zeta}(\mathbf{x},t) = \rho^{\zeta}(\mathbf{x})\ddot{u}^{\zeta}(\mathbf{x},t) \tag{3.5}$$

The boundary conditions are:

$$u^{\zeta}(\mathbf{x},t) = \tilde{u}(\mathbf{x},t); \quad \mathbf{x} \in \Gamma^{u} \tag{3.6a}$$

$$\boldsymbol{\tau}^{\zeta}(\mathbf{x},t).\mathbf{n} = \tilde{t}(\mathbf{x},t); \quad \mathbf{x} \in \Gamma^{t} \tag{3.6b}$$

where, $\mathbf{n}$ denotes the outward unit normal vector along the traction boundaries; $\tilde{u}(\mathbf{x},t)$ and $\tilde{t}(\mathbf{x},t)$ are the displacement and traction data prescribed on Γ^{u} and Γ^{t}, respectively, and $\partial\Omega = \Gamma^{u} \cup \Gamma^{t}$; $\Gamma^{u} \cap \Gamma^{t} = \emptyset$. Homogeneous initial displacement and velocity conditions are assumed:

$$u^{\zeta}(\mathbf{x},0) = 0; \quad \mathbf{x} \in \Omega \tag{3.7a}$$

$$\dot{u}^{\zeta}(\mathbf{x},0) = 0; \quad \mathbf{x} \in \Omega \tag{3.7b}$$

Equations 3.4-3.7 define the initial-boundary value problem in the time domain. The convolutional form of the hereditary integral that describe the viscoelastic behavior allows a simpler formulation of the problem when posed in the Laplace domain [64, 54]. The momentum balance equation, Eq. 3.5, expressed in the Laplace domain is:

$$\boldsymbol{\nabla}_{x}.\boldsymbol{\tau}^{\zeta}(\mathbf{x},s) = \rho^{\zeta}(\mathbf{x})s^{2}u^{\zeta}(\mathbf{x},s) \tag{3.8}$$

where, $s = \sigma + \mathrm{i}w$ is the Laplace variable, $s \in \mathbb{C}$. In the Laplace domain, the response variable u^{ζ} is complex valued and the viscoelastic constitutive relation is written in the proportional form:

$$\boldsymbol{\tau}^{\zeta}(\mathbf{x},s) = G^{\zeta}(\mathbf{x},s)\boldsymbol{\gamma}^{\zeta}(\mathbf{x},s) \tag{3.9}$$

where $G^{\zeta}(\mathbf{x},s) = s\mathscr{L}\left(G^{\zeta}(\mathbf{x},t)\right)$ is the shear modulus function in the Laplace domain.

The boundary conditions in the Laplace domain are written as:

$$u^{\zeta}(\mathbf{x}, s) = \tilde{u}(\mathbf{x}, s); \quad \mathbf{x} \in \Gamma^{u} \tag{3.10a}$$

$$\boldsymbol{\tau}^{\zeta}(\mathbf{x}, s).\mathbf{n} = \tilde{t}(\mathbf{x}, s); \quad \mathbf{x} \in \Gamma^{t} \tag{3.10b}$$

The domain of the canonical unit cell is denoted as $\Theta \in \mathbb{R}^2$ expressed using the Cartesian coordinate, $\mathbf{y}$, which is related to the macroscale coordinate by $\mathbf{y} = \mathbf{x}/\zeta$, where $0 < \zeta \ll 1$ is the small scaling parameter. In the context of wave propagation, the scaling parameter is defined as the ratio between the size of microstructure and the characteristic length of deformation wave (i.e., $\zeta = l/\lambda$, where λ is the characteristic deformation wavelength).

Consider an arbitrary response function, $f^{\zeta}(\mathbf{x}, s)$, which oscillates in space due to fluctuations induced by material heterogeneity. The response field is assumed to allow a two-scale separation in terms of macroscale and microscale coordinates:

$$f^{\zeta}(\mathbf{x}, s) = f(\mathbf{x}, \mathbf{y}(\mathbf{x}), s) \tag{3.11}$$

The shear modulus and material density are taken to depend on the microscale coordinate only, i.e., $G^{\zeta}(\mathbf{x}, s) = G(\mathbf{y}, s)$ and $\rho^{\zeta}(\mathbf{x}) = \rho(\mathbf{y})$. The spatial derivative of f^{ζ} is obtained by applying the chain rule:

$$f^{\zeta}_{,\mathbf{x}}(\mathbf{x}, s) = f_{,\mathbf{x}}(\mathbf{x}, \mathbf{y}, s) + \frac{1}{\zeta} f_{,\mathbf{y}}(\mathbf{x}, \mathbf{y}, s) \tag{3.12}$$

where, subscript comma followed by $\mathbf{x}$ and $\mathbf{y}$ denote the spatial derivative with respect to the macroscale and microscale coordinates, respectively. All response fields are assumed to be locally periodic:

$$f(\mathbf{x}, \mathbf{y}, s) = f(\mathbf{x}, \mathbf{y} + \mathbf{N}\hat{\mathbf{l}}, s) \tag{3.13}$$

where, $\hat{\mathbf{l}} = [\hat{l}_1, \hat{l}_2]^T$ denotes the period of the microstructure in the microscale coordinates, i.e., $\hat{\mathbf{l}} = \mathbf{l}/\zeta$, $\mathbf{l}$ is the period of the microstructure in the physical (macroscale) coordinates, and $\mathbf{N}$ is a 2×2 diagonal matrix with integer components.

3.3 Two-Scale Asymptotic Analysis

Based on the two-scale setting described above, the displacement is approximated by the asymptotic expansion of up to the eighth order:

$$u^{\zeta}(\mathbf{x}, s) \equiv u(\mathbf{x}, \mathbf{y}, s) = u^{(0)}(\mathbf{x}, s) + \sum_{i=1}^{8} \zeta^i u^{(i)}(\mathbf{x}, \mathbf{y}, s) + O(\zeta^9) \tag{3.14}$$

where, $u^{(0)}$ denotes the macroscopic displacement field and is dependent on the macroscale coordinate only [42]; and $u^{(i)}$ are high order displacement fields which depend on both macroscale and microscale coordinates. We note that $u^{(0)}$ depends only on $\mathbf{x}$ if the assumption of moderate material property contrast between the composite constituents is satisfied. For composites with highly contrasted constituents, $u^{(0)}$ depends on both micro- and macroscale coordinates [115, 9]. The shear strain field is obtained as:

$$\boldsymbol{\gamma}^{\zeta}(\mathbf{x}, s) \equiv \boldsymbol{\gamma}(\mathbf{x}, \mathbf{y}, s) = \sum_{\alpha=0}^{7} \zeta^{\alpha} \boldsymbol{\gamma}^{(\alpha)}(\mathbf{x}, \mathbf{y}, s) \tag{3.15}$$

where,

$$\boldsymbol{\gamma}^{(\alpha)}(\mathbf{x}, \mathbf{y}, s) = \left(u^{(\alpha)}_{,x_j} + u^{(\alpha+1)}_{,y_j} \right) \hat{\mathbf{e}}_j \tag{3.16}$$

$(\cdot)_{,x_j} = \partial(\cdot)/\partial x_j$ and $(\cdot)_{,y_j} = \partial(\cdot)/\partial y_j$.

Employing Eq. 3.16 along with the constitutive relation (Eq. 3.9), the shear stress field at order $O(\zeta^{\alpha})$ is obtained as:

$$\boldsymbol{\tau}^{(\alpha)}(\mathbf{x}, \mathbf{y}, s) = G(\mathbf{y}, s) \boldsymbol{\gamma}^{(\alpha)}(\mathbf{x}, \mathbf{y}, s) \tag{3.17}$$

Substituting Eqs. 3.9, 3.14-3.17 into the momentum balance equation (Eq. 3.8), and collecting terms with equal orders yield the balance equations at each order of ζ:

$$O(\zeta^{-1}): \quad \boldsymbol{\nabla}_y.\boldsymbol{\tau}^{(0)}(\mathbf{x},\mathbf{y},s) = 0 \tag{3.18a}$$

$$O(\zeta^{\alpha}): \quad \boldsymbol{\nabla}_x.\boldsymbol{\tau}^{(\alpha)}(\mathbf{x},\mathbf{y},s) + \boldsymbol{\nabla}_y.\boldsymbol{\tau}^{(\alpha+1)}(\mathbf{x},\mathbf{y},s) = \rho(\mathbf{y})s^2u^{(\alpha)}(\mathbf{x},\mathbf{y},s) \tag{3.18b}$$

We start by additively decomposing the displacement field at each order of the asymptotic expansion. Following the procedure proposed in [15], the displacement field at each order is expressed in terms of a macroscopically constant displacement field and series of locally varying fields which have zero average over the unit cell:

$$u^{(i)}(\mathbf{x},\mathbf{y},s) = U^{(i)}(\mathbf{x},s) + \sum_{k=0}^{i-1}\tilde{U}^{(i,k)}(\mathbf{x},\mathbf{y},s) \tag{3.19}$$

where, $\tilde{U}^{(i,k)}(\mathbf{x},\mathbf{y},s)$ is the k^{th} locally varying field of $u^{(i)}(\mathbf{x},\mathbf{y},s)$ and it is associated with the successive gradients of macroscopic strain of an inferior order by a locally periodic influence function that is defined over the unit cell:

$$\tilde{U}^{(i,k)}(\mathbf{x},\mathbf{y},s) = \boldsymbol{H}^{(k+1)}(\mathbf{y},s)(.\boldsymbol{\nabla}_x)^{k+1}U^{(i-k-1)}(\mathbf{x},s) \tag{3.20}$$

where, $\boldsymbol{H}^{(k+1)}$ is the microstructural influence function at order $(k+1)$, and $(.\boldsymbol{\nabla}_x)^{k+1}$ is the $(k+1)^{th}$ gradient with respect to the macroscale coordinate, $\mathbf{x}$, with $k+1$ contractions to the microstructural influence function (e.g., $\tilde{U}^{(3,2)} = \boldsymbol{H}^{(3)}(.\boldsymbol{\nabla}_x)^3U^{(0)}$ is written as $H^{(3)}_{ijk}U^{(0)}_{,x_{ijk}}$ in indicial notation). The microstructural influence function, $\boldsymbol{H}^{(k+1)}$, is an order $(k+1)$ tensor and has $(k+2)$ independent components.

Remark 1. For a k^{th} order tensor $\boldsymbol{H}$ contracting k times with $\boldsymbol{\nabla}^kU$, only the symmetric part of $\boldsymbol{H}$ affects the result of contraction, i.e., $\boldsymbol{H}(.\boldsymbol{\nabla})^kU = \mathrm{Sym}\,(\boldsymbol{H})\,(.\boldsymbol{\nabla})^kU$.

This can be shown by defining the symmetric part of $\boldsymbol{H}$ as [26]:

$$\mathrm{Sym}(\boldsymbol{H}) = \frac{1}{k!}\sum_{\sigma\in\mathfrak{S}}\sigma(\boldsymbol{H}) \tag{3.21}$$

for all permutations $\sigma \in \mathfrak{S}$, and $\mathfrak{S}$ denotes the symmetric group of permutations on $\{1, ..., k\}$. The linear operator σ is defined as: $\sigma(\boldsymbol{v}_{i_1} \otimes \cdots \otimes \boldsymbol{v}_{i_k}) := \boldsymbol{v}_{i_{\sigma(1)}} \otimes \cdots \otimes \boldsymbol{v}_{i_{\sigma(k)}}$ for $\boldsymbol{v}_{i_1} \otimes \cdots \otimes \boldsymbol{v}_{i_k} \in \boldsymbol{H}^k(\mathbb{C}^2)$, where $[i_1, \ \cdots, \ i_k] \in \{1, 2\}$. $\boldsymbol{H}^k(\mathbb{C}^2)$ is the set of all k^{th} order tensors. Because the sequence of differentiation is interchangable, $\boldsymbol{\nabla}^k U$ is invariant under the permutation operation. Since the symmetric part of a scalar is the scalar itself, we have:

$$\boldsymbol{H}(.\boldsymbol{\nabla})^k U = \mathrm{Sym}\left(\boldsymbol{H}(.\boldsymbol{\nabla})^k U\right) = \mathrm{Sym}\left(\boldsymbol{H}\right)(.\boldsymbol{\nabla})^k U \tag{3.22}$$

Substitution of Eqs. 3.16, 3.19 and 3.20 into 3.17 leads to the expression for the stress field at $O(\zeta^\alpha)$:

$$\boldsymbol{\tau}^{(\alpha)}(\mathbf{x}, \mathbf{y}, s) = \sum_{k=0}^{\alpha} \boldsymbol{G}^{(k)}(\mathbf{y}, s).(.\boldsymbol{\nabla}_x)^k \boldsymbol{\nabla}_x U^{(\alpha-k)}(\mathbf{x}, s) \tag{3.23}$$

in which, $\boldsymbol{G}^{(k)}(\mathbf{y}, s)$ is an order $(k + 2)$ tensor and written as:

$$\boldsymbol{G}^{(k)}(\mathbf{y}, s) = G(\mathbf{y}, s)\left[\boldsymbol{H}^{(k)}(\mathbf{y}, s) \otimes \boldsymbol{I} + \boldsymbol{\nabla}_y \boldsymbol{H}^{(k+1)}(\mathbf{y}, s)\right] \tag{3.24}$$

where, $\otimes$ and $\boldsymbol{I}$ are the dyadic product and second order identity tensor, respectively, and $H^{(0)} = 1$. Substituting Eqs. 3.23 and 3.24 into Eq. 3.18a, we obtain the equilibrium equation for $\boldsymbol{H}^{(1)}(\mathbf{y}, s)$:

$$\boldsymbol{\nabla}_y.\left\{G(\mathbf{y}, s)\left[\boldsymbol{I} + \boldsymbol{\nabla}_y \boldsymbol{H}^{(1)}(\mathbf{y}, s)\right]\right\} = 0 \tag{3.25}$$

which is defined over the unit cell domain. $\boldsymbol{H}^{(1)}(\mathbf{y}, s)$ is unique when the local periodicity condition is applied and average is set to vanish, i.e., $\left\langle \boldsymbol{H}^{(1)}(\mathbf{y}, s) \right\rangle = \mathbf{0}$, where the averaging operator $\langle \cdot \rangle$ is defined as:

$$\langle \cdot \rangle = \frac{1}{|\Theta|} \int_{\Theta} (\cdot) \, d\mathbf{y} \tag{3.26}$$

where $|\Theta|$ is the area of the unit cell. The $O(1)$ macroscale balance equation is obtained by applying the averaging operator to Eq. 3.18b (with $\alpha = 0$) and considering Eqs. 3.19 and 3.23:

$$\bar{\boldsymbol{G}}^{(0)} .. \boldsymbol{\nabla}_x^2 U^{(0)}(\mathbf{x}, s) = \rho_0 s^2 U^{(0)}(\mathbf{x}, s) \tag{3.27}$$

where, $\bar{\boldsymbol{G}}^{(0)}(s) = \left\langle \boldsymbol{G}^{(0)}(\mathbf{y}, s) \right\rangle$ is the $O(1)$ homogenized shear moduli, and $\rho_0 = \left\langle \rho(\mathbf{y}) \right\rangle$ is the homogenized density. Overbar denotes the homogenized value throughout this chapter.

The procedure to evaluate influence functions and derive momentum balance equations presented above can be generalized for higher orders, i.e., $\alpha \geq 0$. At order $O(\zeta^{\alpha})$, the equilibrium equation for the influence function, $\boldsymbol{H}^{(\alpha+2)}$, is derived by substituting Eqs. 3.19, 3.20, 3.23, 3.24 and lower order equilibrium equations for the influence functions (e.g., Eq. 3.25) and macroscale balance equations up to order $O(\zeta^{\alpha})$ (e.g., Eq. 3.27) into Eq. 3.18b. The macroscale balance equation at order $O(\zeta^{\alpha+1})$ is then obtained by substituting Eqs. 3.19, 3.20, 3.23, 3.24 and lower order equilibrium equations for influence functions and macroscale balance equations into Eq. 3.18b at $O(\zeta^{\alpha+1})$ and applying the averaging operator. The equilibrium equation for the influence function, $\boldsymbol{H}^{(\alpha+2)}$, is derived as:

$$\boldsymbol{G}^{(\alpha)}(\mathbf{y}, s) + \boldsymbol{\nabla}_y . \boldsymbol{G}^{(\alpha+1)}(\mathbf{y}, s) = \theta(\mathbf{y}) \sum_{j=0}^{\alpha} \boldsymbol{H}^{(j)}(\mathbf{y}, s) \otimes \boldsymbol{D}^{(\alpha-j)}(s) \tag{3.28}$$

Given: Viscoelastic shear modulus, $G(\mathbf{y}, s)$, and density, $\rho(\mathbf{y})$.

Find: Microscale influence functions, $\boldsymbol{H}^{(n+1)}(\mathbf{y}, s)$, and

the homogenized shear moduli, $\boldsymbol{D}^{(n)}(s)$, for $n = 0, 1, ..., 6$, such that:

- Equilibrium:

$$n = 0, \quad \boldsymbol{\nabla}_y . \boldsymbol{G}^{(0)}(\mathbf{y}, s) = 0$$

$$n = 1, ..., 6, \quad \boldsymbol{\nabla}_y . \boldsymbol{G}^{(n)}(\mathbf{y}, s) = \theta(\mathbf{y}) \sum_{j=0}^{n-1} \boldsymbol{H}^{(j)}(\mathbf{y}, s) \otimes \boldsymbol{D}^{(n-1-j)}(s) - \boldsymbol{G}^{(n-1)}(\mathbf{y}, s)$$

- Periodic boundary condition:

$$\boldsymbol{H}^{(n+1)}(\mathbf{y}, s) = \boldsymbol{H}^{(n+1)}(\mathbf{y} + \hat{\mathbf{l}}, s), \quad \mathbf{y} \in \partial\Theta$$

- Normalization condition:

$$\left\langle \boldsymbol{H}^{(n+1)}(\mathbf{y}, s) \right\rangle = 0$$

- The homogenized shear moduli:

$$\boldsymbol{D}^{(0)}(s) = \bar{\boldsymbol{G}}^{(0)}(s)$$

$$\boldsymbol{D}^{(n)}(s) = \bar{\boldsymbol{G}}^{(n)}(s) - \sum_{m=1}^{n} \overline{\theta(\mathbf{y}) \boldsymbol{H}^{(m)}(\mathbf{y}, s)} \otimes \boldsymbol{D}^{(n-m)}(s)$$

Figure 3.1: Boundary value problems for the evaluation of the influence functions and computation of the homogenized shear moduli.

where, $\boldsymbol{D}^{(\alpha-j)}(s)$ is the $O(\zeta^{\alpha-j})$ homogenized shear moduli expressed as:

$$\boldsymbol{D}^{(\alpha-j)}(s) = \bar{\boldsymbol{G}}^{(\alpha-j)}(s) - \sum_{m=1}^{\alpha-j} \overline{\theta(\mathbf{y}) \boldsymbol{H}^{(m)}(\mathbf{y}, s)} \otimes \boldsymbol{D}^{(\alpha-j-m)}(s) \tag{3.29}$$

for $\alpha - j \geq 1$ and $\boldsymbol{D}^{(0)}(s) = \bar{\boldsymbol{G}}^{(0)}(s)$. The macroscale balance equation at $O(\zeta^{\alpha+1})$ is obtained as:

$$\sum_{n=0}^{\alpha} \boldsymbol{D}^{(n)} (. \boldsymbol{\nabla})_x^{n+2} U^{(\alpha-n)}(\mathbf{x}, s) = \rho_0 s^2 U^{(\alpha)}(\mathbf{x}, s) \tag{3.30}$$

The boundary value problems to evaluate the influence functions and compute the homogenized shear moduli are summarized in Fig. 3.1.

3.4 Spatial-Temporal Nonlocal Homogenization Model

3.4.1 Higher order gradient formulation

In this section, we propose a novel spatial-temporal nonlocal homogenization model for anti-plane shear wave propagation in viscoelastic composites. The nonlocal model is of gradient type with fourth order spatial, fourth order temporal and mixed spatial-temporal gradient terms to capture wave dispersion and attenuation beyond the long wavelength regime.

Remark 2. For macroscopically orthotropic composites, the homogenized shear moduli at odd and even orders have the following characteristics: (1) $\boldsymbol{D}^{(i)} = \mathbf{0}$, i is odd; (2) The components of $\boldsymbol{D}^{(0)}$, $\boldsymbol{D}^{(2)}$, $\boldsymbol{D}^{(4)}$, $\boldsymbol{D}^{(6)}$ with odd number of repeated indices are zero (e.g., $D^{(0)}_{12}$=$D^{(2)}_{1112}$=$D^{(4)}_{111112}$=$D^{(6)}_{11111112} = 0$).

This can be shown by considering the two planes of material symmetry that have unit normals, $\hat{\mathbf{e}}_1$ and $\hat{\mathbf{e}}_2$. The corresponding transformation matrix for reflection with respect to the two planes are:

$$\bar{\mathbf{R}} = \begin{bmatrix} -1 & 0 \\ 0 & 1 \end{bmatrix}, \quad \bar{\bar{\mathbf{R}}} = \begin{bmatrix} 1 & 0 \\ 0 & -1 \end{bmatrix}$$

The orthotropy condition requires the shear moduli is invariant under reflection [75], i.e., $\boldsymbol{D}^{(i)} = \bar{\mathbf{R}}^T \boldsymbol{D}^{(i)} \bar{\mathbf{R}} = \bar{\bar{\mathbf{R}}}^T \boldsymbol{D}^{(i)} \bar{\bar{\mathbf{R}}}$, which implies that the components of the moduli tensor with odd number of repeated index have to be 0. For example, $D^{(1)}_{111} = \bar{R}_{11}\bar{R}_{11}\bar{R}_{11}D^{(1)}_{111}$ and $D^{(2)}_{1112} = \bar{R}_{11}\bar{R}_{11}\bar{R}_{11}\bar{R}_{22}D^{(1)}_{1112}$, indicating $D^{(1)}_{111} = 0$ and $D^{(2)}_{1112} = 0$, respectively.

Considering that the macroscopic behavior of the composite is orthotropic and using Remark 2, the macroscale momentum balance equations are written in indicial

notation as:

$$O(1): \quad \rho_0 s^2 U^{(0)}(\mathbf{x},s) - D^{(0)}_{kl}(s) U^{(0)}_{,kl} = 0 \tag{3.31a}$$

$$O(\zeta^1): \quad \rho_0 s^2 U^{(1)}(\mathbf{x},s) - D^{(0)}_{kl}(s) U^{(1)}_{,kl} = 0 \tag{3.31b}$$

$$O(\zeta^2): \quad \rho_0 s^2 U^{(2)}(\mathbf{x},s) - D^{(0)}_{kl}(s) U^{(2)}_{,kl} = D^{(2)}_{klmn}(s) U^{(0)}_{,klmn} \tag{3.31c}$$

$$O(\zeta^3): \quad \rho_0 s^2 U^{(3)}(\mathbf{x},s) - D^{(0)}_{kl}(s) U^{(3)}_{,kl} = D^{(2)}_{klmn}(s) U^{(1)}_{,klmn} \tag{3.31d}$$

$$O(\zeta^4): \quad \rho_0 s^2 U^{(4)}(\mathbf{x},s) - D^{(0)}_{kl}(s) U^{(4)}_{,kl} = D^{(2)}_{klmn}(s) U^{(2)}_{,klmn} + D^{(4)}_{klmnpq}(s) U^{(0)}_{,klmnpq} \tag{3.31e}$$

$$O(\zeta^5): \quad \rho_0 s^2 U^{(5)}(\mathbf{x},s) - D^{(0)}_{kl}(s) U^{(5)}_{,kl} = D^{(2)}_{klmn}(s) U^{(3)}_{,klmn} + D^{(4)}_{klmnpq}(s) U^{(1)}_{,klmnpq} \tag{3.31f}$$

$$O(\zeta^6): \quad \rho_0 s^2 U^{(6)}(\mathbf{x},s) - D^{(0)}_{kl}(s) U^{(6)}_{,kl} = D^{(2)}_{klmn}(s) U^{(4)}_{,klmn} + D^{(4)}_{klmnpq}(s) U^{(2)}_{,klmnpq} + D^{(6)}_{klmnpqrs}(s) U^{(0)}_{,klmnpqrs} \tag{3.31g}$$

$$O(\zeta^7): \quad \rho_0 s^2 U^{(7)}(\mathbf{x},s) - D^{(0)}_{kl}(s) U^{(7)}_{,kl} = D^{(2)}_{klmn}(s) U^{(5)}_{,klmn} + D^{(4)}_{klmnpq}(s) U^{(3)}_{,klmnpq} + D^{(6)}_{klmnpqrs}(s) U^{(1)}_{,klmnpqrs} \tag{3.31h}$$

where, $\boldsymbol{D}^{(0)}$, $\boldsymbol{D}^{(2)}$, $\boldsymbol{D}^{(4)}$, $\boldsymbol{D}^{(6)}$ have 2, 8, 32, 128 non-zero components, respectively. Moreover, only the symmetric parts of these tensors affect the solution, as a consequence of Remark 1. The number of non-zero independent components in the symmetric part, $\mathrm{Sym}(\boldsymbol{D}^{(0)})$, $\mathrm{Sym}(\boldsymbol{D}^{(2)})$, $\mathrm{Sym}(\boldsymbol{D}^{(4)})$, $\mathrm{Sym}(\boldsymbol{D}^{(6)})$ are, 2, 3, 4, 5, respectively. $\mathrm{Sym}(\boldsymbol{D}^{(0)}) = \boldsymbol{D}^{(0)}$.

Equations 3.31a-h are combined into a single homogenized momentum balance equation by averaging the displacement field (Eq. 3.14) at each scale:

$$U(\mathbf{x},s) = \sum_{i=0}^{7} \zeta^i U^{(i)}(\mathbf{x},s) + O(\zeta^8) \tag{3.32}$$

where, $U(\mathbf{x},s)$ denotes the homogenized displacement field of $O(\zeta^8)$ accuracy. Com-

bining the two lowest order balance equations (Eq. 3.31a and Eq. 3.31b) leads to the classical local homogenization model which is valid in the absence of wave dispersion (i.e., when the wavelength is much larger than the microstructure). The spatial nonlocal homogenization model previously studied in Refs. [42, 4, 63] incorporates additional two equations (Eq. 3.31c and Eq. 3.31d). It predicts wave dispersion in the long-wavelength regime in the first pass band. The prediction error increases as the wavelength becomes shorter, therefore, the initiation of the stop band and beyond is not well captured. Following the line of increasing asymptotic accuracy by incorporating higher order momentum balance equations, Eqs. 3.31a-h are combined to construct the proposed spatial-temporal nonlocal homogenization model. The direct weighted summation of Eqs. 3.31a-h results in a spatial nonlocal homogenization model with higher order spatial gradient terms ($\boldsymbol{D}^{(4)}(.\boldsymbol{\nabla}_x)^6U$ and $\boldsymbol{D}^{(6)}(.\boldsymbol{\nabla}_x)^8U$) in addition to the fourth order spatial gradient term ($\boldsymbol{D}^{(2)}(.\boldsymbol{\nabla}_x)^4U$). While it is interesting to probe the role of $\boldsymbol{D}^{(4)}(.\boldsymbol{\nabla}_x)^6U$ and $\boldsymbol{D}^{(6)}(.\boldsymbol{\nabla}_x)^8U$ terms in capturing wave dispersion, we limit our scope to the fourth order gradient nonlocal equation based on the observation that it captures wave dispersion and attenuation beyond the long-wavelength regime [54]. In what follows, we transform the higher order spatial gradient terms in Eqs. 3.31a-h to fourth order gradient terms (i.e., spatial nonlocal, temporal nonlocal, and mixed spatial-temporal nonlocal). It is observed that Eqs. 3.31a, c, e, g and Eqs. 3.31b, d, f, h, have identical equation form and coefficients. Therefore, all derivations on the former equations directly applies to the latter ones. Only the derivations on the even orders (i.e., Eqs. 3.31a, c, e, g) are presented in the remainder of this section.

Considering Remark 1 and without loss of generality, Eq. 3.31g is expressed as:

$$\begin{aligned}\rho_0 s^2 U^{(6)}(\mathbf{x},s) - D^{(0)}_{kl}(s)U^{(6)}_{,kl} &= D^{(2)}_{(klmn)}(s)U^{(4)}_{,klmn} + D^{(4)}_{(klmnpq)}(s)U^{(2)}_{,klmnpq} \\ &+ \nu(s)D^{(6)}_{(klmnpqrs)}(s)U^{(0)}_{,klmnpqrs} + (1-\nu(s))D^{(6)}_{(klmnpqrs)}(s)U^{(0)}_{,klmnpqrs}\end{aligned} \tag{3.33}$$

where, $\nu(s)$ is a scalar parameter. Sym($\boldsymbol{D}^{(6)}$) in the third term on the right side of

Eq. 3.33 is approximated as:

$$D^{(6)}_{(klmnpqrs)}(s) \approx A^{(1)}(s)\text{Sym}\left(D^{(0)}_{kl}(s)D^{(4)}_{(mnpqrs)}(s)\right) \tag{3.34}$$

where, $A^{(1)}(s)$ is a complex valued scalar that minimizes the discrepancy between the non-zero independent components of $\text{Sym}(\boldsymbol{D}^{(6)})$ and $\text{Sym}\left(\boldsymbol{D}^{(0)} \otimes \text{Sym}(\boldsymbol{D}^{(4)})\right)$ in the Euclidean norm, and it is computed by the Moore-Penrose pseudo-inverse. Substituting Eq. 3.34 and Eq. 3.31e into the third term on the right side of Eq. 3.33 and considering Remark 1:

$$\begin{aligned}
&\nu(s)D^{(6)}_{(klmnpqrs)}(s)U^{(0)}_{,klmnpqrs} \approx \nu(s)A^{(1)}(s)\text{Sym}\left(D^{(0)}_{kl}(s)D^{(4)}_{(mnpqrs)}(s)\right)U^{(0)}_{,klmnpqrs} = \\
&\nu(s)A^{(1)}(s)D^{(0)}_{kl}(s)D^{(4)}_{(mnpqrs)}(s)U^{(0)}_{,klmnpqrs} = \\
&\nu(s)A^{(1)}(s)D^{(0)}_{kl}(s)\left[\rho_0 s^2 U^{(4)}(\mathbf{x},s) - D^{(0)}_{mn}(s)U^{(4)}_{,mn} - D^{(2)}_{(mnpq)}(s)U^{(2)}_{,mnpq}\right]_{,kl}
\end{aligned} \tag{3.35}$$

Substituting Eq. 3.35 for the the third term on the right side of Eq. 3.33:

$$\begin{aligned}
&\rho_0 s^2 U^{(6)}(\mathbf{x},s) - D^{(0)}_{kl}(s)U^{(6)}_{,kl} = \left(D^{(2)}_{(klmn)}(s) - \nu(s)A^{(1)}(s)D^{(0)}_{kl}(s)D^{(0)}_{mn}(s)\right)U^{(4)}_{,klmn} + \\
&\nu(s)A^{(1)}(s)\rho_0 s^2 D^{(0)}_{kl}(s)U^{(4)}_{,kl} + \left(D^{(4)}_{(klmnpq)}(s) - \nu(s)A^{(1)}(s)D^{(0)}_{kl}(s)D^{(2)}_{(mnpq)}(s)\right)U^{(2)}_{,klmnpq} + \\
&(1-\nu(s))D^{(6)}_{(klmnpqrs)}(s)U^{(0)}_{,klmnpqrs}
\end{aligned} \tag{3.36}$$

Similar to Eq. 3.34, the non-zero independent components of $\text{Sym}(\boldsymbol{D}^{(4)})$ is approximated as:

$$D^{(4)}_{(klmnpq)}(s) \approx A^{(2)}(s)\text{Sym}\left(D^{(2)}_{(klmn)}(s)D^{(0)}_{pq}(s)\right) \tag{3.37}$$

where $A^{(2)}(s)$ is computed by the Moore-Penrose pseudo-inverse. Substituting Eq. 3.37 into Eq. 3.36, considering Remark 1 and substituting Eq. 3.31c into the resulting equation for $D^{(0)}_{pq}(s)U^{(2)}_{,pq}$, we obtain:

$$\rho_0 s^2 U^{(6)}(\mathbf{x},s) - D^{(0)}_{kl}(s)U^{(6)}_{,kl} = \left(D^{(2)}_{(klmn)}(s) - \nu(s)A^{(1)}(s)D^{(0)}_{kl}(s)D^{(0)}_{mn}(s)\right)U^{(4)}_{,klmn} + \nu(s)A^{(1)}(s)\rho_0 s^2 D^{(0)}_{kl}(s)U^{(4)}_{,kl} + \left(A^{(2)}(s) - \nu(s)A^{(1)}(s)\right)D^{(2)}_{(klmn)}\rho_0 s^2 U^{(2)}_{,klmn} + \left[(1-\nu(s))D^{(6)}_{(klmnpqrs)}(s) - \left(A^{(2)}(s) - \nu(s)A^{(1)}(s)\right)D^{(2)}_{(klmn)}D^{(2)}_{(pqrs)}\right]U^{(0)}_{,klmnpqrs} \tag{3.38}$$

By substituting Eq. 3.31e into Eq. 3.38 and considering Remark 1 and Eq. 3.31a, we arrive at the macroscale momentum balance equation at $O(\zeta^6)$:

$$\rho_0 s^2 U^{(6)}(\mathbf{x},s) - D^{(0)}_{kl}(s)U^{(6)}_{,kl} = \left(D^{(2)}_{(klmn)}(s) - \nu(s)A^{(1)}(s)D^{(0)}_{kl}(s)D^{(0)}_{mn}(s)\right)U^{(4)}_{,klmn} + \left(2\nu(s)A^{(1)}(s) - A^{(2)}(s)\right)\rho_0 s^2 D^{(0)}_{kl}(s)U^{(4)}_{,kl} + \left(A^{(2)}(s) - \nu(s)A^{(1)}(s)\right)\rho_0^2 s^4 U^{(4)} + E_{(klmnpqrs)}(\nu(s),s)U^{(0)}_{,klmnpqrs} \tag{3.39}$$

where the last term is denoted as the error term and $\boldsymbol{E}$ is expressed as:

$$E_{(klmnpqrs)}(\nu(s),s) = \Big[(1-\nu(s))D^{(6)}_{(klmnpqrs)}(s) - \left(A^{(2)}(s) - \nu(s)A^{(1)}(s)\right)\mathrm{Sym}\left(D^{(2)}_{(klmn)}(s)D^{(2)}_{(pqrs)}(s) + D^{(4)}_{(klmnpq)}(s)D^{(0)}_{rs}(s)\right)\Big] \tag{3.40}$$

The momentum balance equations at $O(\zeta^4)$ and $O(\zeta^2)$ are obtained similarly and detailed derivations are provided in Appendix B. The momentum balance equations at $O(\zeta^7)$, $O(\zeta^5)$, $O(\zeta^3)$ are derived by the same procedure as $O(\zeta^6)$, $O(\zeta^4)$, $O(\zeta^2)$, respectively. The resulting macroscale momentum balance equation at order $O(\zeta^k)$

are summarized as follows:

$$\rho_0 s^2 U^{(k)}(\mathbf{x},s) - D^{(0)}_{kl}(s) U^{(k)}_{,kl} = 0; \quad k = 0,1 \tag{3.41a}$$

$$\rho_0 s^2 U^{(k)}(\mathbf{x},s) - D^{(0)}_{kl}(s) U^{(k)}_{,kl} = \left(D^{(2)}_{(klmn)}(s) - \nu(s) A^{(1)}(s) D^{(0)}_{kl}(s) D^{(0)}_{mn}(s) \right) U^{(k-2)}_{,klmn}$$
$$+ \left(2\nu(s) A^{(1)}(s) - A^{(2)}(s) \right) \rho_0 s^2 D^{(0)}_{kl}(s) U^{(k-2)}_{,kl} + \left(A^{(2)}(s) - \nu(s) A^{(1)}(s) \right) \rho_0^2 s^4 U^{(k-2)};$$
$$k = 2,3,4,5 \tag{3.41b}$$

$$\rho_0 s^2 U^{(k)}(\mathbf{x},s) - D^{(0)}_{kl}(s) U^{(k)}_{,kl} = \left(D^{(2)}_{(klmn)}(s) - \nu(s) A^{(1)}(s) D^{(0)}_{kl}(s) D^{(0)}_{mn}(s) \right) U^{(k-2)}_{,klmn}$$
$$+ \left(2\nu(s) A^{(1)}(s) - A^{(2)}(s) \right) \rho_0 s^2 D^{(0)}_{kl}(s) U^{(k-2)}_{,kl} + \left(A^{(2)}(s) - \nu(s) A^{(1)}(s) \right) \rho_0^2 s^4 U^{(k-2)}$$
$$+ E_{(klmnpqrs)}(\nu(s),s) U^{(k-6)}_{,klmnpqrs};$$
$$k = 6,7 \tag{3.41c}$$

Considering the definition for the homogenized displacement field (Eq. 3.32) and the summation of momentum balance equation at order $O(\zeta^k)$ multiplied by ζ^k, result in the homogenized momentum balance equation:

$$\rho_0 s^2 U(\mathbf{x},s) - D^{(0)}_{kl}(s) U_{,kl} = \left(D^{(2)}_{(klmn)}(s) - \nu(s) A^{(1)}(s) D^{(0)}_{kl}(s) D^{(0)}_{mn}(s) \right) U_{,klmn} +$$
$$\left(2\nu(s) A^{(1)}(s) - A^{(2)}(s) \right) \rho_0 s^2 D^{(0)}_{kl}(s) U_{,kl} + \left(A^{(2)}(s) - \nu(s) A^{(1)}(s) \right) \rho_0^2 s^4 U +$$
$$\zeta^6 E_{(klmnpqrs)}(\nu(s),s) U^{(0)}_{,klmnpqrs} + \zeta^7 E_{(klmnpqrs)}(\nu(s),s) U^{(1)}_{,klmnpqrs} + O(\zeta^8) \tag{3.42}$$

Equation 3.42 represents a one-parameter family of nonlocal homogenization models as a function of $\nu(s)$. For arbitrarily chosen $\nu(s)$, these models achieve $O(\zeta^6)$ asymptotic accuracy. The detailed procedure for choosing $\nu(s)$ and obtaining a unique nonlocal model is provided in the next section.

We note that Eq. 3.42 is formally similar to the gradient elasticity models [91, 7, 109, 33] and the homogenization model [125], where spatial nonlocal, temporal nonlocal and mixed spatial-temporal nonlocal terms are present, and the length-scale

parameters associated with these terms are calibrated. The proposed model is unique in that all the model parameters are consistently derived from the homogenization process and it applies to viscoelastic composites.

3.4.2 Identification of $\nu(s)$

It is observed in Eq. 3.42 that the asymptotic error term depends on $\nu(s)$. We therefore seek to set $\nu(s)$ such that the error term is minimized. This requires knowledge of $U^{(0)}_{,klmnpqrs}$ which is not available a-priori. As an alternative, we pursue $\nu(s)$ such that all the independent components of the coefficient tensor of the error term (i.e., $\boldsymbol{E}$) are minimized. To be explicit, they are written in vector form: $\mathbf{e} = [E_{(1\times 8)}\ E_{(1\times 6 2\times 2)}\ E_{(1\times 4 2\times 4)}\ E_{(1\times 2 2\times 6)}\ E_{(2\times 8)}]^T$, where the subscript $(m_{\times n})$ denotes index m repeated n times. In addition, the dynamic stability of the general fourth order governing equation imposes constraints to the model parameters associated with the nonlocal terms. This poses a constrained minimization problem for the identification of $\nu(s)$.

Neglecting the $O(\zeta^6)$ and higher order error terms, Eq. 3.42 is rewritten as:

$$\rho_0 s^2 U(\mathbf{x}, s) - D^{(0)}_{kl}(s) U_{,kl} = \alpha^{(1)}_{(klmn)}(s) U_{,klmn} + \rho_0 s^2 \alpha^{(2)}_{kl}(s) U_{,kl} + \rho_0^2 s^4 \alpha^{(3)}(s) U \quad (3.43)$$

where,

$$\alpha^{(1)}_{(klmn)}(s) = \text{Sym}\left(D^{(2)}_{klmn}(s) - \nu(s) A^{(1)}(s) D^{(0)}_{kl}(s) D^{(0)}_{mn}(s) \right) \quad (3.44a)$$

$$\alpha^{(2)}_{kl}(s) = \left(2\nu(s) A^{(1)}(s) - A^{(2)}(s) \right) D^{(0)}_{kl}(s) \quad (3.44b)$$

$$\alpha^{(3)}(s) = A^{(2)}(s) - \nu(s) A^{(1)}(s) \quad (3.44c)$$

For elastic composites, $\boldsymbol{D}^{(0)}$, $\boldsymbol{\alpha}^{(1)}$, $\boldsymbol{\alpha}^{(2)}$ and $\alpha^{(3)}$ are real-valued constant parameters. For viscoelastic composites, they are complex-valued and functions of the Laplace

variable. Substituting a harmonic wave solution, $U = U_0(s)e^{\mathrm{i}(k_1x_1+k_2x_2)}$, into Eq. 3.43, the resulting equation is expressed in polar coordinate system for the wave vector, $k_1 = k(s,\theta)\cos\theta$ and $k_2 = k(s,\theta)\sin\theta$. In this study, the imaginary and real parts of the wave vector are assumed to be co-linear, thus θ is taken as real-valued. The co-linearity assumption has been previously employed in the dispersion analysis of viscoelastic materials [24, 3]. The dispersion relation in terms of the Laplace variable is obtained as:

$$A(s,\theta)k^4 + B(s,\theta)k^2 + C(s,\theta) = 0 \tag{3.45}$$

where,

$$A(s,\theta) = \alpha^{(1)}_{(1111)}(s)\cos^4\theta + \alpha^{(1)}_{(2222)}(s)\sin^4\theta + 6\alpha^{(1)}_{(1122)}(s)\cos^2\theta\sin^2\theta \tag{3.46a}$$

$$B(s,\theta) = -\left(\alpha^{(2)}_{11}(s)\rho_0 s^2 + D^{(0)}_{11}(s)\right)\cos^2\theta - \left(\alpha^{(2)}_{22}(s)\rho_0 s^2 + D^{(0)}_{22}(s)\right)\sin^2\theta \tag{3.46b}$$

$$C(s,\theta) = \alpha^{(3)}(s)\rho_0^2 s^4 - \rho_0 s^2 \tag{3.46c}$$

The solution of Eq. 3.45, $k(s,\theta)$, relates the wavenumber, the Laplace variable and the direction of wave vector as:

$$\left(k^{\{1,2\}}(s,\theta)\right)^2 = \frac{-B(s,\theta) - \sqrt{B^2(s,\theta) - 4A(s,\theta)C(s,\theta)}}{2A(s,\theta)} \tag{3.47a}$$

$$\left(k^{\{3,4\}}(s,\theta)\right)^2 = \frac{-B(s,\theta) + \sqrt{B^2(s,\theta) - 4A(s,\theta)C(s,\theta)}}{2A(s,\theta)} \tag{3.47b}$$

For elastic composites, the dynamic stability of Eq. 3.43 in terms of the constant model parameters is analyzed by the limit analysis in the frequency domain [91, 109]. Replacing s in Eq. 3.45 with $\mathrm{i}\omega$, the dispersion relation in terms of frequency is obtained. Consider the limiting scenarios: 1) quasi-static (i.e., $\omega \to 0$); and 2)

infinitely long wave (i.e., $k \to 0$), which respectively leads to the solutions:

$$k^{\{1,2\}} = 0, \quad k^{\{3,4\}} = \pm\sqrt{\frac{\left(D_{11}^{(0)}\cos^2\theta + D_{22}^{(0)}\sin^2\theta\right)}{A(\theta)}} \tag{3.48a}$$

$$\omega^{\{1,2\}} = 0, \quad \omega^{\{3,4\}} = \pm\sqrt{-\frac{1}{\alpha^{(3)}\rho_0}} \tag{3.48b}$$

In view of the harmonic wave solution in the frequency domain, $U = U_0 e^{\mathrm{i}(k_1 x_1 + k_2 x_2 - \omega t)}$, the stability of wave propagation in the quasi-static limit requires that k is real; and infinitely long wave limit requires that ω is real. These are achieved by the following constraints:

$$A(\theta) > 0, \quad \alpha^{(3)} < 0 \tag{3.49}$$

In order to generalize these ideas to viscoelastic composites, the following constraints on the model parameters are proposed:

$$\mathrm{Re}\left[A(s,\theta)\right] > 0 \tag{3.50a}$$

$$\mathrm{Re}\left[\alpha^{(3)}(s)\right] < 0, \quad \mathrm{Im}\left[\alpha^{(3)}(s)\right] = 0 \tag{3.50b}$$

In the quasi-static limit, viscoelastic phases within the composites behave as elastic ones, the parameters are independent of the Laplace variable s. Equation 3.50a therefore recovers the constraint for elastic composites. In the infinitely long wave limit, Eq. 3.50b is derived by analyzing the response of governing equation (Eq. 3.43) under an impulse load and examining the location of poles of the transfer function, as a common approach to analyze the system stability in the Laplace domain [49]. The detailed derivation is provided in Appendix C.

Employing the stability constraints introduced above and using the Euclidean norm of $\mathbf{e}$ as the objective function, the identification problem for $\nu(s)$ is stated in Fig. 3.2.

Given: Homogenized material properties, $\boldsymbol{D}^{(0)}(s)$, $\boldsymbol{D}^{(2)}(s)$, ρ_0, and the approximation parameters $A^{(1)}(s)$ and $A^{(2)}(s)$.

Find: $\nu(s)$, such that:

- Minimize: $\left\|\mathbf{e}(\nu, s)\right\|$
- Subject to constraints:

$$\mathrm{Re}\left[A(s,\theta)\right] > 0; \quad \mathrm{Re}\left[\alpha^{(3)}(s)\right] < 0, \quad \mathrm{Im}\left[\alpha^{(3)}(s)\right] = 0, \quad \theta \in [0, \pi/2]$$

Figure 3.2: Summary of the constrained minimization problem for the identification of $\nu(s)$.

3.4.3 Nonlocal effective medium model

Straightforward implementation of the proposed fourth order PDE to simulate transient wave propagation is problematic since the numerical solution contains both the physical and non-physical wavenumber solutions. Furthermore, the evaluation of the fourth order governing equation requires setting high order boundary conditions, which is usually not trivial to obtain. In this section, we propose a nonlocal effective medium model (i.e., second order) based on the spatial-temporal nonlocal homogenization model to simulate the transient behavior of the composite. This is achieved by identifying and retaining the physical wavenumber solutions of the original fourth order PDE, while eliminating the non-physical branches.

The identification and selection of the physical wavenumber is critical in obtaining stable and physically meaningful dynamics [109, 54]. Considering the harmonic solution form, $U = U_0(s)e^{\mathrm{i}(k_1 x_1 + k_2 x_2)}$, negative imaginary part of the wavenumber results in exponentially amplifying harmonic wave. The physically meaningful wavenumber is therefore identified as the one that has non-negative imaginary part. Examining Eq. 3.47 indicates that the physically meaningful wavenumber is:

$$\bar{k}^2(s,\theta) = \begin{cases} \left(k^{\{1,2\}}\right)^2, & \omega \leq \omega_c \\ \left(k^{\{3,4\}}\right)^2, & \omega > \omega_c \end{cases} \tag{3.51}$$

where the switch, ω_c, between the two branches of the solutions is the imaginary part of the critical Laplace variable, $s_c = \sigma + \mathrm{i}\omega_c$. In order to ensure that the continuity of the physical wavenumber at the switch, $\left(k^{\{1,2\}}(s,\theta)\right)^2 = \left(k^{\{3,4\}}(s,\theta)\right)^2$ is satisfied:

$$-\sqrt{B^2(s,\theta) - 4A(s,\theta)C(s,\theta)} = \sqrt{B^2(s,\theta) - 4A(s,\theta)C(s,\theta)} \tag{3.52}$$

The complex-valued equation above is equivalent to the constrained system of equations:

$$\mathrm{Im}\left[B^2(s,\theta) - 4A(s,\theta)C(s,\theta)\right] = 0 \tag{3.53a}$$

$$\mathrm{Re}\left[B^2(s,\theta) - 4A(s,\theta)C(s,\theta)\right] \leq 0 \tag{3.53b}$$

Substituting Eq. 3.46 and s_c into Eq. 3.53a results in an equation from which ω_c is obtained. ω_c is evaluated analytically for elastic composites. For viscoelastic composites, ω_c is solved numerically, since the model parameters are dependent on the Laplace variable, resulting in a nonlinear equation. The inequality condition in Eq. 3.53b provides the criterion to choose the appropriate ω_c among the multiple solutions of Eq. 3.53a.

Selecting only the physical wavenumber for the solution of Eq. 3.45 is captured by the following dispersion equation:

$$k^2 - \bar{k}^2(\theta, s) = 0 \tag{3.54}$$

multiplying Eq. 3.54 with $-\rho_0 s^2/\bar{k}^2(\theta, s)$, the dispersion relation becomes:

$$\phi(s,\theta)\left(D_{11}^{(0)}(s)\cos^2\theta + D_{22}^{(0)}(s)\sin^2\theta\right)k^2 + \rho_0 s^2 = 0 \tag{3.55}$$

where,

$$\phi(s,\theta) = \frac{-\rho_0 s^2}{\bar{k}^2(\theta,s)\left(D_{11}^{(0)}(s)\cos^2\theta + D_{22}^{(0)}(s)\sin^2\theta\right)} \tag{3.56}$$

Equation 3.55 resembles the dispersion relation of the classical homogenization model (Eq. 3.31a) except for the factor $\phi(s,\theta)$, which results from the nonlocal terms in the fourth order governing equation. Compared to the dispersion relation of the original fourth order equation (Eq. 3.45), Eq. 3.55 is regularized in that the dispersion relation contains the physical branches of the solution only and the non-physical branches are suppressed. The regularized nonlocal momentum balance equation is then expressed as:

$$\rho_0 s^2 U(\mathbf{x},s) - D_{kl}^e(s,\theta)U_{,kl} = 0 \tag{3.57}$$

in which, $D_{kl}^e(s,\theta) = \phi(s,\theta)D_{kl}^{(0)}(s)$. The nonlocal factor, $\phi(s,\theta)$, depends on the Laplace variable and the direction of wave propagation. The direction-dependence reveals the anisotropic nature of wave dispersion, which is also observed by Phani et al. [108] and Wautier and Guzina [125].

Equation 3.57 is a second order PDE that shares the same structure as the classical homogenization model but expressed in terms of nonlocal effective stiffness that is frequency- and direction-dependent. In a transient dynamic analysis, computing the direction-dependent nonlocal factor requires knowledge of the direction of local wave vector at each material point which evolves as a function of time. Since the wave vector is normal to the wave front, $\phi(s,\theta)$ can be obtained by solving for the evolution of wave front for any given s. A comprehensive study of techniques to track wave front can be found in [34]. We use a simplified approach that prescribes all the material points to have the same property that captures wave propagation of Eq. 3.57 exactly in $\theta = 0$ and $\theta = \pi/2$ directions only. Substituting test harmonic wave $U = U_0(s)e^{\mathrm{i}(k_1 x_1)}$ and $U = U_0(s)e^{\mathrm{i}(k_2 x_2)}$ into Eq. 3.57, the effective stiffness are obtained: $D_{11}^e(s) = -\rho_0 s^2/\bar{k}^2(s,0)$, $D_{22}^e(s) = -\rho_0 s^2/\bar{k}^2(s,\pi/2)$. The resulting

Given: Effective nonlocal stiffness, $D^e_{kl}(s)$, and homogenized density, ρ_0.

Find: Macroscale displacement $U(\mathbf{x}, s) : \Omega \times \mathbb{C} \to \mathbb{C}$, such that:

- Momentum balance:

$$\rho_0 s^2 U(\mathbf{x}, s) - D^e_{kl}(s) U_{,kl} = 0$$

- Boundary conditions:

$$U(\mathbf{x}, s) = \tilde{u}(\mathbf{x}, s), \quad \mathbf{x} \in \Gamma^u$$

$$D^e_{kl} U_{,l} n_k = \tilde{t}(\mathbf{x}, s), \quad \mathbf{x} \in \Gamma^t$$

Figure 3.3: Boundary value problem for macroscale displacement $U(\mathbf{x}, s)$.

momentum balance equation is:

$$\rho_0 s^2 U(\mathbf{x}, s) - D^e_{kl}(s) U_{,kl} = 0 \tag{3.58}$$

This operation in fact reduces the direction-dependent nonlocal effective stiffness to a direction-independent one. As a result, the reduced dispersion relation matches that of Eq. 3.55 exactly in $\theta = 0$ and $\theta = \pi/2$ directions, whereas the solutions for arbitrary wave direction θ are approximated. The effect of this approximation is discussed in Section 3.6.1. The resulting boundary value problem to evaluate the macroscale displacement is summarized in Fig. 3.3.

3.5 Numerical Implementation

In this section, the numerical evaluation of the microscale influence functions, computation of the homogenized shear moduli and model parameters, and the solution to the macroscale momentum balance equation are presented. The analyses are performed in the Laplace domain using complex algebra. For a fixed but arbitrary Laplace variable, the microscale influence functions are evaluated using the standard finite element method (FEM) with C^0-continuous shape functions. Isogeometric analysis (IGA) with C^1-continuous NURBS (Non-Uniform Rational B-Splines)

basis functions is employed to evaluate the macroscale momentum balance equation. The time domain response is then obtained by numerical inverse Laplace transform.

3.5.1 Microscale problem

The numerical implementation of the first two influence functions, $\boldsymbol{H}^{(1)}$ and $\boldsymbol{H}^{(2)}$, have been previously provided in Refs. [64, 65], and skipped herein for brevity. In what follows, we provide a general procedure to compute the influence functions at higher orders. Considering Eq. 3.24 for $\boldsymbol{G}^{(n)}(\mathbf{y}, s)$, the weak form of equilibrium equation for the $(n+1)^{th}$ influence function (Fig. 3.1, $n \geq 1$) is written as:

$$\int_{\Theta} G(\mathbf{y}, s) \boldsymbol{\nabla}_y w(\mathbf{y}) . \boldsymbol{\nabla}_y \boldsymbol{H}^{(n+1)}(\mathbf{y}, s) d\mathbf{y} = - \int_{\Theta} G(\mathbf{y}, s) \boldsymbol{\nabla}_y w(\mathbf{y}) . \left(\boldsymbol{H}^{(n)}(\mathbf{y}, s) \otimes \boldsymbol{I} \right) d\mathbf{y}$$
$$+ \int_{\Theta} w(\mathbf{y}) \boldsymbol{G}^{(n-1)}(\mathbf{y}, s) d\mathbf{y} - \int_{\Theta} w(\mathbf{y}) \left[\theta(\mathbf{y}) \sum_{j=0}^{n-1} \boldsymbol{H}^{(j)}(\mathbf{y}, s) \otimes \boldsymbol{D}^{(n-1-j)}(s) \right] d\mathbf{y} \quad (3.59)$$

where, $w \in \mathcal{W}_{\text{per}} \subset H^1(\Theta, \mathbb{R})$ is the weighting function; $\mathcal{W}_{\text{per}}$ is space of sufficiently smooth functions that is periodic along the microstructure boundary, Γ_Θ; and $H^1(\Theta, \mathbb{R})$ is the Sobolev space of scalar-valued functions with square integrable first derivative over the domain of microstructure, Θ. Rewriting $\boldsymbol{H}^{(n+1)}(\mathbf{y}, s) = \boldsymbol{H}^{(n+1)}_{\text{re}} + \mathrm{i}\boldsymbol{H}^{(n+1)}_{\text{im}}$, where $\boldsymbol{H}^{(n+1)}_{\text{re}}$ and $\boldsymbol{H}^{(n+1)}_{\text{im}}$ are real. The solutions are sought in the function space, $\mathcal{H}_{\text{per}\{\text{re,im}\}} \subset H^1(\Theta, \mathbb{R}^{n+2})$:

$$\mathcal{H}_{\text{per}\{\text{re,im}\}} := \Big\{ \boldsymbol{H}^{(n+1)}_{\{\text{re,im}\}}(\mathbf{y}, s) \mid \boldsymbol{H}^{(n+1)}_{\{\text{re,im}\}}(\mathbf{y}, s) \text{ is periodic } \forall \mathbf{y} \in \Gamma_\Theta;$$
$$\langle \boldsymbol{H}^{(n+1)}_{\{\text{re,im}\}}(\mathbf{y}, s) \rangle = 0 \Big\} \quad (3.60)$$

In the discrete approximation of $\boldsymbol{H}^{(n+1)}_{\{\text{re,im}\}}$, periodicity is imposed by coupling the nodes at the opposing edges as the master and slave nodes. The degrees of freedom associated with the slave nodes are eliminated through static condensation. To implement this coupling, the microstructure is discretized such that the nodal positions

at the opposing boundaries match exactly. In addition, the value of the influence function is set to zero at corner nodes to eliminate rigid body modes. The normalization condition is imposed by subtracting the microstructural average of the influence functions from each nodal value, which is done as a postprocessing step. The finite dimensional subspace for the trial solutions, $\mathcal{H}^h_{\text{per}} \subset \mathcal{H}_{\text{per}}$, is constructed as:

$$\mathcal{H}^h_{\text{per}\{\text{re,im}\}} := \left\{ \boldsymbol{H}^{(n+1),h}_{\{\text{re,im}\}}(\mathbf{y}, s) \;\middle|\; \boldsymbol{H}^{(n+1),h}_{\{\text{re,im}\}}(\mathbf{y}, s) = \sum_{A=1}^{M} N^{[A]}(\mathbf{y}) \mathbf{H}^{(n+1)[A]}_{\{\text{re,im}\}}(s); \right. \\ \left. \mathbf{H}^{(n+1)[c]}_{\{\text{re,im}\}}(s) = 0 \right\} \quad (3.61)$$

where, $N^{[A]}(\mathbf{y})$ is the shape function, M the number of nodes, superscript h indicates discretization, and $\mathbf{H}^{(n+1)[A]}_{\{\text{re,im}\}}(s)$ denotes the influence function matrix at node A. $\mathbf{H}^{(n+1)[c]}_{\{\text{re,im}\}}(s)$ is the influence function at the corner nodes.

Substituting the discretization of the influence function and the weighting function into the weak form and expressing the terms in matrix-vector form using the Voigt notation yields the following discrete system:

$$\mathbf{K}\mathbf{d}^{(n+1)} = \mathbf{F}^{(n+1)} \quad (3.62)$$

which is formed by assemblying the element matrices:

$$\mathbf{K} = \underset{e=1}{\overset{N_e}{\mathcal{A}}} \mathbf{K}^e; \quad \mathbf{d}^{(n+1)} = \underset{e=1}{\overset{N_e}{\mathcal{A}}} \mathbf{d}^{(n+1)e}; \quad \mathbf{F}^{(n+1)} = \underset{e=1}{\overset{N_e}{\mathcal{A}}} \mathbf{F}^{(n+1)e} \quad (3.63)$$

$\mathcal{A}$ is the assembly operator, superscript e denotes the element index and N_e the number of elements. The element stiffness matrix is expressed as:

$$\mathbf{K}^e = G(\mathbf{y}, s) \int_{\Theta^e} \mathbf{B}^e(\mathbf{y})^T \mathbf{B}^e(\mathbf{y}) \, d\mathbf{y} \quad (3.64)$$

where Θ^e denotes the domain of element e, T the matrix transpose, and

$$\mathbf{B}^e = \left[\begin{array}{cccc} \mathbf{B}^{e[1]} & \mathbf{B}^{e[2]} & \dots & \mathbf{B}^{e[M_e]} \end{array} \right] \tag{3.65a}$$

$$\mathbf{B}^{e[A]} = \left[\begin{array}{cc} N^{e[A]}_{,y_1}(\mathbf{y}) & N^{e[A]}_{,y_2}(\mathbf{y}) \end{array} \right]^T \tag{3.65b}$$

For the convenience and efficiency of numerical implementation, the same discretization of microstructure and shape functions are used for all influence functions, therefore, the stiffness matrix is only assembled and factorized (e.g., LU factorization) once. The right-hand-side force matrices are assembled for each influence function. The components of the influence functions are listed as follows:

$$\mathbf{H}^{(1),h}(\mathbf{y}, s) = \left[H^{(1),h}_1(\mathbf{y}, s) \quad H^{(1),h}_2(\mathbf{y}, s) \right]^T \tag{3.66a}$$

$$\mathbf{H}^{(2),h}(\mathbf{y}, s) = \left[H^{(2),h}_{(11)}(\mathbf{y}, s) \quad H^{(2),h}_{(12)}(\mathbf{y}, s) \quad H^{(2),h}_{(22)}(\mathbf{y}, s) \right]^T \tag{3.66b}$$

$$\vdots$$

$$\begin{aligned} \mathbf{H}^{(7),h}(\mathbf{y}, s) = \Big[& H^{(7),h}_{(1\times 7)}(\mathbf{y}, s) \quad H^{(7),h}_{(1\times 6 2)}(\mathbf{y}, s) \quad H^{(7),h}_{(1\times 5 2\times 2)}(\mathbf{y}, s) \quad H^{(7),h}_{(1\times 4 2\times 3)}(\mathbf{y}, s) \\ & H^{(7),h}_{(1\times 3 2\times 4)}(\mathbf{y}, s) \quad H^{(7),h}_{(1\times 2 2\times 5)}(\mathbf{y}, s) \quad H^{(7),h}_{(1\times 1 2\times 6)}(\mathbf{y}, s) \quad H^{(7),h}_{(2\times 7)}(\mathbf{y}, s) \Big]^T \end{aligned} \tag{3.66c}$$

The element matrix of influence function $\mathbf{H}^{(n+1),h}(\mathbf{y}, s)$ is written as:

$$\mathbf{d}^{(n+1)e}_H = \left[\begin{array}{cccc} \mathbf{H}^{(n+1)e[1]} & \mathbf{H}^{(n+1)e[2]} & \dots & \mathbf{H}^{(n+1)e[M_e]} \end{array} \right]^T \tag{3.67}$$

where, M_e is the number of nodes in the element. The force matrix for element e is written as a summation of three components:

$$\mathbf{F}^{(n+1)e}_H = \mathbf{F}^{(n+1)e}_{H,1} + \mathbf{F}^{(n+1)e}_{H,2} + \mathbf{F}^{(n+1)e}_{H,3} \tag{3.68}$$

where,

$$\mathbf{F}_{H,1}^{(n+1)e} = -G(\mathbf{y},s)\int_{\Theta^e}\mathbf{B}^e\left(\mathbf{y}\right)^T \mathrm{Sym}\left(\mathbf{P}^{(n)e}\left(\mathbf{y},s\right)\right)d\mathbf{y} \tag{3.69a}$$

$$\mathbf{F}_{H,2}^{(n+1)e} = \int_{\Theta^e}\mathbf{N}^e\left(\mathbf{y}\right)^T \mathrm{Sym}\left(\mathbf{G}^{(n-1)e}\left(\mathbf{y},s\right)\right)d\mathbf{y} \tag{3.69b}$$

$$\mathbf{F}_{H,3}^{(n+1)e} = -\int_{\Theta^e}\mathbf{N}^e\left(\mathbf{y}\right)^T \mathrm{Sym}\left(\mathbf{Q}^{(n-1)e}\left(\mathbf{y},s\right)\right)d\mathbf{y} \tag{3.69c}$$

$\mathrm{Sym}\left(\mathbf{P}^{(n)e}\left(\mathbf{y},s\right)\right)$, $\mathrm{Sym}\left(\mathbf{G}^{(n-1)e}\left(\mathbf{y},s\right)\right)$ and $\mathrm{Sym}\left(\mathbf{Q}^{(n-1)e}\left(\mathbf{y},s\right)\right)$ are defined in Eq. 3.75. Assembling the force matrix, imposing periodic boundary condition and setting the degree of freedom at corner nodes to be 0, the boundary value problem is solved with standard finite element method. Upon normalization, the components of influence function $\boldsymbol{H}^{(n+1),h}(\mathbf{y},s)$ are obtained:

$$H_{(\cdot)}^{(n+1),h}(\mathbf{y},s) = \sum_{A=1}^{M} N^{[A]}(\mathbf{y}) H_{(\cdot)}^{(n+1)[A]}(s) \tag{3.70}$$

where, the normalization is computed as:

$$H_{(\cdot)}^{(n+1)[A]}(s) = H_{(\cdot)0}^{(n+1)[A]}(s) - \frac{1}{|\Theta|}\int_{\Theta}\sum_{A=1}^{M} N^{[A]}(\mathbf{y}) H_{(\cdot)0}^{(n+1)[A]}(s)d\mathbf{y} \tag{3.71}$$

in which, $H_{(\cdot)0}^{(n+1)[A]}(s)$ are the nodal values obtained by solving Eq. 3.62 before normalization.

In view of Eq. 3.59, computation of element force matrices requires information from the inferior orders, which results in a successive solution of the influence functions. The detailed evaluation procedure is provided in what follows.

3.5.1.1 *Evaluation of* $\boldsymbol{H}^{(1)}(\mathbf{y}, s)$ *and* $\boldsymbol{D}^{(0)}(s)$

At $n = 0$, the expression for $\mathbf{P}^{(0)e}(\mathbf{y}, s)$ is:

$$\mathbf{P}^{(0)e}(\mathbf{y}, s) = \begin{bmatrix} 1 & 0 \\ 0 & 1 \end{bmatrix} \tag{3.72}$$

whereas $\mathbf{G}^{(-1)e} = \mathbf{0}$ and $\mathbf{Q}^{(-1)e} = \mathbf{0}$. Substituting these expressions into Eq. 3.69, $H_k^{(1),h}(\mathbf{y}, s)$ is obtained from the procedure described above. $G_{kl}^{(0)}(\mathbf{y}, s)$ is obtained by substituting Eq. 3.70 for $H_k^{(1)}(\mathbf{y}, s)$ into Eq. 3.24:

$$G_{kl}^{(0)}(\mathbf{y}, s) = G(\mathbf{y}, s) \left[\delta_{kl} + \sum_{A=1}^{M} B_l^{[A]}(\mathbf{y}) H_k^{(1)[A]}(s) \right] \tag{3.73}$$

where, $B_l^{[A]}(\mathbf{y}) = N_{,l}^{[A]}(\mathbf{y})$. According to Eq. 3.21, the symmetric part is computed as:

$$G_{(kl)}^{(0)}(\mathbf{y}, s) = \frac{1}{2} \left(G_{kl}^{(0)}(\mathbf{y}, s) + G_{lk}^{(0)}(\mathbf{y}, s) \right) \tag{3.74}$$

and $D_{(kl)}^{(0)}(s)$ is computed by Eq. 3.26 accordingly.

3.5.1.2 *Higher order influence functions and homogenized moduli*

The procedure to evaluate higher order influence functions, $\boldsymbol{H}^{(n+1)}(\mathbf{y}, s)$ and homogenized shear moduli, $\boldsymbol{D}^{(n)}(s)$, $n = \{1, 2, ..., 6\}$, is provided in a general form.

$\text{Sym}\left(\mathbf{P}^{(n)e}(\mathbf{y},s)\right)$, $\text{Sym}\left(\mathbf{G}^{(n-1)e}(\mathbf{y},s)\right)$ and $\text{Sym}\left(\mathbf{Q}^{(n-1)e}(\mathbf{y},s)\right)$ are written as:

$$\text{Sym}\left(\mathbf{P}^{(n)e}(\mathbf{y},s)\right) = \frac{1}{(n+1)!}\begin{bmatrix} (n+1)!H^{(n)e}_{(1\times n)} & n(n!)H^{(n)e}_{(1\times(n-1)2)} & \cdots & n!H^{(n)e}_{(2\times n)} & 0 \\ 0 & n!H^{(n)e}_{(1\times n)} & \cdots & n(n!)H^{(n)e}_{(12\times(n-1))} & (n+1)!H^{(n)e}_{(2\times n)} \end{bmatrix} \tag{3.75a}$$

$$\text{Sym}\left(\mathbf{G}^{(n-1)e}(\mathbf{y},s)\right) = \begin{bmatrix} G^{(n-1)e}_{(1\times n)}(\mathbf{y},s) & G^{(n-1)e}_{(1\times(n-1)2)}(\mathbf{y},s) & \cdots & G^{(n-1)e}_{(12\times(n-1))}(\mathbf{y},s) & G^{(n-1)e}_{(2\times n)}(\mathbf{y},s) \end{bmatrix} \tag{3.75b}$$

$$\text{Sym}\left(\mathbf{Q}^{(n-1)e}(\mathbf{y},s)\right) = \theta(\mathbf{y})\begin{bmatrix} Q^{(n-1)e}_{(1\times n)}(\mathbf{y},s) & Q^{(n-1)e}_{(1\times(n-1)2)}(\mathbf{y},s) & \cdots & Q^{(n-1)e}_{(12\times(n-1))}(\mathbf{y},s) & Q^{(n-1)e}_{(2\times n)}(\mathbf{y},s) \end{bmatrix} \tag{3.75c}$$

where, the expressions for $G^{(n-1)e}_{(\cdot)}(\mathbf{y},s)$ and $Q^{(n-1)e}_{(\cdot)}(\mathbf{y},s)$ are provided in Appendix D. Substituting Eq. 3.75 into Eq. 3.69, $H^{(n+1),h}_{(\cdot)}(\mathbf{y},s)$ is obtained using the same procedure as for $H^{(1),h}_{k}(\mathbf{y},s)$. The homogenized moduli $D^{(n)}_{(\cdot)}(s)$ is obtained from Eq. 3.29. The expressions for $D^{(2)}_{(klmn)}(s)$, $D^{(4)}_{(klmnpq)}(s)$ and $D^{(6)}_{(klmnpqrs)}(s)$ are obtained as follows:

$$D^{(2)}_{(klmn)}(s) = \bar{G}^{(2)}_{(klmn)}(\mathbf{y},s) - \text{Sym}\left(\overline{\rho(\mathbf{y})H^{(2)}_{(kl)}(\mathbf{y},s)}D^{(0)}_{(mn)}(s)\right) \tag{3.76a}$$

$$D^{(4)}_{(klmnpq)}(s) = \bar{G}^{(4)}_{(klmnpq)}(\mathbf{y},s) - \text{Sym}\left(\overline{\rho(\mathbf{y})H^{(2)}_{(kl)}(\mathbf{y},s)}D^{(2)}_{(mnpq)}(s)\right) - \text{Sym}\left(\overline{\rho(\mathbf{y})H^{(4)}_{(klmn)}(\mathbf{y},s)}D^{(0)}_{(pq)}(s)\right) \tag{3.76b}$$

$$D^{(6)}_{(klmnpqrs)}(s) = \bar{G}^{(6)}_{(klmnpqrs)}(\mathbf{y},s) - \text{Sym}\left(\overline{\rho(\mathbf{y})H^{(2)}_{(kl)}(\mathbf{y},s)}D^{(4)}_{(mnpqrs)}(s)\right) - \text{Sym}\left(\overline{\rho(\mathbf{y})H^{(4)}_{(klmn)}(\mathbf{y},s)}D^{(4)}_{(pqrs)}(s)\right) - \text{Sym}\left(\overline{\rho(\mathbf{y})H^{(6)}_{(klmnpq)}(\mathbf{y},s)}D^{(0)}_{(rs)}(s)\right) \tag{3.76c}$$

3.5.2 Macroscale problem

The weak form of the boundary value problem defined in Fig. 3.3 is written as:

$$\int_{\Omega} w(\mathbf{x})_{,x_k} D^e_{kl}(s) U_{,x_l}(\mathbf{x},s) d\mathbf{x} + \int_{\Omega} w(\mathbf{x}) \rho_0 s^2 U(\mathbf{x},s) d\mathbf{x} = \int_{\Gamma^t} w(\mathbf{x}) \tilde{t}(\mathbf{x},s) d\mathbf{x} \quad (3.77)$$

The macroscale displacement is rewritten as: $U(\mathbf{x},s) = U_{\text{re}} + \text{i}U_{\text{im}}$, where U_{re} and U_{im} are respectively the real and imaginary parts. Using Galerkin's approximation, the finite dimensional solution space for the macroscale displacement is written as:

$$\mathcal{U}^h_{\{\text{re,im}\}} := \left\{ U^h_{\{\text{re,im}\}}(\mathbf{x},s) \in H^1(\Theta,\mathbb{R}) \;\middle|\; U^h_{\{\text{re,im}\}}(\mathbf{x},s) = \tilde{u}_{\{\text{re,im}\}}(s) \quad \forall \mathbf{x} \in \Gamma^u \right\} \quad (3.78)$$

Equation 3.77 is evaluated by Isogeometric Analysis (IGA) with NURBS basis functions. Among the various desirable characteristics, e.g., exact geometric representation [60], its application in wave propagation problems [61, 62, 126, 31] has demonstrated high rate of convergence due to the so-called k-refinement, by which C^{p-1}-continuity (p is the polynomial order of the basis functions) could be achieved. It is noted that standard FEM with C^0-continuous shape functions can also be employed to numerically evaluate Eq. 3.77, provided that a sufficiently fine mesh is used to avoid numerical dispersion.

In the context of IGA, the basis functions that approximate the solution field are ones representing the geometry of the physical domain. In two-dimensions, the physical domain is represented by the NURBS basis functions through the mapping:

$$\mathbf{x}(\boldsymbol{\xi}) = \sum_{A=1}^{M_{bf}} N^{[A],p}(\boldsymbol{\xi}) \mathbf{P}^{[A]} \quad (3.79)$$

where, $\{\mathbf{P}^{[A]}\}_{A=1}^{M_{bf}} \in \mathbb{R}^2$ is a set of control points in the physical domain, $N^{[A],p}$ is the A^{th} NURBS basis function that is constructed from B-spline basis functions of

polynomial order p. C^1-continuous basis functions are used for all the numerical examples in Section 3.6, therefore $p = 2$. The basis function is parameterized by knot vectors that are defined in the parametric domain $\hat{\Omega} \in \mathbb{R}^2$. The parametric domain is partitioned into elements by knots, which forms the elements in physical domain through mapping Eq. 3.79. A detailed discussion of the NURBS basis functions and IGA are provided in Ref. [27]. By virtue of the isogeometric concept, the macroscale displacement in the parametric domain is approximated by:

$$\hat{U}^h(\boldsymbol{\xi}, s) = \sum_{A=1}^{M_{bf}} N^{[A],p}(\boldsymbol{\xi}) U^{[A]}(s) \tag{3.80}$$

The macroscale displacement in the physical domain is obtained by considering the inverse of the geometric mapping (Eq. 3.79):

$$U^h(\boldsymbol{\xi}, s) = \hat{U}^h(\boldsymbol{\xi}, s) \circ \mathbf{x}^{-1} \tag{3.81}$$

3.5.3 Uncoupled multiscale solution strategy

In this section, we present the solution strategy to the multiscale system. The micro- and macroscale problems are uncoupled because the microscale boundary value problems are independent of the macroscale solution. The microscale boundary value problems are successively evaluated in the Laplace domain to compute the homogenized shear moduli, after which the nonlocal effective stiffness is computed. The macroscale boundary value problem is then solved to obtain the macroscale displacement in the Laplace domain. Numerical inverse Laplace transform is applied to obtain the solution in time domain. The computational flowchart is shown in Fig. 3.4.

A numerical inverse Laplace transform algorithm [29, 16] based on the Fast Fourier Transform is used to transform the solution from the Laplace domain to the time domain. In this algorithm, the accuracy of the numerical inverse transformation

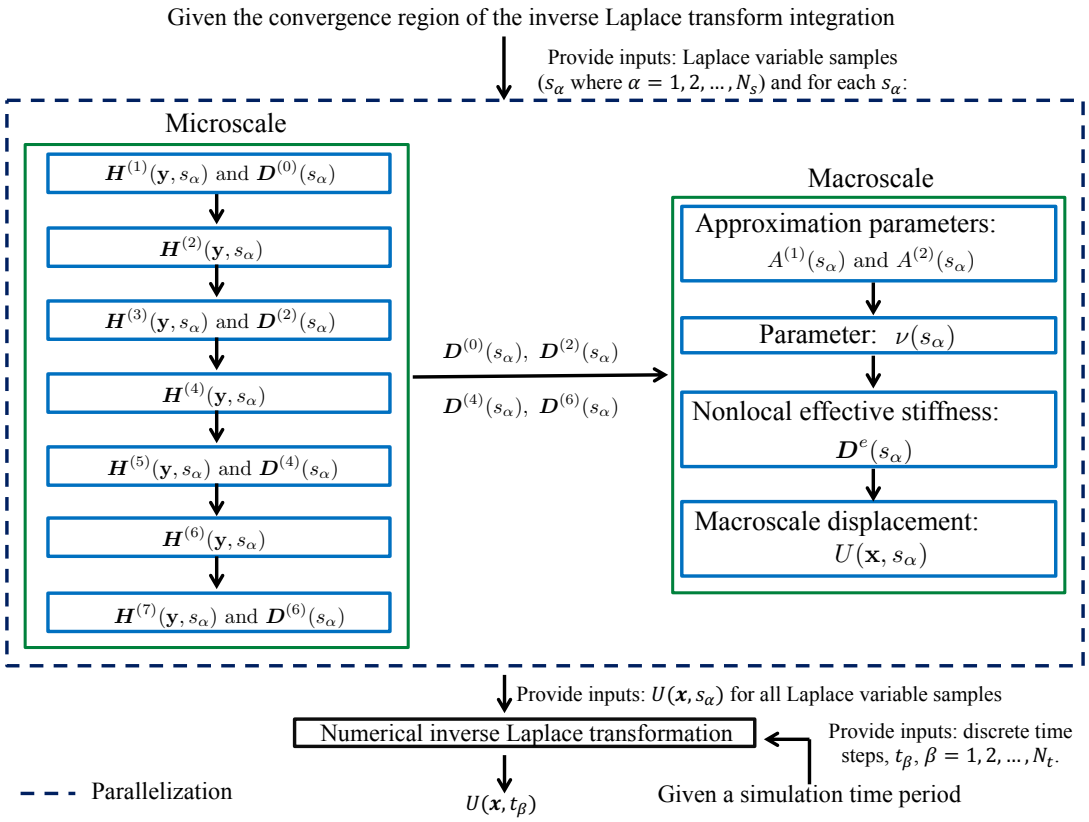

Figure 3.4: Computational flowchart.

is controlled by an algorithm parameter. It is set to provide sufficient numerical accuracy in all simulations. Fast convergence is achieved by employing the ϵ-algorithm [84]. A comprehensive study of this algorithm compared to others can be found in Ref. [30]. With this transformation, the key steps towards obtaining the macroscale displacement, $U(\mathbf{x}, t)$ are described as follows:

1. Given an observation time period, discrete time steps (i.e., t_β where $\beta = 1, 2, \cdots, N_t$ and N_t is the number of time steps) are generated. The Laplace variable, s, is sampled by s_α where $\alpha = 1, 2, \cdots, N_s$ and N_s is the number of samples, within the convergence region of the inverse Laplace transform integration, along a vertical line (i.e., of the same real part) in the complex plane.

2. For each sample, s_α, influence functions, $\boldsymbol{H}^{(n+1)}(\mathbf{y}, s_\alpha)$, and homogenized shear moduli, $\boldsymbol{D}^{(n)}(s_\alpha)$, $n = 1, 2, ..., 6$, are successively evaluated through the proce-

dure in Section 3.5.1.

3. Provided with $\boldsymbol{D}^{(0)}(s_\alpha)$, $\boldsymbol{D}^{(2)}(s_\alpha)$, $\boldsymbol{D}^{(4)}(s_\alpha)$ and $\boldsymbol{D}^{(6)}(s_\alpha)$, the approximation parameters are computed by the Moore-Penrose pseudo-inverse: $A^{(1)}(s_\alpha) = \mathbf{d}^{(6)}(s_\alpha)\left(\mathbf{d}^{(0,4)}(s_\alpha)\right)^{(-m)}$ and $A^{(2)}(s_\alpha) = \mathbf{d}^{(4)}(s_\alpha)\left(\mathbf{d}^{(2,0)}(s_\alpha)\right)^{(-m)}$, where $\mathbf{d}^{(6)}(s_\alpha)$, $\mathbf{d}^{(0,4)}(s_\alpha)$, $\mathbf{d}^{(4)}(s_\alpha)$ and $\mathbf{d}^{(2,0)}(s_\alpha)$ are vectors of the non-zero independent components of $\text{Sym}(\boldsymbol{D}^{(6)})$, $\text{Sym}\left(\boldsymbol{D}^{(0)} \otimes \text{Sym}(\boldsymbol{D}^{(4)})\right)$, $\text{Sym}(\boldsymbol{D}^{(4)})$ and $\text{Sym}\left(\text{Sym}(\boldsymbol{D}^{(2)}) \otimes \boldsymbol{D}^{(0)}\right)$. The parameter, $\nu(s_\alpha)$, is obtained by the constrained minimization problem defined in Fig. 3.2.

4. With all the homogenized moduli and model parameters computed in the higher order gradient nonlocal formulation, the nonlocal effective stiffness, $\boldsymbol{D}^e(s_\alpha)$, for the nonlocal effective medium model is obtained as detailed in Section 3.4.3.

5. The macroscale displacement, $U(\mathbf{x}, s_\alpha)$, is obtained by evaluating the macroscale boundary value problem in Section 3.5.2.

6. Steps 2-5 are repeated N_s times to compute the macroscale displacements for all sampled Laplace variables. The complex valued macroscale displacements, $U(\mathbf{x}, s_\alpha)$ are provided to the numerical inverse Laplace transform algorithm and the macroscale displacements for all the time steps in the time domain are obtained.

The uncoupled solution strategy allows an off-line computation of the required nonlocal effective stiffness for the solution of macroscale displacement for a given microstructure. In particular, microscale problems are evaluated once in the case of composites with elastic constituents, since they are independent of the Laplace variable. For viscoelastic composites, the repeated evaluation of Steps 2-5 are implemented in a parallel environment since all the Laplace variable samples are independent of each other. They are evaluated once for a given period of simulation time.

3.6 Model Verification

In this section, we assess the capability of the proposed spatial-temporal nonlocal homogenization model (STNHM) in capturing wave dispersion and attenuation in both elastic and viscoelastic composites. Two numerical examples are presented to evaluate the proposed model for elastic layered composites and viscoelastic composites with circular inclusions. The dispersion relation and transient wave propagation in elastic layered composite are investigated in the first example. The second example focuses on transient wave propagation in the viscoelastic composite. Time domain response and wave transmission characteristics are examined and compared with the direct numerical simulations. In all numerical examples, the number of Laplace variable samples are chosen large enough such that further increase of the resolution does not significantly alter the simulation results.

3.6.1 Elastic layered composite

3.6.1.1 *Low material property contrast*

We consider a two-dimensional bi-material layered microstructure composed of aluminum and steel, as shown in Fig. 3.5(a). The size of the microstructure is 0.02 m $\times$0.02 m and the volume fraction of steel is 0.5. The shear modulus and density are 26.2 GPa and 2700 kg/m^3 for aluminum, and 80.8 GPa and 7900 kg/m^3 for steel, respectively.

The steady-state wave propagation characteristics of the proposed model is evaluated by comparing the dispersion curves with those obtained from the Bloch wave expansion [66], where an eigenvalue problem of frequency ω is formulated by discretizing the unit cell with finite element method and sampling the wave vector $\mathbf{k}$ within the irreducible Brillouin zone. As shown in Fig. 3.5(b), this approach samples the wave vector within the domain $[0, \pi/l] \times [0, \pi/l]$. The dispersion relation for wave vectors outside of the irreducible Brillouin zone but within $[0, 2\pi/l] \times [0, 2\pi/l]$ is obtained by

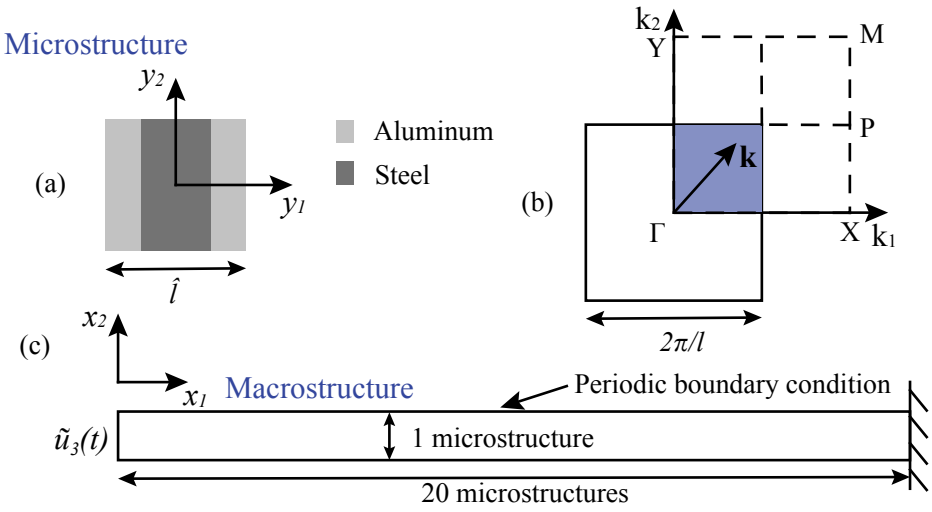

Figure 3.5: (a) Aluminum-steel layered microstructure. (b) Sketch of irreducible Brillouin zone (shaded square) and the probed domain of wave vector (square ΓXMY). (c) Macrostructure and boundary conditions.

shifting the corresponding branch obtained in the irreducible Brillouin zone by π/l. The dispersion curves of the proposed model (STNHM) is computed by sampling the wave vector in $[0, 2\pi/l] \times [0, 2\pi/l]$ and solving for the frequency ω by Eq. 3.54 (s is replaced with iω).

Figure 3.6 shows the dispersion curves of wave vectors sampled in four directions, i.e., ΓX, ΓP, ΓM, ΓY. The dispersion relations of the spatial nonlocal homogenization model (SNHM) proposed in Refs. [64, 43], STNHM with $\nu = 0$ and STNHM, which respectively correspond to the nonlocal homogenization models employing asymptotic expansions of up to the $4^{th}, 6^{th}$ and 8^{th} order, are plotted for comparison. STNHM accurately captures the dispersion in the first pass band, and the initiation and size of the first stop band in all directions. In Fig. 3.6(a) and (b), SNHM behaves as a low-pass filter which prohibits any wave of frequency higher than the cut-off frequency from propagating. In addition, it does not predict the onset of the stop band. By setting $\nu = 0$, STNHM recovers the homogenization model that is derived based on Eqs. 3.31a-f. This model predicts the optical branch due to the presence of temporal nonlocal term, but it is less accurate at the end of the first stop band compared to

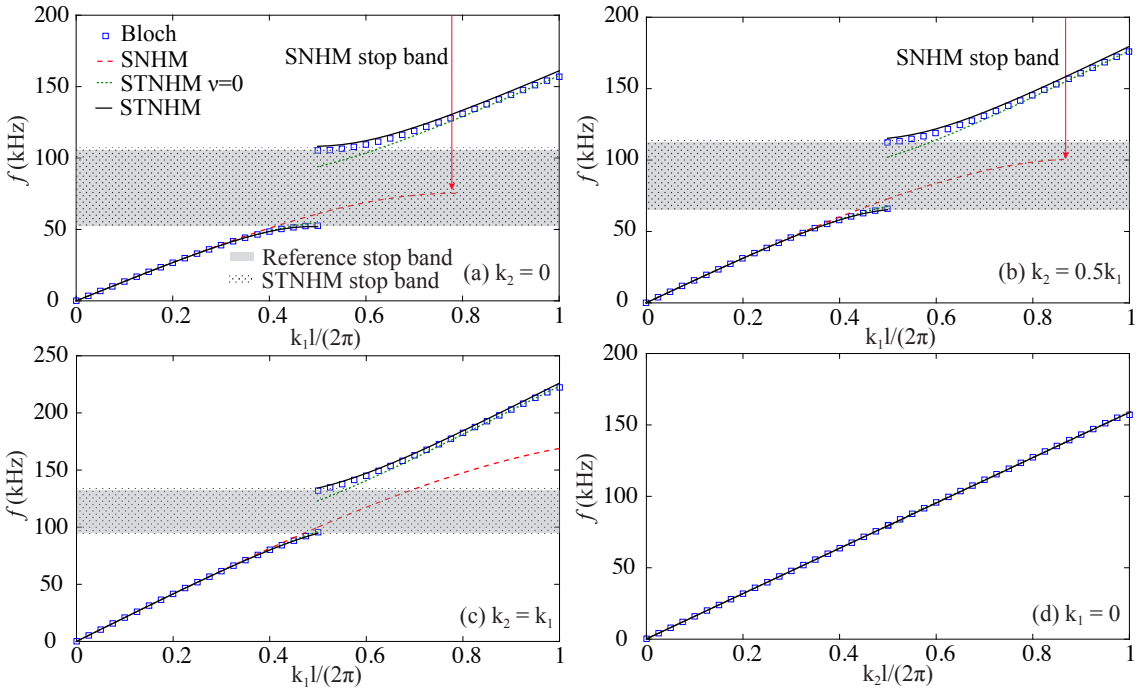

Figure 3.6: Dispersion curves of aluminum-steel layered composite.

STNHM.

Figure 3.7 shows the effect of reducing the direction-dependent nonlocal effective stiffness to a direction-independent one as employed in the nonlocal effective medium (NEM) model. The wavenumber as a function of direction computed by the regularized STNHM (Eq. 3.57), k_{reg}, and NEM (Eq. 3.58), k_{red}, are compared with that from Bloch wave expansion in Fig. 3.7(a). Results obtained at frequencies, $\omega = 2\pi\{10, 20, 30, 40, 50\}$ kHz, are plotted. At low frequencies, both STNHM models predict the wavenumber in all directions accurately. As frequency increases, where significant wave dispersion occurs, NEM captures the dispersion in 0° and 90°, and introduces a slight discrepancy in other directions. The error induced by approximating the direction-dependent nonlocal effective stiffness with one obtained from $\theta = 0$ and $\theta = \pi/2$ is shown in Fig. 3.7(b). The error, $k_{err} = |k_{reg} - k_{red}|/k_{reg}$, measures the normalized absolute difference between wavenumber computed from the regularized STNHM and NEM, as a function of frequency and wave propagation direction. The

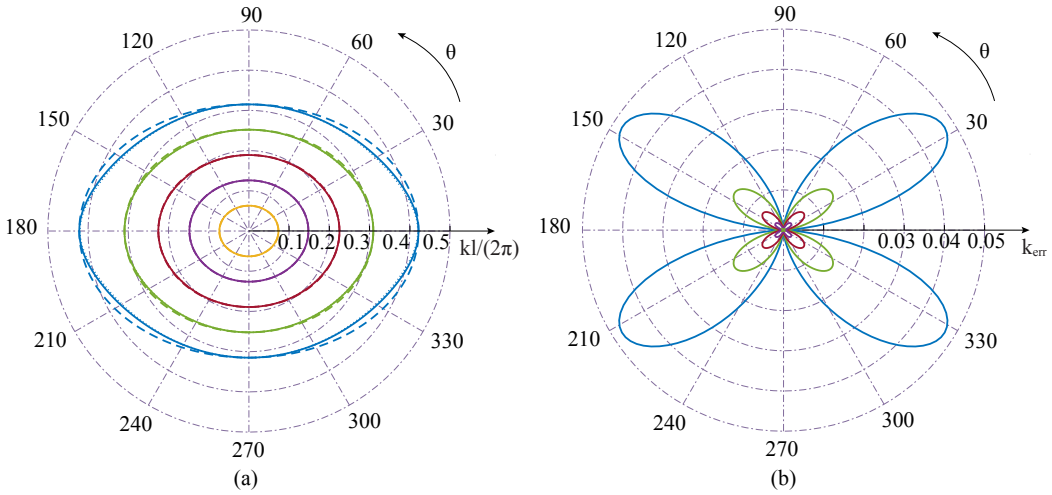

Figure 3.7: (a) Polar plots of the wavenumber $kl/(2\pi)$ as a function of direction θ. Dotted line, '· ·', Bloch wave expansion; Solid line, '—', regularized STNHM; Dashed line, '- -', NEM. (b) Polar plots of the error caused by model reduction. From the center outward, the diagrams are computed for $\omega = 2\pi\{10, 20, 30, 40, 50\}$ kHz.

maximum error is about 0.05 around 30°, 150°, 210°, 330° and when the frequency is near the onset of the stop band. The regularized STNHM predicts the anisotropic wave dispersion characteristics because of the direction-dependent nonlocal effective stiffness. As a result of the model reduction, this feature is captured but with a slightly increased error.

Transient wave propagation is investigated by considering a macrostructure that is composed of 20 microstructures as shown in Fig. 3.5(a). The macrostructure and boundary conditions are shown in Fig. 3.5(c). Sinusoidal out-of-plane displacement load with amplitude M, $\tilde{u}_3(t) = M\sin(2\pi ft)$, is applied at the left boundary of the structure and the right boundary is fixed. Periodic displacement boundary condition is applied to the top and bottom edges. In Fig. 3.8, the normalized displacement (U/M) along the bottom edge of the structure computed from NEM is examined against the reference solution at two time instances, i.e., t=0.5T and t=T. The reference solution is obtained from direct numerical simulations with all the heterogeneities fully resolved by IGA and Newmark-beta method for time integration. It is noted

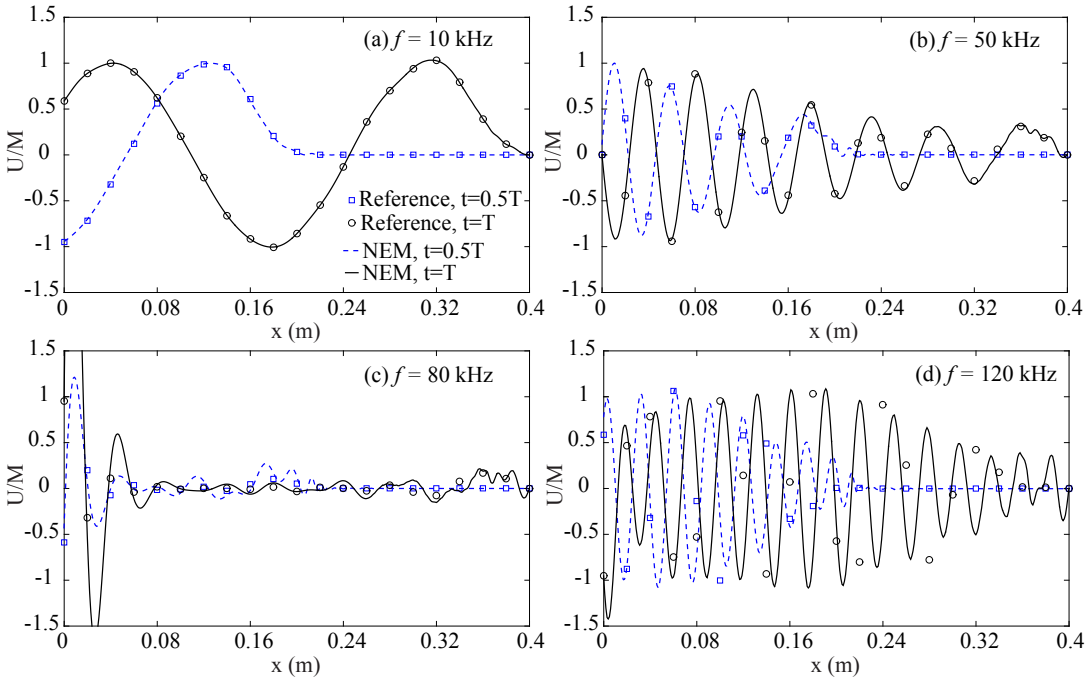

Figure 3.8: Displacement snapshots along the measurement line.

that pointwise comparison of displacement between the homogenization model and direct numerical simulations is only one-to-one at the corner points of the microstructure, where the microscale influence functions are zero (see Section 3.5.1). Because the heterogeneous displacement is equal to the homogenized displacement at these points according to Eqs. 3.14, 3.19, 3.20. Therefore, only the displacements at corner points of each microstructure from the direct numerical simulations are plotted as the reference solution. As is shown in Fig. 3.8, NEM predicts the non-dispersive wave propagation (Fig. 3.8(a)) and wave dispersion (Fig. 3.8(b)) in the first pass band. Further increasing the loading frequency, wave is significantly attenuated in the first stop band (Fig. 3.8(c)). The proposed model captures the attenuated wave reasonably well. Wave propagation in the second pass band is shown in Fig. 3.8(d). At $f = 120$ kHz, a phase shift between NEM and direct numerical simulations is observed. The cause of this error is linked to the fundamental assumption of separation of scales. Although higher order terms in the asymptotic expansion contributes

to a more accurate approximation of the heterogeneous displacement field and allows NEM to predict wave dispersion in the first pass band and attenuation in the first stop band, the accuracy of the proposed model deteriorates as the wavelength decreases. When the wavelength approaches the size of the microstructure, the microscale and macroscale responses are inseparable, and the homogenization model is no longer accurate.

3.6.1.2 *The effect of material property contrast*

A parametric study examining the accuracy of STNHM for different material property contrasts is performed for the layered microstructure. The volume fraction of each phase is set to be 0.5. The dispersion curves for wave propagation in the k_1 direction are shown in Fig. 3.9 for various stiffness contrasts, $r_G = G_{(1)}/G_{(2)}$, and density contrasts, $r_\rho = \rho_{(1)}/\rho_{(2)}$, where $G_{(1)}$, $G_{(2)}$ and $\rho_{(1)}$, $\rho_{(2)}$ are the shear moduli and densities of the two phases, respectively. $\omega l/(2\pi c_1)$ is the normalized frequency and $c_1 = \sqrt{D_{11}^{(0)}/\rho_0}$ is the homogenized wave velocity in the k_1 direction.

For low material property contrast (Fig. 3.9(a)), STNHM accurately captures the acoustic branch. The accuracy in prediction of the end of the stop band decreases as the stiffness contrast increases. Figure 3.9(b) shows the dispersion curves of composites with high stiffness contrast which is typical of the contrast between polymers and metals. In these cases, STNHM accurately predicts wave dispersion in the acoustic regime and the initiation of the stop band. The end of the stop band is over predicted and the optical branch is shifted to higher frequency compared to the Bloch wave solutions. The effect of density contrast is shown in Fig. 3.9(c). As the density contrast increases, the accuracy of STNHM in the short wavelength regime of the acoustic branch decreases. STNHM predicts the trend that the width of the stop band increases as the density contrast increases. However, similar to the behavior when high stiffness contrast is present, the predicted end of the stop band and the

optical branch occur at higher frequency.

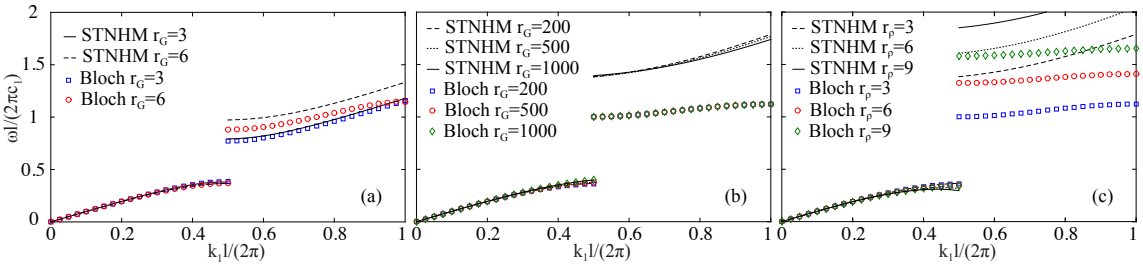

Figure 3.9: Dispersion curves of elastic layered composite with different material property contrasts. (a) Low stiffness contrast with $r_\rho = 3$, (b) High stiffness contrast with $r_\rho = 3$, (c) High density contrast with $r_G = 200$.

3.6.2 Viscoelastic matrix-fiber composite

In this section, we investigate wave propagation in viscoelastic composite with the microstructure that has elastic circular inclusion embedded in viscoelastic matrix and size of 0.02 m $\times$0.02 m. The elastic phase has volume fraction of 0.2. The constitutive relation of the viscoelastic phase is given by Eq. 3.4, where the shear modulus is represented with Prony series in time domain. After Laplace transformation, the modulus function is expressed as:

$$G_{(2)}(s) = G_0 s \left(1 - \sum_{i=1}^{n} p_i \left(1 - \frac{s}{s + 1/q_i}\right)\right) \tag{3.82}$$

where, G_0 is the instantaneous shear modulus describing the elastic behavior, and p_i and q_i are parameters that define the Prony series expansion representing the effect of damping. G_0 and the density are taken as 1.48 GPa and 1142 kg/m^3, according to the experimentally fabricated two-dimensional elastic phononic crystal [124]. Damping effect is introduced by considering the Prony series provided in Table 1 [2].

Table 3.1: Prony series of the viscoelastic phase.

p_1	p_2	p_3	p_4
0.074	0.147	0.313	0.379
q_1 [ms]	q_2 [ms]	q_3 [ms]	q_4 [ms]
463.4	0.06407	1.163×10^{-4}	7.321×10^{-7}

3.6.2.1 *Dispersion analysis*

In this section, we perform dispersion analysis of viscoelastic composites and examine the characteristics of STNHM in capturing wave dispersion and attenuation. The dispersion relation of the proposed model is compared to the Bloch expansion approach [3]. The dispersion curves of both STNHM and the reference are obtained in the frequency domain (replacing s with $\mathrm{i}\omega$) by sampling the frequency and solving for the wavenumber. The analysis is performed for microstructures with different elastic phase properties, while the viscoelastic phase properties are fixed.

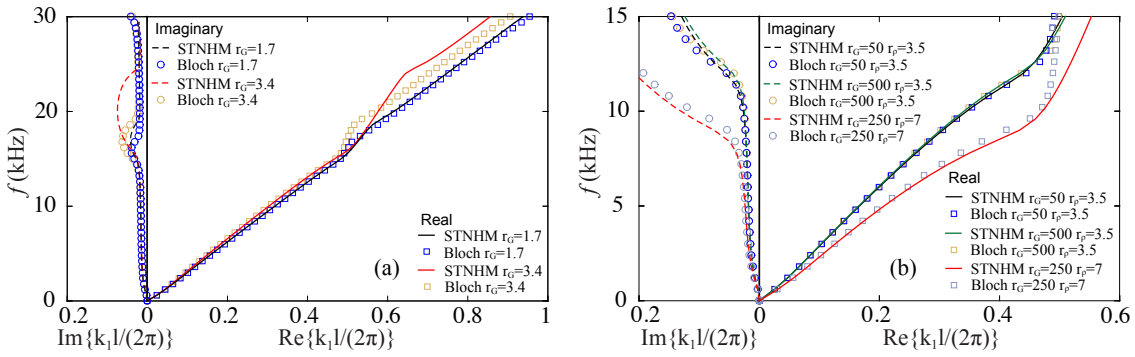

Figure 3.10: Dispersion curves of viscoelastic matrix-fiber composite with different material property contrasts. (a) Low stiffness contrast with $r_\rho = 1.5$, (b) High contrast.

Figure 3.10 shows the dispersion curves (in the k_1 direction) of viscoelastic composites with various property contrasts. The shear modulus of the viscoelastic phase at the frequency, $f = 15$ kHz, is used to evaluate the stiffness contrast, r_G. Both real and imaginary parts of the wavenumber are shown, and they represent the spatial variation of wavefield and attenuation, respectively. Due to the presence of viscoelastic dissipation, wave attenuation increases monotonically as frequency increases in

the pass bands. The stop band is featured by the elevated attenuation within certain frequency ranges. In Fig. 3.10(a), STNHM predicts both real and imaginary parts of wavenumber in the acoustic branch. Similar to the elastic case (Fig. 3.9(a)) the error in the prediction of the end of the stop band increases as the stiffness contrast increases. Figure 3.10(b) shows the dispersion curves of the acoustic branch and a part of the stop band for viscoelastic composite with high material property contrast. STNHM predicts wave dispersion and attenuation in the acoustic regime and the initiation of the stop band for high stiffness contrast. The accuracy decreases as the density contrast increases. This observation is consistent with the example of elastic composite in Fig. 3.9(b)(c).

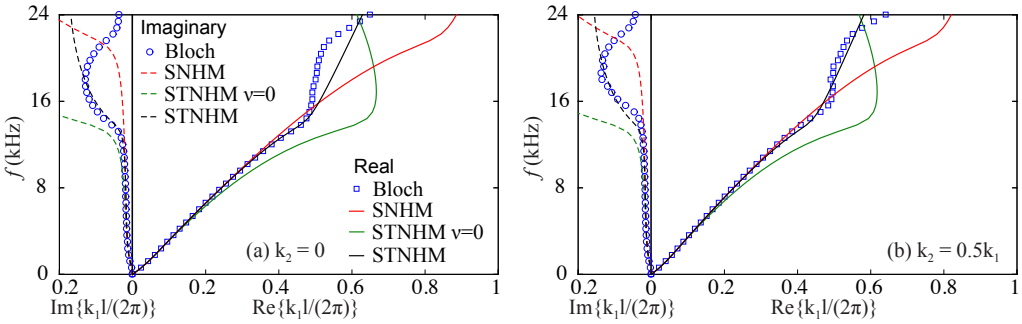

Figure 3.11: Dispersion curves of viscoelastic composite with aluminum inclusion.

Figure 3.11 shows the dispersion curves for viscoelastic composite in two wave vector ($\mathbf{k} = k_1\hat{\mathbf{e}}_1 + k_2\hat{\mathbf{e}}_2$) directions, $k_2 = 0$ and $k_2 = 0.5k_1$. The elastic phase is taken as aluminum. SNHM, STNHM with $\nu = 0$ and STNHM are compared to demonstrate the effect of high order asymptotic expansions. While both SNHM and STNHM capture wave dispersion in the acoustic regime, SNHM does not capture the initiation of the stop band accurately. By incorporation of the temporal nonlocal term, STNHM with $\nu = 0$ improves the prediction of the initiation of the stop band with respect to the frequency compared to SNHM, however, it has significant error in predicting wave dispersion within the first pass band. This manifests the importance of appropriate computation of the parameter ν proposed in Section 3.4.2.

3.6.2.2 *Transient wave propagation in viscoelastic composite*

A numerical example of transient wave propagation in a viscoelastic composite is provided in this section. A macroscopic structure composed of 20×20 microstructures is considered as shown in Fig. 3.12. The material properties are identical to those used in Fig. 3.11. Out-of-plane sinusoidal displacement load is applied at the center of left boundary within $10l$ range and the right boundary is fixed.

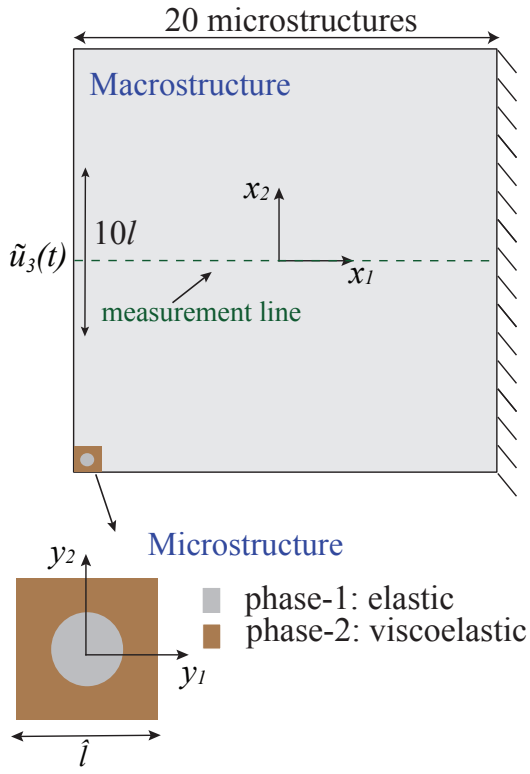

Figure 3.12: Multiscale system of the viscoelastic composite.

Figure 3.13 shows the normalized displacement along the measurement line at the end of the simulation, t=T, for four loading frequencies. The results of NEM are compared to the classical local homogenization model (LHM) and direct numerical simulation (reference). The classical homogenization model, which does not capture the dispersion caused by heterogeneities, is provided to distinguish the dispersion caused by material heterogeneity from material damping. At low frequencies, the wavelength is significantly larger than the microstructure and the dispersion caused

by material heterogeneity is negligible. Both NEM and LHM predict wave propagation with progressively reduced amplitude due to wave spreading and viscoelastic dissipation in Fig. 3.13(a). Increasing the loading frequency leads to shorter deformation wavelength, and dispersion occurs due to interactions between macroscopic wave and the microstructure. As a consequence, the macroscopic wave speed and amplitude decrease. It is shown in Fig. 3.13(b) that NEM predicts wave speed and the displacement along the measurement line. The first stop band occurs when the macroscopic wavelength is about twice of the size of microstructure. As shown in Fig. 3.13(c), the wave is significantly attenuated as a result of stop band formation combined with viscoelastic dissipation. When the frequency is further increased to 24 kHz (Fig. 3.13(d)), the result of direct simulation is within the second pass band. NEM deviates from the reference result.

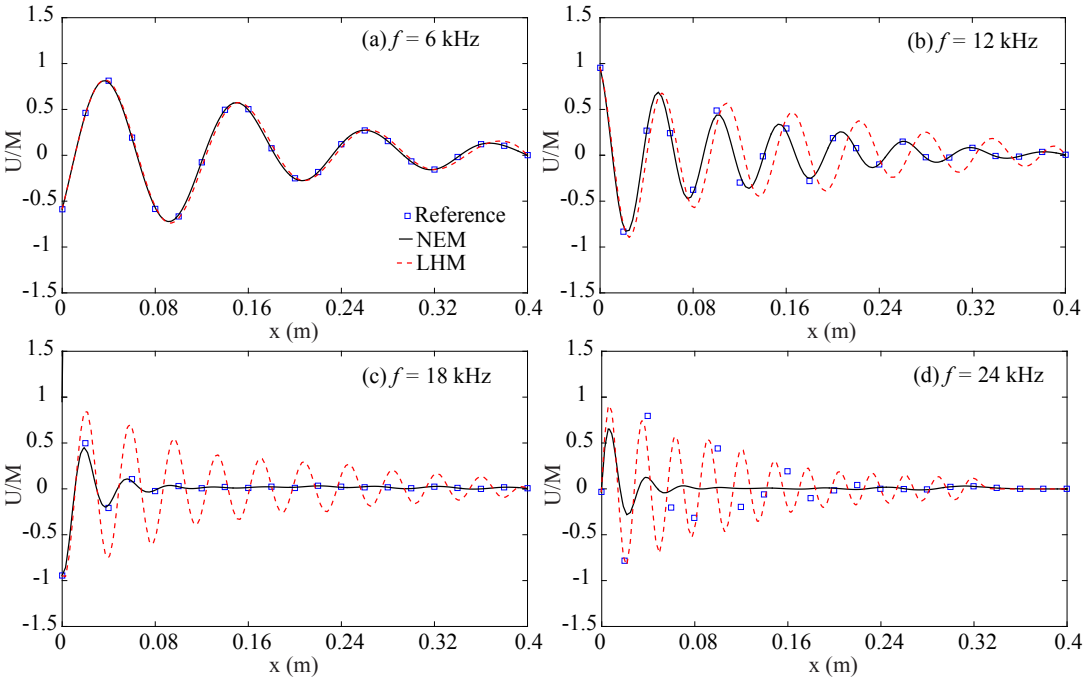

Figure 3.13: Displacement snapshots along the measurement line at t=T.

Figure 3.14 shows the contours of wave propagation in viscoelastic composite compared to the elastic counterpart at fixed loading frequency, $f = 12$ kHz, at two time instances, t=0.5T and t=T. The elastic composite is modeled by replacing the modu-

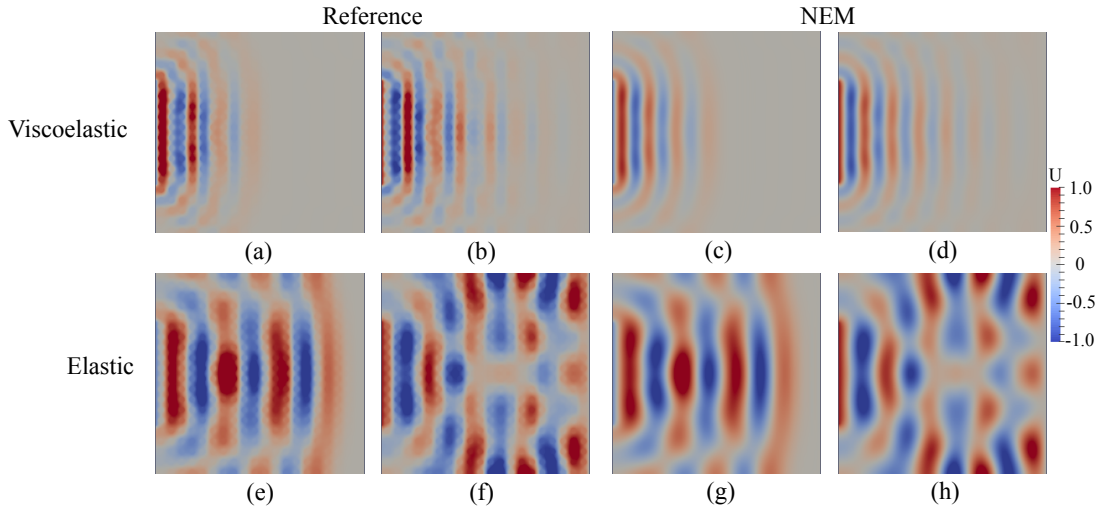

Figure 3.14: Displacement contours of NEM compared to the reference at frequency $f = 12$ kHz. (a), (b), (c), (d) are for viscoelastic composite, and (e), (f), (g), (h) are for elastic composite. (a), (c), (e), (g) are at t=0.5T, and (b), (d), (f), (h) are at t=T.

lus function of the viscoelastic phase, $G_{(2)}(s)$, with the instantaneous shear modulus, G_0. As a result, the matrix material is stiffer than the viscoelastic matrix. Wave propagates at lower speed in the viscoelastic composite compared to the elastic one, leading to reduced wavelength at given frequency, which results in stronger interaction with the microstructure thus more significant dispersion. At t=T, the shear wave propagating in the viscoelastic composite just reaches the right boundary of the domain, whereas in the elastic composite, the reflected and incoming wave superimpose, creating an intensified wave field near the boundary. Within the stop band, the traveling shear wave is subject to significant attenuation. Figure 3.15 shows the displacement contour of viscoelastic and elastic composites, at loading frequencies $f = 18$ kHz and $f = 35$ kHz, respectively, within the stop band. Compared to wave propagating in the elastic composite, more significant attenuation is observed in viscoelastic composite, featured by the almost complete attenuation after two wavelength distance from the left boundary. In Fig. 3.14 and 3.15, the overall wave pattern predicted by NEM matches with the direct simulation for both viscoelastic and elastic composites.

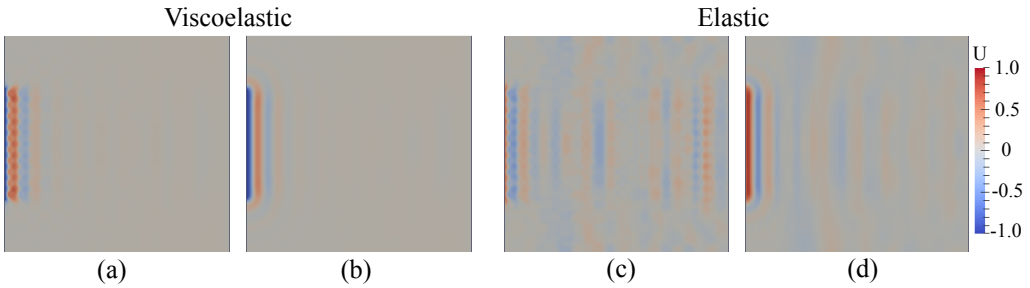

Figure 3.15: Displacement contours of viscoelastic and elastic composites at t=T for loading frequencies within the stop band. (a), (c) are the reference, and (b), (d) are results of NEM.

The wave transmission spectrum provides a more intuitive way to identify and understand wave propagation characteristics in viscoelastic composites in terms of loading frequency. We consider wave propagation in a viscoelastic composite composed of a row of 20 microstructures, as sketched in Fig. 3.5(c). Sinusoidal load is applied to the left boundary with a range of frequencies, $f \in [1, 36]$ kHz, and the displacement is measured 5 unit cells away from the left boundary, i.e., $x_1 = 0.1$ m. Two viscoelastic microstructures are investigated, i.e., matrix-fiber and bi-material layered. The bi-material layered microstructure is shown in Fig. 3.5(a) with steel phase replaced by the viscoelastic phase for which, the material properties are provided earlier in this section. Figure 5.10 shows the normalized maximum transmitted wave amplitude, U_t/M, at the measurement point for the considered two microstructures. As LHM does not capture wave dispersion due to microstructures, it characterizes the viscoelastic dissipation, which monotonically increases as a function of loading frequency. At low frequency, only viscoelastic dissipation causes wave attenuation, therefore, NEM and LHM predict identical wave transmission. As frequency increases, dispersion induced by material heterogeneity enhances wave attenuation. Formation of the stop band is featured by the dip around $f = 13$ kHz, contributing significant wave attenuation. NEM predicts the transmitted wave amplitude up to $f = 22$ kHz and $f = 31$ kHz respectively for matrix-fiber and layered viscoelastic

composites, where the wavelength is about 1.5 times of the size of microstructure. The second pass band starts to form at these frequencies featured by the bump that covers about 5 kHz frequency range. Frequencies higher than 36 kHz are not plotted, because the wavelength is smaller than the size of microstructure within the matrix-fiber composite and asymptotic homogenization is no longer applicable. Comparing Figs. 5.10(a) and (b), the stop band of viscoelastic composite with bi-material layered microstructure covers a much wider frequency range than the one with matrix-fiber microstructure. Moreover, more pronounced wave attenuation is observed within the stop band.

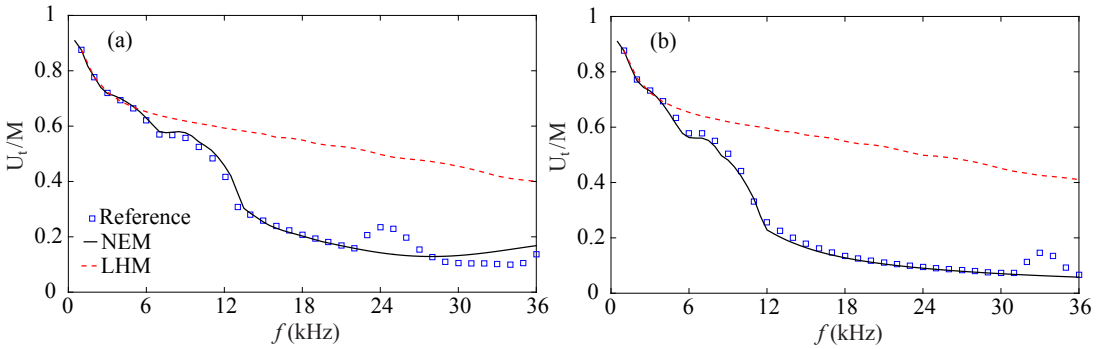

Figure 3.16: Maximum transmitted wave amplitude after 5 unit cells. (a) Matrix-fiber viscoelastic composite. (b) Bi-material layered viscoelastic composite.

3.7 Conclusion

This chapter extended the spatial-temporal nonlocal homogenization model for transient anti-plane shear wave propagation in viscoelastic composite. The proposed model is derived based on asymptotic expansions of up to the eighth order. The homogenized momentum balance equation has higher order gradient terms, i.e., fourth order spatial, fourth order temporal and mixed spatial-temporal derivatives. Transient shear wave propagation is evaluated by an nonlocal effective medium model that shares the same equation structure as the classical homogenization model, while the nonlocal characteristics are retained through the nonlocal effective stiffness. The

major conclusions are summarized as follows:

(1) The spatial-temporal nonlocal homogenization model captures wave dispersion within the first pass band, the initiation of the first stop band and wave attenuation within it for both elastic and viscoelastic composites.

(2) A major contribution of the proposed model is that all model parameters are computed uniquely from the microstructural equilibrium and dependent on the material properties and microstructural geometry only. The computation of model parameters is performed as an off-line process uncoupled from the macroscale solution.

(3) Higher order asymptotic expansions and the derived temporal nonlocal term is critical in extending the applicability of the asymptotic homogenization to shorter wavelength regime, nevertheless, it cannot go beyond the limit of separation of scales.

Chapter 4

SPATIAL-TEMPORAL NONLOCAL HOMOGENIZATION MODEL FOR TRANSIENT IN-PLANE ELASTIC WAVE PROPAGATION IN PERIODIC COMPOSITES

4.1 Introduction

In this chapter, the spatial-temporal nonlocal homogenization model is further developed for transient in-plane wave propagation in periodic composites. The nonlocal homogenization model is then employed to formulate an effective medium model that retains the nonlocal features in the form of a nonlocal effective moduli tensor. It is second order in space, therefore does not require high order boundary conditions for transient simulations. The dispersion curves for layered and matrix-inclusion microstructures are numerically verified. Transient simulations of in-plane wave propagation in an elastic waveguide are performed and compared with the direct numerical simulations. We show that the proposed model captures wave dispersion of longitudinal and shear wave modes up to the first optical branch. It is the first time, to the best of author's knowledge, the gradient-type nonlocal homogenization model captures vector-field elastic wave dispersion beyond the acoustic regime and is applied for transient simulations of wave propagation.

The following notation is used throughout this chapter. Scalars are denoted by italic Roman or Greek characters; vectors by boldface Roman characters; second or higher order tensors by boldface italic Roman and Greek characters. Indicial notation is used when necessary and Einstein summation convention applies to repeated indices. Denoting vectors, second order tensors, n^{th} order tensors respectively as $\mathbf{a}$ and $\mathbf{b}$, $\boldsymbol{A}$ and $\boldsymbol{B}$, $\boldsymbol{C}$ and $\boldsymbol{D}$, the tensor operations are defined as follows. Dyadic product: $\mathbf{a}\otimes\mathbf{b} = a_i b_j \hat{\mathbf{e}}_i \otimes \hat{\mathbf{e}}_j$, where $\hat{\mathbf{e}}_i$ is the Cartesian basis vector. Dot product: $\boldsymbol{A}.\mathbf{b} = A_{ij} b_j \hat{\mathbf{e}}_i$,

double contraction: $\boldsymbol{A}..\boldsymbol{B} = A_{ij}B_{ji}$ and n^{th} contraction: $\boldsymbol{C}(.)^n\boldsymbol{D} = C_{ij...uv}D_{vu...ji}$.

4.2 Multiscale Problem Setting

Consider the domain of a heterogeneous body in the Cartesian coordinate system, $\Omega \in \mathbb{R}^2$, constructed by periodic unit cells composed of two or more constituents, as illustrated in Fig. 4.1. Wave propagation within Ω is governed by the momentum balance equation:

$$\boldsymbol{\nabla}_x.\boldsymbol{\sigma}^\zeta(\mathbf{x},t) = \rho^\zeta(\mathbf{x})\ddot{\mathbf{u}}^\zeta(\mathbf{x},t) \tag{4.1}$$

where, $\boldsymbol{\sigma}^\zeta$ denotes the Cauchy stress tensor; ρ^ζ the density; and $\mathbf{u}^\zeta$ the displacement vector. $\boldsymbol{\nabla}_x.$ is the divergence operator and superimposed dot denotes derivative with respect to time. $\mathbf{x}$ is the position vector of material points. The superscript, ζ, indicates that the response fields oscillate spatially due to the microstructural heterogeneity. Body forces are ignored in the present study.

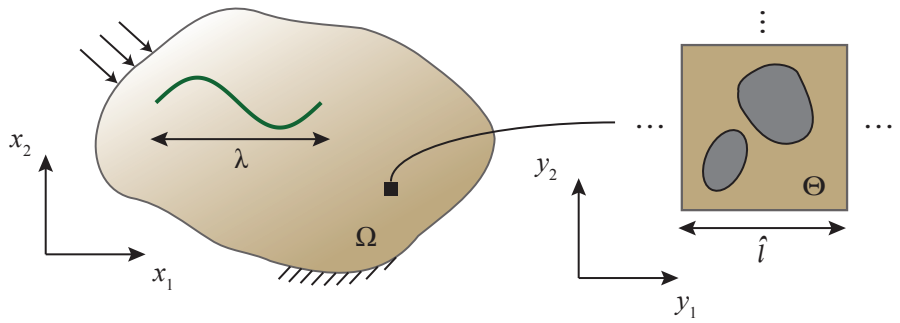

Figure 4.1: Schematic representation of the multiscale problem setting.

The constitutive response of the heterogeneous body is described by the generalized Hooke's law:

$$\boldsymbol{\sigma}^\zeta(\mathbf{x},t) = \boldsymbol{C}^\zeta(\mathbf{x})..\boldsymbol{\epsilon}^\zeta(\mathbf{x},t) \tag{4.2}$$

$\boldsymbol{C}^\zeta(\mathbf{x})$ is the elastic moduli tensor for the constituents and is taken to be strongly elliptic with major and minor symmetries. $\boldsymbol{\epsilon}^\zeta(\mathbf{x},t)$ is the strain tensor under the

assumption of small deformation:

$$\boldsymbol{\epsilon}^{\zeta}(\mathbf{x},t) = \boldsymbol{\nabla}_x^s \mathbf{u}^{\zeta}(\mathbf{x},t) = \frac{1}{2}\left[\boldsymbol{\nabla}_x \mathbf{u}^{\zeta}(\mathbf{x},t) + \left(\boldsymbol{\nabla}_x \mathbf{u}^{\zeta}(\mathbf{x},t)\right)^T\right] \tag{4.3}$$

where $\boldsymbol{\nabla}_x$ and $\boldsymbol{\nabla}_x^s$ are the gradient and the symmetric gradient operators, respectively.

The canonical unit cell domain, $\Theta \in \mathbb{R}^2$, is parameterized using the microscale coordinate, $\mathbf{y}$, which is related to the macroscale coordinate by $\mathbf{y} = \mathbf{x}/\zeta$, where $0 < \zeta < 1$ is the small scaling parameter. The smallness of the scaling parameter sets the premise for the homogenization approach. Asymptotic homogenization is not suitable when $\zeta \geq 1$. In the context of wave propagation, the scaling parameter is defined as the ratio between the size of microstructure, l, and the characteristic length of the deformation wave (i.e., $\zeta = l/\lambda$, where λ is the characteristic deformation wavelength). With the macro- and microscale coordinates, any response field, $f^{\zeta}(\mathbf{x},t)$, is assumed to allow a two-scale description: $f^{\zeta}(\mathbf{x},t) = f(\mathbf{x},\mathbf{y}(\mathbf{x}),t)$. The material properties, i.e., elastic moduli tensor and density, are taken to depend on the microscale coordinate only, i.e., $\boldsymbol{C}^{\zeta}(\mathbf{x}) = \boldsymbol{C}(\mathbf{y})$ and $\rho^{\zeta}(\mathbf{x}) = \rho(\mathbf{y})$. Local periodicity is assumed for all response fields.

We consider periodic composites with low material property contrast between different phases. The mechanism of band gap formation of these composites is mainly due to destructive interaction of incident and scattered waves, i.e., Bragg scattering. The first band gap typically occurs when the macroscopic wavelength is of the same order as the size of the unit cell. Band gaps due to local resonance can occur with wavelength much larger than the size of the unit cell, which requires high contrast in constituent material properties. This type of composites is not considered in this chapter.

4.3 Two-Scale Asymptotic Analysis

The formulation of the proposed model is based on mathematical homogenization with multiple spatial scales. The present approach considers asymptotic expansions of up to the eighth order. The details of the formulation in the context of transient dynamics for scalar-field wave is provided in Chapter 2 and Chapter 3. The overview in this section is a straightforward extension to transient analysis of vector-field problems. The displacement field is approximated using the following decomposition:

$$\mathbf{u}^{\zeta}(\mathbf{x},t) = \mathbf{u}(\mathbf{x},\mathbf{y},t) = \mathbf{u}^{(0)}(\mathbf{x},t) + \sum_{i=1}^{8} \zeta^{i}\mathbf{u}^{(i)}(\mathbf{x},\mathbf{y},t) + O(\zeta^{9}) \tag{4.4}$$

where, $\mathbf{u}^{(0)}$ denotes the macroscopic displacement field and is dependent on the macroscale coordinate only [44] and $\mathbf{u}^{(i)},\ i = 1,...,8$, are the displacement fields of high orders which depend on both macroscale and microscale coordinates. We note that for composites that have constituents with high property contrast (e.g., when the tensors of elastic moduli of the constituents exhibit double porosity-type scaling [115, 9]), $\mathbf{u}^{(0)}$ may depend on both micro- and macroscale coordinates due to local resonance within the microstructures.

The displacement field at each order is decomposed into a macroscopically constant field and summation of a series of locally varying fields with zero mean over the unit cell [15]:

$$\mathbf{u}^{(i)}(\mathbf{x},\mathbf{y},t) = \mathbf{U}^{(i)}(\mathbf{x},t) + \sum_{k=0}^{i-1} \tilde{\mathbf{U}}^{(i,k)}(\mathbf{x},\mathbf{y},t) \tag{4.5}$$

where, $\tilde{\mathbf{U}}^{(i,k)}(\mathbf{x},\mathbf{y},t)$ is the k^{th} locally varying field of $\mathbf{u}^{(i)}(\mathbf{x},\mathbf{y},t)$ and it is assumed to be related to the successive gradients of macroscopic strain of an inferior order by a time-invariant, locally periodic influence function defined over the unit cell:

$$\tilde{\mathbf{U}}^{(i,k)}(\mathbf{x},\mathbf{y},t) = \boldsymbol{H}^{(k+1)}(\mathbf{y})..(.\boldsymbol{\nabla}_x)^{k}\boldsymbol{\nabla}_x^{s}\mathbf{U}^{(i-k-1)}(\mathbf{x},t) \tag{4.6}$$

where, $\boldsymbol{H}^{(k+1)}$ is the periodic microstructural influence function at order $(k+1)$ and it is symmetric in the last two indices that are contracted with $\boldsymbol{\nabla}_x^s \mathbf{U}^{(i-k-1)}$. $(.\boldsymbol{\nabla}_x)^k$ is the $(k)^{th}$ gradient with respect to the macroscale coordinate, $\mathbf{x}$, with k contractions to the microstructural influence function. This construction allows separate evaluation of the microscale influence functions and macroscale momentum balance equations. Employing Eqs. 5.1-4.6, the equilibrium equations for microscale influence functions and macroscale momentum balance equations at each order are successively derived (see Appendix E). The microscale equilibrium equations are:

$$O(\zeta^{-1}): \quad \boldsymbol{\nabla}_y . \boldsymbol{C}^{(0)}(\mathbf{y}) = 0 \tag{4.7a}$$

$$O(\zeta^{\alpha}): \quad \boldsymbol{\nabla}_y . \boldsymbol{C}^{(\alpha+1)}(\mathbf{y}) = \theta(\mathbf{y}) \sum_{j=0}^{\alpha} \boldsymbol{H}^{(j)}(\mathbf{y}) . \boldsymbol{D}^{(\alpha-j)} - \boldsymbol{C}^{(\alpha)}(\mathbf{y}) \tag{4.7b}$$

where $\theta(\mathbf{y}) = \rho(\mathbf{y})/\rho_0$, and $\rho_0 = \overline{\rho(\mathbf{y})}$ is the homogenized density. Overbar indicates averaging operator over the unit cell domain. $\boldsymbol{C}^{(\alpha)}(\mathbf{y})$ $(\alpha = 0, 1, ..., 7)$ is expressed as:

$$\boldsymbol{C}^{(\alpha)}(\mathbf{y}) = \boldsymbol{C}(\mathbf{y}) .. \left[\boldsymbol{H}^{(\alpha)}(\mathbf{y}) \otimes \boldsymbol{I} + \boldsymbol{\nabla}_y \boldsymbol{H}^{(\alpha+1)}(\mathbf{y}) \right] \tag{4.8}$$

where $\boldsymbol{I}$ is the second order identity tensor. The homogenized moduli at each order $\boldsymbol{D}^{(\alpha)}$ is written as:

$$\boldsymbol{D}^{(0)} = \overline{\boldsymbol{C}^{(0)}(\mathbf{y})} \tag{4.9a}$$

$$\boldsymbol{D}^{(\alpha)} = \overline{\boldsymbol{C}^{(\alpha)}(\mathbf{y})} - \sum_{j=1}^{\alpha} \overline{\theta(\mathbf{y}) \boldsymbol{H}^{(j)}(\mathbf{y})} . \boldsymbol{D}^{(\alpha-j)} \tag{4.9b}$$

$\boldsymbol{D}^{(0)}$ is a 4^{th} order tensor that defines the effective moduli in the quasi-static limit and is a function of microstructural geometry and elastic properties only. It possesses major and minor symmetries. The high order moduli, $\boldsymbol{D}^{(\alpha)}$, are $(\alpha+4)^{th}$ order tensors. These moduli are not only functions of microstructural geometry and elastic proper-

ties, but also the densities of the constituents of the microstructure and they contain length-scale of $O(\hat{l}^{\alpha})$. For simplicity of formulation below, we consider microstructures that possess symmetry aligned with the Cartesian coordinate planes. For these microstructures, orthotropic macroscopic properties are observed. As a consequence, $\boldsymbol{D}^{(\alpha)} = \mathbf{0}$ for odd α and the components with odd number of repeated indices are zero for even α [55]. Therefore, the balance equations of odd orders have identical form and parameters as the even order ones of an order inferior.

The macroscale balance equation at $O(\zeta^{\alpha})$ is written as:

$$\boldsymbol{\nabla}_x . \sum_{j=0}^{\alpha} \boldsymbol{D}^{(j)} .. (. \boldsymbol{\nabla}_x)^j \boldsymbol{\nabla}_x^s \mathbf{U}^{(\alpha-j)} = \rho_0 \ddot{\mathbf{U}}^{(\alpha)} \tag{4.10}$$

At the leading order, $\alpha = 0$, the macroscale momentum balance equation is local and describes non-dispersive wave propagation in the long wavelength limit. The balance equations at higher asymptotic orders successively include nonlocal stresses that are of the second order form, $\boldsymbol{D}^{(j)} .. (. \boldsymbol{\nabla}_x)^j \boldsymbol{\nabla}_x^s \mathbf{U}^{(\alpha-j)}$, which are functions of strain gradients of lower asymptotic orders. The contribution of the nonlocal stresses is the volume source disturbance resulting from the lower order displacements. It balances with the stress and momentum of the current order.

4.4 Spatial-Temporal Nonlocal Homogenization Model

In this section, we first propose a fourth-order spatial-temporal nonlocal homogenization model. The structure of the resulting governing equation is similar to those in Chapter 2 and Chapter 3 for scalar-field wave, and include spatial nonlocal, temporal nonlocal and mixed spatial-temporal nonlocal terms. The model parameters are determined using response in high symmetry directions of the first Brillouin zone. Next, we formulate a nonlocal effective medium model that retains the nonlocal characteristics of the corresponding nonlocal homogenization model in high symmetry directions but in the form of a second-order PDE with a frequency-dependent moduli

tensor. The nonlocal effective medium model is used for simulation of transient wave propagation.

The proposed formulation consists of 5 steps: (1) restatement of the governing equations at various asymptotic orders using a series of weighting tensors; (2) application of projection operations to the high order homogenized moduli to achieve a consistent model of the spatial-temporal nonlocal form; (3) identification of the projection tensors based on particular plane wave solutions; (4) identification of the weighting tensors; and (5) model order reduction to devise the effective medium model for transient dynamics simulations. The key ideas, assumptions and concepts in the proposed five-step formulation are discussed below. For clarity of the presentation, we skip the algebraic details. A detailed derivation of the formulation is provided in Appendix F.

4.4.1 Higher order gradient formulation

In what follows, we employ the momentum balance equations, Eq. 4.10 with $\alpha = 0, 2, 4, 6,$ to derive the fourth-order spatial-temporal nonlocal model. The balance equations at odd orders do not contribute to the resulting model under the symmetry conditions discussed above [55]. The homogenized displacement field is expressed as the additive sum of contributions from all even orders:

$$\mathbf{U}(\mathbf{x}, t) = \sum_{i=0}^{3} \zeta^{2i} \mathbf{U}^{(2i)}(\mathbf{x}, t) + O(\zeta^8) \tag{4.11}$$

We start by restating the macroscale balance equations, Eq. 4.10 with $\alpha = 2, 4, 6,$ in alternative forms. Let $\boldsymbol{\nu}^{(j)}$, $j = 1, 2, 3,$ denote three weighting tensors that are applied to the nonlocal stress terms in Eq. 4.10. Without loss of generality, the

macroscale balance equations become:

$$\rho_0 \ddot{\mathbf{U}}^{(\alpha)} - \boldsymbol{\nabla}_x . \left(\boldsymbol{D}^{(0)} .. \boldsymbol{\nabla}_x^s \mathbf{U}^{(\alpha)} \right) = \boldsymbol{\nabla}_x . \sum_{j=1}^{\alpha/2} \boldsymbol{\nu}^{(j)} . \boldsymbol{D}^{(2j)} .. (. \boldsymbol{\nabla}_x)^{2j} \boldsymbol{\nabla}_x^s \mathbf{U}^{(\alpha-2j)} + \boldsymbol{\nabla}_x . \sum_{j=1}^{\alpha/2} \left(\boldsymbol{\delta} - \boldsymbol{\nu}^{(j)} \right) . \boldsymbol{D}^{(2j)} .. (. \boldsymbol{\nabla}_x)^{2j} \boldsymbol{\nabla}_x^s \mathbf{U}^{(\alpha-2j)} \quad (4.12)$$

The additive decomposition in Eq. 4.12 does not introduce any approximation and is valid for any form of the weighting tensors. It is a more general form than those employed in Chapter 2 and Chapter 3 in that the decomposition of all spatial nonlocal terms is considered. This weighted form of the balance equations subsequently allows transformation of weighted spatial nonlocal terms to a temporal nonlocal term and a mixed spatial-temporal nonlocal term as described below. The temporal and mixed spatial-temporal nonlocal terms are derived from the first term on the right hand side of Eq. 4.12, while the second term is referred as the asymptotic residual term. The fractions of spatial nonlocal terms that contribute to the formulation are controlled by $\boldsymbol{\nu}^{(j)}$, where the spatial nonlocal terms are fully incorporated when $\boldsymbol{\nu}^{(j)} = \boldsymbol{\delta}$ and not incorporated when $\boldsymbol{\nu}^{(j)} = \mathbf{0}$. In this work, the weighting tensors are taken to be second-order and diagonal. The choice for the form of the weighting tensors is made to ensure that we introduce as small number of independent parameters as possible, while capturing wave dispersion with reasonable accuracy. The choice of diagonal weighting tensor implies that the contribution of the relevant high order asymptotic term to momentum balance in each direction is weighted using a separate weighting parameter. By this approach, two independent parameters need to be identified for each weighting tensor. These diagonal weighting tensors are uniquely determined by examining the characteristics of the nonlocal governing equation in each coordinate direction as discussed in Section 4.4.3.

The next step in the formulation is the projection of high order moduli as follows:

$$\boldsymbol{\nabla}_x.\left[\boldsymbol{D}^{(6)}..(.\boldsymbol{\nabla}_x)^6\boldsymbol{\nabla}_x^s\mathbf{U}^{(0)}\right]\approx\boldsymbol{\nabla}_x.\left[\left(\boldsymbol{A}^{(1)}.\boldsymbol{D}^{(0)}.\boldsymbol{D}^{(4)}\right)..(.\boldsymbol{\nabla}_x)^6\boldsymbol{\nabla}_x^s\mathbf{U}^{(0)}\right] \tag{4.13a}$$

$$\boldsymbol{\nabla}_x.\left[\left(\boldsymbol{D}^{(0)}.\boldsymbol{D}^{(2)}\right)..(.\boldsymbol{\nabla}_x)^4\boldsymbol{\nabla}_x^s\mathbf{U}^{(2)}\right]\approx\boldsymbol{\nabla}_x.\left[\left(\boldsymbol{A}^{(2)}.\boldsymbol{D}^{(2)}.\boldsymbol{D}^{(0)}\right)..(.\boldsymbol{\nabla}_x)^4\boldsymbol{\nabla}_x^s\mathbf{U}^{(2)}\right] \tag{4.13b}$$

$$\boldsymbol{\nabla}_x.\left[\boldsymbol{D}^{(4)}..(.\boldsymbol{\nabla}_x)^4\boldsymbol{\nabla}_x^s\mathbf{U}^{(2)}\right]\approx\boldsymbol{\nabla}_x.\left[\left(\boldsymbol{A}^{(3)}.\boldsymbol{D}^{(2)}.\boldsymbol{D}^{(0)}\right)..(.\boldsymbol{\nabla}_x)^4\boldsymbol{\nabla}_x^s\mathbf{U}^{(2)}\right] \tag{4.13c}$$

where $\boldsymbol{A}^{(1)}$, $\boldsymbol{A}^{(2)}$ and $\boldsymbol{A}^{(3)}$ are the projection tensors. The projection tensors are second-order and diagonal. A straightforward rearrangement of Eq. 4.13 shows that the moduli tensors $\boldsymbol{D}^{(6)}$, $\boldsymbol{D}^{(0)}.\boldsymbol{D}^{(2)}$ and $\boldsymbol{D}^{(4)}$ on the left hand side are projected onto the corresponding tensors $\boldsymbol{D}^{(0)}.\boldsymbol{D}^{(4)}$, $\boldsymbol{D}^{(2)}.\boldsymbol{D}^{(0)}$ and $\boldsymbol{D}^{(2)}.\boldsymbol{D}^{(0)}$, respectively, for arbitrary high order strain gradient fields (e.g., $(\boldsymbol{\nabla}_x)^4\boldsymbol{\nabla}_x^s\mathbf{U}^{(2)}$ for Eq. 4.13c). In Chapter 3, the projection tensors were identified by Moore-Penrose pseudo inversion, which provides the closest point projection of the projected tensors onto the corresponding tensors. We employ an alternative strategy for the identification of the projection tensors. The projection equations are expressed in the form shown in Eq. 4.13 and the tensors are identified based on strain fields associated with certain plane wave solutions as described in Section 4.4.2.

Employing the high order moduli projection, Eq 4.13, the first spatial nonlocal terms on the right hand side of the restated macroscale balance equations, Eq. 4.12, are transformed into the fourth-order spatial-temporal nonlocal form by replacing spatial nonlocal terms with the terms in balance with them in the macroscale balance equations, Eq. 4.10 with $\alpha = 0, 2, 4$. Employing the definition for the homogenized displacement field (Eq. 4.11), performing the summation of the spatial-temporal nonlocal macroscale balance equations at $O(\zeta^\alpha)$ with $\alpha = 0, 2, 4, 6$, the homogenized

momentum balance equation is obtained as:

$$\rho_0\ddot{\mathbf{U}} - \boldsymbol{\nabla}_x.\left(\boldsymbol{D}^{(0)}..\boldsymbol{\nabla}_x^s\mathbf{U}\right) = \boldsymbol{\nabla}_x.\left(\boldsymbol{\alpha}..(.\boldsymbol{\nabla}_x)^2\boldsymbol{\nabla}_x^s\mathbf{U}\right) + \boldsymbol{\nabla}_x.\left(\boldsymbol{\beta}..\boldsymbol{\nabla}_x^s\ddot{\mathbf{U}}\right) + \boldsymbol{\gamma}.\dddot{\mathbf{U}} + \sum_{i=1}^{3}\zeta^{2i}\mathbf{R}^{(2i)} \tag{4.14}$$

where, the coefficients of the PDE are:

$$\boldsymbol{\alpha} = \boldsymbol{\nu}^{(1)}.\boldsymbol{D}^{(2)} - \boldsymbol{\nu}^{(3)}.\boldsymbol{A}^{(1)}.\boldsymbol{D}^{(0)}.\boldsymbol{D}^{(0)} \tag{4.15a}$$

$$\boldsymbol{\beta} = \rho_0\left[\boldsymbol{\nu}^{(3)}.\boldsymbol{A}^{(1)}.\left(\boldsymbol{I} + \boldsymbol{A}^{(2)}\right) - \boldsymbol{\nu}^{(2)}.\boldsymbol{A}^{(3)}\right].\boldsymbol{D}^{(0)} \tag{4.15b}$$

$$\boldsymbol{\gamma} = \rho_0^2\left(\boldsymbol{\nu}^{(2)}.\boldsymbol{A}^{(3)} - \boldsymbol{\nu}^{(3)}.\boldsymbol{A}^{(1)}.\boldsymbol{A}^{(2)}\right) \tag{4.15c}$$

and the residual vector $\mathbf{R}^{(\alpha)}$ at each order are:

$$\mathbf{R}^{(2)} = \boldsymbol{\nabla}_x.\left(\boldsymbol{E}^{(2)}..(.\boldsymbol{\nabla}_x)^2\boldsymbol{\nabla}_x^s\mathbf{U}^{(0)}\right) \tag{4.16a}$$

$$\mathbf{R}^{(4)} = \boldsymbol{\nabla}_x.\left(\boldsymbol{E}^{(2)}..(.\boldsymbol{\nabla}_x)^2\boldsymbol{\nabla}_x^s\mathbf{U}^{(2)} + \boldsymbol{E}^{(4)}..(.\boldsymbol{\nabla}_x)^4\boldsymbol{\nabla}_x^s\mathbf{U}^{(0)}\right) \tag{4.16b}$$

$$\mathbf{R}^{(6)} = \boldsymbol{\nabla}_x.\left(\boldsymbol{E}^{(2)}..(.\boldsymbol{\nabla}_x)^2\boldsymbol{\nabla}_x^s\mathbf{U}^{(4)} + \boldsymbol{E}^{(4)}..(.\boldsymbol{\nabla}_x)^4\boldsymbol{\nabla}_x^s\mathbf{U}^{(2)} + \boldsymbol{E}^{(6)}..(.\boldsymbol{\nabla}_x)^6\boldsymbol{\nabla}_x^s\mathbf{U}^{(0)}\right) \tag{4.16c}$$

in which, the residual coefficient tensors are:

$$\boldsymbol{E}^{(2)} = (\boldsymbol{\delta} - \boldsymbol{\nu}^{(1)}).\boldsymbol{D}^{(2)} \tag{4.17a}$$

$$\boldsymbol{E}^{(4)} = (\boldsymbol{\delta} - \boldsymbol{\nu}^{(2)}).\boldsymbol{D}^{(4)} \tag{4.17b}$$

$$\boldsymbol{E}^{(6)} = (\boldsymbol{\delta} - \boldsymbol{\nu}^{(3)}).\boldsymbol{D}^{(6)} - \left(\boldsymbol{\nu}^{(2)}.\boldsymbol{A}^{(3)} - \boldsymbol{\nu}^{(3)}.\boldsymbol{A}^{(1)}.\boldsymbol{A}^{(2)}\right).\left(\boldsymbol{D}^{(2)}.\boldsymbol{D}^{(2)} + \boldsymbol{D}^{(4)}.\boldsymbol{D}^{(0)}\right) \tag{4.17c}$$

Equation 4.14 represents a family of nonlocal homogenization models with the coefficient tensors $\boldsymbol{A}^{(1)}$, $\boldsymbol{A}^{(2)}$, $\boldsymbol{A}^{(3)}$, $\boldsymbol{\nu}^{(1)}$, $\boldsymbol{\nu}^{(2)}$ and $\boldsymbol{\nu}^{(3)}$ to be determined. In addition to the terms (left hand side of the equation) pertain to the classical local homogeniza-

tion model that characterize non-dispersive wave propagation, three nonlocal terms, i.e., spatial nonlocal, temporal nonlocal and mixed spatial-temporal nonlocal terms, are present to capture wave dispersion and attenuation. The asymptotic accuracy of Eq. 4.14 is controlled by the residual term. When wavelength is much larger than the size of microstructures, wave propagation is non-dispersive, the contribution of the nonlocal terms compared to local terms is negligible. Compared to the existing gradient-type nonlocal homogenization models [43, 11, 64] for in-plane elastic wave, Eq. 4.14 incorporates the temporal nonlocal term by employing the balance equations of higher orders. The asymptotic residual term is a function of the weighting tensors and homogenized moduli, which is essential in enforcing the uniqueness of the spatial-temporal nonlocal homogenization model. Through minimizing this term, the optimal set of weighting tensors can be obtained that achieves the highest asymptotic accuracy.

4.4.2 Projection tensors

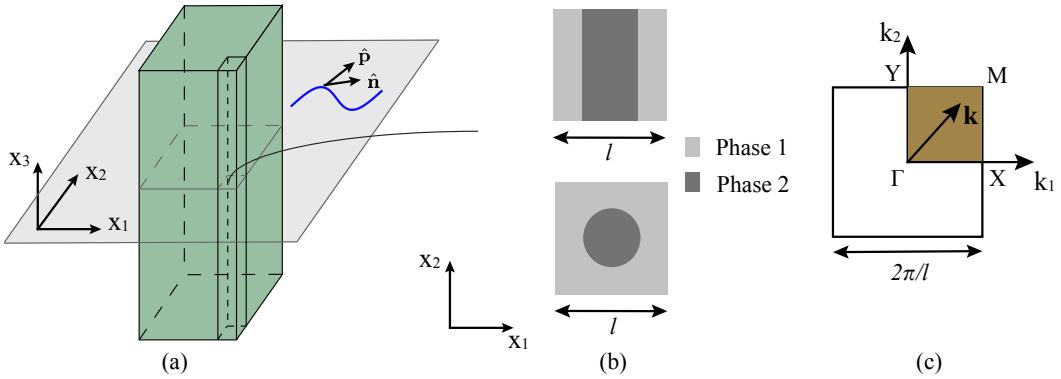

Figure 4.2: (a) Schematic representation of in-plane wave propagation in a macroscopic structure. (b) Layered and matrix-inclusion unit cells as examples for microstructures that possess symmetry with respect to the Cartesian planes. (c) Sketch of the first Brillouin zone for considered microstructures.

The procedure to identify the projection tensors, $\boldsymbol{A}^{(j)}$, is based on examining the propagation of characteristic plane waves in the homogenized medium described by the nonlocal model (Eq. 4.14). Consider three plane waves of the same mode

propagating along the same direction as characteristic waves:

$$\hat{\mathbf{U}}^{(i)}(\mathbf{x},t) = \hat{U}^{(i)}\hat{\mathbf{p}}e^{\mathrm{i}(k^{(i)}\hat{\mathbf{n}}.\mathbf{x}-\omega t)}, \quad i=0,2 \tag{4.18a}$$

$$\hat{\mathbf{U}}(\mathbf{x},t) = \hat{U}\hat{\mathbf{p}}e^{\mathrm{i}(k\hat{\mathbf{n}}.\mathbf{x}-\omega t)} \tag{4.18b}$$

where $\hat{\mathbf{n}}$ and $\hat{\mathbf{p}}$ are unit vectors in fixed directions of wave propagation and polarization, respectively. Without loss of generality, the plane waves are taken to reside in the $[x_1, x_2]$ plane, as shown in Fig. 4.2(a). ω is a positive real-valued scalar denoting the frequency of the plane waves. $\hat{U}$ and $\hat{U}^{(i)}$ are the amplitudes of the homogenized displacement and the two low order components, respectively. k and $k^{(i)}$ denote the wavenumbers. The wavenumbers are complex-valued when the wave frequency is within the stop band, where the positive imaginary part results in the exponential decay of the displacement amplitude. Substituting Eq. 4.18a into Eq. 4.13 (considering equality), the components of the approximation tensors are computed as:

$$A^{(1)}_{[ii]} = d^{(6)}_{[i]}/d^{(04)}_{[i]} \tag{4.19a}$$

$$A^{(2)}_{[ii]} = d^{(02)}_{[i]}/d^{(20)}_{[i]} \tag{4.19b}$$

$$A^{(3)}_{[ii]} = d^{(4)}_{[i]}/d^{(20)}_{[i]} \tag{4.19c}$$

in which,

$$\mathbf{d}^{(6)} = \boldsymbol{D}^{(6)}(.)^9\left[\hat{\mathbf{p}}(\otimes\hat{\mathbf{n}})^8\right] \tag{4.20a}$$

$$\mathbf{d}^{(04)} = \left(\boldsymbol{D}^{(0)}.\boldsymbol{D}^{(4)}\right)(.)^9\left[\hat{\mathbf{p}}(\otimes\hat{\mathbf{n}})^8\right] \tag{4.20b}$$

$$\mathbf{d}^{(4)} = \boldsymbol{D}^{(4)}(.)^7\left[\hat{\mathbf{p}}(\otimes\hat{\mathbf{n}})^6\right] \tag{4.20c}$$

$$\mathbf{d}^{(02)} = \left(\boldsymbol{D}^{(0)}.\boldsymbol{D}^{(2)}\right)(.)^7\left[\hat{\mathbf{p}}(\otimes\hat{\mathbf{n}})^6\right] \tag{4.20d}$$

$$\mathbf{d}^{(20)} = \left(\boldsymbol{D}^{(2)}.\boldsymbol{D}^{(0)}\right)(.)^7\left[\hat{\mathbf{p}}(\otimes\hat{\mathbf{n}})^6\right] \tag{4.20e}$$

Square brackets around indices, $[ii]$, imply that Einstein summation convention is not applied to the subscript. The equality in Eq. 4.19 that fully defines the projection tensors are strictly valid for planes waves associated with a fixed pair $(\hat{\mathbf{n}}, \hat{\mathbf{p}})$. Employing the projection tensors back to Eqs. 4.13 for a different and arbitrary pair of wave and polarization directions $(\mathbf{n}, \mathbf{p})$ would not satisfy the equality and constitute an approximation. In other words, Eqs. 4.13 are equalities only when $\mathbf{n} = \hat{\mathbf{n}}$ and $\mathbf{p} = \hat{\mathbf{p}}$.

In general, the directions of wave propagation and polarization are not necessarily related for an arbitrary plane wave, but the eigenvalues and eigenvectors of a plane wave are related to the direction of wave propagation and the material properties. For plane wave propagation in homogeneous anisotropic materials, the eigenvalues and eigenvectors are obtained by solving the Christoffel equation [98]. In order to characterize the projection tensors and weighting tensors, the characteristic polarization vector, $\hat{\mathbf{p}}$, is taken to be an eigenvector of wave propagation in a selected direction, $\hat{\mathbf{n}}$, thus $\hat{\mathbf{p}} = \hat{\mathbf{p}}(\hat{\mathbf{n}})$. The selection of the characteristic pair $(\hat{\mathbf{n}}, \hat{\mathbf{p}})$ constitutes two steps, i.e., choose $\hat{\mathbf{n}}$ first and then compute $\hat{\mathbf{p}}$ along the selected direction.

Wave dispersion in periodic composites is typically characterized by the Bloch wave expansion approach. This approach evaluates an eigenvalue problem of the unit cell with periodic boundary conditions, either by solving for the frequency with the wavevector sampled within the first Brillouin zone (i.e., $\omega(\mathbf{k})$ method [66, 73]) or by solving for the wavenumber along a prescribed direction with frequency sampled (i.e., $\mathbf{k}(\omega)$ method [76, 3, 74]). The unit cell averaged Bloch mode shapes describe the effective polarization of the media when the frequency and wavenumber are within the homogenizable regime [99, 118], including the acoustic branch and the first optical branch of the dispersion curves. Therefore, the averaged Bloch mode shapes are used as the characteristic polarization vector, $\hat{\mathbf{p}}$.

Although there are infinite number of Bloch modes within or on the edges of the first Brillouin zone, the Bloch modes at high symmetry points are typically selected

as the projection basis for reduced representation of the dispersion characteristics of periodic composites. For example, Hussein [66] used high symmetry modes as basis for model order reduction of unit cell dispersion analysis. Sridhar et al. [117] employed high symmetry modes to formulate a generalized homogenization model. In order to capture the dispersion behavior at the high symmetry points, we select the directions of wave propagation from the center to the high symmetry points on the edges of the first Brillouin zone (i.e., high symmetry directions) as the characteristic wave propagation directions $\hat{\mathbf{n}}$. For instance, $\Gamma-X$, $\Gamma-M$ and $\Gamma-Y$ directions in Fig. 4.2(c) are chosen as $\hat{\mathbf{n}}$ for the microstructures shown in Fig. 4.2(b). Since the nonlocal terms in Eq. 4.14 do not contribute to non-dispersive wave propagation, i.e., lower acoustic branches, Bloch modes of high symmetry points on the edges of the first Brillouin zone are used. At these points, wave propagation is dispersive. However, only the modes of acoustic branches (constituent phases moving in-phase) and the first optical branches (constituent phases moving out-of-phase [18]) can be employed, because higher modes correspond to wave propagation of wavelengths shorter than the size of microstructures, violating the scale separation assumption. In addition, the prediction of the optical branch is more sensitive to the magnitude of the asymptotic residual (Eq. 4.14), since the residual grows as a function of the wavenumber. Therefore, the lowest optical Bloch mode is used to compute the characteristic polarization vectors, $\hat{\mathbf{p}}$.

Selecting $(\hat{\mathbf{n}}, \hat{\mathbf{p}})$ in high symmetry directions results in spatial-temporal nonlocal homogenization models that are in the same form, with different model parameters. The projection tensors of each model are uniquely computed in a direction of high symmetry. As a result, the homogenization model most accurately characterizes wave dispersion in that direction. As the direction of wave propagation migrates away from the selected direction, the error of prediction increases.

4.4.3 Weighting tensors

In this section, we propose two approaches to identify the weighting tensors $\boldsymbol{\nu}^{(j)}$: asymptotic residual minimization, and band gap size matching. The asymptotic residual minimization approach determines the weighting tensors through a constrained optimization problem that minimizes the asymptotic residual term in Eq. 4.14, where the constraint is imposed by considering the dispersion characteristics of the nonlocal governing equation. In the band gap size matching approach, the weighting tensors are identified by minimizing the discrepancy between the band gap size predicted by the nonlocal homogenization model and those computed based on the Bloch wave analysis in prescribed directions.

4.4.3.1 *Asymptotic residual minimization*

The first approach we propose in the identification of the weighting tensors, $\boldsymbol{\nu}^{(j)}$, is the idea of minimizing the asymptotic residual term in Eq. 4.14. The order of the residual is $O(\zeta^2)$ and is expressed as a function of all three weighting tensors. In view of Eqs. 4.16 and 4.17, the $O(\zeta^2)$ and $O(\zeta^4)$ terms in the expression of the residual is eliminated by simply setting $\boldsymbol{\nu}^{(1)} = \boldsymbol{I}$ and $\boldsymbol{\nu}^{(2)} = \boldsymbol{I}$, resulting in a residual of $O(\zeta^6)$. The weighting tensor $\boldsymbol{\nu}^{(3)}$ is selected such that the remaining residual is minimized, while considering constraints imposed by physical considerations of wave dispersion.

Considering plane wave propagation with the direction and polarization vectors set to $(\hat{\mathbf{n}}, \hat{\mathbf{p}})$, substituting Eq. 4.18b into Eq. 4.14 and neglecting the residual term, the characteristic equations of the nonlocal homogenization model are obtained as:

$$A_i k^4 + B_i(\omega) k^2 + C_i(\omega) = 0 \tag{4.21a}$$

$$\tilde{A}_i \omega^4 + \tilde{B}_i(k) \omega^2 + \tilde{C}_i(k) = 0 \tag{4.21b}$$

where,

$$A_i = \alpha_{ijpqmn}\hat{p}_n\hat{n}_m\hat{n}_q\hat{n}_p\hat{n}_j, \quad \tilde{A}_i = \gamma_{in}\hat{p}_n \tag{4.22a}$$

$$B_i = (\omega^2\beta_{ijmn} - D^{(0)}_{ijmn})\hat{p}_n\hat{n}_m\hat{n}_j, \quad \tilde{B}_i = (k^2\beta_{ijmn}\hat{n}_m\hat{n}_j + \rho_0\delta_{in})\hat{p}_n \tag{4.22b}$$

$$C_i = (\omega^4\gamma_{in} + \rho_0\omega^2\delta_{in})\hat{p}_n, \quad \tilde{C}_i = (k^4\alpha_{ijpqmn}\hat{n}_m\hat{n}_q\hat{n}_p\hat{n}_j - k^2D^{(0)}_{ijmn}\hat{n}_m\hat{n}_j)\hat{p}_n \tag{4.22c}$$

The dispersion relation between ω and k for the pair $(\hat{\mathbf{n}}, \hat{\mathbf{p}})$ is obtained either by solving for k given ω (Eq. 4.21a), or by solving for ω given k (Eq. 4.21b). According to the plane wave solution form, Eq. 4.18b, the stop band occurs at frequencies that result in complex-valued wavenumbers when k is solved in terms of ω. ω is required to be real-valued when ω is solved in terms of k. The expressions:

$$\phi_i(\omega) = B^2_{[i]}(\omega) - 4A_{[i]}C_{[i]}(\omega) = a_i\omega^4 + b_i\omega^2 + c_i \tag{4.23a}$$

$$\tilde{\phi}_i(k) = \tilde{B}^2_{[i]}(k) - 4\tilde{A}_{[i]}\tilde{C}_{[i]}(k) = a_ik^4 + \tilde{b}_ik^2 + \tilde{c}_i \tag{4.23b}$$

determine the roots of Eqs. 4.21, k^2 and ω^2, being real- or complex-valued. a_i, b_i, c_i, $\tilde{b}_i$ and $\tilde{c}_i$ are functions of $\boldsymbol{\nu}^{(3)}$ only and their expressions are provided in Appendix G. In order to constrain the solutions of k when k is solved in terms of ω, and ω when ω is solved in terms of k, constraints on $\boldsymbol{\nu}^{(3)}$ are imposed through considering the behaviors of $\phi_i(\omega)$ and $\tilde{\phi}_i(k)$.

In view of Eqs. 4.23, the stop band (k being complex) appears in the frequency range that corresponds to $\phi_i(\omega) < 0$ and the existence of real-valued solution of ω requires $\tilde{\phi}_i(k) > 0$. The bounds on the selection of $\boldsymbol{\nu}^{(3)}$ are found by constraining the characteristics of the solutions of Eqs. 4.21 as follows: (1) a stop band exists and it has finite size, (2) for any given k, there exists a real-valued solution of ω. Since c_i and $\tilde{c}_i$ are positive, in order to satisfy the two conditions, the following inequality

constraints are imposed on the selection of $\boldsymbol{\nu}^{(3)}$:

$$a_i > 0 \tag{4.24a}$$

$$b_{[i]}^2 - 4a_{[i]}c_{[i]} \geq 0 \tag{4.24b}$$

$$\tilde{b}_{[i]}^2 - 4a_{[i]}\tilde{c}_{[i]} < 0 \tag{4.24c}$$

Equation 4.24a ensures that the size of the stop band is not infinite. We make a distinction between the existence of a stop band with zero width (Eq. 4.24b in equality form) and nonexistence of a stop band (i.e., $b_{[i]}^2 - 4a_{[i]}c_{[i]} < 0$). The conditions where "apparent" lack of stop band is therefore captured by Eq. 4.24b in its equality form. Compared to those imposed based on stability arguments discussed in Chapter 3 in the context of anti-plane shear wave, the proposed constraints are conceptually more restrictive. This is because the stability arguments proposed in Chapter 3 are applied at frequencies and wavenumbers associated with the quasistatic and infinitely long wave conditions only. The proposed constraints affect the behavior of dispersion for all frequencies and wavenumbers. Subject to the constraints in Eq. 4.24, the weighting tensor $\boldsymbol{\nu}^{(3)}$ is uniquely determined by minimizing Eq. 4.16c in the Euclidean norm under the condition of plane wave propagation.

4.4.3.2 *Band gap size matching*

Similar to above, the weighting tensors $\boldsymbol{\nu}^{(1)}$ and $\boldsymbol{\nu}^{(2)}$ are determined by eliminating the $O(\zeta^2)$ and $O(\zeta^4)$ residuals (i.e., $\boldsymbol{\nu}^{(1)} = \boldsymbol{\nu}^{(2)} = \boldsymbol{I}$). Considering the characteristic equation of the nonlocal governing equation for plane wave propagation in a prescribed direction, the wavenumbers and polarization vectors for quasi-longitudinal (P) and vertically polarized quasi-shear (SV) modes in $[x_1, x_2]$ plane in Fig. 4.2(a) satisfy the

following relation:

$$B_{in}(\omega, k, \hat{\mathbf{n}}, \boldsymbol{\nu}^{(3)})p_n = \begin{bmatrix} B_{11} & B_{12} \\ B_{21} & B_{22} \end{bmatrix} \begin{bmatrix} p_1 \\ p_2 \end{bmatrix} = 0 \tag{4.25}$$

where,

$$B_{in} = k^4 \alpha_{ijpqmn} \hat{n}_m \hat{n}_q \hat{n}_p \hat{n}_j + k^2(\omega^2 \beta_{ijmn} - D^{(0)}_{ijmn}) \hat{n}_m \hat{n}_j + (\omega^4 \gamma_{in} + \rho_0 \omega^2 \delta_{in}) \tag{4.26}$$

For any given ω and $\hat{\mathbf{n}}$, the wavenumbers for P and SV modes are computed by equating the determinant of $\mathbf{B}$ in Eq. 4.25 to zero and the corresponding polarization vectors, $\mathbf{p}$, are obtained by substituting the wavenumbers back into Eq. 4.25. The P and SV modes are generally coupled. In the special case when the wave is propagating along the x_1 or x_2 planes (i.e., $\hat{\mathbf{n}} = [1, 0]^T$ or $\hat{\mathbf{n}} = [0, 1]^T$), the off-diagonal terms of $\mathbf{B}$ vanish and the resulting two polarization vectors are along and orthogonal to the wave vector, resulting in the uncoupling of the longitudinal and shear modes. Equating the determinant of $\mathbf{B}$ in Eq. 4.25 to zero results in the following expression:

$$B_{11}(\omega, k, \boldsymbol{\nu}^{(3)}) B_{22}(\omega, k, \boldsymbol{\nu}^{(3)}) = 0 \tag{4.27}$$

The equality in Eq. 4.27 can be satisfied by either setting $B_{11} = 0$ or $B_{22} = 0$. These expressions correspond to the dispersion relations for the uncoupled longitudinal and shear wave modes, allowing us to determine the band structure of each mode given an arbitrary weighting tensor. The frequency range of the stop band for each mode is obtained in the analytical form:

$$\varphi_i = \frac{\sqrt{\bar{b}^2_{[i]} - 4\bar{a}_{[i]}\bar{c}_{[i]}}}{\bar{a}_{[i]}} \tag{4.28}$$

where, $\bar{a}_{[i]}$, $\bar{b}_{[i]}$ and $\bar{c}_{[i]}$ are respectively computed using the expressions for a_i, b_i and c_i with $\hat{\mathbf{n}} = [1, 0]^T$ or $\hat{\mathbf{n}} = [0, 1]^T$. With the analytical expression of the width of the stop bands, $\boldsymbol{\nu}^{(3)}$ is obtained by solving the constrained minimization problem with the objective function: $\left|\boldsymbol{\varphi} - \boldsymbol{\varphi}^{(B)}\right|$. $\boldsymbol{\varphi}^{(B)}$ is the frequency range of the first stop band of the P and SV modes calculated using the Bloch wave expansion approach. The constraints in Eq. 4.24 are imposed in this minimization problem. Wave propagation in more general situations (arbitrary $\hat{\mathbf{n}}$) couples the P and SV modes. Performing the calibration described above may be significantly more involved, since the analytical expression for the frequency range of the stop band for each mode may not be readily available.

4.4.4 Nonlocal effective medium model

Direct numerical implementation of the fourth-order initial-boundary value problem governed by Eq. 4.14 for transient wave propagation in a composite medium poses two challenges. First, high order boundary conditions need to be imposed due to the presence of the fourth order spatial term. The form of these high order boundary conditions has been subject to a number of investigations, but remain to be controversial [6]. Second, both physical and non-physical wave number solutions are present in Eq. 4.14. The non-physical wavenumbers may result in severe instability in the numerical solution [55]. In order to avoid these issues, we propose a second-order nonlocal effective medium model for transient wave propagation simulations. The model is formulated in the Laplace domain and by employing the spatial-temporal nonlocal homogenization model with projection tensors and weighting tensors computed in different high symmetry directions. The nonlocal features of the homogenization model are retained by a nonlocal moduli tensor that is dependent on the Laplace variable (i.e., frequency).

Applying the Laplace transformation to Eq. 4.14 and neglecting the residual term,

the spatial-temporal nonlocal equation is expressed in the Laplace domain:

$$\rho_0 s^2 \mathbf{U} - \boldsymbol{\nabla}_x . \left(\boldsymbol{D}^{(0)} .. \boldsymbol{\nabla}_x^s \mathbf{U} \right) = \boldsymbol{\nabla}_x . \left(\boldsymbol{\alpha} .. (. \boldsymbol{\nabla}_x)^2 \boldsymbol{\nabla}_x^s \mathbf{U} \right) + s^2 \boldsymbol{\nabla}_x . \left(\boldsymbol{\beta} .. \boldsymbol{\nabla}_x^s \mathbf{U} \right) + s^4 \boldsymbol{\gamma} . \mathbf{U} \tag{4.29}$$

where $s = \sigma + \mathrm{i}\omega$ is the complex-valued Laplace variable. We seek the nonlocal effective medium model in the form of a second-order PDE:

$$\rho_0 s^2 \mathbf{U} - \boldsymbol{\nabla}_x . \left(\boldsymbol{D}^{(e)}(s) .. \boldsymbol{\nabla}_x^s \mathbf{U} \right) = \mathbf{0} \tag{4.30}$$

where, $D^{(e)}_{ijmn}(s)$ is the nonlocal effective moduli tensor that has minor symmetry in the last two indices, $D^{(e)}_{ijmn} = D^{(e)}_{ijnm}$, due to the symmetry of local strain tensor. Considering macroscopic orthotropy, it has 6 non-zero independent components for 2D in-plane wave propagation problems. Inserting a plane wave, $\mathbf{U}(\mathbf{x}, s) = U(s)\mathbf{p}e^{\mathrm{i}k\mathbf{n}.\mathbf{x}}$, into Eq. 4.29 and 4.30, the following relations are satisfied respectively for the homogenization model and the effective medium model:

$$\tilde{B}_{in}(s, k, \mathbf{n}) p_n = \left[\alpha_{ijprmn} n_m n_r n_p n_j k^4 + (-s^2 \beta_{ijmn} - D^{(0)}_{ijmn}) n_m n_j k^2 + (s^4 \gamma_{in} - \rho_0 s^2 \delta_{in}) \right] p_n = 0 \tag{4.31a}$$

$$\bar{B}_{in}(s, k, \mathbf{n}, \boldsymbol{D}^{(e)}) p_n = \left[\rho_0 s^2 \delta_{in} + D^{(e)}_{ijmn} n_m n_j k^2 \right] p_n = 0 \tag{4.31b}$$

For any given s and $\mathbf{n}$, the wavenumbers and polarization vectors of the nonlocal homogenization model are computed by taking the determinant of $\tilde{\mathbf{B}}$ to be zero. Both physical and non-physical wavenumber solutions exist, and the non-physical wavenumbers are identified as those that have negative imaginary parts, which result in amplifying plane waves and instability in transient simulations. Only the physical wavenumbers that have non-negative imaginary parts are employed in the deriva-

tion of the nonlocal effective medium model. The nonlocal effective moduli tensor is determined such that the discrepancy of wavenumbers computed from the nonlocal effective medium model, Eq. 4.31b, and the physical wavenumbers of the nonlocal homogenization model, Eq. 4.31a, is minimized for any s along high symmetry directions, $\hat{\mathbf{n}}$. For each direction, the model parameters of the nonlocal homogenization model is computed as discussed in Section 4.4.2 and 4.4.3.

The components of the nonlocal effective moduli tensor are determined in two steps. First, the wavenumbers of directions along the x_1 and x_2 planes computed by Eq. 4.31b are matched to those computed by Eq. 4.31a, since P and SV modes are uncoupled in these directions and the wavenumber of each mode of the nonlocal effective medium model is uniquely determined by one component of $D^{(e)}_{ijmn}(s)$ that $j = m$:

$$D^{(e)}_{1111} = -\rho_0 s^2/\tilde{k}^2_{(11)}, \quad D^{(e)}_{2112} = -\rho_0 s^2/\tilde{k}^2_{(12)} \tag{4.32a}$$

$$D^{(e)}_{1221} = -\rho_0 s^2/\tilde{k}^2_{(21)}, \quad D^{(e)}_{2222} = -\rho_0 s^2/\tilde{k}^2_{(22)} \tag{4.32b}$$

where $\tilde{k}^2_{(ij)}$ is the square of the physical wavenumber of j-direction-polarized wave propagating in the i-direction, computed from Eq. 4.31a. Equation 4.32 ensures that the wave dispersion predicted by the nonlocal homogenization model in these orthogonal high symmetry directions $\big($e.g., $\Gamma - X$ and $\Gamma - Y$ directions in Fig. 4.2(c)$\big)$ is captured by the nonlocal effective medium model. Second, in order to compute the components that $j \neq m$ (i.e., $D^{(e)}_{1122}$, $D^{(e)}_{2211}$), we incorporate the high symmetry direction that is not aligned in the coordinate planes $\big($e.g., $\Gamma - M$ in Fig. 4.2(c)$\big)$ and minimize the discrepancy between wavenumbers computed from Eq. 4.31b and Eq. 4.31a. Denote the wavenumbers and polarization vectors computed from equating the determinant of $\tilde{\mathbf{B}}$ to zero as: $\tilde{\mathbf{k}} = [\tilde{k}_{(P)}, \tilde{k}_{(SV)}]^T$ and $\tilde{\mathbf{P}} = [\tilde{\mathbf{p}}_{(P)}, \tilde{\mathbf{p}}_{(SV)}]$. Substituting $\tilde{\mathbf{p}}_{(\cdot)}$, $(\bullet)$ indicating P mode or SV mode, into Eq. 4.31b, the wavenumber of the nonlocal

effective medium model, $\bar{k}^2_{(\bullet)}$, is respectively related to $D^{(e)}_{1122}$ and $D^{(e)}_{2211}$:

$$\bar{k}^2_{(\bullet)}\left(D^{(e)}_{1122}\right) = \frac{-\rho_0 s^2 \tilde{p}_{(\bullet)1}}{\left(D^{(e)}_{1111}\hat{n}_1\hat{n}_1 + D^{(e)}_{1221}\hat{n}_2\hat{n}_2\right)\tilde{p}_{(\bullet)1} + \left(D^{(e)}_{1122}\hat{n}_2\hat{n}_1 + D^{(e)}_{1212}\hat{n}_1\hat{n}_2\right)\tilde{p}_{(\bullet)2}} \tag{4.33a}$$

$$\bar{k}^2_{(\bullet)}\left(D^{(e)}_{2211}\right) = \frac{-\rho_0 s^2 \tilde{p}_{(\bullet)2}}{\left(D^{(e)}_{2112}\hat{n}_1\hat{n}_1 + D^{(e)}_{2222}\hat{n}_2\hat{n}_2\right)\tilde{p}_{(\bullet)2} + \left(D^{(e)}_{2211}\hat{n}_1\hat{n}_2 + D^{(e)}_{2121}\hat{n}_2\hat{n}_1\right)\tilde{p}_{(\bullet)1}} \tag{4.33b}$$

$D^{(e)}_{1122}$ and $D^{(e)}_{2211}$ are respectively solved by eliminating the total normalized error of wavenumbers in the two modes:

$$\Phi_1\left(D^{(e)}_{1122}\right) = \left|\frac{\tilde{k}^2_{(P)} - \bar{k}^2_{(P)}\left(D^{(e)}_{1122}\right)}{\tilde{k}^2_{(P)}}\right| + \left|\frac{\tilde{k}^2_{(SV)} - \bar{k}^2_{(SV)}\left(D^{(e)}_{1122}\right)}{\tilde{k}^2_{(SV)}}\right| = 0 \tag{4.34a}$$

$$\Phi_2\left(D^{(e)}_{2211}\right) = \left|\frac{\tilde{k}^2_{(P)} - \bar{k}^2_{(P)}\left(D^{(e)}_{2211}\right)}{\tilde{k}^2_{(P)}}\right| + \left|\frac{\tilde{k}^2_{(SV)} - \bar{k}^2_{(SV)}\left(D^{(e)}_{2211}\right)}{\tilde{k}^2_{(SV)}}\right| = 0 \tag{4.34b}$$

Compared to the local homogenization model which has static moduli tensor, the effective medium is nonlocal and its moduli tensor depends on the Laplace variable, which captures wave dispersion caused by the microstructures. Taking the real part of the Laplace variable asymptote to 0, the dynamic behavior of the moduli tensor can be interpreted in terms of frequency. In low frequency regime, the nonlocal homogenization model is non-dispersive, therefore the nonlocal effective moduli tensor recovers the local counterpart and the nonlocal effective medium model recovers local homogenization model. As the frequency increases, wave dispersion occurs. The nonlocal effective medium model matches the dispersion of the nonlocal homogenization model in high symmetry directions and approximates wave dispersion in other directions.

4.5 Model Implementation

In this section, we briefly present the implementation procedure of the multiscale system for transient wave propagation simulations. As is shown in Fig. 4.3, the overall procedure consists of two steps: (1) microscale problem solution and coefficient tensors computation; (2) Laplace domain macroscale problem evaluation and inverse Laplace transform.

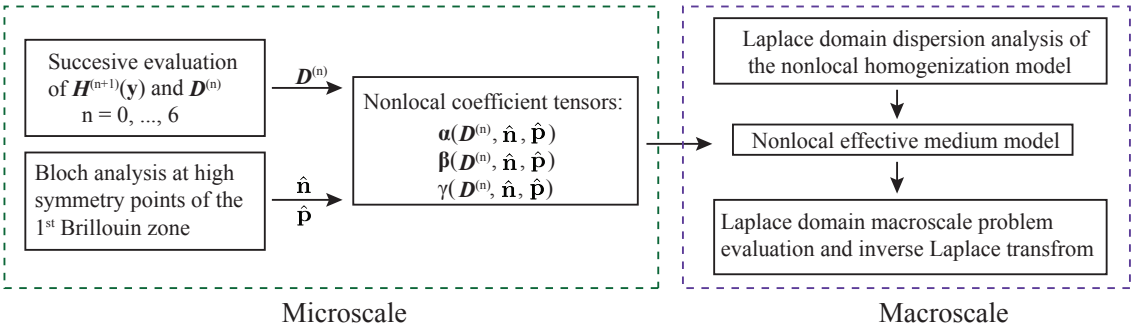

Figure 4.3: Computational flowchart.

Microscale problems defined over the domain of the unit cell constitute evaluation of influence functions and homogenized moduli, as well as Bloch analysis for the characteristic waves. The influence functions $\boldsymbol{H}^{(n+1)}$ and homogenized moduli $\boldsymbol{D}^{(n)}$ are evaluated sequentially using the finite element method (FEM). Periodic boundary conditions are applied at the microstructure boundary nodes. $\boldsymbol{H}^{(n+1)}$ is an order $(n+3)$ tensor and has 6×2^n independent components. Since the sequence of taking the $(n)^{th}$ gradient of $\boldsymbol{\nabla}_x^s \mathbf{U}^{(i-n-1)}(\mathbf{x}, t)$ in Eq. 4.6 is interchangable, when the resulting tensor is contracted with the microstructural influence function, only the symmetric part of $\boldsymbol{H}^{(n+1)}$ in those n dimensions, $\boldsymbol{H}_{sym,n}^{(n+1)}(\mathbf{y})$, affects the contraction [55]. Therefore, $\boldsymbol{H}_{sym,n}^{(n+1)}(\mathbf{y})$ is computed instead and the number of independent component is $6(n+1)$. Similarly, only the symmetric part of $\boldsymbol{D}^{(n)}$ in dimensions contracted with $(\boldsymbol{\nabla}_x)^n \boldsymbol{\nabla}_x^s \mathbf{U}^{(\alpha-n)}$ is computed in Eq. 4.10. The resulting number of computed independent component of $\boldsymbol{D}^{(n)}$ is $12(n+1)$.

The Bloch analysis is performed using the same finite element discretization of

the microstucture. $\omega(\mathbf{k})$ method is used and the prescribed wavevector is taken as the positions of the high symmetry points of the first Brillouin zone. Three symmetry points are selected to compute $(\hat{\mathbf{n}}, \hat{\mathbf{p}})$ of the characteristic waves, which are then used to compute the projection tensors (Section 4.4.2) and weighting tensors (Section 4.4.3). Thus a unique set of coefficient tensors of the spatial-temporal nonlocal homogenization model is determined for each of the selected high symmetry directions.

The single-variable constrained minimization problems in Sections 4.4.3.1 and 4.4.3.2 are implemented using the *fminbnd* function in MATLAB, which is based on Brent's method [17] and it combines the golden section search algorithm with successive parabolic interpolation. The microscale problems and computation of the nonlocal coefficient tensors are independent of the macroscale problem, therefore are implemented off-line as a preprocessing step.

The macroscale problem is implemented in the Laplace domain by sampling the Laplace variable. For each sampled Laplace variable, a dispersion analysis is performed for the fourth-order nonlocal homogenization model with projection tensors and weighting tensors computed in high symmetry directions to obtain the physical wavenumbers in these directions. The nonlocal effective medium model is formulated using the physical wavenumbers following the procedure in Section 4.4.4. The macroscale displacement field is obtained by solving the nonlocal effective medium model using Isogeometric analysis (IGA) [60] with C^1 continuity. Compared to FEM with quadratic Lagrange shape functions, IGA achieves higher convergence rate [61], therefore accurately describes high frequency waves with fewer degrees of freedom. Time domain response is obtained by a numerical inverse Laplace transform algorithm [29]. The evaluation of macroscale problem for each sampled Laplace variable is independent of another, therefore, the implementation for the macroscale problem is easily parallelized.

4.6 Model Verification

We evaluate the proposed approach in three aspects, (1) dispersion relation of the nonlocal homogenization model (Eq. 4.14), (2) dispersion relation of the nonlocal effective medium model (Eq. 4.30), and (3) transient wave propagation simulation using the nonlocal effective medium model. Two-dimensional in-plane elastic wave propagation in two types of composites are considered, i.e., bi-material layered and matrix reinforced with a circular inclusion.

4.6.1 Dispersion of the nonlocal homogenization model

Wave dispersion of two types of unit cells are considered, as shown Fig. 4.2(b), where the length of the unit cell is $l = 0.02$ m. The density, Young's modulus and Poisson's ratio are respectively taken as 2700 kg/m^3, 68 GPa and 0.3 for Phase 1, and 7900 kg/m^3, 210 GPa and 0.3 for Phase 2. The volume fraction of Phase 2 is 0.5 and 0.2 for the layered and matrix-inclusion unit cells respectively. The first Brillouin zone of the unit cells is shown in Fig. 4.2(c) and only the shaded area is considered due to the symmetry of the unit cells.

4.6.1.1 *Verification of dispersion relation*

The dispersion curves using the spatial-temporal nonlocal homogenization model (referred to as STNHM) are computed for each high symmetry direction of the first Brillouin zone, i.e., $\Gamma - X$, $\Gamma - M$, $\Gamma - Y$ in Fig. 4.2(c), using Eq. 4.31a by sampling the imaginary part and taking the real part of s as a much smaller number (10^{-6} is used in the current analysis). In this limiting case, the Laplace domain dispersion analysis can be viewed similar to the frequency domain analysis, while the complex-valued wavenumbers can be identified as physical (wavenumbers with positive real part and positive imaginary part) or non-physical (wavenumbers with positive real part and negative imaginary part). Only the physical wavenumbers are studied here since the

non-physical wavenumbers lead to unstable waves and are suppressed in transient simulations. Wavenumbers with positive real part and non-negative imaginary part computed from the Bloch wave expansion using the $\mathbf{k}(\omega)$ approach [3, 74] are employed as reference solutions. The stop band is defined as the frequency range that no propagating Bloch wavenumber solutions exist. This not only includes the situations, where real wavenumber solutions do not exist (as is often used for identifying the stop band), but also the situations, where the wavenumber is evanescent [76]. In case of evanescent waves, the wavenumber is complex-valued and wave propagation is exponentially attenuated due to the presence of the imaginary part. The lowest 10 Bloch wavenumbers are computed and sorted. The first optical Bloch wavenumber branch is plotted by mirroring the corresponding one within the first Brillouin zone, so that positive group velocity is obtained as it is in the acoustic branch. The different wave modes (P and SV modes) of STNHM and the reference solutions are classified by projecting respectively the normalized mode shapes (the real part of the eigenvector) and normalized unit cell averaged mode shapes onto the direction of wave propagation. The P and SV modes are identified as the absolute values of this projection being greater and less than $\sqrt{2}/2$, respectively.

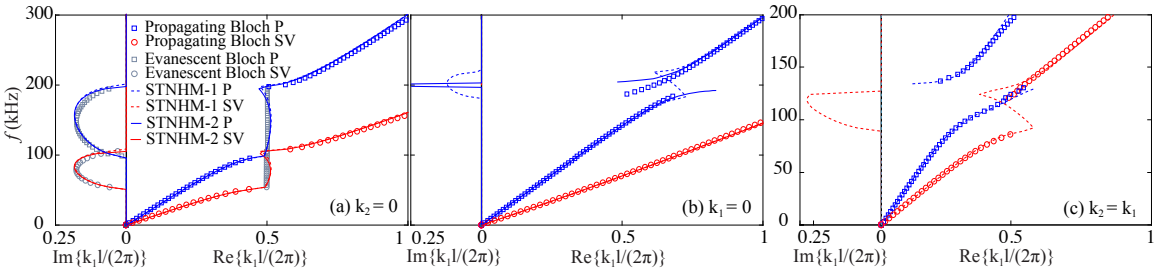

Figure 4.4: Dispersion curves of the layered microstructure for wave propagation in (a) $\Gamma - X$ direction, (b) $\Gamma - Y$ and (c) $\Gamma - M$ direction.

Figure 4.4 shows the lowest wavenumber of each mode computed using STNHM and the Bloch wave expansion for the layered microstructure, where the real part is normalized and plotted in the right panel and the imaginary part is plotted in the

left panel. Wave dispersion in $\Gamma - X$ direction is shown in Fig. 4.4(a). The homogenization models with the weighting tensor $\boldsymbol{\nu}^{(3)}$ obtained by minimizing the asymptotic error (Section 4.4.3.1) and calibrating the stop band width (Section 4.4.3.2) are denoted as STNHM-1 and STNHM-2, respectively. Both methods of determining the model parameters result in accurate prediction of the acoustic branch ($\mathrm{Re}\left\{k_1 l/(2\pi)\right\} < 0.5$), the first stop band ($\mathrm{Re}\left\{k_1 l/(2\pi)\right\} = 0.5$) and the first optical branch ($\mathrm{Re}\left\{k_1 l/(2\pi)\right\} > 0.5$). The stop bands of Bloch waves for P and SV modes are featured by the wavenumber solutions that have both positive real and imaginary parts. While wave propagation is supported by the real part of solution, it is exponentially attenuated due to the imaginary part. Within the first stop band, STNHM captures both real part and imaginary part of the lowest evanescent Bloch modes. The stop band of SV mode occurs at a lower frequency and has a smaller size compared to the P mode. The dispersion curves beyond $\mathrm{Re}\left\{k_1 l/(2\pi)\right\} = 1$ are not plotted since the wavelength is smaller than the size of microstructure and the asymptotic homogenization does not apply in that regime. Figure 4.4(b) shows wave dispersion in the $\Gamma - Y$ direction. The SV mode is non-dispersive and both STNHM models predict this behavior. P mode is dispersive only at high frequency, where the lowest eigenvalue switches from one branch to another. This switch is captured by the STNHM models. While Bloch P mode is propagative (eigenvalues are real-valued) for all frequencies, $f \in [0, 300]$ kHz, STNHM P modes become evanescent at the switch. STNHM models capture the propagating mode at higher frequencies. Wave dispersion in $\Gamma - M$ direction is shown in Fig. 4.4(c). STNHM-1 predicts wave dispersion of the acoustic branch and the first optical branch. The stop band is not observed in both Bloch and STNHM P modes since real-valued eigenvalues exist for all frequencies, $f \in [0, 200]$ kHz. At $\mathrm{Re}\left\{k_1 l/(2\pi)\right\} = 0.5$, the SV mode enters the stop band, which is featured by the fact that the Bloch waves do not have a propagating SV mode. STNHM-1 captures the location and size of the stop band. However,

instead of having an absence of wavenumber solutions, it predicts evanescent waves that are strongly attenuated by the imaginary part.

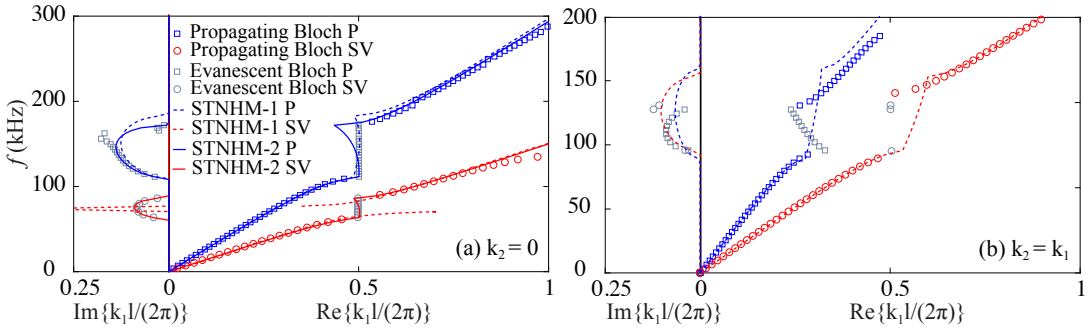

Figure 4.5: Dispersion curves of the matrix-inclusion microstructure.

Figure 4.5 shows the dispersion curves of the matrix-inclusion microstructure in directions $\Gamma - X$ and $\Gamma - M$. The response in the $\Gamma - Y$ direction is identical to that of $\Gamma - X$ due to symmetry. In Fig. 4.5(a), both STNHM-1 and STNHM-2 capture the acoustic branch and the first optical branch of P and SV modes. Compared to determining $\boldsymbol{\nu}^{(3)}$ by minimizing the asymptotic error, calibrating $\boldsymbol{\nu}^{(3)}$ by minimizing the discrepancy of stop band width prediction between STNHM and Bloch solutions results in more accurate prediction in the width of the stop band and wave attenuation caused by the imaginary part of the wavenumber. This is natural as the model is optimized to capture particularly this behavior. In the $\Gamma - M$ direction, Fig. 4.5(b), STNHM-1 accurately predicts the acoustic branch of P and SV modes. While STNHM-1 predicts the initiation of the stop band, the error increases in the prediction of the attenuation and end of the stop band that occurs at higher frequency. Wave propagation in the first optical branch is captured well. STNHM-1 predicts the group velocity (slope of the dispersion curves) of both modes, while the phase velocity of P wave is over predicted since the optical P branch is shifted to higher frequency due to the error in the prediction of the onset of the optical pass band.

It is observed that the propagating Bloch wavenumbers captured by STNHM are

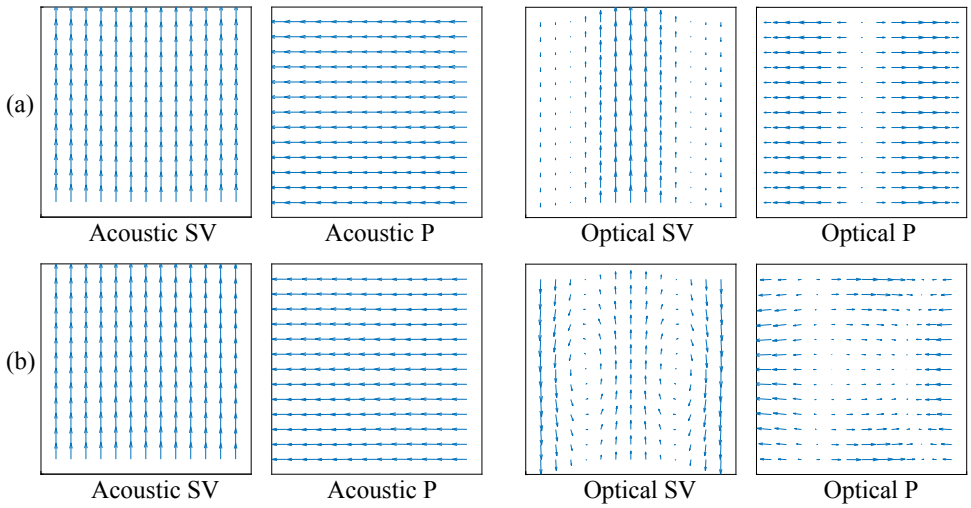

Figure 4.6: Typical acoustic and optical Bloch mode shapes in the $\Gamma - X$ direction.

the ones of the lowest rank of P and SV modes, i.e., the acoustic and first optical branch. In fact, there are infinitely many wavenumber solutions for any given frequency, which correspond to wavenumbers of different multiplicity of $2\pi/l$. The typical Bloch mode shapes of the acoustic and first optical branch are shown in Fig. 4.6. Figures 4.6(a) and (b) illustrate the displacement field of the unit cell when the wave is propagating in the $\Gamma - X$ direction for the layered and matrix-inclusion unit cells, respectively. The acoustic and optical mode shapes are plotted at $\mathrm{Re}\left\{k_1 l/(2\pi)\right\} = 0.25$ and $\mathrm{Re}\left\{k_1 l/(2\pi)\right\} = 0.75$. For both cases, the entire unit cell move uniformly in the acoustic regime, parallel and perpendicular to the direction of wave propagation for P and SV waves respectively. The optical modes are featured by the out-of-phase displacement field. The material points change direction of motion within a distance of about half of the unit cell in the direction of wave propagation. Higher optical modes that are not captured correspond to the displacement field varies more rapidly (e.g., the displacement field changes direction of motion multiple times within the unit cell) in the direction of wave propagation, or varies not only in the direction of wave propagation, but also along the transverse direction.

4.6.1.2 *Effects of the nonlocal terms*

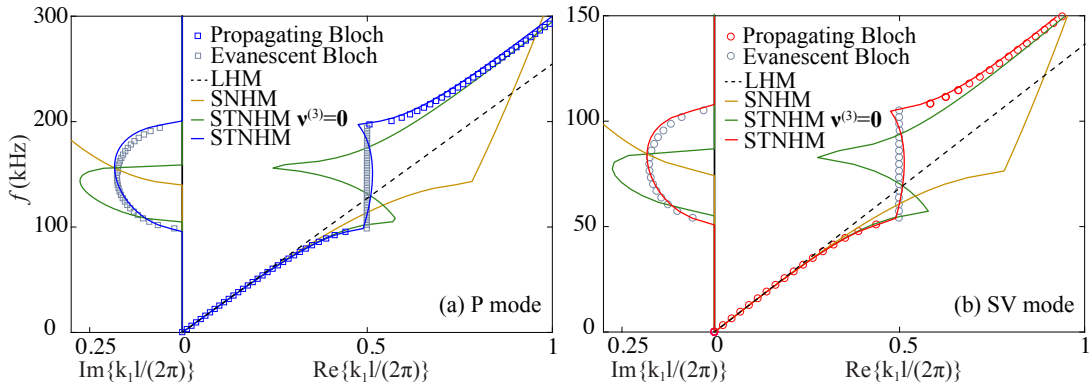

Figure 4.7: Dispersion curves of different asymptotic homogenization models.

The nonlocal terms in the homogenization model, Eq. 4.14, contribute to its capability in capturing wave dispersion. By setting the weighting tensors, $\boldsymbol{\nu}^{(1)}$, $\boldsymbol{\nu}^{(2)}$, $\boldsymbol{\nu}^{(3)}$, all equal to $\mathbf{0}$, nonlocal terms of the spatial-temporal nonlocal homogenization model vanish and it recovers the local homogenization model (LHM) with asymptotic residual of $O(\zeta^2)$. The spatial nonlocal homogenization model proposed in Refs. [43, 64] (SNHM) is recovered by setting $\boldsymbol{\nu}^{(1)} = \boldsymbol{I}$, $\boldsymbol{\nu}^{(2)} = \boldsymbol{\nu}^{(3)} = \mathbf{0}$, which is of order $O(\zeta^4)$. An alternative spatial-temporal nonlocal homogenization model is obtained by using $\boldsymbol{\nu}^{(1)} = \boldsymbol{\nu}^{(2)} = \boldsymbol{I}$, $\boldsymbol{\nu}^{(3)} = \mathbf{0}$. This model can be derived by employing macroscale balance equations (Eq. 4.10) up to $O(\zeta^4)$ therefore has asymptotic accuracy of $O(\zeta^6)$. Figure 4.7 compares the dispersion behaviors predicted by these models with the STNHM model with $\boldsymbol{\nu}^{(3)}$ computed by minimizing the $O(\zeta^6)$ asymptotic residual in the $\Gamma - X$ direction.

For both P and SV modes, STNHM with minimized asymptotic residual achieves the best accuracy. LHM predicts wave propagation without dispersion which is valid up to $\mathrm{Re}\left\{k_1 l/(2\pi)\right\} = 0.2$. The spatial nonlocal term enables SNHM to predict wave dispersion in the long wavelength regime, $\mathrm{Re}\left\{k_1 l/(2\pi)\right\} < 0.4$. Although it introduces wave attenuation, the initiation of the stop band is not well predicted. Moreover, its dispersion relation behaves as a low-pass filter, which artificially atten-

uates all the high frequency waves. The significance of the temporal nonlocal term and mixed spatial-temporal nonlocal term is that they restrict the stop band to a finite size, which allows STNHM to capture the optical branch, as is demonstrated by STNHM with $\boldsymbol{\nu}^{(3)} = \mathbf{0}$. Furthermore, the increased asymptotic accuracy results in more accurate prediction in the acoustic regime, $\mathrm{Re}\left\{k_1 l/(2\pi)\right\} < 0.5$. By minimizing the asymptotic error, STNHM improves the accuracy in the prediction of dispersion of shorter waves, $0.5 < \mathrm{Re}\left\{k_1 l/(2\pi)\right\} < 1$. However, due to the limit of separation of scales, STNHM cannot be applied to situations where the wavelength is shorter than the size of microstructure.

4.6.1.3 *Effects of material property contrast*

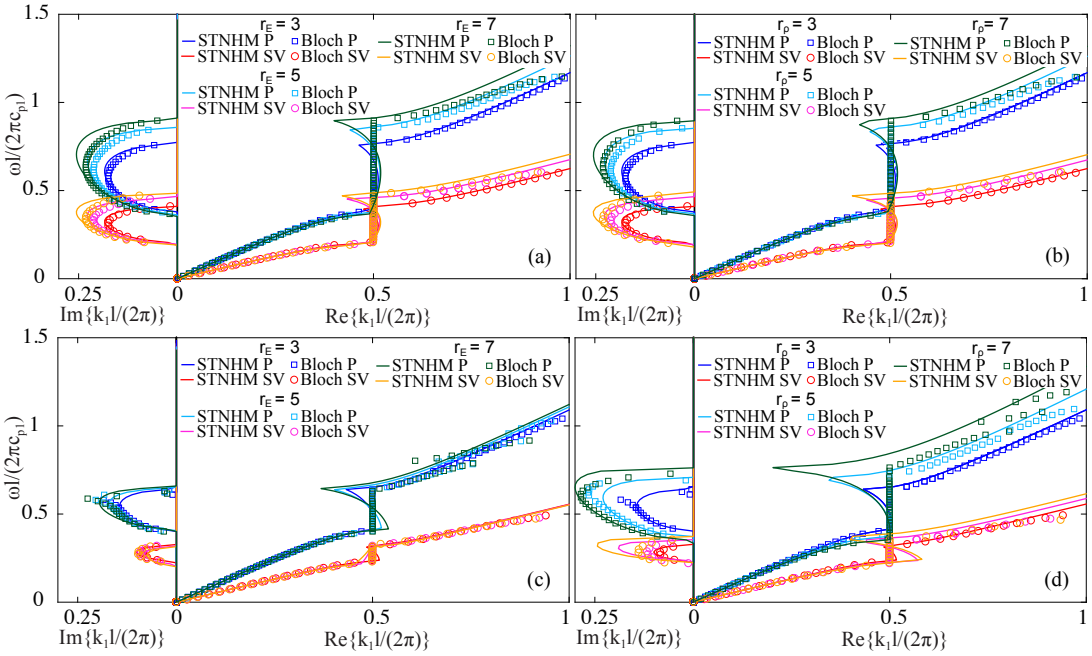

Figure 4.8: Dispersion curves of wave propagation in the $\Gamma - X$ direction. (a) Layered microstructure with $r_\rho = 3$. (b) Layered microstructure with $r_E = 3$. (c) matrix-inclusion microstructure with $r_\rho = 3$. (d) matrix-inclusion microstructure with $r_E = 3$.

The accuracy of the proposed nonlocal homogenization model, when the weighting tensor $\boldsymbol{\nu}^{(3)}$ is determined by minimizing the asymptotic residual, depends on the

contrast between the properties of constituent materials. It has been demonstrated that wave dispersion up to the initiation of the stop band is not affected significantly with the property contrast, the error in the prediction of the size of the stop band increases as the material property contrast increases in the context of scalar-field waves [54, 55]. The alternative approach of computing $\boldsymbol{\nu}^{(3)}$, i.e., calibrating the width of the stop band (STNHM-2) naturally guarantees the accuracy in predicting the width of the stop band independent of the material property contrast.

Figure 4.8 presents a parametric study of the accuracy of STNHM-2 against the Bloch wave solution, in predicting wave dispersion in the $\Gamma - X$ direction for the unit cells in Fig. 4.2(b). The vertical axis $\omega l/(2\pi c_{P1})$ is the normalized frequency, where c_{P1} is the P wave velocity of the homogenization model in the quasi-static condition, i.e., $c_{P1} = \sqrt{D^{(0)}_{1111}/\rho_0}$. The parametric study is performed by fixing the properties of Phase 1 and varying the Young's modulus and density of Phase 2. The contrast is measured by ratio between Phase 2 and Phase 1, e.g., $r_E = E_2/E_1$. The investigated material properties remain in the low contrast regime. For all studied cases, the general trend is that the prediction of dispersion within the acoustic branch, and the initiation and size of the stop band is accurate and not sensitive to the contrast in Young's modulus and density. Wave attenuation, due to the imaginary part of the wavenumber, within the stop band in the high frequency regime and the wave dispersion within the optical branch are affected, i.e., the prediction error increases as the material property contrast increases. The proposed approach captures the group velocity in the lower optical branch. As the wavelength decreases in higher frequency regime and approaches the limit of separation of scales, the model becomes non-dispersive, featured by the constant group velocity. While this behavior matches with Bloch waves for unit cells with low material property contrast, i.e., $r_E = 3$ and $r_\rho = 3$. The discrepancy becomes significant as the material property contrast increases.

4.6.2 Dispersion of the nonlocal effective medium model

In this section, we investigate the dispersion behavior predicted by the nonlocal effective medium (NEM) model for the microstructures shown in Fig. 4.2(b) with material properties used in Section 4.6.1.1. The NEM model is formulated based on the procedure described in Section 4.4.4, where the spatial-temporal nonlocal homogenization models with projection tensors and weighting tensors evaluated in $\Gamma - X$, $\Gamma - Y$ and $\Gamma - M$ directions are employed. The homogenization models with $\boldsymbol{\nu}^{(3)}$ determined by the band gap size matching approach are used in $\Gamma - X$ and $\Gamma - Y$ directions, and the asymptotic residual minimization approach is used in the $\Gamma - M$ direction. Wavenumbers computed by Eq. 4.30 at two frequencies, $f = 50$ kHz and $f = 80$ kHz, in all directions within the $[x_1, x_2]$ plane are compared with the Bloch waves. Polar representation is employed to reveal the different dispersion behavior in different directions of wave propagation.

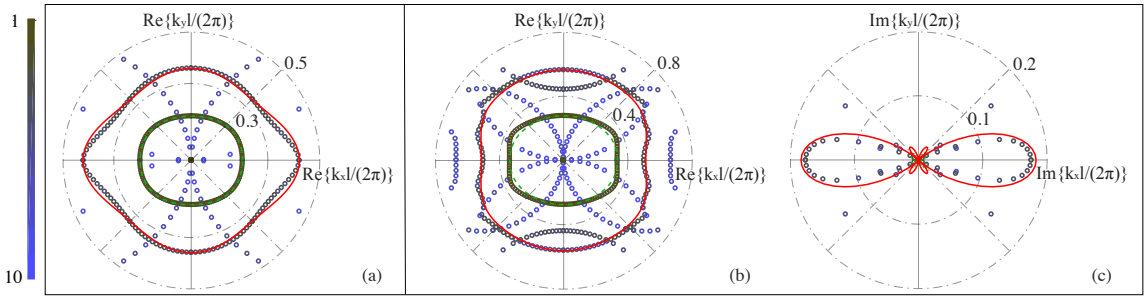

Figure 4.9: Wavenumbers in polar coordinate for the layered microstructure. (a) Real part of the wavenumber at $f = 50$ kHz. (b) Real part of the wavenumber at $f = 80$ kHz. (c) Imaginary part of the wavenumber at $f = 80$ kHz. Solid line, '—', SV mode; Dashed line, '- -', P mode; Circles, 'o', Bloch waves. The rank of Bloch eigenvalues increases as the color scale changes from dark to light.

Figure 4.9 shows the dispersion relation for the layered microstructure. It is observed from Fig. 4.4 that P wave is non-dispersive at $f = 50$ kHz in $\Gamma - X$, $\Gamma - Y$ and $\Gamma - M$ directions. As a result, the predicted P wavenumber is non-dispersive and matches with the lowest Bloch eigenvalue exactly in all directions in Fig. 4.9(a). SV wave has slower wave speed and larger wavenumber at this frequency. It enters

the dispersive acoustic regime in $\Gamma - X$ and $\Gamma - M$ directions. NEM accurately captures the wavenumber in these directions. The prediction error increases as the direction of wave propagation migrates away from the high symmetry directions, e.g., the noticeable discrepancy in 25°. As wave frequency is increased to $f = 80$ kHz, SV mode within (-30°, 30°) enters the stop band as is indicated by the imaginary part of the wavenumber shown in Fig. 4.9(c). P mode becomes dispersive which is revealed in the change of the shape of wavesurface (Fig. 4.9(b)) compared to Fig. 4.9(a)). The proposed model predicts the wavesurfaces of both P and SV modes. It captures the SV imaginary wavenumber in the directions that reside in the stop band. We observe that spurious imaginary SV and P wavenumbers are introduced in the directions of 50° and 40°, respectively. This is linked to the formulation of the nonlocal effective moduli tensor of Eq. 4.30 based on selected directions. When the SV mode in the $\Gamma - X$ direction enters the stop band, the computed value of $D^{(e)}_{2112}$ is complex, thus introducing imaginary part to wavenumbers of SV and P modes in all directions, not only within (-30°, 30°) where Bloch wavenumber is complex-valued, but also the directions that no wave attenuation occurs (e.g, 50°). Nevertheless, they have small magnitudes in the studied cases, therefore, do not result in significant artificial wave attenuation.

Figure 4.10 shows the dispersion relation for the matrix-inclusion microstructure at the same frequencies as Fig. 4.9. At $f = 50$ kHz, the non-dispersive P wavesurface is circular-shaped, indicating isotropic macroscopic wave propagation. The SV wavesurface is distorted due to wave dispersion, which has larger magnitude in 0° and 90° compared to 45°. NEM captures both P and SV wavesurfaces very accurately. At $f = 80$ kHz, the SV mode within (-30°, 30°) and (60°, 120°) enters the stop band. The proposed model predicts the wavenumbers of SV and P modes. In Figs. 4.9 and 4.10, the proposed model matches with the dark-colored Bloch eigenvalues only. The light-colored Bloch eigenvalues correspond to evanescent waves that

are of higher rank. Although their real parts fall inside the first Brillouin zone due to the periodicity of the wave vector in the Bloch theory, they are usually subject to strong attenuation [76] and do not contribute to wave propagation in the investigated frequency regime.

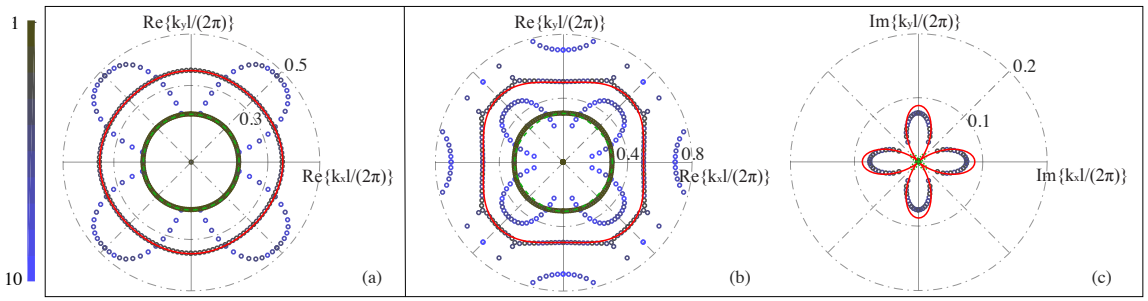

Figure 4.10: Wavenumbers in polar coordinate for the matrix-inclusion microstructure. (a) Real part of the wavenumber at $f = 50$ kHz. (b) Real part of the wavenumber at $f = 80$ kHz. (c) Imaginary part of the wavenumber at $f = 80$ kHz.

4.6.3 Transient elastic wave propagation

In this section, we investigate the transient elastic wave propagation in composites made of periodic layered microstructures. The volume fraction, size and material properties of the unit cell are identical to those in Section 4.6.1.1. Two examples are provided to evaluate the performance of the proposed model in predicting wave dispersion and attenuation, i.e., (1) transient uni-directional elastic wave propagation in the layered composite, (2) transient two-dimensional wave propagation in an elastic waveguide. Direct simulations of the heterogeneous structure are employed as the reference. IGA with sufficient refinement is used to discretize the structure for both direct simulation and the nonlocal effective medium model. Time integration of the direct simulation is implemented using the Newmark-beta implicit method.

4.6.3.1 *Transient uni-directional elastic wave propagation*

We consider transient wave propagation in a composite structure made of a row of 20 layered microstructures as shown in Fig. 4.11. The structure is fixed at the right

edge and periodic boundary conditions are applied on the top and bottom edges. Two types of sinusoidal in-plane displacement load are applied at the left edge, i.e., $\tilde{u}_1(t) = M\sin(2\pi ft)$ and $\tilde{u}_2(t) = M\sin(2\pi ft)$, which respectively generate P and SV waves.

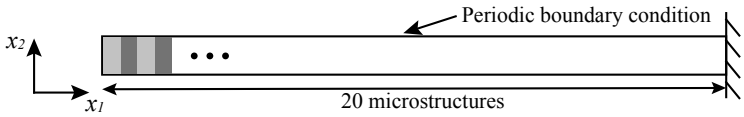

Figure 4.11: Periodic layered composite and boundary conditions.

Figure 4.12 shows the displacement snapshots measured along the bottom edge of the structure at $t = 0.06$ ms. The vertical axis U/M is the displacement normalized by the amplitude of applied load. Since only the displacement at the corner points of the unit cell allows one-to-one comparison between the direct simulation and the homogenization model [55], the displacement of direct simulation at these points are plotted as the reference. In Fig. 4.12(a), both SV and P waves are within the acoustic regime and dispersion occurs for the SV wave as manifested by the distorted wave front. As the frequency is increased to 60 kHz, SV wave enters the stop band and P wave becomes dispersive. Within the stop band, SV wave amplitude is significantly reduced. Further increase in the loading frequency results in shorter waves. At $f = 120$ kHz, SV wave enters the first optical branch while P wave falls inside the stop band. At all three frequencies, NEM accurately predicts the displacement of the reference model.

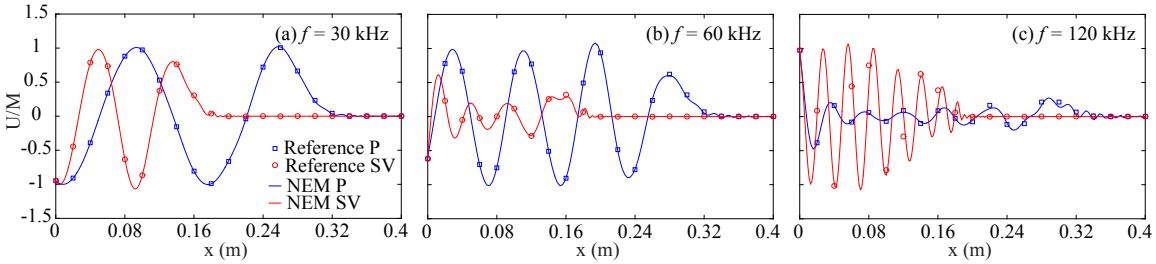

Figure 4.12: Displacement snapshots along the bottom edge of the structure.

4.6.3.2 *Elastic waveguide*

Figure 4.13 shows the two-dimensional elastic waveguide and the boundary conditions for the simulation. The waveguide ($2l \leq x_1 \leq 14l$) is made by inserting Phase 2 layers into the base material, Phase 1, within the region labeled as Heterogeneous Medium. The structure is fixed on the right edge. Sinusoidal displacement load, $\tilde{u}_1(t) = M\sin(2\pi ft)$, is applied at the center of the left edge within $5l$. The rest of edges are traction free.

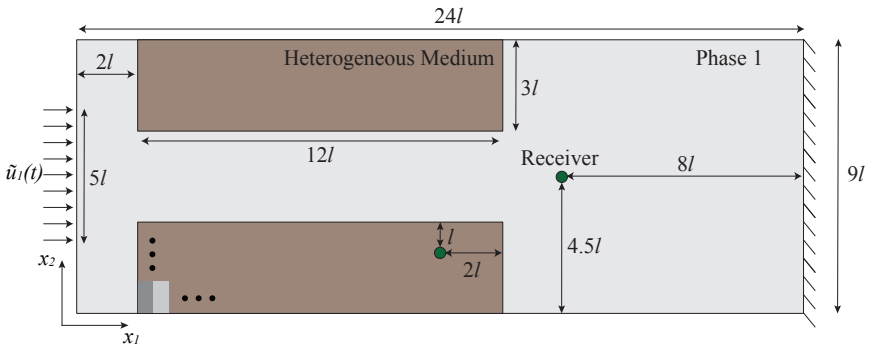

Figure 4.13: Sketch of the elastic waveguide and boundary conditions.

Figure 4.14 shows the displacement fields of NEM (the Heterogeneous Medium is modeled using the NEM model) compared with the direct simulation at $f = 60$ kHz. The total simulation time is $T = 0.1$ ms and the displacement fields are taken at $t = 0.3T$, $0.6T$ and T. At this frequency, the overall wave field predicted by NEM, Eq. 4.30, matches with the direct simulation. Propagation of macroscopic wave through the layered composite is allowed, the propagating wave and reflected wave at the traction free boundary superimpose, resulting in the short wavelength pattern in x_2 direction (right columns of figures), not only in the base material but also in the layered composite. When the loading frequency is increased to $f = 150$ kHz as shown in Fig. 4.15, wave propagation is highly confined in the homogeneous base material as the wave passes the waveguide. Much smaller wave amplitude is observed within the layered composite compared to the base material. NEM captures the wave fields within the waveguide and after the wave exits the waveguide.

Comparing Fig. 4.15 with 4.14, the predicted wave fields differs from the direct

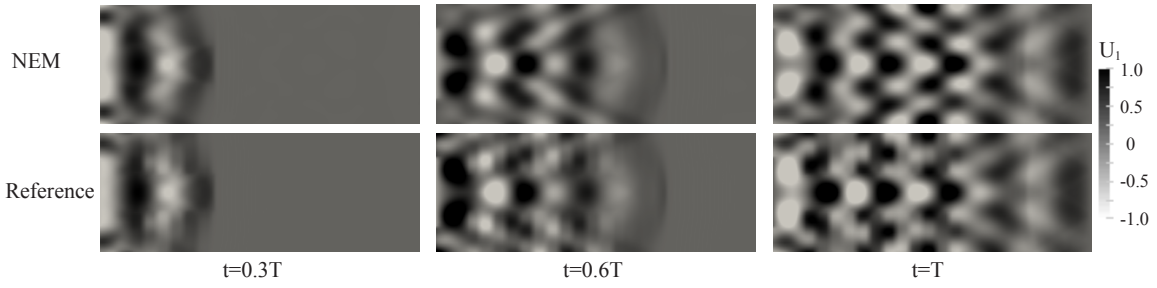

Figure 4.14: Displacement fields of wave propagation at $f = 60$ kHz.

simulations at the waveguide entrance ($x_1 \leq 2l$) at high frequency. The cause of this discrepancy is that the homogenization model is formulated for the heterogeneous domain without considering its interface with other domains. It could be addressed by introducing a boundary layer between the domain of homogenized medium and adjacent domains, where energy flux balance and continuity conditions between these domains are enforced [119].

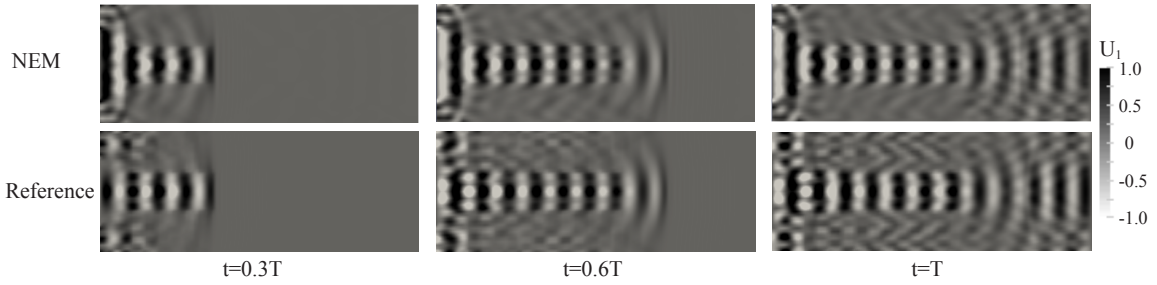

Figure 4.15: Displacement fileds of wave propagation at $f = 150$ kHz.

In order to quantitatively compare the results of NEM to the reference at different frequencies, the maximum transmitted wave amplitude U_t is recorded at two locations, $(12l, 2l)$ and $(16l, 4.5l)$ in Fig. 4.13, while sweeping the loading frequency within the range $[0, 150]$ kHz. Figure 4.16 shows the normalized transmitted wave amplitude spectrum. NEM captures the overall wave transmission pattern and the prediction error increases at high frequencies. At both locations, good accuracy is observed for $f \in [0, 60]$ kHz. Increased error is observed for $f \in [65, 75]$ kHz and $f \in [100, 130]$

at the Receiver located within the base material, and $f \in [70, 85]$ kHz and $f \in [125, 135]$ at the Receiver located within the layered composite. These errors result from three factors. First, the current homogenization model does not account for the presence of interface between the homogenized domain and the homogeneous domain, which results in prediction error at high frequency, as is observed in Fig. 4.15. Second, NEM is formulated based on the high symmetry directions of the Brillouin zone. However, for transient wave propagation in a two-dimensional domain, wave modes in all directions occur. Although these modes may be approximated by the nonlocal effective medium (Fig. 4.9), the approximation becomes less accurate at high frequency. Third, the fundamental assumption of separation of scales restricts the capability of the nonlocal effective medium model from predicting wave propagation of wavelength shorter than the size of unit cell and the accuracy of NEM decreases in high frequency regime. For the present in-plane wave propagation problem, this limit is imposed by the SV wave which propagates in shorter length compared to P wave at the same frequency.

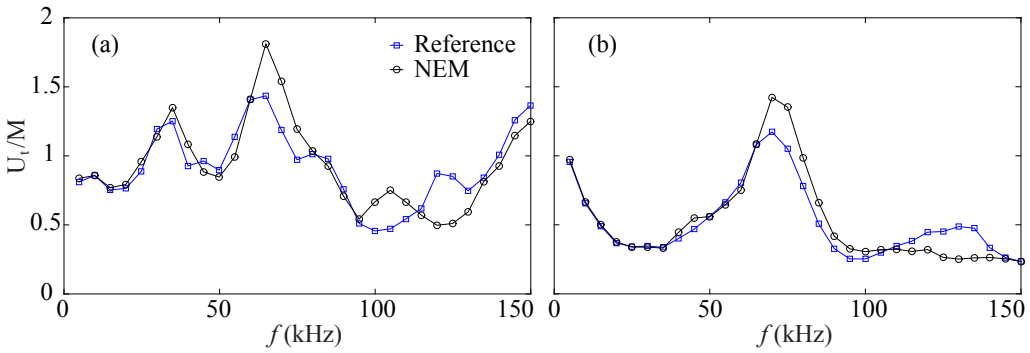

Figure 4.16: Transmitted wave amplitude spectrum at locations (a) $(12l, 2l)$ and (b) $(16l, 4.5l)$.

4.7 Conclusion

This chapter developed a spatial-temporal nonlocal homogenization model and a nonlocal effective medium model for in-plane wave propagation in periodic compos-

ites, accounting for wave dispersion and attenuation due to the Bragg scattering. In order to derive the nonlocal homogenization model and extend the applicability of asymptotic homogenization to short wavelength regime, asymptotic expansions of up to the eighth order are employed. The resulting homogenized momentum balance equation has higher order gradient terms, which are critical in capturing the stop band and optical branch of the dispersion curves.

A nonlocal effective medium model is formulated for transient elastic wave propagation based on the nonlocal homogenization model with model parameters computed from high symmetry directions of the first Brillouin zone. The effective medium model is a second order PDE, which shares the same structure as the classical local homogenization model. However, the nonlocal effective moduli is frequency dependent and carries the nonlocal characteristics of the fourth-order nonlocal homogenization model. Transient in-plane wave propagation is simulated using the nonlocal effective medium model.

The proposed model is verified for in-plane elastic wave propagation in two-dimensional composite configurations. It is shown that the nonlocal homogenization model captures the acoustic branch, the stop band and the first optical branch of the dispersion curves in the direction of high symmetry points of the first Brillouin zone. A general trend is that the accuracy decreases as the frequency increases beyond the acoustic regime and as the material property contrast increases. The nonlocal effective medium model matches the dispersion behavior of the spatial-temporal nonlocal homogenization model in the high symmetry directions and approximates it in other directions with reasonable accuracy. It accurately predicts uni-directional wave propagation and the overall wave dispersion and attenuation behavior of wave propagation in a two-dimensional waveguide.

Chapter 5

SPECTRAL VARIATIONAL MULTISCALE MODEL FOR TRANSIENT WAVE PROPAGATION IN PHONONIC CRYSTALS AND ACOUSTIC METAMATERIALS

5.1 Introduction

Phononic crystals and acoustic metamaterials are architectured composites that exhibit unique capabilities in controlling mechanical waves. Of particular interest is the control of band gaps that are generated by Bragg scattering in phononic crystals and local resonance in acoustic metamaterials. Tailoring material microstructures to achieve band gaps in desired frequency ranges presents tremendous potential in novel applications such as elastic cloaking [120], seismic wave mitigation [19, 25], acoustic superlens [79, 71], topological insulators [97] and waveguides [72] among others.

In design and analysis of phononic crystals and acoustic metamaterials, numerical simulations are employed either to characterize the unit cell band structure, or in structural scale wave propagation analyses. The former approach typically characterizes the band gaps of a periodic unit cell based on the Floquet-Bloch theorem. Significant advances have been recently made in efficient computation of dispersion band structures (see Refs. [66, 73]). The structural scale simulation of wave propagation typically relies on the transient dynamic analysis of the structural domain, where the microstructural features are fully resolved [72, 120, 97]. Clearly, the computational cost for such direct numerical simulations is prohibitive particularly when the structural domain size is large compared to that of the microstructure or when the microstructure is complex. This motivates the development of multiscale methods towards modeling the dynamic response of architectured composites in a more computationally efficient manner.

Based on the assumption of scale separation, i.e., the size of microstructures is much smaller than the wavelength, various homogenization approaches have been proposed to model wave propagation in heterogeneous materials. Computational homogenization [107, 116, 80, 81, 112, 113] evaluates nested initial-boundary value problems at the macro- and microscales, which are coupled through the Hill-Mandel energy consistency condition. In the macroscale problem, the constitutive behavior at a quadrature point is obtained through the numerical evaluation of an attached microstructure problem. This approach has been demonstrated to successfully capture the band gaps due to local resonance within acoustic metamaterials, which occur when the macroscopic deformation wavelength is considerably large compared to the size of the microstructure. In contrast, band gaps in phononic crystals occur when the macroscopic wavelength is of the same order as the microstructure size. In order to extend the applicability of homogenization to the short wavelength regime, asymptotic homogenization models with higher-order asymptotic expansions have been proposed [15, 42, 64, 65, 54, 55, 56]. Hu and Oskay [54, 55, 56] recently proposed a nonlocal asymptotic homogenization approach to accurately predict wave propagation in phononic crystals up to the second pass band. Despite significant progress in homogenization-based methods in capturing high frequency dynamics, the applicability of this approach is inherently constrained by the assumption of scale separation. When the deformation wavelength is approaching or smaller than the size of microstructure, the assumption of scale separation is no longer valid. Multiscale methods, such as the elastodynamic homogenization models based on Willis' theory [127, 93, 101, 100, 117, 88], multiscale finite element method [53, 20, 21] and the method of computational continua [41, 35, 38], that do not rely on the scale separation assumption, offer an alternative pathway to modeling wave propagation in this regime.

Another widely used multiscale method that does not make assumptions on the

length scales of continuum models is the variational multiscale method [59]. This framework is based on an additive split of the solution into coarse (resolved) scale and fine (unresolved) scale. The decomposition of solution results in two separate variational equations for the coarse and fine scale, respectively. A crucial step in achieving both accuracy and numerical efficiency using this method is the appropriate evaluation of the fine-scale Green's function. While it can be evaluated analytically for certain problems [102], the analytical form of the Green's function is generally not available when complex physics are involved for 2D and 3D problems. Several variants of the variational multiscale method have been developed employing numerical evaluation of the fine-scale problem to capture the highly complex behavior of heterogeneous materials, including the numerical subgrid upscaling method [5], the stochastic variational multiscale method [8, 46], and the variational multiscale enrichment method [103, 132, 133, 134].

This manuscript proposes a spectral variational multiscale model for transient wave propagation in phononic crystals and acoustic metamaterials. The proposed model is developed based on the variational multiscale enrichment principles [103]. Using the additive split of the displacement field, a system of multiscale governing equations is consistently derived in the variational form. In order to accurately represent wave propagation in short wavelength regimes, we employ spectral representation of the displacement field at the coarse scale. Serendipity elements of up to the septic order are used as the coarse-scale basis. In order to achieve the computational efficiency, a reduced order model is proposed for the fine-scale problem. The model order reduction is achieved using a material-phase-based mode synthesis approach that relies on the Craig-Bampton component mode synthesis [28] and characteristic constraint mode reduction [22]. The proposed model reduction approach efficiently captures the fine-scale transient dynamics with a set of reduced modal basis. To the best of the authors' knowledge, the present work is the first to model transient

wave propagation in composite materials using the variational multiscale ideas. A significant advantage of the proposed spectral variational multiscale model compared to the homogenization models is that it is not restricted by the material property contrast of the constituents or scale separation assumption. We demonstrate that the proposed model is effective in transient wave propagation in both phononic crystals and acoustic metamaterials for a broad frequency range.

The remainder of this manuscript is organized as follows: Section 2 derives the two-scale momentum balance equations in variational form. Section 3 presents the discrete multiscale system of equations. Section 4 elaborates the reduced order model for the fine-scale problems. Section 5 provides details in numerical implementation of the proposed model. Section 6 verifies the proposed model in three examples, i.e., unidirectional wave propagation in phononic crystals and acoustic metamaterials, and wave propagation in a 2D phononic crystal waveguide. The accuracy and computational efficiency are examined against direct numerical simulations. The conclusions and future research directions are presented in Section 7.

5.2 Variational Multiscale Model for Wave Propagation

We consider the transient response within a heterogeneous body, $\Omega \in \mathbb{R}^2$, an open and bounded domain constructed by periodic unit cells composed of two or more constituents. Dirichlet and Neumann boundary conditions are respectively applied at $\Gamma^u \subset \partial\Omega$ and $\Gamma^t \subset \partial\Omega$, $\Gamma^t \cap \Gamma^u = \emptyset$ and $\Gamma^t \cup \Gamma^u = \partial\Omega$. The momentum balance equation that governs wave propagation within this body is expressed as:

$$\boldsymbol{\nabla}.\boldsymbol{\sigma}(\mathbf{x},t) = \rho(\mathbf{x})\ddot{\mathbf{u}}(\mathbf{x},t); \quad \mathbf{x} \in \Omega, \quad t \in [0,\ T] \tag{5.1}$$

where, $\boldsymbol{\sigma}$ denotes the stress tensor; ρ the density; and $\mathbf{u}$ the displacement vector. $\mathbf{x}$ and t are the Cartesian spatial coordinate and time coordinate, respectively. $\boldsymbol{\nabla}.$ is the divergence operator and superimposed dot denotes derivative with respect to time.

The constitutive response of the heterogeneous body is described by the generalized Hooke's law:

$$\boldsymbol{\sigma} = \boldsymbol{C}(\mathbf{x}) : \boldsymbol{\epsilon}(\mathbf{x}, t) \tag{5.2}$$

$\boldsymbol{C}$ is the elastic moduli tensor that varies as a function of the position vector to account for the material heterogeneity. $\boldsymbol{\epsilon}$ is the strain tensor under the assumption of small deformation:

$$\boldsymbol{\epsilon} = \boldsymbol{\nabla}^s \mathbf{u} = \frac{1}{2}\left[\boldsymbol{\nabla}\mathbf{u} + (\boldsymbol{\nabla}\mathbf{u})^T\right] \tag{5.3}$$

where $\boldsymbol{\nabla}$ and $\boldsymbol{\nabla}^s$ are the gradient and symmetric gradient operators, respectively. The boundary and initial conditions are:

$$\text{B.C.} \qquad \mathbf{u}(\mathbf{x}, t) = \tilde{\mathbf{u}}(\mathbf{x}, t); \quad \mathbf{x} \in \Gamma^u, \qquad \boldsymbol{\sigma}(\mathbf{x}, t).\mathbf{n} = \tilde{\mathbf{t}}(\mathbf{x}, t); \quad \mathbf{x} \in \Gamma^t \tag{5.4a}$$

$$\text{I.C.} \qquad \mathbf{u}(\mathbf{x}, 0) = \mathbf{u}_0; \quad \mathbf{x} \in \Omega, \qquad \dot{\mathbf{u}}(\mathbf{x}, 0) = \mathbf{v}_0; \quad \mathbf{x} \in \Omega \tag{5.4b}$$

where $\tilde{\mathbf{u}}$ and $\tilde{\mathbf{t}}$ are respectively the prescribed displacement and traction along the boundary, and $\mathbf{u}_0$ and $\mathbf{v}_0$ are respectively the initial displacement and velocity.

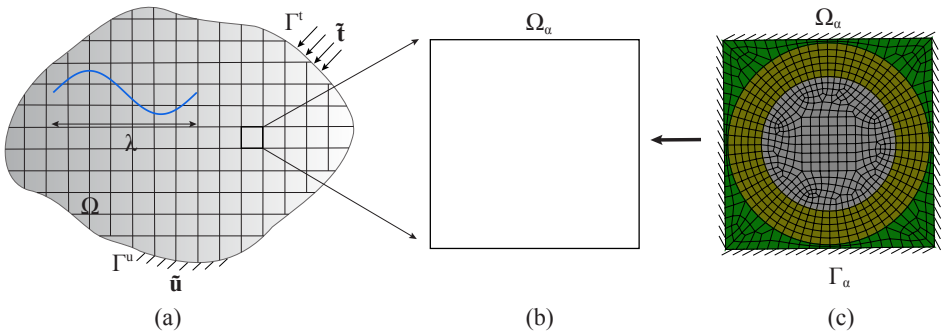

Figure 5.1: The two-scale problem setting for wave propagation in periodic composites. (a) Composite domain discretized using coarse mesh. (b) One coarse-scale element. (c) The associated fine-scale mesh.

Using the standard arguments, the problem is stated in the variational form:

$$\int_\Omega \mathbf{w}(\mathbf{x}).\left(\rho\ddot{\mathbf{u}}\right)\, d\Omega + \int_\Omega \boldsymbol{\nabla}^s\mathbf{w}(\mathbf{x}) : \boldsymbol{C} : \boldsymbol{\nabla}^s\mathbf{u}\, d\Omega = \int_{\Gamma^t} \mathbf{w}(\mathbf{x}).\tilde{\mathbf{t}}\, d\Gamma \tag{5.5}$$

in which, the function spaces for the displacement trial solution and the weighting function are respectively:

$$\mathcal{V} = \left\{ \mathbf{u} \middle| \ \mathbf{u} \in \mathcal{H}^1(\Omega),\ \mathbf{u} = \tilde{\mathbf{u}} \text{ on } \Gamma^u \right\} \tag{5.6a}$$

$$\mathcal{W} = \left\{ \mathbf{w} \middle| \ \mathbf{w} \in \mathcal{H}^1(\Omega),\ \mathbf{w} = \mathbf{0} \text{ on } \Gamma^u \right\} \tag{5.6b}$$

where, $\mathcal{H}^1(\Omega)$ is the Sobolev space that contains functions with sufficient smoothness.

We proceed with partitioning the problem domain Ω into n_{nc} non-overlapping open and simply connected subdomains. Each subdomain is one coarse-scale element and align with one unit cell. The interior of the coarse-scale element is denoted as Ω_α and $\bar{\Omega} = \bigcup_{\alpha=1}^{n_{\text{ec}}} \bar{\Omega}_\alpha$, where the overbar indicates the closure of a domain. The choice of using one coarse-scale element to represent one unit cell is made in view of the periodic arrangement of microstructures. Each coarse-scale element can be different when each unit cell contains different microstructures.

The displacement field over the domain Ω is expressed in terms of coarse-scale and fine-scale components through an additive two-scale decomposition:

$$\mathbf{u}(\mathbf{x}, t) = \mathbf{u}^c(\mathbf{x}, t) + \sum_{\alpha=1}^{n_{\text{ec}}} \mathbf{u}_\alpha^f(\mathbf{x}, t) \tag{5.7}$$

Superscripts c and f denote the coarse and fine scales, respectively. In the classical variational multiscale method, the coarse-scale component approximates the solution resolved by a coarse mesh, whereas the fine-scale component is the associated error. The fine-scale component remains unresolved, and is typically approximated by an analytical function (e.g., residual free bubble function [59]). In the variational multiscale enrichment approach, the fine-scale problem is numerically evaluated, similar to the numerical subgrid upscaling method [5]. For wave propagation in composites, the material heterogeneity is not resolved at the coarse scale, and $\mathbf{u}^c$ refers to the

"homogenized" wave field solution. Numerical solution of $\mathbf{u}_\alpha^f$ captures the rapid wave field oscillations within a coarse-scale element Ω_α, where material heterogeneity is resolved by the fine-scale mesh.

The weighting function is approximated in a similar fashion using a two-scale decomposition:

$$\mathbf{w}(\mathbf{x}) = \mathbf{w}^c(\mathbf{x}) + \sum_{\alpha=1}^{n_{\text{ec}}} \mathbf{w}_\alpha^f(\mathbf{x}) \tag{5.8}$$

The displacements and weighting functions at the two scales are respectively sought in the function spaces $\mathcal{V}^c$, $\mathcal{W}^c$ and $\mathcal{V}_\alpha^f$, $\mathcal{W}_\alpha^f$. The solution space of the displacement field, $\mathbf{u}$, and weighting function, $\mathbf{w}$, are therefore respectively restricted to the direct sum of the coarse- and fine-scale solution spaces [59]. The fine-scale spaces are defined such that the trial solution and the weighting function are localized within the corresponding coarse-scale element Ω_α and vanish elsewhere:

$$\mathcal{V}_\alpha^f = \mathcal{W}_\alpha^f = \left\{ {\mathbf{v}_\alpha}^f \,\middle|\, \mathbf{v}_\alpha^f = \mathbf{0} \text{ on } \bar{\Omega} \setminus \Omega_\alpha \right\} \tag{5.9}$$

The function spaces for the finite dimensional approximation to the coarse-scale fields are chosen as C^0 continuous:

$$\mathcal{V}^c = \left\{ \mathbf{u}^c \,\middle|\, \mathbf{u}^c \in C^0(\Omega) \cap \mathcal{V},\ \mathbf{u}^c(\Omega_\alpha) \in \mathcal{P}^p(\Omega_\alpha) \right\} \tag{5.10a}$$

$$\mathcal{W}^c = \left\{ \mathbf{w}^c \,\middle|\, \mathbf{w}^c \in C^0(\Omega) \cap \mathcal{W},\ \mathbf{w}^c(\Omega_\alpha) \in \mathcal{P}^p(\Omega_\alpha) \right\} \tag{5.10b}$$

where $\mathcal{P}^p(\Omega_\alpha)$ denotes the set of complete polynomials of order p over Ω_α. This choice for the coarse-scale displacement field indicates that high-order spectral functions are admissible within each element, whereas the displacement is C^0 continuous across the element interfaces.

Remark 3. The approximation space defined in Eq. 5.9 implies the fine-scale homogeneous Dirichlet boundary conditions along the boundaries of Ω_α. This boundary

condition is widely used [86, 87, 103, 133] due to its simplicity and is adopted in this study. We note that other fine-scale boundary conditions can also be applied, such as, mixed boundary conditions [104, 132], edge bubbles for interface problems [123], and mixed use of bubbles and other Dirichlet boundary conditions for strain localization problems [48]. While these boundary conditions may improve the numerical accuracy, the possible interactions of the fine-scale problems between neighboring coarse-scale elements may result in significant complexity in numerical implementation and increased computational cost.

Substituting the two-scale decompositions (Eqs. 5.7, 5.8) into Eq. 5.5, the variational form is decomposed into a coarse-scale problem defined over Ω and a series of fine-scale problems defined within each coarse-scale element Ω_α. At the coarse scale:

$$\int_\Omega \mathbf{w}^c . \left(\rho \ddot{\mathbf{u}}^c\right)\ d\Omega + \int_\Omega \boldsymbol{\nabla}^s \mathbf{w}^c : \boldsymbol{C} : \boldsymbol{\nabla}^s \mathbf{u}^c\ d\Omega\ = \\ -\sum_{\alpha=1}^{n_{\text{ec}}} \int_{\Omega_\alpha} \mathbf{w}^c . \left(\rho \ddot{\mathbf{u}}_\alpha^f\right)\ d\Omega_\alpha - \sum_{\alpha=1}^{n_{\text{ec}}} \int_{\Omega_\alpha} \boldsymbol{\nabla}^s \mathbf{w}^c : \boldsymbol{C} : \boldsymbol{\nabla}^s \mathbf{u}_\alpha^f\ d\Omega_\alpha\ + \int_{\Gamma^t} \mathbf{w}^c . \tilde{\mathbf{t}}\ d\Gamma \quad (5.11)$$

The terms on the left hand side are the virtual kinetic energy and strain energy, whereas the first two terms on the right hand side describe the total coarse-scale virtual work due to fine-scale dynamics within all coarse-scale elements. At the fine scale, the variational form for Ω_α, is:

$$\int_{\Omega_\alpha} \mathbf{w}^f . \left(\rho \ddot{\mathbf{u}}^f\right)\ d\Omega_\alpha + \int_{\Omega_\alpha} \boldsymbol{\nabla}^s \mathbf{w}^f : \boldsymbol{C} : \boldsymbol{\nabla}^s \mathbf{u}^f\ d\Omega_\alpha\ = \\ -\int_{\Omega_\alpha} \mathbf{w}^f . \left(\rho \ddot{\mathbf{u}}^c\right)\ d\Omega_\alpha - \int_{\Omega_\alpha} \boldsymbol{\nabla}^s \mathbf{w}^f : \boldsymbol{C} : \boldsymbol{\nabla}^s \mathbf{u}^c\ d\Omega_\alpha \quad (5.12)$$

The traction term is not present in Eq. 5.12 because the fine-scale weighting function vanishes at all coarse-scale element domain boundaries via Eq. 5.9. The fine-scale problem states that the virtual kinetic energy and strain energy of each coarse-scale element domain at the fine scale is balanced with the local virtual work due to the

dynamics of the coarse-scale. Equations 5.11 and 5.12 constitute a coupled problem for evaluating the dynamic response of the composite domain.

In what follows, we provide an approach to directly evaluate this system of equations. It is important to highlight that the direct evaluation of this system does not reduce the computational cost compared with the direct numerical simulation of the governing equation, Eq. 5.5. Alternatively, direct evaluation of the two-scale system forms the foundation for the reduced basis approximation we later introduce for the fine-scale problem.

5.3 Spectral Variational Multiscale Model

In this section, we propose a spectral approach to capture the transient dynamic response of periodic composites by numerically evaluating the coarse- and fine-scale variational forms provided in Eqs. 5.11 and 5.12.

The selection of the size of coarse-scale element and the order of the corresponding shape functions depends on the characteristic wavelength of the associated problem. For static problems [132, 133], the wavelength is infinitely long and it typically suffices to use linear elements at the coarse scale. For wave propagation problems, sufficiently fine resolution is necessary to accurately capture the wave field and avoid numerical dispersion [32]. Fine resolution can be achieved through h-refinement or p-refinement, and their application in dynamic problems has been extensively discussed in the literature in the context of single scale analysis (see e.g., Refs. [122, 10, 68, 69, 70]). In the proposed multiscale model, the size of the coarse-scale elements is fixed to the size of the underlying microstructure. We employ high order shape functions to accurately capture high frequency wave propagation through a p-refinement strategy at the coarse scale.

Lagrange polynomials are used as shape functions for the coarse-scale elements. In two dimensions, the classical quadrilateral Lagrange elements contain $(p+1)^2$ nodes.

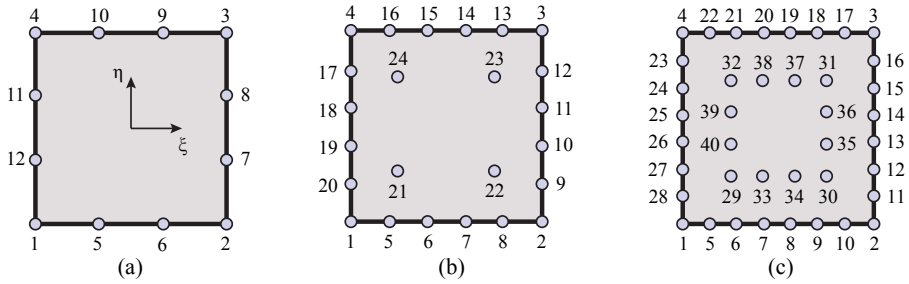

Figure 5.2: Quadrilateral serendipity elements of (a) cubic (3^{rd}), (b) quintic (5^{th}) and (c) septic (7^{th}) orders.

Due to the presence of large numbers of bubble nodes, Lagrange elements pose significant computational cost for higher spectral orders. Instead, serendipity quadrilateral elements achieve the same order of approximation with fewer nodes. The higher-order serendipity elements developed in Refs. [110, 111] are adopted herein. In this family of serendipity elements, the number of nodes is minimized while maintaining the required polynomial completeness. Figure 5.2 shows the elements of cubic, quintic and septic orders, which respectively have 12, 24 and 40 nodes per element. The formulas for the shape functions and locations of the nodal points are provided in Ref. [110].

The fine-scale trial solution and weighting function are approximated using standard bilinear finite elements. This selection of fine-scale elements has also been used in Refs. [47, 104]. Along with the homogeneous Dirichlet type fine-scale boundary conditions, this choice ensures linear independence of the solution spaces at the coarse and fine scales and the direct sum relationship between the multiscale fields is valid.

Employing the classical Bubnov-Galerkin approach, the coarse-scale displacement, weighting function and their gradients within a coarse-scale element are written as:

$$\mathbf{u}^c_\alpha = \mathbf{N}^c_\alpha \mathbf{d}^c_\alpha = \mathbf{N}^c_\alpha \mathbf{L}^c_\alpha \mathbf{d}^c; \quad \mathbf{w}^c_\alpha = \mathbf{N}^c_\alpha \mathbf{c}^c_\alpha = \mathbf{N}^c_\alpha \mathbf{L}^c_\alpha \mathbf{c}^c \tag{5.13a}$$

$$[\boldsymbol{\nabla}^s \mathbf{u}^c_\alpha] = \mathbf{B}^c_\alpha \mathbf{d}^c_\alpha = \mathbf{B}^c_\alpha \mathbf{L}^c_\alpha \mathbf{d}^c; \quad [\boldsymbol{\nabla}^s \mathbf{w}^c_\alpha] = \mathbf{B}^c_\alpha \mathbf{c}^c_\alpha = \mathbf{B}^c_\alpha \mathbf{L}^c_\alpha \mathbf{c}^c \tag{5.13b}$$

where, $\mathbf{u}^c_\alpha(\mathbf{x}, t) := \mathbf{u}^c(\mathbf{x} \in \Omega_\alpha, t)$ with the corresponding weighting function analo-

gously defined. $\mathbf{N}^c_\alpha$ and $\mathbf{B}^c_\alpha$ are respectively the coarse-scale element shape function matrix and strain-displacement matrix (detailed definition of these matrices is provided in Ref. [39]) within the coarse-scale element, Ω_α. Einstein summation does not apply to the subscripts. The square bracket indicates the vectorized form of the corresponding tensors. $\mathbf{d}^c_\alpha$ and $\mathbf{c}^c_\alpha$ are the element nodal displacement and weighting function vectors, and they are related to the global vectors, $\mathbf{d}^c$ and $\mathbf{c}^c$, through the mapping matrix $\mathbf{L}^c_\alpha$, which assembles the global vectors from the element vectors [39].

Each coarse-scale element is associated with a heterogeneous microstructure (also denoted as Ω_α in Fig. 5.1). Equation 5.12 is evaluated to compute the fine-scale fields for all microstructures within the problem domain. Consider the discretization of the microstructure, Ω_α into n_{ef} fine-scale elements. The fine-scale displacement, weighting function and their gradients for the fine-scale element e within the microstructure Ω_α are expressed as:

$$\mathbf{u}^f_{e,\alpha} = \mathbf{N}^f_{e,\alpha}\mathbf{d}^f_{e,\alpha} = \mathbf{N}^f_{e,\alpha}\mathbf{L}^f_{e,\alpha}\mathbf{d}^f_\alpha; \quad \mathbf{w}^f_{e,\alpha} = \mathbf{N}^f_{e,\alpha}\mathbf{c}^f_{e,\alpha} = \mathbf{N}^f_{e,\alpha}\mathbf{L}^f_{e,\alpha}\mathbf{c}^f_\alpha \tag{5.14a}$$

$$\left[\boldsymbol{\nabla}^s\mathbf{u}^f_{e,\alpha}\right] = \mathbf{B}^f_{e,\alpha}\mathbf{d}^f_{e,\alpha} = \mathbf{B}^f_{e,\alpha}\mathbf{L}^f_{e,\alpha}\mathbf{d}^f_\alpha; \quad \left[\boldsymbol{\nabla}^s\mathbf{w}^f_{e,\alpha}\right] = \mathbf{B}^f_{e,\alpha}\mathbf{c}^f_{e,\alpha} = \mathbf{B}^f_{e,\alpha}\mathbf{L}^f_{e,\alpha}\mathbf{c}^f_\alpha \tag{5.14b}$$

where, $\mathbf{N}^f_{e,\alpha}$ and $\mathbf{B}^f_{e,\alpha}$ are respectively the fine-scale element shape function matrix and strain-displacement matrix within the fine-scale element, Ω^e_α. $\mathbf{d}^f_{e,\alpha}$ and $\mathbf{c}^f_{e,\alpha}$ are the fine-scale element nodal displacement and weighting vectors, related to the vector of the fine-scale nodal displacement and weighting functions within the microstructure through $\mathbf{L}^f_{e,\alpha}$. Employing Eqs. 5.13 and 5.14, the discretized forms of Eqs. 5.11 and 5.12 are obtained as:

$$\mathbf{K}^{cc}\mathbf{d}^c + \mathbf{M}^{cc}\ddot{\mathbf{d}}^c + \sum_{\alpha=1}^{n_{\text{ec}}}\mathbf{K}^{cf_\alpha}\mathbf{d}^{f_\alpha} + \sum_{\alpha=1}^{n_{\text{ec}}}\mathbf{M}^{cf_\alpha}\ddot{\mathbf{d}}^{f_\alpha} = \mathbf{F}^c \tag{5.15a}$$

$$\mathbf{K}^{f_\alpha c}\mathbf{d}^c + \mathbf{M}^{f_\alpha c}\ddot{\mathbf{d}}^c + \mathbf{K}^{f_\alpha f_\alpha}\mathbf{d}^{f_\alpha} + \mathbf{M}^{f_\alpha f_\alpha}\ddot{\mathbf{d}}^{f_\alpha} = \mathbf{0}, \quad \alpha = 1, ..., n_{\text{ec}} \tag{5.15b}$$

where, $\mathbf{K}^{f_\alpha f_\alpha}$, $\mathbf{M}^{f_\alpha f_\alpha}$ and $\mathbf{K}^{cc}$, $\mathbf{M}^{cc}$ are respectively the stiffness and mass matrices of the fine-scale problem in Ω_α and the coarse-scale problem. $\mathbf{K}^{cf_\alpha}$ and $\mathbf{M}^{cf_\alpha}$ are the stiffness and mass matrices due to interactions between the two scales. $\mathbf{F}^c$ is the coarse-scale force vector. They are obtained by assembling the element matrices and the force vectors as:

$$\mathbf{K}^{f_\alpha f_\alpha} = \sum_{e=1}^{n_{\text{ef}}} \left(\mathbf{L}^f_{e,\alpha}\right)^T \mathbf{K}^{f_\alpha f_\alpha}_e \mathbf{L}^f_{e,\alpha}; \quad \mathbf{M}^{f_\alpha f_\alpha} = \sum_{e=1}^{n_{\text{ef}}} \left(\mathbf{L}^f_{e,\alpha}\right)^T \mathbf{M}^{f_\alpha f_\alpha}_e \mathbf{L}^f_{e,\alpha} \tag{5.16a}$$

$$\mathbf{K}^{cc} = \sum_{\alpha=1}^{n_{\text{ec}}} \left(\mathbf{L}^c_\alpha\right)^T \mathbf{K}^{cc}_\alpha \mathbf{L}^c_\alpha; \quad \mathbf{M}^{cc} = \sum_{\alpha=1}^{n_{\text{ec}}} \left(\mathbf{L}^c_\alpha\right)^T \mathbf{M}^{cc}_\alpha \mathbf{L}^c_\alpha \tag{5.16b}$$

$$\mathbf{K}^{cf_\alpha} = \left(\mathbf{K}^{f_\alpha c}\right)^T = \left(\mathbf{L}^c_\alpha\right)^T \sum_{e=1}^{n_{\text{ef}}} \mathbf{K}^{cf_\alpha}_e \mathbf{L}^f_{e,\alpha}; \quad \mathbf{M}^{cf_\alpha} = \left(\mathbf{M}^{f_\alpha c}\right)^T = \left(\mathbf{L}^c_\alpha\right)^T \sum_{e=1}^{n_{\text{ef}}} \mathbf{M}^{cf_\alpha}_e \mathbf{L}^f_{e,\alpha} \tag{5.16c}$$

$$\mathbf{F}^c = \sum_{\alpha=1}^{n_{\text{ec}}} \left(\mathbf{L}^c_\alpha\right)^T \mathbf{f}_\alpha \tag{5.16d}$$

n_{ef} is the number of fine-scale elements used to discretize Ω_α. The element matrices and the force vector are:

$$\mathbf{K}^{cc}_\alpha = \int_{\Omega_\alpha} (\mathbf{B}^c_\alpha)^T \mathbf{C}(\mathbf{x}) \mathbf{B}^c_\alpha \, d\Omega_\alpha; \quad \mathbf{M}^{cc}_\alpha = \int_{\Omega_\alpha} (\mathbf{N}^c_\alpha)^T \rho(\mathbf{x}) \mathbf{N}^c_\alpha \, d\Omega_\alpha \tag{5.17a}$$

$$\mathbf{K}^{f_\alpha f_\alpha}_e = \int_{\Omega^e_\alpha} (\mathbf{B}^f_{e,\alpha})^T \mathbf{C}_e \mathbf{B}^f_{e,\alpha} \, d\Omega^e_\alpha; \quad \mathbf{M}^{f_\alpha f_\alpha}_e = \int_{\Omega^e_\alpha} (\mathbf{N}^f_{e,\alpha})^T \rho_e \mathbf{N}^f_{e,\alpha} \, d\Omega^e_\alpha \tag{5.17b}$$

$$\mathbf{K}^{cf_\alpha}_e = \int_{\Omega^e_\alpha} (\mathbf{B}^c_{e,\alpha})^T \mathbf{C}_e \mathbf{B}^f_{e,\alpha} \, d\Omega^e_\alpha; \quad \mathbf{M}^{cf_\alpha}_e = \int_{\Omega^e_\alpha} (\mathbf{N}^c_{e,\alpha})^T \rho_e \mathbf{N}^f_{e,\alpha} \, d\Omega^e_\alpha \tag{5.17c}$$

$$\mathbf{f}_\alpha = \int_{\Gamma^t_\alpha} (\mathbf{N}^c_\alpha)^T \, \tilde{\mathbf{t}} \, d\Gamma^t_\alpha \tag{5.17d}$$

where $\mathbf{C}_e$ and ρ_e are respectively the elastic moduli and density of the e^{th} fine-scale element. The evaluation of the pure fine-scale matrices in Eq. 5.17b and the coarse-scale force vector in Eq. 5.17d is straightforward and performed using the standard element level integration procedure. Evaluating Eqs. 5.17a and c is not standard and the detailed evaluation procedure for coarse-scale and scale interaction matrices is

provided in Section 5.5.2.

The construction of global matrices constitutes the assembly of the coarse-scale stiffness and mass matrices and the corresponding fine-scale matrices of all subdomains. The global displacement vector that contains coarse-scale and fine-scale degrees of freedom (DOFs) are arranged as follows:

$$\mathbf{d}_{SVM} = \left[(\mathbf{d}^c)^T,\ \left(\mathbf{d}^{f_1}\right)^T,\ \left(\mathbf{d}^{f_2}\right)^T,\ ...,\ \left(\mathbf{d}^{f_{n_{\text{ec}}}}\right)^T \right]^T \tag{5.18}$$

Accordingly, the global stiffness matrix is constructed by block assembly of the coarse-scale, fine-scale and the interaction matrices (Eqs. 5.17a-c) of all microstructures:

$$\mathbf{K}_{SVM} = \begin{bmatrix} \mathbf{K}^{cc} & \mathbf{K}^{cf_1} & \mathbf{K}^{cf_2} & \dots & \mathbf{K}^{cf_{n_{\text{ec}}}} \\ \mathbf{K}^{f_1c} & \mathbf{K}^{f_1f_1} & \mathbf{0} & \dots & \mathbf{0} \\ \mathbf{K}^{f_2c} & \mathbf{0} & \mathbf{K}^{f_2f_2} & \dots & \mathbf{0} \\ \vdots & \vdots & \vdots & \ddots & \vdots \\ \mathbf{K}^{f_{n_{\text{ec}}}c} & \mathbf{0} & \mathbf{0} & \dots & \mathbf{K}^{f_{n_{\text{ec}}}f_{n_{\text{ec}}}} \end{bmatrix} \tag{5.19}$$

The global mass matrix is assembled similarly. The global force vector has the form: $\mathbf{F}_{SVM} = \left[(\mathbf{F}^c)^T,\ \mathbf{0}^T,\ \mathbf{0}^T,\ ...,\ \mathbf{0}^T \right]^T$. The DOFs associated with Dirichlet boundary conditions of both coarse and fine scales are eliminated using static condensation. The resulting global system of equations is:

$$\mathbf{K}_{SVM}\mathbf{d}_{SVM} + \mathbf{M}_{SVM}\ddot{\mathbf{d}}_{SVM} = \mathbf{F}_{SVM} \tag{5.20}$$

Equation 5.20 constitutes the full system of equations of the spectral variational multiscale (SVM) model for wave propagation in periodic composites, where the dynamics at both scales are fully resolved.

5.4 Phase Mode Synthesis for Basis Reduction at Fine Scale

Evaluating Eq. 5.20 directly does not provide significant numerical efficiency compared to single scale finite element simulation when the same level of mesh density is used to discretize the microstructure. The multiscale system of equations have slightly fewer DOFs since the boundary DOFs at the fine scale are condensed out. Nevertheless, the system size remains relatively large. In this section, we propose a basis reduction strategy at the fine scale to improve the computational efficiency.

The basis reduction at the fine scale is performed as a two-step component mode synthesis procedure that combines the Craig-Bampton method [28] and the characteristic constraint mode reduction [22], which were originally developed for reduced representation of structural components in analyzing the vibration response of large-scale structural systems. The key idea in this approach is that the dynamic behavior of a structural system is decomposed into its structural components. The dynamic response of each component is expressed as the superposition of its internal dynamics with the component-structure interface fixed, and the static response of the component due to the deformation of the component-structure interface. The internal dynamics of the component is approximated using a truncated modal basis. The constraint mode reduction refers to a reduced modal basis representation of the deformation along the component-structure interface.

We adopt this idea in the analysis of the fine-scale problem and employ a phase-based basis reduction approach. In this context, the subdomains of the microstructure that are occupied by separate constituent materials (i.e., phases) are considered as the "components". The material interfaces become the "component-structure interfaces". Craig-Bampton mode synthesis is employed to express the response of each material phase using a truncated set of modal basis functions. The interface degrees of freedom are then reduced through constraint mode reduction.

Consider a microstructure Ω_α that consists of n^{ph} material phases and n^{int} in-

terfaces. The interfaces are assumed to be non-intersecting, and separate only two phases. The fine-scale stiffness matrix of each microstructure $\mathbf{K}^{ff}$ (subscript α is omitted for clarity) is partitioned and rearranged as follows:

$$\mathbf{K}^{ff} = \begin{bmatrix} \mathbf{K}^{P_1P_1} & \mathbf{0} & \dots & \mathbf{0} & \mathbf{K}^{P_1I_1} & \mathbf{K}^{P_1I_2} & \dots & \mathbf{K}^{P_1I_{n^{\text{int}}}} \\ \mathbf{0} & \mathbf{K}^{P_2P_2} & \dots & \mathbf{0} & \mathbf{K}^{P_2I_1} & \mathbf{K}^{P_2I_2} & \dots & \mathbf{K}^{P_2I_{n^{\text{int}}}} \\ \vdots & \vdots & \ddots & \vdots & \vdots & \vdots & \ddots & \vdots \\ \mathbf{0} & \mathbf{0} & \dots & \mathbf{K}^{P_{n^{\text{ph}}}P_{n^{\text{ph}}}} & \mathbf{K}^{P_{n^{\text{ph}}}I_1} & \mathbf{K}^{P_{n^{\text{ph}}}I_2} & \dots & \mathbf{K}^{P_{n^{\text{ph}}}I_{n^{\text{int}}}} \\ \mathbf{K}^{I_1P_1} & \mathbf{K}^{I_1P_2} & \dots & \mathbf{K}^{I_1P_{n^{\text{ph}}}} & \mathbf{K}^{I_1I_1} & \mathbf{0} & \dots & \mathbf{0} \\ \mathbf{K}^{I_2P_1} & \mathbf{K}^{I_2P_2} & \dots & \mathbf{K}^{I_2P_{n^{\text{ph}}}} & \mathbf{0} & \mathbf{K}^{I_2I_2} & \dots & \mathbf{0} \\ \vdots & \vdots & \ddots & \vdots & \vdots & \vdots & \ddots & \vdots \\ \mathbf{K}^{I_{n^{\text{int}}}P_1} & \mathbf{K}^{I_{n^{\text{int}}}P_2} & \dots & \mathbf{K}^{I_{n^{\text{int}}}P_{n^{\text{ph}}}} & \mathbf{0} & \mathbf{0} & \dots & \mathbf{K}^{I_{n^{\text{int}}}I_{n^{\text{int}}}} \end{bmatrix} \tag{5.21}$$

where $\mathbf{K}^{P_iP_i}$ and $\mathbf{K}^{I_jI_j}$ are the matrix blocks associated with phase P_i and interface I_j, respectively. $\mathbf{K}^{P_iI_j} = \left(\mathbf{K}^{I_jP_i}\right)^T$ denotes the interaction matrix between phase P_i and interface I_j. The mass matrix $\mathbf{M}^{ff}$ is partitioned and rearranged similarly.

Equation 5.21 shows the general structure of the fine-scale stiffness matrix of a multi-phase microstructure, where the fine-scale mesh conforms to the material interfaces and the interfaces do not intersect. The type of microstructures under these restrictions cover a broad class of phononic crystal and acoustic metamaterial designs [83, 85]. For these microstructures, sufficiently fine mesh ensures that the DOFs of two different interfaces do not have direct interactions, therefore, $\mathbf{K}^{I_iI_j} = \mathbf{0}$, $i \neq j$. In addition, $\mathbf{K}^{P_iI_j} = \mathbf{0}$ when phase P_i is not connected with interface I_j.

The overall strategy for the material-phase-based mode synthesis is illustrated in Fig. 5.3. Using the Craig-Bampton (CB) method [28], the dynamic response of the microstructure is expressed in terms of a truncated set of fixed-interface normal modes of each material phase and the interface nodal constraint modes. The characteristic constraint (CC) mode synthesis is then employed to represent the interface

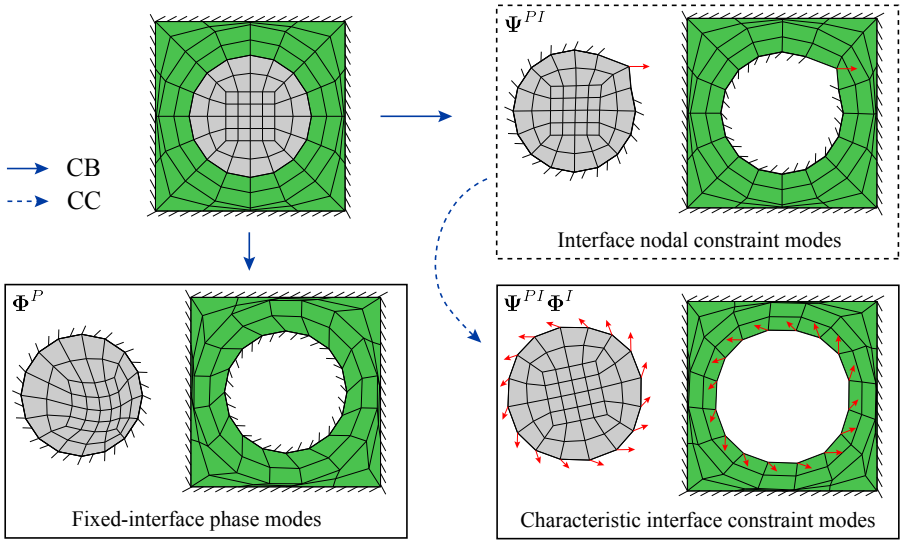

Figure 5.3: Material-phase-based mode synthesis strategy.

deformation using a truncated set of characteristic interface constraint modes. The normal modes of a material phase P_i, $i = 1, ..., n^{\text{ph}}$, are obtained by solving the eigenvalue problem:

$$\left(\mathbf{K}^{P_iP_i} - \lambda^{P_i}\mathbf{M}^{P_iP_i}\right)\boldsymbol{\phi}^{P_i} = \mathbf{0} \tag{5.22}$$

All boundaries of the phase are fixed. Solving Eq. 5.22 results in m^{P_i} normal modes and they are sorted according to their corresponding eigenvalues in the ascending order: $\{\boldsymbol{\phi}_1^{P_i}, \boldsymbol{\phi}_2^{P_i}, ..., \boldsymbol{\phi}_{m^{P_i}}^{P_i}\}$. Model order reduction is achieved by selecting a truncated set of normal modes as basis for the solution of the dynamics within phase P_i. The lowest l^{P_i} modes are selected to form the normal mode matrix: $\boldsymbol{\Phi}^{P_i} = \left[\boldsymbol{\phi}_1^{P_i}, \boldsymbol{\phi}_2^{P_i}, ..., \boldsymbol{\phi}_{l^{P_i}}^{P_i}\right]$.

The effect of deformation along an interface on the adjacent material phases is taken into account by considering the static interface constraint modes. The interface modes are computed by evaluating the static deformation of phase P_i subjected to perturbations along the interface I_j. Let $\boldsymbol{\Psi}^{P_iI_j}$ denote the interface constraint mode matrix. Each column in the constraint mode matrix contains the nodal displacements in phase P_i subjected to a unit displacement applied at an interface node along one spatial direction while all other interface nodal DOFs are set to vanish. It is

straightforward to show that the interface constraint mode matrix is expressed as:

$$\mathbf{\Psi}^{P_i I_j} = -\left(\mathbf{K}^{P_i P_i}\right)^{-1} \mathbf{K}^{P_i I_j} \tag{5.23}$$

The fine-scale DOFs within each material phase is represented using the generalized basis that is composed of the fixed-interface normal modes and the interface constraint modes. The original DOFs are related to the reduced DOFs by the modal transformation matrix $\mathbf{T}^P$:

$$\mathbf{T}^P = \begin{bmatrix} \mathbf{\Phi}^{P_1} & \mathbf{0} & \dots & \mathbf{0} & \mathbf{\Psi}^{P_1 I_1} & \mathbf{\Psi}^{P_1 I_2} & \dots & \mathbf{\Psi}^{P_1 I_{n^{\text{int}}}} \\ \mathbf{0} & \mathbf{\Phi}^{P_2} & \dots & \mathbf{0} & \mathbf{\Psi}^{P_2 I_1} & \mathbf{\Psi}^{P_2 I_2} & \dots & \mathbf{\Psi}^{P_2 I_{n^{\text{int}}}} \\ \vdots & \vdots & \ddots & \vdots & \vdots & \vdots & \ddots & \vdots \\ \mathbf{0} & \mathbf{0} & \dots & \mathbf{\Phi}^{P_{n^{\text{ph}}}} & \mathbf{\Phi}^{P_{n^{\text{ph}}} I_1} & \mathbf{\Phi}^{P_{n^{\text{ph}}} I_2} & \dots & \mathbf{\Phi}^{P_{n^{\text{ph}}} I_{n^{\text{int}}}} \\ \mathbf{0} & \mathbf{0} & \dots & \mathbf{0} & \mathbf{I}^{I_1} & \mathbf{0} & \dots & \mathbf{0} \\ \mathbf{0} & \mathbf{0} & \dots & \mathbf{0} & \mathbf{0} & \mathbf{I}^{I_2} & \dots & \mathbf{0} \\ \vdots & \vdots & \ddots & \vdots & \vdots & \vdots & \ddots & \vdots \\ \mathbf{0} & \mathbf{0} & \dots & \mathbf{0} & \mathbf{0} & \mathbf{0} & \dots & \mathbf{I}^{I_{n^{\text{int}}}} \end{bmatrix} \tag{5.24}$$

where $\mathbf{I}^{I_j}$ is the identity matrix of the same size as $\mathbf{K}^{I_j I_j}$. Applying this transformation to the fine-scale stiffness and mass matrix:

$$\mathbf{K}_{R1}^{ff} = \left(\mathbf{T}^P\right)^T \mathbf{K}^{ff} \mathbf{T}^P \tag{5.25a}$$

$$\mathbf{M}_{R1}^{ff} = \left(\mathbf{T}^P\right)^T \mathbf{M}^{ff} \mathbf{T}^P \tag{5.25b}$$

$\mathbf{K}_{R1}^{ff}$ and $\mathbf{M}_{R1}^{ff}$ are the reduced stiffness and mass matrices due to the truncated selection of normal modes of each material phase.

While the above procedure reduces the degrees of freedom within each material phase, the number of interface degrees of freedom can be significant, especially

for complex microstructures where a fine mesh is required at the interface region. We perform a secondary model order reduction using the characteristic constraint mode reduction approach [22]. The interface degrees of freedom is reduced by using truncated normal modes to represent the interface dynamics. The normal modes of interface I_j are computed by the eigenvalue analysis of the interface partition of $\mathbf{K}_{R1}^{ff}$ and $\mathbf{M}_{R1}^{ff}$:

$$\left(\mathbf{K}_{R1}^{I_jI_j} - \lambda^{I_j}\mathbf{M}_{R1}^{I_jI_j}\right)\boldsymbol{\phi}^{I_j} = \mathbf{0} \tag{5.26}$$

The reduced basis is obtained by sorting the interface normal modes and selecting those with the lowest l^{I_j} eigenvalues to construct the interface normal mode matrix: $\boldsymbol{\Phi}^{I_j} = \left[\boldsymbol{\phi}_1^{I_j}, \boldsymbol{\phi}_2^{I_j}, ..., \boldsymbol{\phi}_{l^{I_j}}^{I_j}\right]$. The interface modal transformation matrix is defined as:

$$\mathbf{T}^I = \begin{bmatrix} \boldsymbol{I}_{R_1}^{P_1} & \mathbf{0} & \dots & \mathbf{0} & \mathbf{0} & \mathbf{0} & \dots & \mathbf{0} \\ \mathbf{0} & \boldsymbol{I}_{R_1}^{P_2} & \dots & \mathbf{0} & \mathbf{0} & \mathbf{0} & \dots & \mathbf{0} \\ \vdots & \vdots & \ddots & \vdots & \vdots & \vdots & \ddots & \vdots \\ \mathbf{0} & \mathbf{0} & \dots & \boldsymbol{I}_{R_1}^{P_{n^{\text{ph}}}} & \mathbf{0} & \mathbf{0} & \dots & \mathbf{0} \\ \mathbf{0} & \mathbf{0} & \dots & \mathbf{0} & \boldsymbol{\Phi}^{I_1} & \mathbf{0} & \dots & \mathbf{0} \\ \mathbf{0} & \mathbf{0} & \dots & \mathbf{0} & \mathbf{0} & \boldsymbol{\Phi}^{I_2} & \dots & \mathbf{0} \\ \vdots & \vdots & \ddots & \vdots & \vdots & \vdots & \ddots & \vdots \\ \mathbf{0} & \mathbf{0} & \dots & \mathbf{0} & \mathbf{0} & \mathbf{0} & \dots & \boldsymbol{\Phi}^{I_{n^{\text{int}}}} \end{bmatrix} \tag{5.27}$$

where $\boldsymbol{I}_{R_1}^{P_i}$ is the identity matrix of the same size as the partition of the reduced stiffness matrix corresponding to the i^{th} material phase, $\mathbf{K}_{R_1}^{P_iP_i}$. The secondary reduction to the stiffness and mass matrix is obtained by:

$$\mathbf{K}_{R2}^{ff} = \left(\mathbf{T}^I\right)^T \mathbf{K}_{R1}^{ff}\mathbf{T}^I = \left(\mathbf{T}^P\mathbf{T}^I\right)^T \mathbf{K}^{ff}\mathbf{T}^P\mathbf{T}^I \tag{5.28a}$$

$$\mathbf{M}_{R2}^{ff} = \left(\mathbf{T}^I\right)^T \mathbf{M}_{R1}^{ff}\mathbf{T}^I = \left(\mathbf{T}^P\mathbf{T}^I\right)^T \mathbf{M}^{ff}\mathbf{T}^P\mathbf{T}^I \tag{5.28b}$$

The coarse-fine interaction matrices in Eq. 5.15 are reduced similarly by post-multiplying the phase and interface modal transformation matrices:

$$\mathbf{K}_{R2}^{cf_\alpha} = \left(\mathbf{K}_{R2}^{f_\alpha c}\right)^T = \mathbf{K}^{cf_\alpha}\mathbf{T}^P\mathbf{T}^I \tag{5.29a}$$

$$\mathbf{M}_{R2}^{cf_\alpha} = \left(\mathbf{M}_{R2}^{f_\alpha c}\right)^T = \mathbf{M}^{cf_\alpha}\mathbf{T}^P\mathbf{T}^I \tag{5.29b}$$

The reduced order multiscale system of equations is written as:

$$\mathbf{K}^{cc}\mathbf{d}^c + \mathbf{M}^{cc}\ddot{\mathbf{d}}^c + \sum_{\alpha=1}^{n_{\text{ec}}} \mathbf{K}_{R2}^{cf_\alpha}\mathbf{g}^{f_\alpha} + \sum_{\alpha=1}^{n_{\text{ec}}} \mathbf{M}_{R2}^{cf_\alpha}\ddot{\mathbf{g}}^{f_\alpha} = \mathbf{F}^c \tag{5.30a}$$

$$\mathbf{K}_{R2}^{f_\alpha c}\mathbf{d}^c + \mathbf{M}_{R2}^{f_\alpha c}\ddot{\mathbf{d}}^c + \mathbf{K}_{R2}^{f_\alpha f_\alpha}\mathbf{g}^{f_\alpha} + \mathbf{M}_{R2}^{f_\alpha f_\alpha}\ddot{\mathbf{g}}^{f_\alpha} = \mathbf{0}, \quad \alpha = 1, ..., n_{\text{ec}} \tag{5.30b}$$

where $\mathbf{g}^{f_\alpha} = \left[\left(\mathbf{g}_{P_1}^{f_\alpha}\right)^T,\ \left(\mathbf{g}_{P_2}^{f_\alpha}\right)^T,\ ...,\ \left(\mathbf{g}_{P_{n^{\text{ph}}}}^{f_\alpha}\right)^T,\ \left(\mathbf{g}_{I_1}^{f_\alpha}\right)^T,\ \left(\mathbf{g}_{I_2}^{f_\alpha}\right)^T,\ ...,\ \left(\mathbf{g}_{I_{n^{\text{int}}}}^{f_\alpha}\right)^T\right]^T$, is the vector of the generalized degrees of freedom associated with the normal modes of the material phases and interfaces of the microstructure. The fine-scale nodal DOFs are recovered from the generalized DOFs using the transformation matrices:

$$\mathbf{d}^{f_\alpha} = \mathbf{T}^P\mathbf{T}^I\mathbf{g}^{f_\alpha} \tag{5.31}$$

Due to the periodic arrangement of unit cells, the model order reduction is performed only once for one unit cell and the same reduced stiffness and mass matrices are used for all unit cells. The global matrices and the force vector are assembled similarly as the full multiscale model in Section 5.3. The two-step model order reduction presented above significantly reduces the number of DOFs of the full spectral variational multiscale model and it is referred as reduced spectral variational multiscale (RSVM) model hereafter.

Another model order reduction strategy that can be used for reducing the fine-scale

degrees of freedom is the unit cell based Craig-Bampton component mode synthesis (UCRSVM), which employs the unit cell normal modes as the reduced basis for the fine-scale problem, without distinguishing the material phases and interfaces and performing model order reduction to each of them. The fine-scale unit cell normal modes are obtained by solving the eigenvalue problem:

$$\left(\mathbf{K}^{f_\alpha f_\alpha} - \lambda^{f_\alpha}\mathbf{M}^{f_\alpha f_\alpha}\right)\boldsymbol{\phi}^{f_\alpha} = \mathbf{0} \tag{5.32}$$

Similar to RSVM, the normal mode matrix is constructed by truncating the higher frequency modes and the size of the stiffness and mass matrix is reduced by matrix transformation of the original matrices using the normal mode matrix (e.g., Eq. 5.25). This approach has been successfully applied in modeling the acoustic metamaterials using the computational homogenization framework [116, 112]. In these works, periodic boundary conditions are applied at the fine scale, the local resonance modes are identified and used as reduced basis. In the current work, since homogeneous Dirichlet boundary condition is used at the fine scale, the resulting normal modes are fixed-boundary vibration modes. It is observed that these modes do not well capture the wave propagation at the fine scale. A comparison of UCRSVM to RSVM is provided in Section 5.6.2.

5.5 Implementation Details

In this section, we provide implementation details of the proposed spectral variational multiscale model, including coarse-scale and fine-scale discretization, evaluation of element matrices, selection of the normal modes for reduced basis approximation, and time integration.

5.5.1 Multiscale discretization

The proposed multiscale approach has been verified on coarse-scale domains, where the domain of the coarse-scale element in the discretization conforms to that of a unit cell. The domain is first discretized using linear quadrilateral elements (the edges of the elements remain straight). Higher-order serendipity elements are then achieved by adding edge nodes and bubble nodes to the linear base element. The coordinates of the added nodes are linearly interpolated using the corner nodes of the linear base element. The node numbering and positioning in the cubic, quintic and septic elements are shown in Fig. 5.2. Each coarse-scale element is associated with the same unit cell morphology, which is meshed using the bilinear quadrilateral elements at the fine scale. In order to avoid numerical dispersion, sufficient spectral order has to be employed for the coarse-scale element, and at least 10 elements have been used to resolve one wavelength at the fine scale. In a composite medium undergoing wave propagation at a given frequency, the softer material phases require more refinement, since the wave speed is slower and the wavelength is shorter in the softer material phases.

5.5.2 Element matrices

Construction of the appropriate element matrices requires numerical integration of the element matrices that involves fine-scale basis functions only (Eq. 5.17b), coarse-scale basis functions only (Eq. 5.17a) and the coupling terms with both coarse- and fine-scale basis functions (Eq. 5.17c). The integration of Eq. 5.17b for an arbitrary fine-scale element, Ω_α^e, is standard and performed using the Gaussian quadrature. The integration procedure for Eqs. 5.17a and c is non-standard and described below for the stiffness matrix in Eq. 5.17a. The mass matrix in Eqs. 5.17a and c are integrated in a similar fashion and skipped for brevity.

The integration of a function $f(\mathbf{x})$ over the fine-scale element domain is approxi-

mated as:

$$\int_{\Omega_\alpha^e} f(\mathbf{x})\ d\Omega_\alpha^e = \int_{\square^f} f\left(\mathbf{x}(\boldsymbol{\xi}^f)\right) J^f(\boldsymbol{\xi}) d\square^f \approx \sum_{l=1}^{n_{\text{int}}^f} f(\boldsymbol{\xi}_l^f) J^f(\boldsymbol{\xi}_l^f) W_l \tag{5.33}$$

where, $J^f = \det(\partial \mathbf{x}/\partial \boldsymbol{\xi}^f)$, is the fine-scale element Jacobian determinant and $\square^f$ is the fine-scale parent domain. n_{int}^f is the number of integration points to accurately evaluate the integrand. $\boldsymbol{\xi}_l^f$ and W_l are respectively the coordinates and weight of the integration point, l. In order to resolve the material heterogeneity within coarse-scale elements, each coarse-scale element is partitioned using the fine-scale mesh. The element stiffness matrix in Eq. 5.17a is expressed as:

$$\mathbf{K}_\alpha^{cc} = \int_{\Omega_\alpha} (\mathbf{B}_\alpha^c)^T \mathbf{C}(\mathbf{x}) \mathbf{B}_\alpha^c\ d\Omega_\alpha = \sum_{e=1}^{n_{\text{ef}}} \int_{\Omega_\alpha^e} (\mathbf{B}_\alpha^c)^T \mathbf{C}_e \mathbf{B}_\alpha^c\ d\Omega_\alpha^e \tag{5.34}$$

The evaluation of Eq. 5.34 using Eq. 5.33 requires the interpolated values of the spectral coarse-scale basis functions and their derivatives at the integration points within the fine-scale parent domain. The interpolated values are not readily available for the coarse-scale shape functions since they are defined in the coarse-scale parent domain, $\square^c$. In order to obtain the coarse-scale shape functions and their derivatives at the integration points within the fine-scale parent domain, a two-scale mapping procedure is employed.

Figure 5.4 schematically illustrates this mapping process for a cubic coarse-scale element. Let $\mathcal{M}^f$ and $\mathcal{M}^c$ respectively denote the fine-scale and coarse-scale isoparametric mappings that map functions defined in the fine-scale and coarse-scale parent domains to the physical domain. For any quadrature point within the fine-scale parent domain, its corresponding location in the coarse-scale parent domain is obtained by first employing the fine-scale element isoparametric mapping to find its location in the physical domain, then applying the coarse-scale element inverse isoparametric

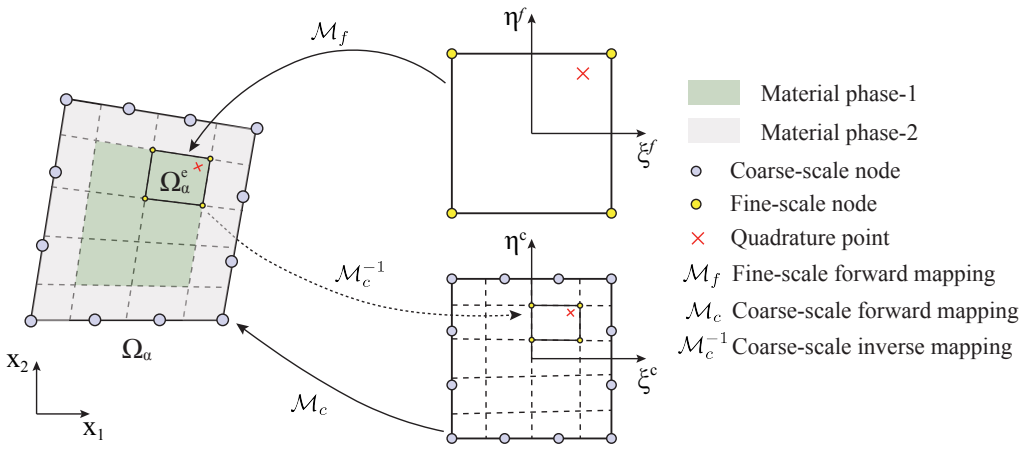

Figure 5.4: The two-scale element mapping relationship.

mapping:

$$\boldsymbol{\xi}^c = \mathcal{M}_c^{-1}(\mathcal{M}_f(\boldsymbol{\xi}^f)) \tag{5.35}$$

where $\mathcal{M}_c^{-1}$ denotes the inverse mapping. The procedure of inverse mapping was originally proposed in Refs. [77, 78] and is elaborated in Appendix H. The inverse mapping for spectral elements is developed based on the theory of differential geometry and has been previously used in the context of distortion measures for 2D 8-node serendipity element and 3D hexahedron elements [131].

Gauss-Legendre quadrature rule is employed for numerical integration. Since linear quadrilateral element is used for the fine-scale discretization, integration of Eq. 5.17b is exact with 2×2 integration points. The number of integration points required to exactly evaluate Eqs. 5.17a and c depends on the spectral order of the coarse-scale shape functions. For a p^{th} order coarse-scale spectral element, the minimum number of integration points for Eqs. 5.17a and c are $(p+1) \times (p+1)$ and $(\frac{p}{2}+1) \times (\frac{p}{2}+1)$, respectively. For each integration point within the fine-scale parent domain, its corresponding location in the coarse-scale parent domain is obtained by Eq. 5.35. The coarse-scale shape functions and their derivatives are evaluated at this mapped point. Equation 5.17d that provides the force term at the coarse scale is

integrated using the standard procedure over the coarse-scale element assuming that the boundary tractions remain unresolved at the fine scale.

5.5.3 Normal mode selection

The retained normal modes in the Craig-Bampton component mode synthesis and characteristic constraint mode reduction is typically selected by truncating the modes with higher natural frequencies [28, 22, 73]. The number of the normal modes is determined using a heuristic approach, based on ensuring that the desired accuracy is achieved with the resulting reduced order model. The appropriate number of material phase and interface normal modes used in RSVM are determined by gradually truncating the higher frequency modes, while evaluating the accuracy of the resulting transient response field compared to SVM. Parametric studies are provided in the next section for phononic crystals and acoustic metamaterials.

The general trend for the relation between wave frequency and the number of normal modes required for accuracy is that the required number of normal modes increases as the wave frequency increases. At low frequency, a few normal modes suffice to accurately predict wave propagation in the composite. As frequency increases, more modes need to be incorporated to retain accuracy, and the number of normal modes required for each material phase and interface varies depending on the constituent material properties.

Truncation of higher frequency modes is performed starting from the phase modes. Among all material phases, the normal modes of the stiff material phases are truncated first, since they have higher natural frequencies and typically only a few normal modes are important at the wave frequency of interest. The soft material phases require more normal modes to capture the deformation states during wave propagation, since their natural frequencies are lower than the stiff phases and more normal modes are excited. The interface normal modes of higher natural frequencies are truncated after the

phase modes are selected. Since the reduced interface normal modes directly control the static deformation of adjacent material phases, the number of interface normal modes is chosen to be relatively large to accurately capture the static deformation of adjacent material phases. This relation is also observed in Refs. [22, 52] in the context of model order reduction of homogeneous structures. In the current study, the number of interface normal modes is selected such that it is larger than the smallest number of selected normal modes of adjacent material phases.

This heuristic way of mode selection can be improved by establishing a relationship between the number of modes for material phases and interfaces with the microstructure morphology, material properties and wave frequency. Such an effort would require a systematic study of the mode selection strategy for different phononic crystal and acoustic metamaterial designs and is beyond the scope of this manuscript.

5.5.4 Time integration

The monolithic time integration with Newmark's family of methods is employed in solving the discretized system of equations. In particular, we use the implicit unconditionally stable "Average acceleration" method [58]. Explicit time integration with lumped mass matrix is typically more efficient for wave propagation in homogeneous materials. In contrast, explicit integration for wave propagation in complex composites does not guarantee numerical efficiency over implicit methods, due to the large stiffness contrast between the constituents and variations in mesh size [50]. The time step size in the implicit time integration approach adopted herein is controlled by accuracy considerations only. Sufficiently fine time step size is used in the numerical examples below to resolve the temporal oscillations at each material point.

In the implicit time integration, inversion of global coefficient matrix $\mathbf{M}_{SVM} + \beta\Delta t^2\mathbf{K}_{SVM}$ or $\mathbf{M}_{RSVM} + \beta\Delta t^2\mathbf{K}_{RSVM}$ (β is the algorithmic parameter in the Newmark's method and Δt is the time step size) is performed at every time step. Since

the coefficient matrix does not change during the time integration, it is decomposed only once before the time integration. A substitution is performed at each time step to update the solution.

5.6 Model Verification

In this section, we assess the capability of SVM and RSVM in modeling transient wave propagation in periodic composites. Numerical examples of wave propagation in phononic crystals (PC) and acoustic metamaterials (AMM) are presented. The proposed model is verified against direct numerical simulations (DNS) using the finite element method for a wide range of frequencies. The effects of coarse-scale element spectral order, material property contrast and the number of fine-scale normal modes on the accuracy and efficiency of the proposed model are discussed.

Figure 5.5(a) shows the two-dimensional unit cells of the acoustic metamaterial and phononic crystal that are used in the numerical examples. All examples are performed in plane strain condition. The acoustic metamaterial unit cell consists of three material phases: epoxy matrix, rubber coating and lead core. Under dynamic excitation, this material absorbs kinetic energy through locally resonant motion of the rubber coating and the lead core. This acoustic metamaterial design is originally proposed by Liu et al. [82] and has been analyzed using the computational homogenization framework [107]. In the current work, the dimensions of the unit cell, rubber coating and lead core, as well as the material properties of each phase are identical to those used in Ref. [82]. The phononic crystal unit cell is designed to have the same size as acoustic metamaterial unit cell. The steel inclusion has identical geometry as the lead core of the acoustic metamaterial unit cell. The material properties of epoxy used for the phononic crystal are identical to those used for the acoustic metamaterial. The material properties used in the simulations are summarized in Table 5.1.

Each acoustic metamaterial unit cell is discretized using 2,752 linear quadrilateral

Table 5.1: Material properties used in simulations.

Material	Young's modulus (GPa)	Poisson's ratio	Density (kg/m^3)
Epoxy	3.6	0.3679	$1,180$
Rubber	11.8×10^{-5}	0.4688	$1,300$
Lead	40.8	0.3698	$11,600$
Steel	210	0.3	$7,900$

elements and it contains 5,346 fine-scale DOFs. A fine mesh is used in the rubber coating phase with 10 elements in the radial direction in order to capture the resonant motion. The number of DOFs associated with the epoxy matrix, matrix-coating interface, rubber coating, coating-core interface and lead core are respectively 782, 256, 2,304, 256 and 1,748. The same mesh is used for the phononic crystal unit cell. The number of DOFs associated with epoxy matrix, matrix-inclusion interface and steel inclusion is respectively 3,342, 256 and 1,748. The proposed multiscale method leverage the periodic arrangement of unit cell discretization, therefore the element matrices are evaluated only for one unit cell and they are assembled block-by-block to construct the global matrices. In direct finite element simulations, each unit cell is discretized identically as the fine-scale discretization of the proposed multiscale method, i.e., 2,752 elements are used for each unit cell. Two composite structure configurations are investigated below, and transient sinusoidal velocity is applied for both cases, $\tilde{v}_x(t) = \sin(2\pi f t)$ m/s. The time step size is determined such that each loading cycle is resolved by 100 time steps: $\Delta t = 0.01/f$. It is verified that decreasing the time step size does not change the results significantly.

Both direct numerical simulations and the proposed model are excuted on a 4-core desktop with 2.3 GHz Intel processors and 16 GB of memory. In direct numerical simulations, the matrices of each element within each unit cell is computed and assembled. The time integration scheme and time step size are identical to the proposed multiscale method. For all simulations (DNS, SVM and RSVM), sparse matrix stor-

age is used for the global matrices and sparse matrix Cholesky decomposition is applied to the global coefficient matrix.

5.6.1 Spectral variational multiscale model

In this section, we investigate wave propagation in the phononic crystal and acoustic metamaterial as shown in Fig. 5.5 using SVM. The composite structure is composed of a row of n_{ec} microstructures. The right edge is fixed and the left edge is subject to sinusoidal velocity load, $\tilde{v}_x$. Periodic boundary condition is applied to the top and bottom edges. n_{ec} is 50 for acoustic metamaterial and 20 for phononic crystal examples. The simulation time is $T = 1/f$ s for acoustic metamaterial and $T = 1.5 \times 10^{-4}$ s for phononic crystal examples. The simulation setup for the acoustic metamaterial example is identical to that used in Ref. [107].

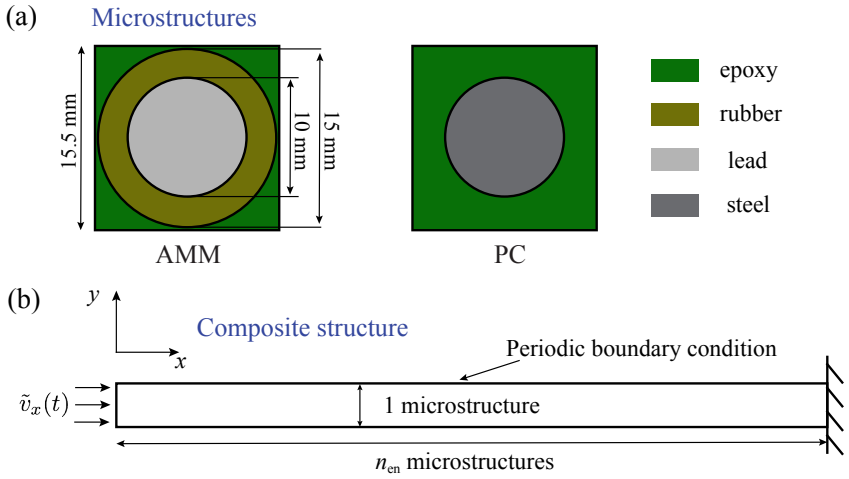

Figure 5.5: (a) Acoustic metamaterial and phononic crystal unit cells. (b) Composite structure and boundary conditions.

5.6.1.1 *Accuracy of SVM at various wave frequencies*

Figure 5.6 shows the velocity profiles along the bottom edge of the phononic crystal structure at time $t = T$ as predicted by SVM and the reference simulations. The vertical axis label v_x denotes the measured velocity in x direction. The responses

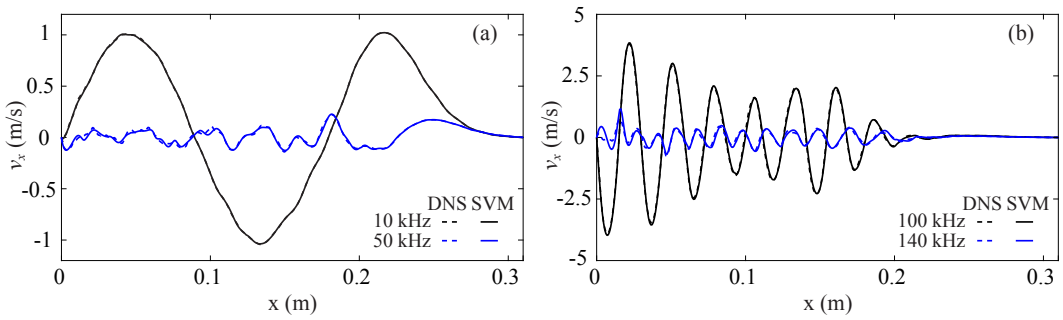

Figure 5.6: Velocity profiles as predicted by SVM and reference simulations along the bottom edge of the PC structure at $t = T$: (a) 10 and 50 kHz, (b) 100 and 140 kHz.

at the applied frequencies of 10, 50, 100, 140 kHz are shown. The frequencies are respectively in the first pass band, the first stop band, the second pass band and the second stop band. For all applied loading frequencies, SVM very accurately captures the wave field, including wave dispersion in the acoustic regime (10 kHz), wave attenuation in the stop bands (50 kHz and 140 kHz) and wave amplification in the optical regime (100 kHz). Within the second stop band ($f = 140$ kHz), the wavelength is shorter than the microstructure. Since the present approach does not rely on the assumption of separation of scales, the short wavelength response is accurately captured. The lateral velocity contours within the phononic crystal for the aforementioned four frequencies are shown in Fig. 5.7. In the first pass band, the wave propagates through both the matrix and inclusion with similar amplitudes. In contrast, the wave appears to propagate through the matrix only when its frequency is within the second pass band. While both the first and second stop bands feature a significant reduction in wave amplitude, the distribution of the kinetic energy density within the phases is different. The kinetic energy is concentrated in the inclusion within the first stop band, whereas it is concentrated in the matrix when the wave frequency is within the second stop band. SVM accurately predicts the wave patterns at all four frequency regimes.

Figure 5.8 shows the velocity profiles along the bottom edge of the structure when

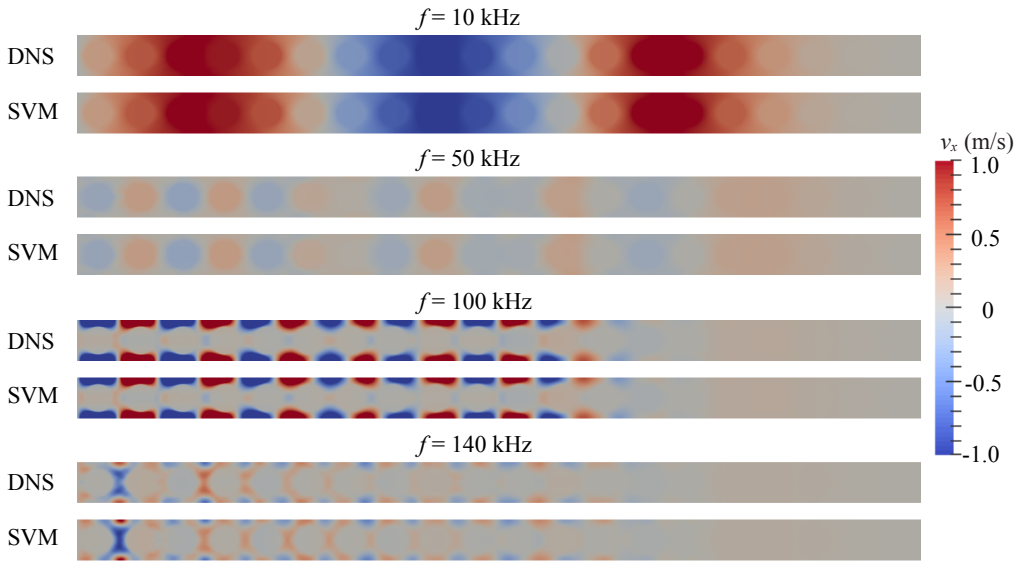

Figure 5.7: Velocity contours of the PC structure as predicted by SVM and reference simulations at $t = T$.

acoustic metamaterial unit cell is used. Compared to the phononic crystal, wave attenuation occurs at much lower frequencies in the acoustic metamaterial. At these frequencies, the wavelength is much larger than the size of microstructures. The mechanism of wave attenuation is the local resonance. As shown in Fig. 5.9, the local resonance is mainly due to the resonant motion of the lead core at $f = 500$ Hz. As the wave frequency increases, a transition from the core resonance to the coating resonance occurs ($f = 700$ Hz). At $f = 1,300$ Hz, the coating resonance becomes dominant. This observation is consistent with Ref. [82]. The local resonance becomes weaker as the wave frequency further increases ($f = 2,700$ Hz). The rubber-coated lead inclusion behaves more like a soft scatterer than a resonator and less kinetic energy is absorbed in the lead core and the rubber coating. As a consequence, the wave amplitude increases at high frequencies as shown in Fig. 5.8(b).

The transmitted wave amplitude spectra for the phononic crystal and acoustic metamaterial are shown in Fig. 5.10. The spectra are built based on wave amplitudes measured along the bottom edge of the composite structure (Fig. 5.5(b)) at $t = T$.

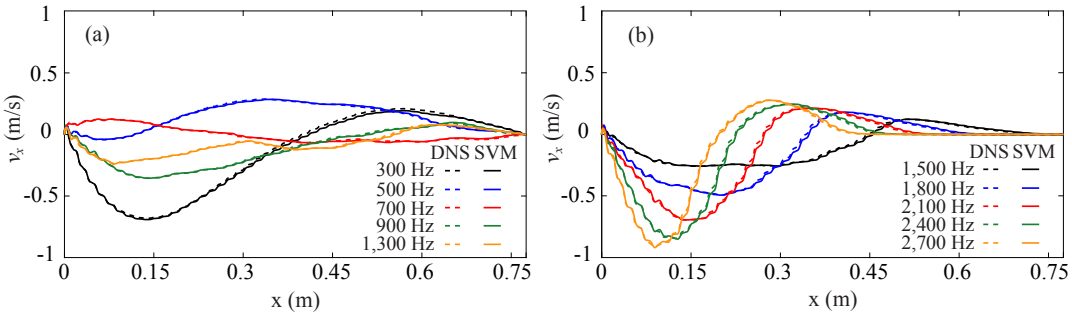

Figure 5.8: Velocity profiles as predicted by SVM and reference simulations along the bottom edge of the AMM structure at $t = T$: (a) 300, 500, 700, 900 and 1,300 Hz, (b) 1,500, 1,800, 2,100, 2,400 and 2,700 Hz.

Along the measurement line (i.e., the bottom edge), the maximum amplitude of the velocity field is employed for the acoustic metamaterial spectrum, whereas the maximum amplitude of the velocity field 5 unit cells away from the loaded end is used for the phononic crystal spectrum. The probed frequency range covers up to the third pass band for the phononic crystal and the pass band beyond the local resonance stop band for the acoustic metamaterial. For wave propagation in the phononic crystal (Fig. 5.10(a)), SVM accurately captures the transmission spectrum up to the second stop band. The accuracy decreases as the wave frequency increases. In the third pass band, the wavelength is much shorter than the length of the unit cell. The septic shape functions used at the coarse scale does not provide sufficient resolution to accurately capture the wave field, and the error is therefore larger in this regime. For wave propagation in the acoustic metamaterial (Fig. 5.10(b)), SVM is accurate in the entire range of probed frequencies.

5.6.1.2 *Parametric study for accuracy assessment*

A parametric study is performed to examine the accuracy of SVM as a function of the spectral order of the coarse-scale shape functions. Figure 5.11 compares the velocity field obtained using SVM with spectral coarse-scale elements of different orders with the reference simulations. The composite structure made of phononic crystal

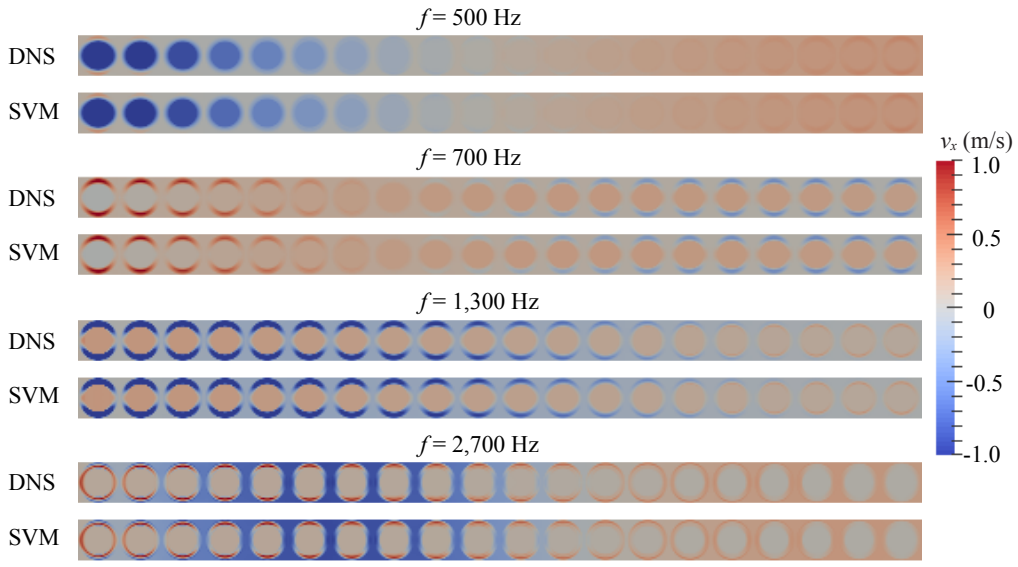

Figure 5.9: Velocity contours of the AMM structure as predicted by SVM and reference simulations at $t = T$.

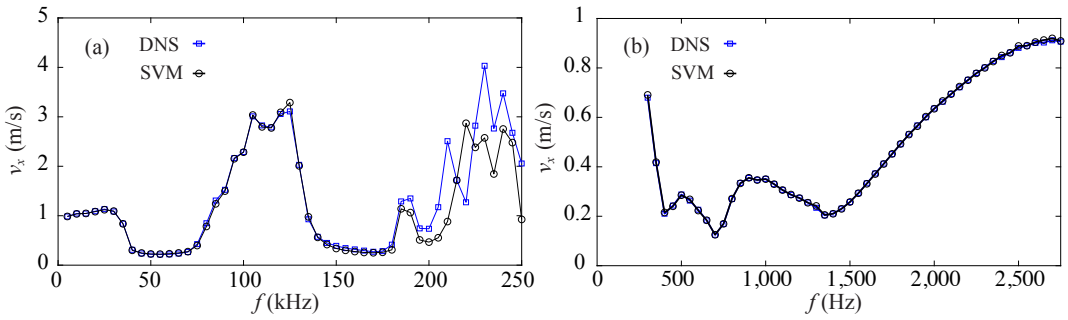

Figure 5.10: Transmitted wave amplitude spectra for (a) phononic crystal, and (b) acoustic metamaterial.

unit cells is considered in this study. The structure is excited at two frequencies. At $f = 10$ kHz, the wavelength is about 12 times of the size of a coarse-scale element. A slight numerical dispersion is observed when linear elements are used. Simulations with higher-order spectral elements agree very well with the reference simulations. At $f = 100$ kHz, linear coarse-scale element fails to capture the propagation of the high frequency wave, and a significant phase shift is observed for cubic element. Quintic and septic coarse-scale elements accurately capture the wave field. This observation confirms the importance of using higher-order spectral elements at the coarse scale

to capture the high frequency waves using the proposed multiscale approach.

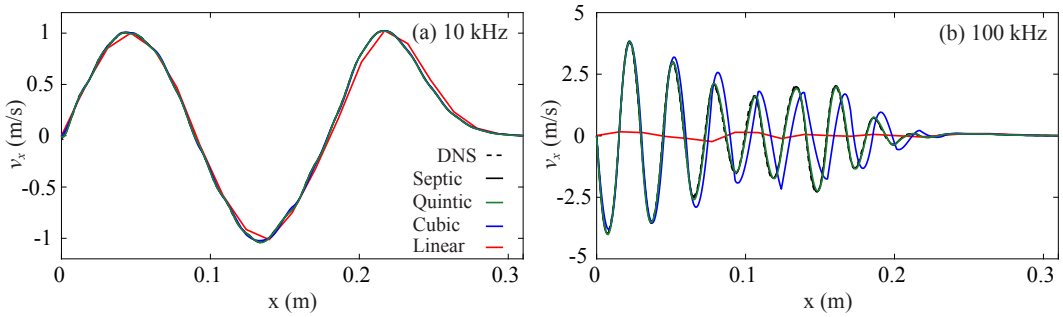

Figure 5.11: The effect of the spectral order of coarse-scale element on the accuracy of SVM for the phononic crystal structure simulation: (a) $f = 10$ kHz, and (b) $f = 100$ kHz.

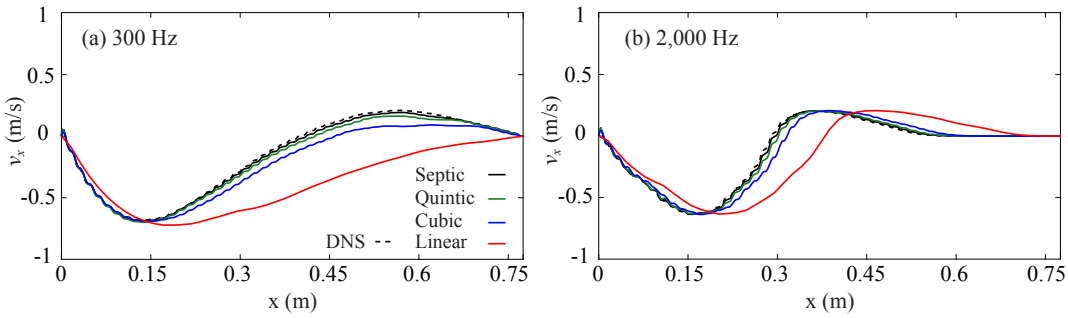

Figure 5.12: The effect of the spectral order of coarse-scale element on the accuracy of SVM for the acoustic metamaterial simulation: (a) $f = 300$ Hz, and (b) $f = 2,000$ Hz.

Similar to the observations for phononic crystals, the accuracy of SVM requires sufficiently high order spectral coarse-scale elements in modeling acoustic metamaterials. Figure 5.12 shows the velocity profiles predicted by SVM with varying orders of coarse-scale elements compared with the reference simulations under two loading frequencies. The figure demonstrates convergence to the reference simulations as the order of the coarse-scale elements is increased. At $f = 300$ Hz and $f = 2,000$ Hz, the wavelength within the epoxy matrix is much larger compared to the size of coarse-scale element. However, the velocity profiles predicted by models using linear and cubic elements show significant discrepancy. This is attributed to the observation that the

wavelength within the rubber coating is much shorter than it is in the epoxy matrix, and these short waves could not be accurately captured using low-order elements.

Next, we assess the accuracy of the proposed multiscale approach in capturing the transient dynamic response within the composite domain as a function of contrast in the constituent elastic moduli. Figure 5.13 shows the velocity profiles as predicted by SVM and reference simulations for various Young's modulus contrasts. The parametric study is performed by varying the Young's modulus ratio by 0.1 times ($r_E = 5.83$ for PC and $r_E = 3.5 \times 10^4$ for AMM) or 10 times ($r_E = 583$ for PC and $r_E = 3.5 \times 10^6$ for AMM) compared to the Young's modulus ratio used in previous examples ($r_E = 58.3$ for PC and $r_E = 3.5 \times 10^5$ for AMM). Varying Young's modulus contrast is achieved by varying the Young's modulus of epoxy for phononic crystals and rubber for acoustic metamaterials, while other material properties remain unchanged. In the phononic crystal case (Fig. 5.13(a)), a change in the Young's modulus of the matrix constituents results in a significant change in the length of the propagating wave when excited with a frequency of 20 kHz. Compared to $r_E = 58.3$, increasing the modulus ratio by decreasing the modulus of the matrix leads to shorter wavelength, resulting in strong destructive interactions and stop band formation when $r_E = 583$. When the acoustic metamaterial is excited at $f = 2,000$ Hz, the wavelength remains nearly unchanged when the modulus of the coating is decreased 10 times. Contrary to the strong attenuation observed in the phononic crystal, increasing the modulus contrast results in weaker attenuation. This is because the stop band shifts to lower frequencies due to the decreased coating modulus. The loading frequency is further away from the stop band. On the other hand, reducing the modulus contrast leads to stronger attenuation at $f = 2,000$ Hz, as the frequency range for the stop band is shifted to higher frequencies and $f = 2,000$ Hz falls in the stop band.

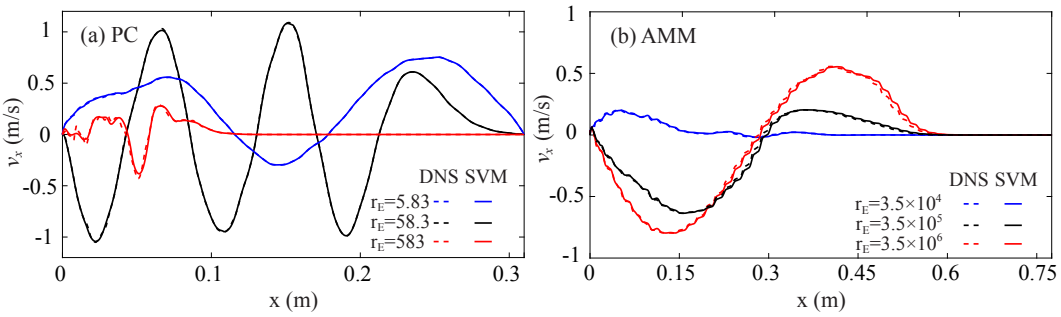

Figure 5.13: The effect of the material property contrast on the accuracy of SVM: (a) PC at $f = 20$ kHz, (b) AMM at $f = 2,000$ Hz.

5.6.2 Reduced order spectral variational multiscale model

In this section, we investigate the accuracy and numerical efficiency of the proposed reduced order spectral multiscale model for wave propagation in the phononic crystal and acoustic metamaterial. The geometry, boundary and loading conditions for the numerical example are identical to those described in Section 5.6.1. Septic coarse-scale basis functions are employed for RSVM.

Figure 5.14 shows the velocity profiles along the bottom edge of the phononic crystal evaluated using RSVM compared to reference simulations and UCRSVM. The selected number of normal modes for RSVM are 20, 40, 80, 160. The numbers of selected modes for matrix, matrix-inclusion interface and inclusion are respectively 5-10-5, 10-20-10, 20-40-20 and 40-80-40. UCRSVM incorporates the first 320 unit cell normal modes. In the first pass band (Fig. 5.14(a)), RSVM agrees well with the reference simulations using as few as 40 modes. Using fewer modes results in a slight phase shift. Even with significantly larger number of modes, UCRSVM does not capture the wave field as accurately. As the wave frequency increases, the wavelength becomes shorter, and additional modes are required to capture the wave field with similar accuracy. At $f = 50$ kHz (the first stop band), 40 modes are not sufficient to accurately capture the wave field. RSVM with 80 modes agrees well with the reference simulations. At higher frequencies, in the second pass band and second stop band,

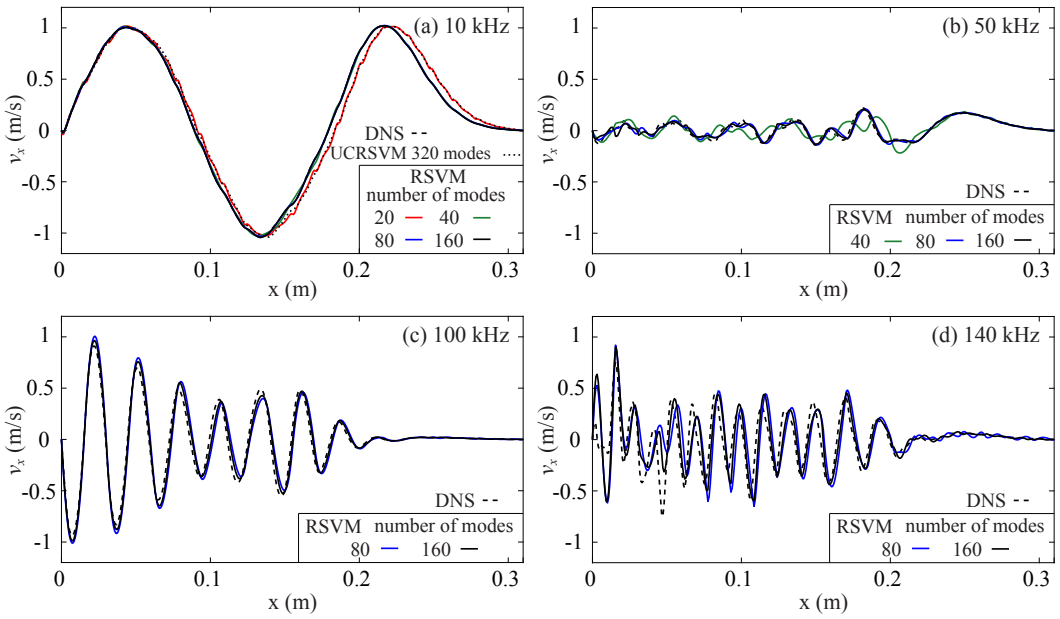

Figure 5.14: Velocity profiles as predicted by RSVM with different number of modes and reference simulations along the bottom edge of the PC structure at $t = T$: (a) 10 kHz, (b) 50 kHz, (c) 100 kHz, (d) 140 kHz.

while RSVM with 80 and 160 modes both predict the short wavelength responses, it is apparent that more retained modes result in better accuracy. The computational efficiency decreases as the number of modes increases. It is important to note that due to the high modulus contrast between epoxy and steel, the critical time step size for explicit time integration is approximately 3.6×10^{-9} s. Using vectorized explicit time integration for reference simulations in fact is more computationally expensive than the implicit time integration.

Figure 5.15 shows the velocity profiles as predicted using RSVM with 80, 160 and 320 modes, compared to reference simulations and UCRSVM for the acoustic metamaterial. The numbers of modes for the epoxy matrix, matrix-coating interface, rubber coating, coating-core interface and lead core are respectively 10-20-30-10-10, 20-40-70-20-10 and 20-100-150-40-10. The number of modes selected for the lead core is much smaller than the others since it undergoes primarily rigid body motion

due to high density and modulus compared to the soft rubber coating. The wave within the epoxy matrix can also be well captured with relatively small number of modes, because the wavelength within the epoxy matrix is much larger than the size of the unit cell in the frequency range of interest. The rubber coating requires significant number of modes to accurately capture its deformation since higher natural modes of vibration can be easily excited even at low frequency. As the number of selected modes increases, more modes are incorporated for the rubber coating and the adjacent interfaces, while the numbers of modes for the epoxy matrix and lead core remains unchanged. The number of modes for the rubber coating is approximately 1.5 and 3 to 4 times the numbers of modes for the coating-core interface and matrix-coating interface, respectively. The latter interface retains more modes because more modes are selected for the epoxy matrix than the lead core. Figure 5.15 shows that the accuracy of RSVM improves with increasing number of modes. Compared to the phononic crystal example, modeling acoustic metamaterial requires more modes to accurately predict the wave field. This is due to the more complex unit cell architecture with more phases and interfaces, and the presence of the soft rubber phase that requires a large number of modes to resolve its deformation. The UCRSVM approach exhibits significant discrepancy even with a large number of modes (800). This implies that the unit cell normal modes with homogeneous boundaries are not proper basis for the fine-scale problem for the proposed multiscale formulation, and justifies the phase mode synthesis strategy.

The computational efficiency of the example in Fig. 5.15(a) is shown in Table 5.2. the normalized computation time indicates the computation time of RSVM divided by the computation time of the reference simulation during the preprocessing and time integration. The preprocessing step includes element matrices evaluation and global matrices assembly for the reference simulation, and element matrices evaluation at both scales, fine-scale model basis reduction and global matrices assembly for RSVM.

Significant computational efficiency is achieved at both preprocessing and time integration steps. As more modes are incorporated, the computation time remains nearly unchanged in preprocessing, and increases in time integration. For preprocessing, the efficiency is mainly attributed to that the coarse- and fine-scale element matrices are evaluated only once for one unit cell and the block-by-block global matrices assembly. The computational efficiency of RSVM in time integration is achieved due to the reduced global matrices size compared to reference simulations.

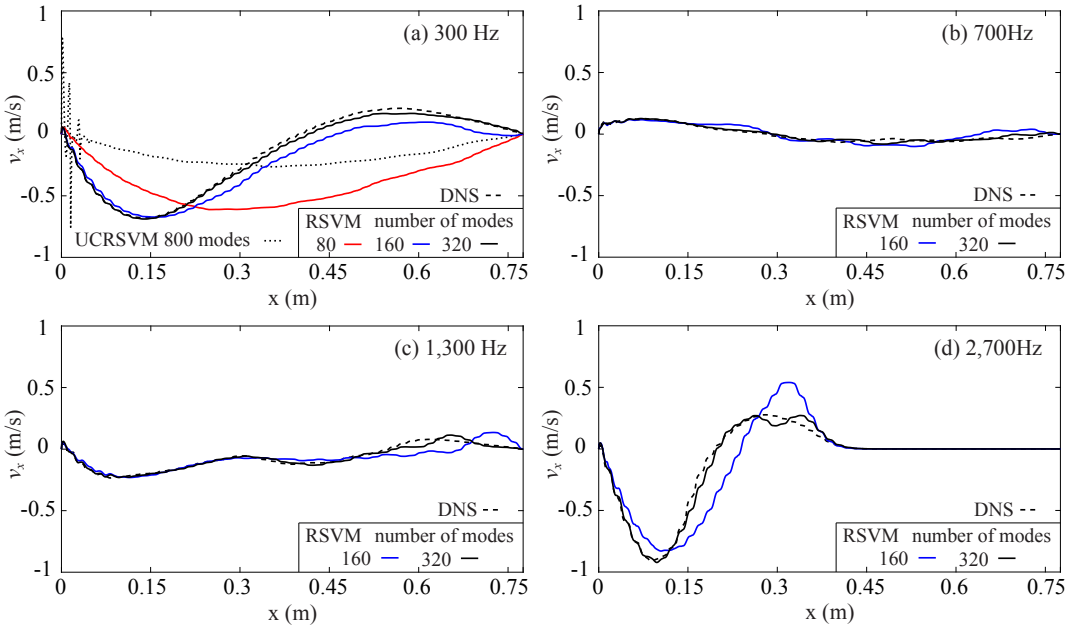

Figure 5.15: Velocity profiles as predicted by RSVM with different number of modes and reference simulations along the bottom edge of the AMM structure at $t = T$: (a) 300 Hz, (b) 700 Hz, (c) 1,300 Hz, (d) 2,700 Hz

Table 5.2: Normalized computation time of RSVM for the AMM simulation.

Number of modes	Preprocessing	Time integration
80	0.343	0.034
160	0.345	0.082
320	0.349	0.185

5.6.3 Elastic waveguide simulation using RSVM

In this section, we investigate the transient wave propagation in an elastic waveguide shown in Fig. 5.16. The length and height of the structure are 15 unit cells and 12 unit cells, respectively. The waveguide is constructed as the periodic arrangement of the phononic crystal unit cell (Fig. 5.5), except along an elbow path made of homogeneous epoxy. This design has been previously investigated experimentally and numerically in the context of acoustic wave guiding [72] in water using periodic array of steel cylinders. The right boundary of the waveguide is fixed and sinusoidal velocity is applied along the left boundary. The total simulation time is $T = 4 \times 10^{-4}$ s.

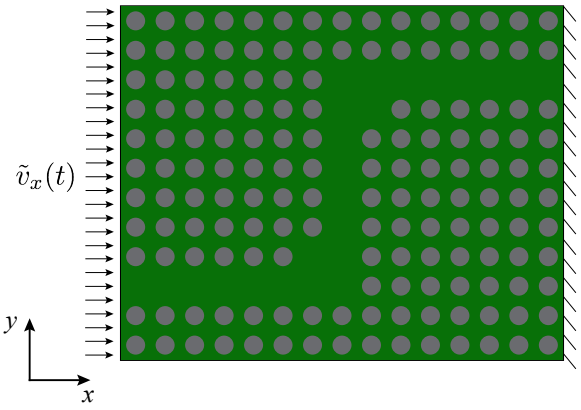

Figure 5.16: The geometry and boundary conditions of the elastic waveguide simulation.

The discretization for the phononic crystal unit cell is identical to the previous sections for both DNS and RSVM. In reference simulations, 495,360 elements are used to discretize the domain. In multiscale simulations, the elements within the homogeneous path region are not enriched with the fine-scale problem, but are discretized using the septic coarse-scale shape functions. 80 modes are incorporated as the fine-scale basis and the number of modes for epoxy matrix, interface and steel inclusion are respectively 20, 40 and 20. The total numbers of DOFs for DNS and RSVM are respectively 991,439 and 21,605.

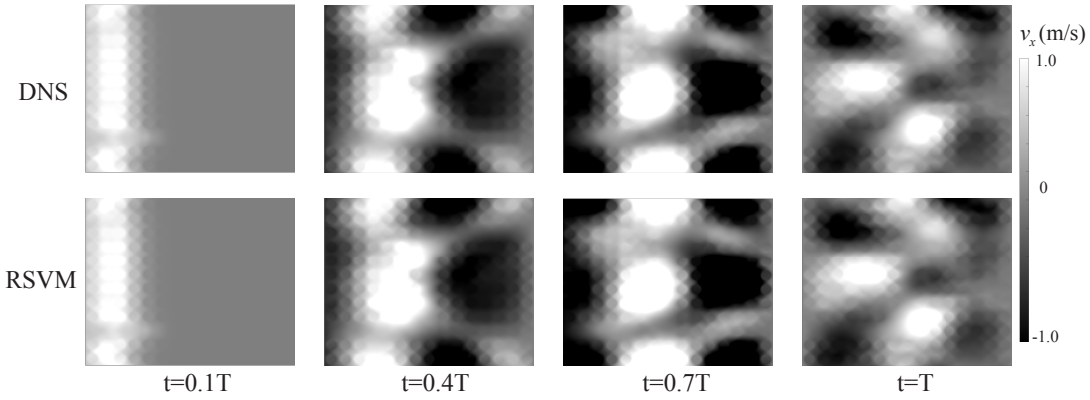

Figure 5.17: Velocity contours of wave propagation in elastic waveguide, $f = 10$ kHz.

Figure 5.17 shows the velocity contours of wave propagation in the composite structure. Sinusoidal velocity at a frequency of $f = 10$ kHz is applied to the left boundary and the snapshots are taken at 4 separate time instances. The elastic wave travels through the entire composite structure and forms a complex wave pattern due to reflections at the structural boundaries. The dispersion induced by the microstructures is relatively minor, because the macroscopic wavelength is significantly larger than the size of the microstructure. When the wave frequency is increased to 60 kHz, the frequency falls within the first stop band (Fig. 5.10). At this frequency, the wavelength is approximately twice of the unit cell size, resulting in significant destructive interactions within the composite structure. Because of the stop band formation, the elastic wave is only permitted to propagate within the homogeneous guide, as shown in Fig. 5.18. The wave amplitude outside of the guide is strongly attenuated and is much lower than it is within the guide. At both of these frequencies, it is observed that RSVM with 80 modes accurately captures the overall wave field.

The computation time for DNS and RSVM in preprocessing and time integration is shown in Table 5.3. Similar to the acoustic metamaterial case shown in Table 5.2, RSVM is significantly faster than DNS in both preprocessing and time integration. In the present numerical example, since a relatively short period of time is simulated,

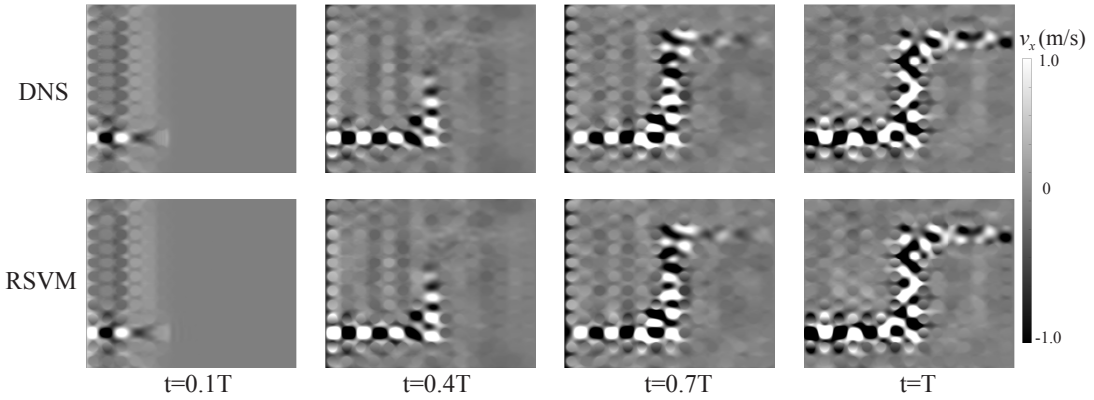

Figure 5.18: Velocity contours of wave propagation in elastic waveguide, $f = 60$ kHz.

the time integration is less computationally expensive than the preprocessing. The computation time of time integration linearly increases as longer total simulation time is investigated.

Table 5.3: Computation time in the phononic crystal waveguide simulation.

Simulation model	Preprocessing	Time integration
DNS	9.5 hours	765.7 seconds
RSVM	0.5 hours	4.7 seconds

5.7 Conclusion

This manuscript presented a spectral variational multiscale model for transient wave propagation in phononic crystals and acoustic metamaterials. The proposed model is developed based on the variational multiscale enrichment method, employing the additive split of the solution field and numerically evaluating the coupled system of equations at two scales. Spectral elements are employed at the coarse scale to accurately resolve the wave field. A material-phase-based model order reduction method is proposed for efficient evaluation of the fine-scale numerical solution. Based on the Craig-Bampton component mode synthesis and the characteristic constraint mode reduction, the proposed approach distinguishes material phases and interfaces

at the fine scale and perform modal reduction individually.

A novel contribution of the proposed model is that it does not introduce drastic accuracy reduction in composites with high material property contrast and it does not employ the scale separation principle. This permits the proposed model to accurately capture wave propagation in both phononic crystals and acoustic metamaterials over a wide frequency range. The accuracy and computational efficiency of the spectral variational multiscale model is demonstrated for both phononic crystals and acoustic metamaterials. It is shown that the wave field in the phononic crystal is accurately predicted by the proposed model up to the second stop band, where the wavelength is shorter than the microstructure. The proposed model well captures the local resonance and wave attenuation in acoustic metamaterials. Computational cost reduction is achieved in both preprocessing and time integration for the reduced order model. The computational efficiency decreases as the number of incorporated modes increases. It is observed that more modes are required to accurately capture the wave field in acoustic metamaterials than phononic crystals, due to the increased number of modes to resolve the soft material phase and adjacent interfaces.

In the near future, the current model will be extended to 3D for more general applications in design and analysis of phononic crystals and acoustic metamaterials. Furthermore, a broader range of material constitutive behaviors need to be investigated, including the viscoelasticity and thermal effect [57], in order to explore undiscovered design space for exotic dynamic properties of architectured composites. From the computational perspective, the use of other fine-scale boundary conditions (e.g., periodic boundary condition) and modal basis functions will be investigated for improved accuracy and computational efficiency.

Chapter 6

CONCLUSION AND FUTURE WORK

6.1 Conclusion

This dissertation has focused on advancing the multiscale computational methods for wave propagation in periodic composites including phononic crystals and acoustic metamaterials. In particular, it is devoted to modeling wave dispersion and attenuation associated with the band gap phenomenon within these architectured materials. Multiscale methods in two categories are proposed: (1) scale separation assumption dependent and (2) scale separation assumption independent. The key contributions of this dissertation are concluded as follows:

1. *Development of a spatial-temporal nonlocal homogenization model for transient wave propagation in periodic elastic and viscoelastic composites.*

   A spatial-temporal nonlocal homogenization model has been developed for transient wave propagation in periodic elastic and viscoelastic composites. The homogenization model is derived by employing high order asymptotic expansions, extending the applicability of asymptotic homogenization to the short wavelength regime. A gradient-type spatial-temporal nonlocal macroscopic governing equation is consistently derived from the momentum balance equations of successive asymptotic orders. All the model parameters are uniquely computed from the microscale equilibrium equations that are independent of the macroscale displacement, therefore, computed as an off-line process. The proposed model is formally similar to the gradient elasticity models. It is unique in that it applies to wave propagation in two-dimensional composites without the model parameter tuning. A nonlocal effective medium model, in the form of second order PDE with nonlocal effective moduli tensor, is developed based on

the nonlocal homogenization model. The effective medium model retains the nonlocal features of the homogenization model in high symmetry directions of the first Brillouin zone, while suppressing the non-physical wavenumbers that result in instability.

The proposed model is verified for wave propagation in several composite configurations including: 1D wave in elastic and viscoelastic layered composites, anti-plane shear wave in 2D elastic and viscoelastic composites, and in-plane wave in 2D elastic composite. It is shown that the nonlocal homogenization model captures the acoustic branch, the stop band and the first optical branch of the dispersion curves in the direction of high symmetry points of the first Brillouin zone. The accuracy decreases as the frequency increases beyond the acoustic regime and as the material property contrast increases. The nonlocal effective medium model matches the dispersion behavior of the spatial-temporal nonlocal homogenization model in the high symmetry directions and approximates it in other directions with reasonable accuracy, and it accurately predicts uni-directional wave propagation and the overall wave dispersion and attenuation behavior of wave propagation in a simple 2D phononic crystal waveguide.

2. *Development of a spectral variational multiscale model for transient wave propagation in phononic crystals and acoustic metamaterials.*

   The proposed model employs the additive split of the solution field and numerically evaluates the coupled system of equations at two scales. Spectral elements are employed at the coarse scale to accurately resolve the wave field. A material phase based model order reduction method is proposed for efficient evaluation of the fine-scale numerical solution. Based on the Craig-Bampton component mode synthesis and the characteristic constraint mode reduction, the proposed approach distinguishes material phases and interfaces at the fine-scale and perform modal reduction individually. An important feature of the pro-

posed model is that it does not make assumptions on the relative size between macroscopic wave and microstructures, and the material property contrast of the constituents. This permits the proposed model to accurately capture wave propagation in both phononic crystals and acoustic metamaterials over a wide frequency range.

The accuracy and computational efficiency of the spectral variational multiscale model is demonstrated for both phononic crystals and acoustic metamaterials. It is shown that the wave field in the phononic crystal is accurately predicted even when the wavelength is shorter than the microstructure. The proposed model well captures the local resonance and wave attenuation in acoustic metamaterials. Computational cost reduction is achieved in both preprocessing and time integration using the reduced order spectral variational multiscale model. The computational efficiency decreases as the number of incorporated modes increases. It is demonstrated that the proposed model accurately predicts the wave dispersion and attenuation within a 2D phononic crystal waveguide with significant computational efficiency.

6.2 Recommendations for the Future Work

From the method development point of view, the following directions are recommended:

1. The multiscale models developed in this dissertation are verified in two-dimensions. It is desirable to extend the current methods to three-dimensions in order for these models to be applied in more general settings.
2. The current development is limited to elastic and viscoelastic composites. Development of computationally efficient multiscale models in the nonlinear regime, incorporating material nonlinearity and geometric nonlinearity, is an impor-

tant step towards exploring the undiscovered design space for exotic dynamic properties of architectured composites.

From the method application point of view, the following directions are recommended:

1. Applying the proposed multiscale models to facilitate the design and analysis of novel applications, such as seismic wave mitigation [19, 25], acoustic superlens [79, 71] and topological insulators [97], will have an profound impact on advancing the respective fields. Design optimization can be achieved in a more efficient manner by employing these multiscale models.

Appendix A

Analytical expression for $\hat{E}_k$

$$
\begin{aligned}
\hat{E}_k = \frac{\alpha^2(1-\alpha)^2(E_1\rho_1 - E_2\rho_2)^2 E_0 \hat{l}^6}{60480\rho_0^6(E_1(1-\alpha)+\alpha E_2)^6}\Bigg\{\Bigg[(1-\alpha)^4 E_1^4\Big(\\
32(1-\alpha)^4\rho_2^4 - 160\alpha(1-\alpha)^3\rho_1\rho_2^3 + 192\alpha^2(1-\alpha)^2\rho_1^2\rho_2^2 +\\
108\alpha^3(1-\alpha)\rho_1^3\rho_2 + 3\alpha^4\rho_1^4\Big)\Bigg] +\\
\Bigg[\alpha(1-\alpha)^3 E_1^3 E_2\Big(-160(1-\alpha)^4\rho_2^4 + 944\alpha(1-\alpha)^3\rho_1\rho_2^3 -\\
1580\alpha^2(1-\alpha)^2\rho_1^2\rho_2^2 - 12\alpha^3(1-\alpha)\rho_1^3\rho_2 + 108\alpha^4\rho_1^4\Big)\Bigg] +\\
\Bigg[\alpha^2(1-\alpha)^2 E_1^2 E_2^2\Big(192(1-\alpha)^4\rho_2^4 - 1580\alpha(1-\alpha)^3\rho_1\rho_2^3 +\\
3826\alpha^2(1-\alpha)^2\rho_1^2\rho_2^2 - 1580\alpha^3(1-\alpha)\rho_1^3\rho_2 + 192\alpha^4\rho_1^4\Big)\Bigg] +\\
\Bigg[\alpha^3(1-\alpha)E_1 E_2^3\Big(-160\alpha^4\rho_1^4 + 944\alpha^3(1-\alpha)\rho_1^3\rho_2 -\\
1580\alpha^2(1-\alpha)^2\rho_1^2\rho_2^2 - 12\alpha(1-\alpha)^3\rho_1\rho_2^3 + 108(1-\alpha)^4\rho_2^4\Big)\Bigg] +\\
\Bigg[\alpha^4 E_2^4\Big(32\alpha^4\rho_1^4 - 160\alpha^3(1-\alpha)\rho_1^3\rho_2 + 192\alpha^2(1-\alpha)^2\rho_1^2\rho_2^2 +\\
108\alpha(1-\alpha)^3\rho_1\rho_2^3 + 3(1-\alpha)^4\rho_2^4\Big)\Bigg]\Bigg\}
\end{aligned}
\tag{A.1}
$$

Appendix B

Momentum balance equations at $O(\zeta^4)$ and $O(\zeta^2)$

The derivation of macroscale momentum balance equations at $O(\zeta^4)$ and $O(\zeta^2)$ are provided in this appendix.

Equation 3.31e is rewritten as:

$$\begin{aligned}
&\rho_0 s^2 U^{(4)}(\mathbf{x},s) - D^{(0)}_{kl}(s)U^{(4)}_{,kl} = \left(D^{(2)}_{(klmn)}(s) - \nu(s)A^{(1)}(s)D^{(0)}_{kl}(s)D^{(0)}_{mn}(s)\right)U^{(2)}_{,klmn} \\
&+ \nu(s)A^{(1)}(s)\rho_0 s^2 D^{(0)}_{kl}(s)U^{(2)}_{,kl} + \nu(s)A^{(1)}(s)D^{(0)}_{kl}(s)D^{(0)}_{mn}(s)U^{(2)}_{,klmn} \\
&- \nu(s)A^{(1)}(s)\rho_0 s^2 D^{(0)}_{kl}(s)U^{(2)}_{,kl} + D^{(4)}_{(klmnpq)}(s)U^{(0)}_{,klmnpq}
\end{aligned} \tag{B.1}$$

Multiplying Eq. 3.31c with $\rho_0 s^2$ and considering Eq. 3.31a:

$$\rho_0^2 s^4 U^{(2)}(\mathbf{x},s) - \rho_0 s^2 D^{(0)}_{kl}(s)U^{(2)}_{,kl} = \rho_0 s^2 D^{(2)}_{(klmn)}(s)U^{(0)}_{,klmn} = D^{(2)}_{(klmn)}(s)D^{(0)}_{pq}(s)U^{(0)}_{,klmnpq} \tag{B.2}$$

we recall Eq. 3.37 and plug Eq. B.2 into Eq. B.1:

$$\begin{aligned}
&\rho_0 s^2 U^{(4)}(\mathbf{x},s) - D^{(0)}_{kl}(s)U^{(4)}_{,kl} = \left(D^{(2)}_{(klmn)}(s) - \nu(s)A^{(1)}(s)D^{(0)}_{kl}(s)D^{(0)}_{mn}(s)\right)U^{(2)}_{,klmn} \\
&+ \nu(s)A^{(1)}(s)\rho_0 s^2 D^{(0)}_{kl}(s)U^{(2)}_{,kl} + A^{(2)}(s)\left(\rho_0^2 s^4 U^{(2)} - \rho_0 s^2 D^{(0)}_{kl}(s)U^{(2)}_{,kl}\right) \\
&- \nu(s)A^{(1)}(s)\rho_0 s^2 D^{(0)}_{kl}(s)U^{(2)}_{,kl} + \nu(s)A^{(1)}(s)D^{(0)}_{kl}(s)D^{(0)}_{mn}(s)U^{(2)}_{,klmn}
\end{aligned} \tag{B.3}$$

Taking two spatial derivatives of Eq. 3.31c and substituting the resulting expression

for the last two terms of Eq. B.3 and collecting terms:

$$\rho_0 s^2 U^{(4)}(\mathbf{x},s) - D^{(0)}_{kl}(s)U^{(4)}_{,kl} = \left(D^{(2)}_{(klmn)}(s) - \nu(s)A^{(1)}(s)D^{(0)}_{kl}(s)D^{(0)}_{mn}(s)\right)U^{(2)}_{,klmn}$$
$$+ \left(\nu(s)A^{(1)}(s) - A^{(2)}(s)\right)\rho_0 s^2 D^{(0)}_{kl}(s)U^{(2)}_{,kl} + A^{(2)}(s)\rho_0^2 s^4 U^{(2)}$$
$$- \nu(s)A^{(1)}(s)D^{(0)}_{kl}D^{(2)}_{mnpq}(s)U^{(0)}_{,klmnpq} \tag{B.4}$$

Substituting Eq. 3.31a into the last term of Eq. B.4 and plugging Eq. 3.31c into the resulting expression, we obtain the momentum balance equation at $O(\zeta^4)$:

$$\rho_0 s^2 U^{(4)}(\mathbf{x},s) - D^{(0)}_{kl}(s)U^{(4)}_{,kl} = \left(D^{(2)}_{(klmn)}(s) - \nu(s)A^{(1)}(s)D^{(0)}_{kl}(s)D^{(0)}_{mn}(s)\right)U^{(2)}_{,klmn}$$
$$+ \left(2\nu(s)A^{(1)}(s) - A^{(2)}(s)\right)\rho_0 s^2 D^{(0)}_{kl}(s)U^{(2)}_{,kl} + \left(A^{(2)}(s) - \nu(s)A^{(1)}(s)\right)\rho_0^2 s^4 U^{(2)} \tag{B.5}$$

In view of Eq. 3.31a, the momentum balance equation at $O(\zeta^2)$ is obtained by rewriting Eq. 3.31c:

$$\rho_0 s^2 U^{(2)}(\mathbf{x},s) - D^{(0)}_{kl}(s)U^{(2)}_{,kl} = \left(D^{(2)}_{(klmn)}(s) - \nu(s)A^{(1)}(s)D^{(0)}_{kl}(s)D^{(0)}_{mn}(s)\right)U^{(0)}_{,klmn}$$
$$+ \left(2\nu(s)A^{(1)}(s) - A^{(2)}(s)\right)\rho_0 s^2 D^{(0)}_{kl}(s)U^{(0)}_{,kl} + \left(A^{(2)}(s) - \nu(s)A^{(1)}(s)\right)\rho_0^2 s^4 U^{(0)} \tag{B.6}$$

Appendix C

Laplace domain stability analysis for infinitely long wave

The stability of Eq. 3.43 is analyzed by moving the nonlocal terms to the left hand side and applying a spatial-harmonic-time-impulse load at the right hand side, which is expressed as $Fe^{\mathrm{i}(k_1x_1+k_2x_2)}$ in the Laplace domain. Assuming the spatial response is harmonic, $U(s) = U_0(s)e^{\mathrm{i}(k_1x_1+k_2x_2)}$, substituting the impulse load expression and spatial-harmonic displacement into Eq. 3.43 and using the polar representation of the wave vector, the transfer function is written as:

$$T(s) = \frac{U_0(s)}{F} = \frac{-1}{A(s,\theta)k^4 + B(s,\theta)k^2 + C(s,\theta)} \tag{C.1}$$

where, $A(s,\theta)$, $B(s,\theta)$, $C(s,\theta)$ are given in Eq. 3.46a-c. Taking the infinitely long wave limit, i.e., $k \to 0$, the poles of the rational transfer function are found by $C(s,\theta) = 0$:

$$s^{\{1,2\}} = 0, \quad s^{\{3,4\}} = \pm\sqrt{\frac{1}{\alpha^{(3)}(s)\rho_0}} \tag{C.2}$$

In the complex plane, any pole of the transfer function that has a positive real part results in exponentially unstable response [49]. Therefore, in order to avoid exponential instability, $s^{\{3,4\}}$ must have real part to be zero. According to the rule of computing square root of complex number [95], Eq. 3.50b has to be satisfied.

Appendix D

Expressions for $G^{(n-1)e}_{(\cdot)}(\mathbf{y},s)$ and $Q^{(n-1)e}_{(\cdot)}(\mathbf{y},s)$

The expression for $G^{(1)e}_{klm}(\mathbf{y},s)$ is:

$$G^{(1)e}_{klm}(\mathbf{y},s) = G(\mathbf{y},s)\left[\sum_{B=1}^{M_e} N^{[B]}(\mathbf{y})H^{(1)[B]}_{k}(s)\delta_{lm} + \sum_{B=1}^{M_e} B^{[B]}_{m}(\mathbf{y})H^{(2)[B]}_{(kl)}(s)\right] \tag{D.1}$$

According to Eq. 3.21, the symmetric part is computed as summation of components of all permutations divided by the total number of permutations:

$$\begin{aligned} G^{(1)e}_{(klm)}(\mathbf{y},s) =& \frac{1}{6}\Big(G^{(1)e}_{klm}(\mathbf{y},s) + G^{(1)e}_{lkm}(\mathbf{y},s) + G^{(1)e}_{lmk}(\mathbf{y},s) \\ &+ G^{(1)e}_{mlk}(\mathbf{y},s) + G^{(1)e}_{kml}(\mathbf{y},s) + G^{(1)e}_{mkl}(\mathbf{y},s)\Big) \end{aligned} \tag{D.2}$$

The expression for $Q^{(1)e}_{klm}(\mathbf{y},s)$ is:

$$Q^{(1)e}_{klm}(\mathbf{y},s) = \sum_{B=1}^{M_e} N^{[B]}(\mathbf{y})H^{(1)e[B]}_{k}(s)D^{(0)}_{(lm)}(s) \tag{D.3}$$

The symmetric part of $Q^{(1)e}_{klm}(\mathbf{y},s)$ is computed by replacing $G^{(1)e}_{(\cdot)}(\mathbf{y},s)$ with $Q^{(1)e}_{(\cdot)}(\mathbf{y},s)$ in Eq. D.2. We provide the expressions for $G^{(n-1)e}_{(\cdot)}(\mathbf{y},s)$ and $Q^{(n-1)e}_{(\cdot)}(\mathbf{y},s)$ in what follows, and the symmetric part is computed by Eq. 3.21 .

$$G^{(2)e}_{klmn}(\mathbf{y},s) = G(\mathbf{y},s)\left[\sum_{B=1}^{M_e} N^{[B]}(\mathbf{y})H^{(2)[B]}_{(kl)}(s)\delta_{mn} + \sum_{B=1}^{M_e} B^{[B]}_{n}(\mathbf{y})H^{(3)[B]}_{(klm)}(s)\right] \tag{D.4}$$

$$Q^{(2)e}_{klmn}(\mathbf{y},s) = \sum_{B=1}^{M_e} N^{[B]}(\mathbf{y})H^{(2)e[B]}_{(kl)}(s)D^{(0)}_{(mn)}(s) + D^{(2)}_{(klmn)}(s) \tag{D.5}$$

$$G^{(3)e}_{klmnp}(\mathbf{y},s) = G(\mathbf{y},s)\left[\sum_{B=1}^{M_e} N^{[B]}(\mathbf{y})H^{(3)[B]}_{(klm)}(s)\delta_{np} + \sum_{B=1}^{M_e} B^{[B]}_{p}(\mathbf{y})H^{(4)[B]}_{(klmn)}(s)\right] \tag{D.6}$$

$$Q^{(3)e}_{klmnp}(\mathbf{y},s)=\sum_{B=1}^{M_e}N^{[B]}(\mathbf{y})H^{(3)e[B]}_{(klm)}(s)D^{(0)}_{(nq)}(s)+\sum_{B=1}^{M_e}N^{[B]}(\mathbf{y})H^{(1)e[B]}_{k}(s)D^{(2)}_{(lmnp)}(s) \tag{D.7}$$

$$G^{(4)e}_{klmnpq}(\mathbf{y},s)=G(\mathbf{y},s)\left[\sum_{B=1}^{M_e}N^{[B]}(\mathbf{y})H^{(4)[B]}_{(klmn)}(s)\delta_{pq}+\sum_{B=1}^{M_e}B^{[B]}_{q}(\mathbf{y})H^{(5)[B]}_{(klmnp)}(s)\right] \tag{D.8}$$

$$Q^{(4)e}_{klmnpq}(\mathbf{y},s)=\sum_{B=1}^{M_e}N^{[B]}(\mathbf{y})H^{(4)e[B]}_{(klmn)}(s)D^{(0)}_{(pq)}(s)+ \sum_{B=1}^{M_e}N^{[B]}(\mathbf{y})H^{(2)e[B]}_{(kl)}(s)D^{(2)}_{(mnpq)}(s)+D^{(4)}_{(klmnpq)}(s) \tag{D.9}$$

$$G^{(5)e}_{klmnpqr}(\mathbf{y},s)=G(\mathbf{y},s)\left[\sum_{B=1}^{M_e}N^{[B]}(\mathbf{y})H^{(5)[B]}_{(klmnp)}(s)\delta_{qr}+\sum_{B=1}^{M_e}B^{[B]}_{r}(\mathbf{y})H^{(6)[B]}_{(klmnpq)}(s)\right] \tag{D.10}$$

$$Q^{(5)e}_{klmnpqr}(\mathbf{y},s)=\sum_{B=1}^{M_e}N^{[B]}(\mathbf{y})H^{(5)e[B]}_{(klmnp)}(s)D^{(0)}_{(qr)}(s)+ \sum_{B=1}^{M_e}N^{[B]}(\mathbf{y})H^{(3)e[B]}_{(klm)}(s)D^{(2)}_{(npqr)}(s)+\sum_{B=1}^{M_e}N^{[B]}(\mathbf{y})H^{(1)e[B]}_{k}(s)D^{(4)}_{(lmnpqr)}(s) \tag{D.11}$$

Appendix E

Asymptotic analysis procedure

The derivation of equilibrium equations for microscale influence functions and macroscale balance equations are provided in this appendix.

Substituting Eqs. 5.2, 5.3, 4.4 into Eq. 5.1, the balance equations at each order is obtained:

$$O(\zeta^{-1}): \quad \boldsymbol{\nabla}_y.\boldsymbol{\sigma}^{(0)}(\mathbf{x},\mathbf{y},t) = 0 \tag{E.1a}$$

$$O(\zeta^{\alpha}): \quad \boldsymbol{\nabla}_x.\boldsymbol{\sigma}^{(\alpha)}(\mathbf{x},\mathbf{y},t) + \boldsymbol{\nabla}_y.\boldsymbol{\sigma}^{(\alpha+1)}(\mathbf{x},\mathbf{y},t) = \rho(\mathbf{y})\ddot{\mathbf{u}}^{(\alpha)}(\mathbf{x},\mathbf{y},t) \tag{E.1b}$$

where,

$$\boldsymbol{\sigma}^{(\alpha)}(\mathbf{x},\mathbf{y},t) = \boldsymbol{C}(\mathbf{y})..\left[\boldsymbol{\nabla}_x^s\mathbf{u}^{(\alpha)}(\mathbf{x},\mathbf{y},t) + \boldsymbol{\nabla}_y^s\mathbf{u}^{(\alpha+1)}(\mathbf{x},\mathbf{y},t)\right] \tag{E.2}$$

Substituting Eqs. 4.5 and 4.6 into Eq. E.2, $\boldsymbol{\sigma}^{(\alpha)}(\mathbf{x},\mathbf{y},t)$ is written as:

$$\boldsymbol{\sigma}^{(\alpha)}(\mathbf{x},\mathbf{y},t) = \sum_{k=0}^{\alpha}\boldsymbol{C}^{(k)}(\mathbf{y})..(.\boldsymbol{\nabla}_x)^k\boldsymbol{\nabla}_x^s\mathbf{U}^{(\alpha-k)}(\mathbf{x},t) \tag{E.3}$$

where, the expression for $\boldsymbol{C}^{(k)}(\mathbf{y})$ is given in Eq. 4.8. Substituting Eqs. E.3 and 4.8 with $\alpha = 0$ into Eq. E.1a, the equilibrium equation for $\boldsymbol{H}^{(1)}(\mathbf{y})$ is obtained:

$$\boldsymbol{\nabla}_y.\left\{\boldsymbol{C}(\mathbf{y})..\left[\boldsymbol{I} + \boldsymbol{\nabla}_y\boldsymbol{H}^{(1)}(\mathbf{y})\right]\right\} = 0 \tag{E.4}$$

The boundary value problem is defined on the microscale and depends on the microstructure and material properties only. It is evaluated following the procedure in Ref. [64]. Applying the unit cell averaging operator to Eq. E.1b with $\alpha = 0$, the

macroscale balance equation at $O(1)$ is obtained:

$$\boldsymbol{\nabla}_x . \left(\boldsymbol{D}^{(0)} .. \boldsymbol{\nabla}_x^s \mathbf{U}^{(\alpha)} \right) = \rho_0 \ddot{\mathbf{U}}^{(\alpha)} \tag{E.5}$$

Generalization of this procedure for higher orders results in the equilibrium equations for microscale influence functions (Eq. 4.7), the expressions for higher order homogenized moduli (Eq. 4.9) and the macroscale balance equations at higher orders (Eq. 4.10). At order $O(\zeta^\alpha)$, the equilibrium equation for the influence function, $\boldsymbol{H}^{(\alpha+2)}(\mathbf{y})$, is obtained through substituting Eqs. 4.5, 4.6, E.3, 4.8, equilibrium equations for influence functions of lower orders and macroscale balance equations up to order $O(\zeta^\alpha)$ into Eq. E.1b. Employing these equations and applying the averaging operator to Eq. E.1b at $O(\zeta^{\alpha+1})$, the macroscale balance equation is obtained.

Appendix F

Derivation of the spatial-temporal nonlocal governing equations

This appendix first derives the spatial-temporal nonlocal macroscale balance equations at $O(\zeta^6)$, $O(\zeta^4)$ and $O(\zeta^2)$. The spatial-temporal nonlocal homogenized momentum balance equation, Eq. 4.14, is then derived by employing the macroscale balance equations at $O(\zeta^\alpha)$ with $\alpha = 0, 2, 4, 6$.

Rewritting Eq. 4.12 with $\alpha = 6$ in indicial notation:

$$\begin{aligned}
&\rho_0 \ddot{U}_i^{(6)} - D_{ijmn}^{(0)} e_{xnm}(\mathbf{U}^{(6)})_{,x_j} = \nu_{iq}^{(1)} D_{qjprmn}^{(2)} e_{xnm}(\mathbf{U}^{(4)})_{,x_{rpj}} + \\
&\nu_{iq}^{(2)} D_{qjprstmn}^{(4)} e_{xnm}(\mathbf{U}^{(2)})_{,x_{tsrpj}} + \nu_{iq}^{(3)} D_{qjprstuvmn}^{(6)} e_{xnm}(\mathbf{U}^{(0)})_{,x_{vutsrpj}} + \\
&(\delta_{iq} - \nu_{iq}^{(1)}) D_{qjprmn}^{(2)} e_{xnm}(\mathbf{U}^{(4)})_{,x_{rpj}} + (\delta_{iq} - \nu_{iq}^{(2)}) D_{qjprstmn}^{(4)} e_{xnm}(\mathbf{U}^{(2)})_{,x_{tsrpj}} + \\
&(\delta_{iq} - \nu_{iq}^{(3)}) D_{qjprstuvmn}^{(6)} e_{xnm}(\mathbf{U}^{(0)})_{,x_{vutsrpj}}
\end{aligned} \tag{F.1}$$

Substituting Eq. 4.13a into the third term on the right side of Eq. F.1, taking two spatial derivatives and inserting Eq. 4.10 with $\alpha = 4$ into the resulting expression of Eq. F.1 and considering Eqs. 4.13b and 4.13c:

$$\begin{aligned}
&\rho_0 \ddot{U}_i^{(6)} - D_{ijmn}^{(0)} e_{xnm}(\mathbf{U}^{(6)})_{,x_j} = \left(\nu_{iq}^{(1)} D_{qjprmn}^{(2)} - \nu_{iq}^{(3)} A_{qk}^{(1)} D_{kjpl}^{(0)} D_{lrmn}^{(0)} \right) e_{xnm}(\mathbf{U}^{(4)})_{,x_{rpj}} \\
&+ \left(\nu_{iq}^{(2)} A_{qk}^{(3)} - \nu_{iq}^{(3)} A_{qw}^{(1)} A_{wk}^{(2)} \right) D_{kjprsl}^{(2)} D_{ltmn}^{(0)} e_{xnm}(\mathbf{U}^{(2)})_{,x_{tsrpj}} + \\
&\rho_0 \nu_{iq}^{(3)} A_{qk}^{(1)} D_{kjmn}^{(0)} e_{xnm}(\ddot{\mathbf{U}}^{(4)})_{,x_j} + (\delta_{iq} - \nu_{iq}^{(1)}) D_{qjprmn}^{(2)} e_{xnm}(\mathbf{U}^{(4)})_{,x_{rpj}} + \\
&(\delta_{iq} - \nu_{iq}^{(2)}) D_{qjprstmn}^{(4)} e_{xnm}(\mathbf{U}^{(2)})_{,x_{tsrpj}} + (\delta_{iq} - \nu_{iq}^{(3)}) D_{qjprstuvmn}^{(6)} e_{xnm}(\mathbf{U}^{(0)})_{,x_{vutsrpj}}
\end{aligned} \tag{F.2}$$

Taking four spatial derivatives and substituting Eq. 4.10 with $\alpha = 2$ into the second

term on the right side of Eq. F.2:

$$\rho_0\ddot{U}_i^{(6)} - D_{ijmn}^{(0)}e_{xnm}(\mathbf{U}^{(6)})_{,x_j} = \left(\nu_{iq}^{(1)}D_{qjprmn}^{(2)} - \nu_{iq}^{(3)}A_{qk}^{(1)}D_{kjpl}^{(0)}D_{lrmn}^{(0)}\right)e_{xnm}(\mathbf{U}^{(4)})_{,x_{rpj}} +$$
$$\rho_0\left(\nu_{iq}^{(2)}A_{qk}^{(3)} - \nu_{iq}^{(3)}A_{qw}^{(1)}A_{wk}^{(2)}\right)D_{kjprmn}^{(2)}e_{xnm}(\ddot{\mathbf{U}}^{(2)})_{,x_{rpj}} + \rho_0\nu_{iq}^{(3)}A_{qk}^{(1)}D_{kjmn}^{(0)}e_{xnm}(\ddot{\mathbf{U}}^{(4)})_{,x_j} +$$
$$(\delta_{iq} - \nu_{iq}^{(1)})D_{qjprmn}^{(2)}e_{xnm}(\mathbf{U}^{(4)})_{,x_{rpj}} + (\delta_{iq} - \nu_{iq}^{(2)})D_{qjprstmn}^{(4)}e_{xnm}(\mathbf{U}^{(2)})_{,x_{tsrpj}} +$$
$$\left[(\delta_{iq} - \nu_{iq}^{(3)})D_{qjprstuvmn}^{(6)} - \left(\nu_{iq}^{(2)}A_{qk}^{(3)} - \nu_{iq}^{(3)}A_{qw}^{(1)}A_{wk}^{(2)}\right)D_{kjprsl}^{(2)}D_{ltuvmn}^{(2)}\right]e_{xnm}(\mathbf{U}^{(0)})_{,x_{vutsrpj}} \tag{F.3}$$

Taking two time derivatives of Eq. 4.10 with $\alpha = 4$, substituting the resulting expression into the second term on the right side of Eq. F.3 and using Eq. 4.10 with $\alpha = 0$, we arrive at the spatial-temporal nonlocal momentum balance equation at $O(\zeta^6)$:

$$\rho_0\ddot{U}_i^{(6)} - D_{ijmn}^{(0)}e_{xnm}(\mathbf{U}^{(6)})_{,x_j} = \left(\nu_{iq}^{(1)}D_{qjprmn}^{(2)} - \nu_{iq}^{(3)}A_{qk}^{(1)}D_{kjpl}^{(0)}D_{lrmn}^{(0)}\right)e_{xnm}(\mathbf{U}^{(4)})_{,x_{rpj}} +$$
$$\rho_0\left[\nu_{iq}^{(3)}A_{qw}^{(1)}\left(\delta_{wk} + A_{wk}^{(2)}\right) - \nu_{iq}^{(2)}A_{qk}^{(3)}\right]D_{kjmn}^{(0)}e_{xnm}(\ddot{\mathbf{U}}^{(4)})_{,x_j} +$$
$$\rho_0^2\left(\nu_{iq}^{(2)}A_{qk}^{(3)} - \nu_{iq}^{(3)}A_{qw}^{(1)}A_{wk}^{(2)}\right)\dddot{U}_k^{(4)} + E_{ijprmn}^{(2)}e_{xnm}(\mathbf{U}^{(4)})_{,x_{rpj}} +$$
$$E_{ijprstmn}^{(4)}e_{xnm}(\mathbf{U}^{(2)})_{,x_{tsrpj}} + E_{ijprstuvmn}^{(6)}e_{xnm}(\mathbf{U}^{(0)})_{,x_{vutsrpj}} \tag{F.4}$$

where $\boldsymbol{E}^{(2)}$, $\boldsymbol{E}^{(4)}$ and $\boldsymbol{E}^{(6)}$ are:

$$E_{ijprmn}^{(2)} = (\delta_{iq} - \nu_{iq}^{(1)})D_{qjprmn}^{(2)} \tag{F.5a}$$
$$E_{ijprstmn}^{(4)} = (\delta_{iq} - \nu_{iq}^{(2)})D_{qjprstmn}^{(4)} \tag{F.5b}$$
$$E_{ijprstuvmn}^{(6)} = -\left(\nu_{iq}^{(2)}A_{qk}^{(3)} - \nu_{iq}^{(3)}A_{qw}^{(1)}A_{wk}^{(2)}\right)\left(D_{kjprsl}^{(2)}D_{ltuvmn}^{(2)} + D_{kjprstul}^{(4)}D_{lvmn}^{(0)}\right)$$
$$+ (\delta_{iq} - \nu_{iq}^{(3)})D_{qjprstuvmn}^{(6)} \tag{F.5c}$$

Rewritting Eq. 4.12 with $\alpha = 4$:

$$\begin{aligned}
&\rho_0 \ddot{U}_i^{(4)} - D_{ijmn}^{(0)} e_{xnm}(\mathbf{U}^{(4)})_{,x_j} = \left(\nu_{iq}^{(1)} D_{qjprmn}^{(2)} - \nu_{iq}^{(3)} A_{qk}^{(1)} D_{kjpl}^{(0)} D_{lrmn}^{(0)}\right) e_{xnm}(\mathbf{U}^{(2)})_{,x_{rpj}} \\
&+ \rho_0 \nu_{iq}^{(3)} A_{qk}^{(1)} D_{kjmn}^{(0)} e_{xnm}(\ddot{\mathbf{U}}^{(2)})_{,x_j} + \nu_{iq}^{(3)} A_{qk}^{(1)} D_{kjpl}^{(0)} D_{lrmn}^{(0)} e_{xnm}(\mathbf{U}^{(2)})_{,x_{rpj}} \\
&- \rho_0 \nu_{iq}^{(3)} A_{qk}^{(1)} D_{kjmn}^{(0)} e_{xnm}(\ddot{\mathbf{U}}^{(2)})_{,x_j} + \nu_{iq}^{(2)} D_{qjprstmn}^{(4)} e_{xnm}(\mathbf{U}^{(2)})_{,x_{tsrpj}} \\
&+ E_{ijprmn}^{(2)} e_{xnm}(\mathbf{U}^{(2)})_{,x_{rpj}} + E_{ijprstmn}^{(4)} e_{xnm}(\mathbf{U}^{(0)})_{,x_{tsrpj}}
\end{aligned} \tag{F.6}$$

Taking two time derivatives of Eq. 4.10 with $\alpha = 2$, multiplying the resulting equation with ρ_0 and employing Eq. 4.10 with $\alpha = 0$:

$$\begin{aligned}
&\rho_0^2 \ddddot{U}_i^{(2)} - \rho_0 D_{ijmn}^{(0)} e_{xnm}(\ddot{\mathbf{U}}^{(2)})_{,x_j} = \rho_0 D_{ijprmn}^{(2)} e_{xnm}(\ddot{\mathbf{U}}^{(0)})_{,x_{rpj}} = \\
&D_{ijprsl}^{(2)} D_{ltmn}^{(0)} e_{xnm}(\mathbf{U}^{(0)})_{,x_{tsrpj}}
\end{aligned} \tag{F.7}$$

Using the approximation Eq. 4.13c and substituting Eq. F.7 into Eq. F.6:

$$\begin{aligned}
&\rho_0 \ddot{U}_i^{(4)} - D_{ijmn}^{(0)} e_{xnm}(\mathbf{U}^{(4)})_{,x_j} = \left(\nu_{iq}^{(1)} D_{qjprmn}^{(2)} - \nu_{iq}^{(3)} A_{qk}^{(1)} D_{kjpl}^{(0)} D_{lrmn}^{(0)}\right) e_{xnm}(\mathbf{U}^{(2)})_{,x_{rpj}} \\
&+ \rho_0 \left(\nu_{iq}^{(3)} A_{qk}^{(1)} - \nu_{iq}^{(2)} A_{qk}^{(3)}\right) D_{kjmn}^{(0)} e_{xnm}(\ddot{\mathbf{U}}^{(2)})_{,x_j} + \nu_{iq}^{(3)} A_{qk}^{(1)} D_{kjpl}^{(0)} D_{lrmn}^{(0)} e_{xnm}(\mathbf{U}^{(2)})_{,x_{rpj}} \\
&- \rho_0 \nu_{iq}^{(3)} A_{qk}^{(1)} D_{kjmn}^{(0)} e_{xnm}(\ddot{\mathbf{U}}^{(2)})_{,x_j} + \rho_0^2 \nu_{iq}^{(2)} A_{qk}^{(3)} \ddddot{U}_k^{(2)} \\
&+ E_{ijprmn}^{(2)} e_{xnm}(\mathbf{U}^{(2)})_{,x_{rpj}} + E_{ijprstmn}^{(4)} e_{xnm}(\mathbf{U}^{(0)})_{,x_{tsrpj}}
\end{aligned} \tag{F.8}$$

Taking two spatial derivatives of Eq. 4.10 with $\alpha = 2$, substituting the resulting expression into $\nu_{iq}^{(3)} A_{qk}^{(1)} D_{kjpl}^{(0)} D_{lrmn}^{(0)} e_{xnm}(\mathbf{U}^{(2)})_{,x_{rpj}} - \rho_0 \nu_{iq}^{(3)} A_{qk}^{(1)} D_{kjmn}^{(0)} e_{xnm}(\ddot{\mathbf{U}}^{(2)})_{,x_j}$ and

recalling the approximation Eq. 4.13b:

$$\begin{aligned}
&\rho_0\ddot{U}_i^{(4)} - D_{ijmn}^{(0)} e_{xnm}(\mathbf{U}^{(4)})_{,x_j} = \left(\nu_{iq}^{(1)} D_{qjprmn}^{(2)} - \nu_{iq}^{(3)} A_{qk}^{(1)} D_{kjpl}^{(0)} D_{lrmn}^{(0)}\right) e_{xnm}(\mathbf{U}^{(2)})_{,x_{rpj}} \\
&+ \rho_0 \left(\nu_{iq}^{(3)} A_{qk}^{(1)} - \nu_{iq}^{(2)} A_{qk}^{(3)}\right) D_{kjmn}^{(0)} e_{xnm}(\ddot{\mathbf{U}}^{(2)})_{,x_j} + \rho_0^2 \nu_{iq}^{(2)} A_{qk}^{(3)} \ddddot{U}_k^{(2)} \\
&- \nu_{iq}^{(3)} A_{qw}^{(1)} A_{wk}^{(2)} D_{kjprsl}^{(2)} D_{ltmn}^{(0)} e_{xnm}(\mathbf{U}^{(0)})_{,x_{tsrpj}} \\
&+ E_{ijprmn}^{(2)} e_{xnm}(\mathbf{U}^{(2)})_{,x_{rpj}} + E_{ijprstmn}^{(4)} e_{xnm}(\mathbf{U}^{(0)})_{,x_{tsrpj}}
\end{aligned} \tag{F.9}$$

Taking four spatial derivatives of Eq. 4.10 with $\alpha = 0$, substituting the resulting expression into the fourth term on the right side of Eq. F.9 and employing Eq.4.10 with $\alpha = 2$ taken two time derivatives, we obtain the spatial-temporal nonlocal momentum balance equation at $O(\zeta^4)$:

$$\begin{aligned}
&\rho_0\ddot{U}_i^{(4)} - D_{ijmn}^{(0)} e_{xnm}(\mathbf{U}^{(4)})_{,x_j} = \left(\nu_{iq}^{(1)} D_{qjprmn}^{(2)} - \nu_{iq}^{(3)} A_{qk}^{(1)} D_{kjpl}^{(0)} D_{lrmn}^{(0)}\right) e_{xnm}(\mathbf{U}^{(2)})_{,x_{rpj}} \\
&+ \rho_0 \left[\nu_{iq}^{(3)} A_{qw}^{(1)} \left(\delta_{wk} + A_{wk}^{(2)}\right) - \nu_{iq}^{(2)} A_{qk}^{(3)}\right] D_{kjmn}^{(0)} e_{xnm}(\ddot{\mathbf{U}}^{(2)})_{,x_j} \\
&+ \rho_0^2 \left(\nu_{iq}^{(2)} A_{qk}^{(3)} - \nu_{iq}^{(3)} A_{qw}^{(1)} A_{wk}^{(2)}\right) \ddddot{U}_k^{(2)} \\
&+ E_{ijprmn}^{(2)} e_{xnm}(\mathbf{U}^{(2)})_{,x_{rpj}} + E_{ijprstmn}^{(4)} e_{xnm}(\mathbf{U}^{(0)})_{,x_{tsrpj}}
\end{aligned} \tag{F.10}$$

The spatial-temporal nonlocal momentum balance equation at $O(\zeta^2)$ is obtained by rewritting Eq. 4.12 with $\alpha = 2$ while considering the momentum balance of Eq. 4.10 with $\alpha = 0$:

$$\begin{aligned}
&\rho_0\ddot{U}_i^{(2)} - D_{ijmn}^{(0)} e_{xnm}(\mathbf{U}^{(2)})_{,x_j} = \left(\nu_{iq}^{(1)} D_{qjprmn}^{(2)} - \nu_{iq}^{(3)} A_{qk}^{(1)} D_{kjpl}^{(0)} D_{lrmn}^{(0)}\right) e_{xnm}(\mathbf{U}^{(0)})_{,x_{rpj}} \\
&+ \rho_0 \left[\nu_{iq}^{(3)} A_{qw}^{(1)} \left(\delta_{wk} + A_{wk}^{(2)}\right) - \nu_{iq}^{(2)} A_{qk}^{(3)}\right] D_{kjmn}^{(0)} e_{xnm}(\ddot{\mathbf{U}}^{(0)})_{,x_j} \\
&+ \rho_0^2 \left(\nu_{iq}^{(2)} A_{qk}^{(3)} - \nu_{iq}^{(3)} A_{qw}^{(1)} A_{wk}^{(2)}\right) \ddddot{U}_k^{(0)} + E_{ijprmn}^{(2)} e_{xnm}(\mathbf{U}^{(0)})_{,x_{rpj}}
\end{aligned} \tag{F.11}$$

Employing Eqs F.4, F.10, F.11 and 4.10 with $\alpha = 0$, and using the summation of macroscale displacement from all orders, Eq. 4.11, the spatial-temporal nonlocal homogenized momentum balance equation is obtained as:

$$\rho_0 \ddot{U}_i - D^{(0)}_{ijmn} e_{xnm}(\mathbf{U})_{,x_j} = \left(\nu^{(1)}_{iq} D^{(2)}_{qjprmn} - \nu^{(3)}_{iq} A^{(1)}_{qk} D^{(0)}_{kjpl} D^{(0)}_{lrmn}\right) e_{xnm}(\mathbf{U})_{,x_{rpj}} +$$
$$\rho_0 \left[\nu^{(3)}_{iq} A^{(1)}_{qw} \left(\delta_{wk} + A^{(2)}_{wk}\right) - \nu^{(2)}_{iq} A^{(3)}_{qk}\right] D^{(0)}_{kjmn} e_{xnm}(\ddot{\mathbf{U}})_{,x_j} +$$
$$\rho_0^2 \left(\nu^{(2)}_{iq} A^{(3)}_{qk} - \nu^{(3)}_{iq} A^{(1)}_{qw} A^{(2)}_{wk}\right) \dddot{U}_k + \zeta^2 E^{(2)}_{ijprmn} e_{xnm}(\mathbf{U}^{(0)})_{,x_{rpj}} +$$
$$\zeta^4 \left(E^{(2)}_{ijprmn} e_{xnm}(\mathbf{U}^{(2)})_{,x_{rpj}} + E^{(4)}_{ijprstmn} e_{xnm}(\mathbf{U}^{(0)})_{,x_{tsrpj}}\right) +$$
$$\zeta^6 \left(E^{(2)}_{ijprmn} e_{xnm}(\mathbf{U}^{(4)})_{,x_{rpj}} + E^{(4)}_{ijprstmn} e_{xnm}(\mathbf{U}^{(2)})_{,x_{tsrpj}} + E^{(6)}_{ijprstuvmn} e_{xnm}(\mathbf{U}^{(0)})_{,x_{vutsrpj}}\right) \tag{F.12}$$

Appendix G

Expressions of a_i, b_i, c_i, $\tilde{b}_i$ and $\tilde{c}_i$

$$a_i = \left(\beta_{[i]jmn}\beta_{[i]pqr} - 4\alpha_{[i]jpqmn}\gamma_{[i]r}\right)\hat{n}_j\hat{n}_m\hat{n}_p\hat{n}_q\hat{p}_n\hat{p}_r \tag{G.1a}$$

$$b_i = -2\left(\beta_{[i]jmn}D^{(0)}_{[i]pqr} + 2\rho_0\alpha_{[i]jpqmn}\delta_{[i]r}\right)\hat{n}_j\hat{n}_m\hat{n}_p\hat{n}_q\hat{p}_n\hat{p}_r \tag{G.1b}$$

$$c_i = D^{(0)}_{[i]jmn}D^{(0)}_{[i]pqr}\hat{n}_j\hat{n}_m\hat{n}_p\hat{n}_q\hat{p}_n\hat{p}_r \tag{G.1c}$$

$$\tilde{b}_i = 2\left(\beta_{[i]jmn}\delta_{[i]r}\rho_0 + 2D^{(0)}_{[i]jmn}\gamma_{[i]r}\right)\hat{n}_j\hat{n}_m\hat{p}_n\hat{p}_r \tag{G.1d}$$

$$\tilde{c}_i = \rho_0^2\delta_{[i]n}\delta_{[i]r}\hat{p}_n\hat{p}_r \tag{G.1e}$$

For a selected pair of vectors $(\hat{\mathbf{n}}, \hat{\mathbf{p}})$, $c_i > 0$ and $\tilde{c}_i > 0$.

Appendix H

Inverse isoparametric mapping

This appendix provides the detailed procedure of the inverse isoparametric mapping for 2D quadrilateral elements. The procedure is developed based on Ref. [78] that maps any point within the coarse-scale element in Cartesian coordinates to the isoparametric coordinates.

The inverse isoparametric mapping for a higher order element is performed based on its cord element, which is the 4-node linear quadrilateral element that is formed by the corner nodes of the quadrilateral, i.e., node $1, 2, 3, 4$ in Fig. 5.2. The isoparametric mapping for the cord element is expressed as:

$$\begin{Bmatrix} x \\ y \end{Bmatrix} = \begin{Bmatrix} a_0 + a_1\xi + a_2\xi\eta + a_3\eta \\ b_0 + b_1\xi + b_2\xi\eta + b_3\eta \end{Bmatrix} \tag{H.1}$$

where,

$$\begin{aligned} a_0 &= \frac{1}{4}(x_1 + x_2 + x_3 + x_4); \quad b_0 = \frac{1}{4}(y_1 + y_2 + y_3 + y_4) \\ a_1 &= \frac{1}{4}(-x_1 + x_2 + x_3 - x_4); \quad b_1 = \frac{1}{4}(-y_1 + y_2 + y_3 - y_4) \\ a_2 &= \frac{1}{4}(x_1 - x_2 + x_3 - x_4); \quad b_2 = \frac{1}{4}(y_1 - y_2 + y_3 - y_4) \\ a_3 &= \frac{1}{4}(-x_1 - x_2 + x_3 + x_4); \quad b_3 = \frac{1}{4}(-y_1 - y_2 + y_3 + y_4) \end{aligned} \tag{H.2}$$

Following the formula provided in Ref. [78], the geodesic parameters are written as:

$$\begin{aligned} \xi^g &= \bar{\xi} - \gamma\bar{\xi}\bar{\eta} + (\alpha\gamma\bar{\xi}^2\bar{\eta} + \gamma^2\bar{\xi}\bar{\eta}^2) - (\alpha^2\gamma\bar{\xi}^3\bar{\eta} + 2\alpha\gamma^2\bar{\xi}^2\bar{\eta}^2 + \gamma^3\bar{\xi}\bar{\eta}^3) \\ \eta^g &= \bar{\eta} - \alpha\bar{\xi}\bar{\eta} + (\alpha^2\bar{\xi}^2\bar{\eta} + \alpha\gamma\bar{\xi}\bar{\eta}^2) - (\alpha^3\bar{\xi}^3\bar{\eta} + 2\alpha^2\gamma\bar{\xi}^2\bar{\eta}^2 + \alpha\gamma^2\bar{\xi}\bar{\eta}^3) \end{aligned} \tag{H.3}$$

where,

$$\begin{Bmatrix} \bar{\xi} \\ \bar{\eta} \end{Bmatrix} = \frac{1}{J_0} \begin{bmatrix} b_3 & -a_3 \\ -b_1 & a_1 \end{bmatrix} \begin{Bmatrix} x \\ y \end{Bmatrix} \tag{H.4}$$

The parameters are:

$$\begin{aligned} J_0 &= a_1 b_3 - a_3 b_1 \\ \alpha &= (a_1 b_2 - a_2 b_1)/J_0 \\ \gamma &= (a_2 b_3 - a_3 b_2)/J_0 \end{aligned} \tag{H.5}$$

A linear mapping is then performed to map the geodesic parameters to the isoparametric variables:

$$\begin{Bmatrix} \xi \\ \eta \end{Bmatrix} = \begin{Bmatrix} \hat{a}_0 + \hat{a}_1 \xi^g + \hat{a}_2 \xi^g \eta^g + \hat{a}_3 \eta^g \\ \hat{b}_0 + \hat{b}_1 \xi^g + \hat{b}_2 \xi^g \eta^g + \hat{b}_3 \eta^g \end{Bmatrix} \tag{H.6}$$

where, $\hat{a}_i$ and $\hat{b}_i$, $i = 1, 2, 3, 4$, are computed using Eq. H.2 with (x_i, y_i) taken as: $(-1, -1)$, $(-1, 1)$, $(1, 1)$ and $(-1, 1)$, respectively.

BIBLIOGRAPHY

[1] M. M. Ameen, R. H. J. Peerlings, and M. G. D. Geers. A quantitative assessment of the scale separation limits of classical and higher-order asymptotic homogenization. *Eur. J. Mech. A.*, 71:89–100, 2018.

[2] A. V. Amirkhizi, J. Isaacs, J. McGee, and S. Nemat-Nasser. An experimentally-based viscoelastic constitutive model for polyurea, including pressure and temperature effects. *Philos. Mag.*, 86(36):5847–5866, 2006.

[3] E. Andreassen and J. S. Jensen. Analysis of phononic bandgap structures with dissipation. *J. Vib. Acoust.*, 135(4):041015, 2013.

[4] I. V. Andrianov, V. I. Bolshakov, V. V. Danishevs' kyy, and D. Weichert. Higher order asymptotic homogenization and wave propagation in periodic composite materials. *Proc. R. Soc. London, Ser. A*, 464:1181–1201, 2008.

[5] T. Arbogast. Implementation of a locally conservative numerical subgrid upscaling scheme for two-phase darcy flow. *Comput. Geosci.*, 6(3-4):453–481, 2002.

[6] H. Askes and E. C. Aifantis. Gradient elasticity in statics and dynamics: an overview of formulations, length scale identification procedures, finite element implementations and new results. *Int. J. Solids Struct.*, 48(13):1962–1990, 2011.

[7] H. Askes, A. V. Metrikine, A. V. Pichugin, and T. Bennett. Four simplified gradient elasticity models for the simulation of dispersive wave propagation. *Philos. Mag.*, 88:3415–3443, 2008.

[8] B. V. Asokan and N. Zabaras. A stochastic variational multiscale method for diffusion in heterogeneous random media. *J. Comput. Phys.*, 218(2):654–676, 2006.

[9] J. L. Auriault and C. Boutin. Long wavelength inner-resonance cut-off frequencies in elastic composite materials. *Int. J. Solids Struct.*, 49:3269–3281, 2012.

[10] I. Babuška and M. Suri. The p-and hp versions of the finite element method, an overview. *Comput. Methods Appl. Mech. Eng.*, 80(1-3):5–26, 1990.

[11] A. Bacigalupo and L. Gambarotta. Second-gradient homogenized model for wave propagation in heterogeneous periodic media. *Int. J. Solids Struct.*, 51 (5):1052–1065, 2014.

[12] A. Bedford and D. S. Drumheller. *Elastic wave propagation*. Wiley, 1994.

[13] A. Bensoussan, J.-L. Lions, and G. Papanicolaou. *Asymptotic Analysis for Periodic Structures*. North-Holland, Amsterdam, 1978.

[14] C. Boutin. Microstructural effects in elastic composites. *Int. J. Solids Struct.*, 33:1023–1051, 1996.

[15] C. Boutin and J. L. Auriault. Rayleigh scattering in elastic composite materials. *Int. J. Eng. Sci.*, 31:1669–1689, 1993.

[16] L. Brancik. Programs for fast numerical inversion of laplace transforms in matlab language environment. In *Konference MATLAB '99-Praha. MATLAB '99, Praha: Konference MATLAB '99, Praha*, pages 27–39, 1999.

[17] R. P. Brent. *Algorithms for minimization without derivatives*. Courier Corporation, 2013.

[18] L. Brillouin. *Wave propagation in periodic structures: electric filters and crystal lattices*. Courier Corporation, 2003.

[19] S. Brûlé, E. H. Javelaud, S. Enoch, and S. Guenneau. Experiments on seismic metamaterials: molding surface waves. *Phys. Rev. Lett.*, 112(13):133901, 2014.

[20] F. Casadei, J. J. Rimoli, and M. Ruzzene. A geometric multiscale finite element method for the dynamic analysis of heterogeneous solids. *Comput. Methods Appl. Mech. Eng.*, 263:56–70, 2013.

[21] F. Casadei, J. J. Rimoli, and M. Ruzzene. Multiscale finite element analysis of wave propagation in periodic solids. *Finite Elem. Anal. Des.*, 108:81–95, 2016.

[22] M. P. Castanier, Y. C. Tan, and C. Pierre. Characteristic constraint modes for component mode synthesis. *AIAA journal*, 39(6):1182–1187, 2001.

[23] W. Chen and J. Fish. A dispersive model for wave propagation in periodic heterogeneous media based on homogenization with multiple spatial and temporal scales. *J. Appl. Mech.*, 68:153–161, 2001.

[24] M. Collet, M. Ouisse, M. Ruzzene, and M. N. Ichchou. Floquet–bloch decomposition for the computation of dispersion of two-dimensional periodic, damped mechanical systems. *Int. J. Solids Struct.*, 48(20):2837–2848, 2011.

[25] A. Colombi, P. Roux, S. Guenneau, P. Gueguen, and R. V. Craster. Forests as a natural seismic metamaterial: Rayleigh wave bandgaps induced by local resonances. *Sci. Rep.*, 6:19238, 2016.

[26] P. Comon, G. Golub, L. Lim, and B. Mourrain. Symmetric tensors and symmetric tensor rank. *SIAM J. Matrix Anal. Appl.*, 30(3):1254–1279, 2008.

[27] J. A. Cottrell, T. J. R. Hughes, and Y. Bazilevs. *Isogeometric analysis: toward integration of CAD and FEA*. John Wiley & Sons, 2009.

[28] R. Craig and M. Bampton. Coupling of substructures for dynamic analyses. *AIAA journal*, 6(7):1313–1319, 1968.

[29] K. S. Crump. Numerical inversion of laplace transforms using a fourier series approximation. *J. ACM*, 23(1):89–96, 1976.

[30] B. Davies and B. Martin. Numerical inversion of the laplace transform: a survey and comparison of methods. *J. Comput. Phys.*, 33(1):1–32, 1979.

[31] L. Dedè, C. Jäggli, and A. Quarteroni. Isogeometric numerical dispersion analysis for two-dimensional elastic wave propagation. *Comput. Methods Appl. Mech. Eng.*, 284:320–348, 2015.

[32] A. Deraemaeker, I. Babuška, and P. Bouillard. Dispersion and pollution of the fem solution for the helmholtz equation in one, two and three dimensions. *Int. J. Numer. Methods Eng.*, 46(4):471–499, 1999.

[33] E. V. Dontsov, R. D. Tokmashev, and B. B. Guzina. A physical perspective of the length scales in gradient elasticity through the prism of wave dispersion. *Int. J. Solids Struct.*, 50:3674–3684, 2013.

[34] B. Engquist and O. Runborg. Computational high frequency wave propagation. *Acta numerica*, 12:181–266, 2003.

[35] D. Fafalis and J. Fish. Computational aspects of dispersive computational continua for elastic heterogeneous media. *Comput. Mech.*, 56(6):931–946, 2015.

[36] N. Fang, D. Xi, J. Xu, M. Ambati, W. Srituravanich, C. Sun, and X. Zhang. Ultrasonic metamaterials with negative modulus. *Nat. Mater.*, 5(6):452–456, 2006.

[37] F. Feyel and J. Chaboche. FE2 multiscale approach for modelling the elastoviscoplastic behaviour of long fibre sic/ti composite materials. *Comput. Methods Appl. Mech. Eng.*, 183(3-4):309–330, 2000.

[38] V. Filonova, D. Fafalis, and J. Fish. Dispersive computational continua. *Comput. Methods Appl. Mech. Eng.*, 298:58–79, 2016.

[39] J. Fish and T. Belytschko. *A first course in finite elements.* John Wiley & Sons Ltd., Chichester, West Sussex, UK, 2007.

[40] J. Fish and W. Chen. Higher-order homogenization of initial/boundary-value problem. *J. Eng. Mech.*, 127:1223–1230, 2001.

[41] J. Fish and S. Kuznetsov. Computational continua. *Int. J. Numer. Methods Eng.*, 84(7):774–802, 2010.

[42] J. Fish, W. Chen, and G. Nagai. Non-local dispersive model for wave propagation in heterogeneous media: one-dimensional case. *Int. J. Numer. Methods Eng.*, 54(3):331–346, 2002.

[43] J. Fish, W. Chen, and G. Nagai. Non-local dispersive model for wave propagation in heterogeneous media: multi-dimensional case. *Int. J. Numer. Methods Eng.*, 54:347–363, 2002.

[44] Jacob Fish. *Practical multiscaling.* John Wiley & Sons, 2013.

[45] B. Gambin and E. Kröner. Higher-order terms in the homogenized stress-strain relation of periodic elastic media. *Phys. Status Solidi B*, 151:513–519, 1989.

[46] B. Ganapathysubramanian and N. Zabaras. Modeling diffusion in random heterogeneous media: Data-driven models, stochastic collocation and the variational multiscale method. *J. Comput. Phys.*, 226(1):326–353, 2007.

[47] K. Garikipati and T. J. R. Hughes. A study of strain localization in a multiple scale framework-the one-dimensional problem. *Comput. Methods Appl. Mech. Eng.*, 159(3-4):193–222, 1998.

[48] K. Garikipati and T. J. R. Hughes. A variational multiscale approach to strain localization–formulation for multidimensional problems. *Comput. Methods Appl. Mech. Eng.*, 188(1-3):39–60, 2000.

[49] T. H. Glisson Jr. *Introduction to Circuit Analysis and Design*. Springer, 2011.

[50] G. L. Goudreau and R. L. Taylor. Evaluation of numerical integration methods in elastodynamics. *Comput. Methods Appl. Mech. Eng.*, 2(1):69–97, 1973.

[51] Z. V. I. Hashin. Complex moduli of viscoelastic composites i. general theory and application to particulate composites. *Int. J. Solids Struct.*, 6(5):539–552, 1970.

[52] S. K. Hong, B. I. Epureanu, and M. P. Castanier. Next-generation parametric reduced-order models. *Mech. Syst. Sig. Process.*, 37(1-2):403–421, 2013.

[53] T. Y. Hou and X. Wu. A multiscale finite element method for elliptic problems in composite materials and porous media. *J. Comput. Phys.*, 134(1):169–189, 1997.

[54] R. Hu and C. Oskay. Nonlocal homogenization model for wave dispersion and attenuation in elastic and viscoelastic periodic layered media. *J. Appl. Mech.*, 84(3):031003, 2017.

[55] R. Hu and C. Oskay. Spatial-temporal nonlocal homogenization model for transient anti-plane shear wave propagation in periodic viscoelastic composites. *Comput. Methods Appl. Mech. Eng.*, 342:1–31, 2018.

[56] R. Hu and C. Oskay. Multiscale nonlocal effective medium model for in-plane elastic wave dispersion and attenuation in periodic composites. *J. Mech. Phys. Solids*, 124:220–243, 2019.

[57] R. Hu, C. Prakash, V. Tomar, M. Harr, I. E. Gunduz, and C. Oskay. Experimentally-validated mesoscale modeling of the coupled mechanical–thermal response of ap-htpb energetic material under dynamic loading. *Int. J. Fract.*, 203(1):277–298, 2017.

[58] T. J. R. Hughes. *The finite element method: linear static and dynamic finite element analysis*. Dover Publications, Mineola, New York, 2000.

[59] T. J. R. Hughes, G. R. Feijóo, L. Mazzei, and J. B. Quincy. The variational multiscale method-a paradigm for computational mechanics. *Comput. Methods Appl. Mech. Eng.*, 166(1-2):3–24, 1998.

[60] T. J. R. Hughes, J. A. Cottrell, and Y. Bazilevs. Isogeometric analysis: Cad, finite elements, nurbs, exact geometry and mesh refinement. *Comput. Methods Appl. Mech. Eng.*, 194(39):4135–4195, 2005.

[61] T. J. R. Hughes, A. Reali, and G. Sangalli. Duality and unified analysis of discrete approximations in structural dynamics and wave propagation: comparison of p-method finite elements with k-method nurbs. *Comput. Methods Appl. Mech. Eng.*, 197(49):4104–4124, 2008.

[62] T. J. R. Hughes, J. A. Evans, and A. Reali. Finite element and nurbs approximations of eigenvalue, boundary-value, and initial-value problems. *Comput. Methods Appl. Mech. Eng.*, 272:290–320, 2014.

[63] T. Hui and C. Oskay. A nonlocal homogenization model for wave dispersion in dissipative composite materials. *Int. J. Solids Struct.*, 50:38 – 48, 2013.

[64] T. Hui and C. Oskay. A high order homogenization model for transient dynamics of heterogeneous media including micro-inertia effects. *Comput. Methods Appl. Mech. Eng.*, 273:181–203, 2014.

[65] T. Hui and C. Oskay. Laplace-domain, high-order homogenization for transient dynamic response of viscoelastic composites. *Int. J. Numer. Methods Eng.*, 103 (13):937–957, 2015.

[66] M. I. Hussein. Reduced bloch mode expansion for periodic media band structure calculations. *Proc. R. Soc. London, Ser. A*, 465(2109):2825–2848, 2009.

[67] M. I. Hussein. Theory of damped bloch waves in elastic media. *Phys. Rev. B*, 80(21):212301, 2009.

[68] F. Ihlenburg and I. Babuška. Dispersion analysis and error estimation of galerkin finite element methods for the helmholtz equation. *Int. J. Numer. Methods Eng.*, 38(22):3745–3774, 1995.

[69] F. Ihlenburg and I. Babuška. Finite element solution of the helmholtz equation with high wave number part i: The h-version of the fem. *Comput. Math. Appl.*, 30(9):9–37, 1995.

[70] F. Ihlenburg and I. Babuska. Finite element solution of the helmholtz equation with high wave number part ii: the hp version of the fem. *SIAM J. Numer. Anal.*, 34(1):315–358, 1997.

[71] N. Kaina, F. Lemoult, M. Fink, and G. Lerosey. Negative refractive index and acoustic superlens from multiple scattering in single negative metamaterials. *Nature*, 525(7567):77, 2015.

[72] A. Khelif, A. Choujaa, S. Benchabane, B. Djafari-Rouhani, and V. Laude. Guiding and bending of acoustic waves in highly confined phononic crystal waveguides. *Appl. Phys. Lett.*, 84(22):4400–4402, 2004.

[73] D. Krattiger and M. I. Hussein. Generalized bloch mode synthesis for accelerated calculation of elastic band structures. *J. Comput. Phys.*, 357:183–205, 2018.

[74] A. O. Krushynska, V. G. Kouznetsova, and M. G. D. Geers. Visco-elastic effects

on wave dispersion in three-phase acoustic metamaterials. *J. Mech. Phys. Solids*, 96:29–47, 2016.

[75] M. Lai, D. H. Rubin, E. Krempl, and D. Rubin. *Introduction to continuum mechanics*. Butterworth-Heinemann, 2009.

[76] V. Laude, Y. Achaoui, S. Benchabane, and A. Khelif. Evanescent Bloch waves and the complex band structure of phononic crystals. *Phys. Rev. B*, 80(9): 092301, 2009.

[77] N. Lautersztajn-S and A. Samuelsson. On application of differential geometry to computational mechanics. *Comput. Methods Appl. Mech. Eng.*, 150(1-4): 25–38, 1997.

[78] N. Lautersztajn-S and A. Samuelsson. Distortion measures and inverse mapping for isoparametric 8-node plane finite elements with curved boundaries. *Commun. Numer. Methods Eng.*, 14(2):87–101, 1998.

[79] J. Li, L. Fok, X. Yin, G. Bartal, and X. Zhang. Experimental demonstration of an acoustic magnifying hyperlens. *Nat. Mater.*, 8(12):931, 2009.

[80] C. Liu and C. Reina. Variational coarse-graining procedure for dynamic homogenization. *J. Mech. Phys. Solids*, 104:187 – 206, 2017.

[81] C. Liu and C. Reina. Dynamic homogenization of resonant elastic metamaterials with space/time modulation. *Comput. Mech.*, pages 1–15, 2018.

[82] Z. Liu, X. Zhang, Y. Mao, Y. Y. Zhu, Z. Yang, C. T. Chan, and P. Sheng. Locally resonant sonic materials. *Science*, 289:1734–1736, 2000.

[83] G. Ma and P. Sheng. Acoustic metamaterials: From local resonances to broad horizons. *Sci. Adv.*, 2(2):e1501595, 2016.

[84] J. R. Macdonald. Accelerated convergence, divergence, iteration, extrapolation, and curve fitting. *J. Appl. Phys.*, 35(10):3034–3041, 1964.

[85] M. Maldovan. Sound and heat revolutions in phononics. *Nature*, 503(7475): 209, 2013.

[86] A. Masud and R. A. Khurram. A multiscale/stabilized finite element method for the advection–diffusion equation. *Comput. Methods Appl. Mech. Eng.*, 193 (21-22):1997–2018, 2004.

[87] A. Masud and K. Xia. A variational multiscale method for inelasticity: Application to superelasticity in shape memory alloys. *Comput. Methods Appl. Mech. Eng.*, 195(33-36):4512–4531, 2006.

[88] S. Meng and B. B. Guzina. On the dynamic homogenization of periodic media: Willis' approach versus two-scale paradigm. *Proc. R. Soc. A*, 474(2213): 20170638, 2018.

[89] B. Merheb, P. A. Deymier, M. Jain, M. Aloshyna-Lesuffleur, S. Mohanty, A. Berker, and R. W. Greger. Elastic and viscoelastic effects in rubber/air acoustic band gap structures: A theoretical and experimental study. *J. Appl. Phys.*, 104(6):064913, 2008.

[90] B. Merheb, P. A. Deymier, K. Muralidharan, J. Bucay, M. Jain, M. Aloshyna-Lesuffleur, R. W. Greger, S. Mohanty, and A. Berker. Viscoelastic effect on acoustic band gaps in polymer-fluid composites. *Modell. Simul. Mater. Sci. Eng.*, 17(7):075013, 2009.

[91] A. V. Metrikine. On causality of the gradient elasticity models. *J. Sound Vib.*, 297:727–742, 2006.

[92] C. Miehe, J. Schröder, and J. Schotte. Computational homogenization analysis in finite plasticity simulation of texture development in polycrystalline materials. *Comput. Methods Appl. Mech. Eng.*, 171(3-4):387–418, 1999.

[93] G. W. Milton and J. R. Willis. On modifications of newton's second law and linear continuum elastodynamics. *Proc. R. Soc. London, Ser. A*, 463(2079): 855–880, 2007.

[94] R. D. Mindlin. Micro-structure in linear elasticity. *Arch. Ration. Mech. Anal.*, 16:51–78, 1964.

[95] A. Mostowski and M. Stark. *Introduction to Higher Algebra*. Pergamon Press, 1964.

[96] H. Moulinec and P. Suquet. A numerical method for computing the overall response of nonlinear composites with complex microstructure. *Comput. Methods Appl. Mech. Eng.*, 157(1-2):69–94, 1998.

[97] S. H. Mousavi, A. B. Khanikaev, and Z. Wang. Topologically protected elastic waves in phononic metamaterials. *Nat. Commun.*, 6:8682, 2015.

[98] M. J. P. Musgrave. *Crystal acoustics*. Acoustical Society of America New York, 2003.

[99] H. Nassar, Q.-C. He, and N. Auffray. Willis elastodynamic homogenization theory revisited for periodic media. *J. Mech. Phys. Solids*, 77:158–178, 2015.

[100] H. Nassar, Q-C He, and N. Auffray. A generalized theory of elastodynamic homogenization for periodic media. *Int. J. Solids Struct.*, 84:139–146, 2016.

[101] S. Nemat-Nasser and A. Srivastava. Overall dynamic constitutive relations of layered elastic composites. *J. Mech. Phys. Solids*, 59(10):1953–1965, 2011.

[102] A. A. Oberai and P. M. Pinsky. A multiscale finite element method for the helmholtz equation. *Comput. Methods Appl. Mech. Eng.*, 154(3-4):281–297, 1998.

[103] C. Oskay. Variational multiscale enrichment for modeling coupled mechano-diffusion problems. *Int. J. Numer. Methods Eng.*, 89(6):686–705, 2012.

[104] C. Oskay. Variational multiscale enrichment method with mixed boundary conditions for modeling diffusion and deformation problems. *Comput. Methods Appl. Mech. Eng.*, 264:178–190, 2013.

[105] C. Oskay and J. Fish. Eigendeformation-based reduced order homogenization for failure analysis of heterogeneous materials. *Comput. Methods Appl. Mech. Eng.*, 196:1216–1243, 2007.

[106] Y. Pennec, J. O. Vasseur, B. Djafari-Rouhani, L. Dobrzyński, and P. A. Deymier. Two-dimensional phononic crystals: Examples and applications. *Surf. Sci. Rep.*, 65(8):229–291, 2010.

[107] K. Pham, V. G. Kouznetsova, and M. G. D. Geers. Transient computational homogenization for heterogeneous materials under dynamic excitation. *J. Mech. Phys. Solids*, 61(11):2125–2146, 2013.

[108] A. S. Phani, J. Woodhouse, and N. A. Fleck. Wave propagation in two-dimensional periodic lattices. *J. Acoust. Soc. Am.*, 119(4):1995–2005, 2006.

[109] A. V. Pichugin, H. Askes, and A. Tyas. Asymptotic equivalence of homogenisation procedures and fine-tuning of continuum theories. *J. Sound Vib.*, 313(3): 858–874, 2008.

[110] H. T. Rathod and S. Kilari. General complete lagrange family for the cube

in finite element interpolations. *Comput. Methods Appl. Mech. Eng.*, 181(1-3): 295–344, 2000.

[111] H. T. Rathod and K. Sridevi. General complete lagrange interpolations with applications to three-dimensional finite element analysis. *Comput. Methods Appl. Mech. Eng.*, 190(26-27):3325–3368, 2001.

[112] D. Roca, O. Lloberas-Valls, J. Cante, and J. Oliver. A computational multi-scale homogenization framework accounting for inertial effects: Application to acoustic metamaterials modelling. *Comput. Methods Appl. Mech. Eng.*, 330: 415–446, 2018.

[113] D. Roca, D. Yago, J. Cante, O. Lloberas-Valls, and J. Oliver. Computational design of locally resonant acoustic metamaterials. *Comput. Methods Appl. Mech. Eng.*, 345:161–182, 2019.

[114] E. Sanchez-Palencia. Non-homogeneous media and vibration theory. In *Non-homogeneous media and vibration theory*, volume 127, 1980.

[115] V. P. Smyshlyaev. Propagation and localization of elastic waves in highly anisotropic periodic composites via two-scale homogenization. *Mech. Mater.*, 41:434–447, 2009.

[116] A. Sridhar, V. G. Kouznetsova, and M. G. D. Geers. Homogenization of locally resonant acoustic metamaterials towards an emergent enriched continuum. *Comput. Mech.*, 57(3):423–435, 2016.

[117] A. Sridhar, V. G. Kouznetsova, and M. G. D. Geers. A general multiscale framework for the emergent effective elastodynamics of metamaterials. *J. Mech. Phys. Solids*, 111:414–433, 2018.

[118] A. Srivastava and S. Nemat-Nasser. On the limit and applicability of dynamic homogenization. *Wave Motion*, 51(7):1045–1054, 2014.

[119] A. Srivastava and J. R. Willis. Evanescent wave boundary layers in metamaterials and sidestepping them through a variational approach. *Proc. R. Soc. A*, 473(2200):20160765, 2017.

[120] N. Stenger, M. Wilhelm, and M. Wegener. Experiments on elastic cloaking in thin plates. *Phys. Rev. Lett.*, 108(1):014301, 2012.

[121] E. S. Suhubi and A. C. Eringen. Nonlinear theory of micro-elastic solids-ii. *Int. J. Eng. Sci.*, 2(4):389 – 404, 1964.

[122] L. L. Thompson and P. M. Pinsky. Complex wavenumber fourier analysis of the p-version finite element method. *Comput. Mech.*, 13(4):255–275, 1994.

[123] T. J. Truster and A. Masud. Primal interface formulation for coupling multiple pdes: a consistent derivation via the variational multiscale method. *Comput. Methods Appl. Mech. Eng.*, 268:194–224, 2014.

[124] J. O. Vasseur, P. A. Deymier, G. Frantziskonis, G. Hong, B. Djafari-Rouhani, and L. Dobrzynski. Experimental evidence for the existence of absolute acoustic band gaps in two-dimensional periodic composite media. *J. Phys.: Condens. Matter*, 10(27):6051, 1998.

[125] A. Wautier and B. B. Guzina. On the second-order homogenization of wave motion in periodic media and the sound of a chessboard. *J. Mech. Phys. Solids*, 78:382–414, 2015.

[126] C. Willberg, S. Duczek, J. M. V. Perez, D. Schmicker, and U. Gabbert. Comparison of different higher order finite element schemes for the simulation of lamb waves. *Comput. Methods Appl. Mech. Eng.*, 241:246–261, 2012.

[127] J. R. Willis. Dynamics of composites. In *Continuum micromechanics*, pages 265–290. Springer, 1997.

[128] Y. Yi, S. Park, and S. Youn. Asymptotic homogenization of viscoelastic composites with periodic microstructures. *Int. J. Solids Struct.*, 35(17):2039–2055, 1998.

[129] Q. Yu and J. Fish. Multiscale asymptotic homogenization for multiphysics problems with multiple spatial and temporal scales: a coupled thermo-viscoelastic example problem. *Int. J. Solids Struct.*, 39(26):6429–6452, 2002.

[130] S. Yu, C. He, Z. Wang, F. Liu, X. Sun, Z. Li, H. Lu, M. Lu, X. Liu, and Y. Chen. Elastic pseudospin transport for integratable topological phononic circuits. *Nat. Commun.*, 9(1):3072, 2018.

[131] K. Y. Yuan, Y. S. Huang, H. T. Yang, and T. H. H. Pian. The inverse mapping and distortion measures for 8-node hexahedral isoparametric elements. *Comput. Mech.*, 14(2):189–199, 1994.

[132] S. Zhang and C. Oskay. Variational multiscale enrichment method with mixed boundary conditions for elasto-viscoplastic problems. *Comput. Mech.*, 55(4): 771–787, 2015.

[133] S. Zhang and C. Oskay. Reduced order variational multiscale enrichment method for elasto-viscoplastic problems. *Comput. Methods Appl. Mech. Eng.*, 300:199–224, 2016.

[134] S. Zhang and C. Oskay. Reduced order variational multiscale enrichment method for thermo-mechanical problems. *Comput. Mech.*, 59(6):887–907, 2017.

[135] X. Zhang and C. Oskay. Eigenstrain based reduced order homogenization for

polycrystalline materials. *Comput. Methods Appl. Mech. Eng.*, 297:408–436, 2015.

[136] X. Zhang and C. Oskay. Sparse and scalable eigenstrain-based reduced order homogenization models for polycrystal plasticity. *Comput. Methods Appl. Mech. Eng.*, 326:241–269, 2017.

[137] Y. Zhao and P. Wei. The band gap of 1d viscoelastic phononic crystal. *Comput. Mater. Sci*, 46(3):603–606, 2009.